A.I.Ch.E. JOURNAL

MARCH 1958 · VOL. 4, NO. 1

The A. I. Ch. E. Journal, an official publication of the American Institute of Chemical Engineers, is devoted in the main to theoretical developments and research in chemical engineering and allied branches of engineering and science. Manuscripts should be submitted to the New York office.

Publication Office, Richmond, Virginia. Published quarterly in March, June, September, and December by the American Institute of Chemical Engineers, 25 West 45 Street, New York 36 New York. Manuscripts and other communications should be sent to the New York office. Correspondence with the editor may be addressed to him at Yale University, 225 Prospect Street, New Haven 11, Connecticut. Statements and opinions in the *A.I.Ch.E. Journal* are those of the contributors, and the American Institute of Chemical Engineers assumes no responsibility for them. Subscriptions: one year, member $4.50, nonmember $9.00; two years, member $7.50, nonmember $15.00; additional yearly postage, Canada 50 cents, Pan American Union $1.50, other foreign $2.00 (foreign subscriptions payable in advance). Single copies: $3.00. Second-class mail privileges authorized at Richmond, Virginia. National headquarters of A.I.Ch.E. is concerned about nondelivery of copies of the *A.I.Ch.E. Journal* and urgently requests subscribers to give prompt notification of any change of address. Sixty days must be allowed for changes to be made in the records.

A.I.Ch.E. JOURNAL

You Can't Put Tail-fins on Data

One hears a great deal these days to the effect that we should have more scientists and engineers; that we should have more technical education; that we should go all-out with "crash programs," "beefed-up" curricula, and so on to solve the acute shortage. Well, it may be so. This observer certainly will agree that we need more *first-class* scientists and engineers just as we need more *first-class* lawyers, doctors, statesmen, and everyone else. The greater need, however, is for a better educated, more discerning public at large, a citizenry capable of distinguishing truth from error and fact from fancy. Since such discernment is the essence of science, it might be that our greatest contribution to the grave problems of our time would be more scientific education, and not necessarily more scientists.

This suggestion is made not because scientific education is necessarily applicable to the broader problems of life but rather because such education is strict, difficult, disciplined, and thorough—adjectives which do not exactly describe most of the group-oriented "togetherness" which passes for education these days. Certainly most of our students are capable of a lot more advanced work than they are now given. Certainly they could profit by the study of a field of knowledge in which orderly thinking is of paramount importance. And they could gain thereby some capacity for critical judgment, which would be most useful in ordinary life.

A properly taught course in almost any field of science could arouse in the high school student

1. A respect for critical inquiry. Science, and particularly natural science, began with asking questions about the world around us. Evoking a questioning attitude in students should be one of the first aims of a teacher. It is this aspect of science which leads, particularly in physical science and engineering, to the statement of a problem. It is this which can lead a neophyte to a concentration of his thinking and to a critical examination of the questions he is asking. A good student may soon learn that his questions are outpacing his capacity to find answers; there we have the beginnings of a specialist.
2. A sense of order. Nearly every branch of science and engineering stresses classification. When the natural world is explored, points of sameness and points of difference appear. These, too, can help a student with concentration of his thinking.
3. A respect for demonstrable truths. In science everything is capable of independent experimental verification. The chemistry laboratory is particularly suited for this. The idea that substances gain weight on combustion is not inherent in our natures. It can, however, be proved incontrovertibly in a simple experiment, and this could be used as a basis for explanations to the student that such proof is possible for every idea and concept in science.
4. A healthy skepticism. Once the questions are asked, skepticism about the answers follows. Physics and chemistry are full of erroneous starts which were corrected only by doubters. The caloric theory of heat and the phlogiston theory of combustion are typical. The student may even learn to question what he sees on the TV screen.
5. A sense of self-criticism and responsibility. The scientific worker poses a problem, devises a way to make measurements, observes the data, and reports his results. This is done quietly and without fanfare and with the full knowledge that some skeptical readers will probably doubt his conclusions. The scientist knows that he cannot dress up the data with tail-fins, he cannot obscure the issue by sheer lung power, and he cannot lure the skeptic into acquiescence by the soft sell, the hard sell, or even beautiful girls.

Acquaintance with such a branch of knowledge through reading scientific books and papers is certain to influence favorably the maturing process of a student. It is, of course, true that the problems of life are vastly more difficult than the special problems of science and engineering. But life can very probably be met more successfully through the aid of the scientific approach, with its free inquiry, orderliness, skepticism, and responsibility. Perhaps all our high school students should have some experience with it.

H.B.

Radiant Heat Exchange in a Gas-filled Enclosure: Allowance for Nonuniformity of Gas Temperature

H. C. HOTTEL and E. S. COHEN

Massachusetts Institute of Technology, Cambridge, Massachusetts

A method is presented for predicting the effect of allowance for radiation exchange on the distribution of temperature and heat transfer within a furnace chamber. The system is divided into surface zones and gas zones, the number being dependent on the desired accuracy of the result. Direct-exchange factors are available for gas-gas, gas-surface, and surface-surface zone interchange. From these factors one can determine the net exchange factor for any zone pair, making due allowance for interaction with all other zones. The resultant factors are then fed into a set of energy balances, one on each zone, which by simultaneous solution permit a determination of the space distribution of gas and surface temperatures and the distribution of heat flux over the surfaces.

The problem of the performance of an industrial furnace of specified shape and size, fed with fuel and air at specified rates and in a specified pattern, may be said to be solved when the temperature pattern in the gas space and along the walls can be predicted. The problem is in principle of course capable of solution if sufficient knowledge exists concerning the factors which control the flow pattern, the progress of combustion, and the transfer of heat by radiation and convection at every point in the system, but no one expects that an early solution to so extraordinarily complex a problem will be soon forthcoming. Presently available methods (*5*) permit determining the details of surface-temperature variation and surface–heat-flux variation for the special case of an assumed uniform temperature and composition of the gases in the furnace enclosure. The object here is to advance one stage further toward a general solution by removing the restriction of gas-temperature uniformity and to establish, in the course of the solution, space variation both in surface and in gas temperatures. The analysis is limited, however, to solution of the heat transfer problem; i.e., a description of the combustion and mixing patterns in the furnace enclosure is assumed available. Although the analysis is not limited to a system in which all parts of the gas volume are assumed to have identical values of absorption coefficient, allowance for departure from that assumption is only approximate. Despite these limitations, the new method enormously widens the range of problem types capable of solution. Although directed primarily toward application to industrial furnace chambers, the method can be used on such problems as studying temperature distribution in a glass pot.

If the bounding walls of an enclosure and the gas space in it are both divided into zones small enough to be considered isothermal, an energy balance may be made on each zone. For a gas zone the sum of the radiant energy ultimately received from all zones in the system (both gas and surface) plus the net conduction or convection to it from adjacent gas or surface elements plus the net enthalpy flux (chemical and sensible) to it due to bulk flow must equal the radiation originating within the gas zone—plus any increase in enthalpy of the zone during the time interval if the process is unsteady in time. Similarly, for a surface zone the sum of the radiant energy received from all zones (gas and surface) plus the net convection to the surface must equal the sum of the emission from the surface, the net flux out through it, and—if the process is unsteady in time—its increase in enthalpy. For any specific problem for which the flow pattern is given or assumed, every term in these equations, with the exception of the net wall fluxes, may be written as a function of unknown temperatures only, and the number of equations will be found equal to the number of unknowns—temperatures or wall fluxes. A solution of a set of these equations, one for each zone in the system, would yield the desired distribution of temperature and flux throughout the enclosure. The reader will note that when the zones are made infinitesimal the resulting quantitative relation is an integral equation and that the complicated boundary conditions make an analytical solution out of the question. The concept of a finite number of zones must consequently be retained.

It is necessary to evaluate the emission from either a gas zone or a surface zone and the radiant interchange between any two of these zones, making due allowance for absorption along every beam from one zone to another and for partial diffuse reflection of every beam at every surface, *ad infinitum*. Solution of the geometrical portion of this problem independently of the temperature distribution necessitates first a choice of a specific geometrical grid system. The choice was made of gas cubes or shapes constructable from cubes, and surface squares or shapes constructable from squares, with both the cube edge and the square side designated as B. With few exceptions, all enclosures of industrial importance may be adequately approximated as a cube-square system. (Work on the cylinder system is in progress.)

Initially, discussion will be restricted to a gas the absorptivity of which is independent of wave length and temperature, a "gray" gas. (This restriction will be removed later.) It may readily be shown that the emission rate dE_g from a volume dV of gas is given by

$$dE_g = 4K\mu^2\, dV \cdot \sigma T_g^4 \qquad (1)$$

where k is the absorption coefficient or fractional absorption by the gas per unit path length as the latter approaches zero, μ is the refractive index of the medium, and σT_g^4 is the rate of emission, into a medium of refractive index 1, of radiation from the unit area of a black surface or complete radiator at temperature T_g.

Then the emission rate E_g from a cube of a gray gas of edge B is given by

$$E_g = 4(kB)(B^2) \cdot \phi \cdot \mu^2 \sigma T_g^4 \qquad (2)$$

where ϕ is the fraction of the energy originating within the cube which leaves the boundaries of the cube. The escape factor ϕ, which is a function of kB only, has been obtained by multiple graphical integration as described in Appendix 1. A plot of the factor ϕ against kB is shown in Figure 1.

The emission rate from a surface square of side B into the medium of refractive index μ is given by

$$E_s = \epsilon_s (B^2) \cdot \mu^2 \sigma T_s^4 \qquad (3)$$

where ϵ_s is the emissivity of the surface, and all other symbols are as before except that the subscript s indicates that reference is to a surface zone. For enclo-

sures containing gas, μ is nearly 1 and may be ignored.

DIRECT INTERCHANGE BETWEEN ANY TWO ZONES

The interchange between any two zones in the system is the sum of the direct radiant flux between the two zones and the infinite number of reflected beams within the enclosure due to energy originating at either of the zones under consideration. (Note that the other zones in the system enter this formulation, if they are surfaces, only as reflectors and not as original radiators, and if they are gas zones, only as absorbers.) It is profitable to consider first only the direct interchange between two zones, i.e., the interchange in a black-walled system.

The following nomenclature will be established for one-way radiation flux, surface to surface, surface to gas, gas to to surface, and gas to gas, respectively:

$$q_{s_i s_j} = (\overline{s_i s_j})\mu^2\sigma T_{s_i}{}^4 \quad (4)$$

$$q_{s_i g_j} = (\overline{s_i g_j})\mu^2\sigma T_{s_i}{}^4 \quad (5)$$

$$q_{g_i s_j} = (\overline{g_i s_j})\mu^2\sigma T_{g_i}{}^4 \quad (6)$$

$$q_{g_i g_j} = (\overline{g_i g_j})\mu^2\sigma T_{g_i}{}^4 \quad (7)$$

Here q is the one-way radiant heat transfer from the source zone, indicated by the first subscript, to the receiver zone, indicated by the second; the terms $\overline{s_i s_j}$, $\overline{s_i g_j}$, $\overline{g_i s_j}$, and $\overline{g_i g_j}$, are designated as *direct-interchange areas—direct interchange* to remind the reader that a description of both the sender and the receiver of the radiation is essential and *area* to indicate the dimensions of the term.

The direct-interchange area may be thought of as the product of two terms. The first, having the dimensions of area, is the actual area for a surface zone and (4) (volume) (absorption coefficient) for a gas zone. The second is the *reception factor* f of one of three kinds. When the receiver is a surface element separated from the emitter by a nonabsorbing gas and the emitter is a surface element, f has been referred to in the literature as the *direct-view factor* F (5). For flux from emitter through an absorbing gas to a surface, f is the product of a direct-view factor and a gas transmittance τ, although the two are not strictly separable after integration over a finite receiver. When a gas volume is the receiver, f includes as an additional multiplier the absorptivity α of the receiver (again, $f \equiv F\tau\alpha$ is not separable into F, τ, and α). In general, then, f is the fraction of the energy originating in any zone in the enclosure which reaches and is absorbed by any other zone (surfaces are for this definition black). The two subscripts on f indicate in sequence the emitter and absorber.

Values of these reception factors, f, for the interchange between two squares in either parallel or perpendicular planes, for a square and a cube, and for two cubes have been obtained by multiple graphical integration as described in Appendix 2. A set of recommended working plots, Figures 2 through 5, give the various types of reception factors as functions of $\Delta x/B$, $\Delta y/B$, and $\Delta z/B$—the distances between the centers of two zones measured along the three coordinate axes—and kB, where k is the absorption coefficient of the gas. For parallel squares, Figure 2, the unique dimension z is the distance between their planes; x and y are interchangeable. For perpendicular squares, Figure 3, the unique dimension z is the distance not perpendicular to the plane of either square. For cubes to squares, Figure 4, the unique dimension z is the perpendicular distance from the square plane. For Figure 5 all three dimensions are interchangeable. To condense Figures 4 and 5 it was found that division of f by ϕ (Figure 4) and by $kB\phi$ (Figure 5) was desirable before plotting. It is to be noted that for any gas cube g_i the escape factor ϕ used in correlation is equal to $(1 - f_{g_i g_i})$, or the complement of the self-irradiation factor of the cube.

Figures 2 to 5 give f's for values of the ratio (center-to-center distance between radiator and receiver)/(edge dimension of either) up to at least 3. For greater separating distances, f rapidly approaches a limiting value capable of simple analytical expression. (See Appendix 3.)

Since the net flux between a gas volume and a surface element, equal to the difference of two one-way flux terms, must become zero when the two radiators are at the same temperature, it follows that, if the absorption coefficient is the same in the two one-way terms regardless of temperature, then

$$\left.\begin{aligned} \overline{g_1 s_2} &= \overline{s_2 g_1} \\ \text{or} \quad 4kV_{g_1}\cdot f_{g_1 s_2} &= A_{s_2} f_{s_2 g_1} \\ \text{or} \quad 4kBf_{g_1 s_2} &= f_{s_2 g_1} \end{aligned}\right\} \quad (8)$$

Similarly,

$$\overline{g_1 g_2} = \overline{g_2 g_1}, \quad \text{and} \quad \overline{s_1 s_2} = \overline{s_2 s_1} \quad (9)$$

These constitute, for direct radiation exchange, the general statement of reciprocity, of which the older relation, $A_1F_{12} = A_2F_{21}$ (or $\overline{12} = \overline{21}$)(5), was a specific example.

Since the reception factors have been evaluated for cubes and squares, the enclosure must be so divided into isothermal zones that the latter can be built up from cubical or square units. The value of B to be used is the largest factor common to every zone in the enclosure. The size of the zone is limited by the maximum volume or area which is justifiably considered isothermal and to a lesser extent by the desire to keep the "view" of surrounding zones the same for all the units comprising the zone in question. This second limitation is of lesser importance, since it affects only the distribution of radiation on reflection or reemission following absorption, and not any original beams. The technique of building up the factors for more complicated shapes may be illustrated by reference to Figure 6. The one-way reception of energy at gas zone g_1 consisting of two units, due to emission from the gas contained in gas zone g_1, is

$$\frac{q_{g_1 \to g_1}}{\mu^2\sigma T_{g_1}{}^4} \equiv \overline{g_1 g_1}$$

$$= 4kB^3(f_{g_a g_b} + f_{g_a g_a} + f_{g_b g_a} + f_{g_b g_b})$$

$$= 4(kB)(B^2)(2f_{g_a g_b} + 2(1 - \phi)) \quad (10)$$

Similarly, the reception at surface zone s_1, consisting of three units, from gas zone g_1 is

$$\frac{q_{g_1 \to s_1}}{\mu^2\sigma T_{g_1}{}^4} \equiv \overline{g_1 s_1}$$

$$= 4(kB)(B^2)(f_{g_a s_c} + f_{g_a s_d} + f_{g_a s_e} + f_{g_b s_c} + f_{g_b s_d} + f_{g_b s_e}) \quad (11)$$

A corollary of this discussion is that the total of all the "areas" representing flux from any one zone to each of the others in the enclosure, including itself, must equal the energy originating from that zone, per unit emissive power, or

$$\overline{s_1 s_1} + \overline{s_1 s_2} + \overline{s_1 s_3} + \cdots + \overline{s_1 g_1} + \overline{s_1 g_2} + \overline{s_1 g_3} + \cdots = A_{s_1} \quad (12)$$

or

$$\sum_i \overline{s_1 s_i} + \sum_i \overline{s_1 g_i} = A_{s_1} \quad (13)$$

and

$$\overline{g_1 g_1} + \overline{g_1 g_2} + \overline{g_1 g_3} + \cdots + \overline{g_1 s_1} + \overline{g_1 s_2} + \overline{g_1 s_3} + \cdots = 4kV_{g_1} \quad (14)$$

or

$$\sum_i g_1 g_i + \sum_i g_1 s_i = 4kV_{g_1} \quad (15)$$

TOTAL INTERCHANGE BETWEEN ANY TWO ZONES: ALLOWANCE FOR REFLECTIONS AT THE WALLS

Discussion so far has been restricted to a black-walled system. Actual furnace walls, however, are partial reflectors and, fortunately for the present purpose, much more nearly diffuse than specular reflectors; i.e., their reflection, like black-surface emission, follows Lambert's cosine law. This reflected energy is distributed among all the gas and all the surfaces in accordance with the geometrical configuration of the various surfaces and the absorbing power of the gas, and that portion incident on the surfaces is again partially absorbed and partially reflected, to repeat the process *ad infinitum*.

The technique for making allowance for this complicated problem is an extension of one presented (5) for the one-gas–zone, multisurfaced enclosure. As

in the earlier published treatment where the direct interchange between two zones was equal to the difference in emissive powers multiplied by $A_1F_{12}\tau_{12}$ when the zones were surface elements, or a gas-emissivity–area product when one element was the gas zone, so in the present case is the direct interchange equal to a term $\overline{s_1s_2}$, $\overline{g_1g_2}$, $\overline{g_1s_2}$, etc. Similarly, if one allows for the multiple reflections within the enclosure, in the earlier treatment the net interchange per unit difference in emissive powers became $A_1\mathfrak{F}_{12}$ or $A_1\mathfrak{F}_{1\sigma}$; in the present case it may be defined as $\overline{S_1S_2}$, $\overline{G_1S_2}$, or $\overline{G_1G_2}$. And just as it was possible to obtain the values of $A\mathfrak{F}$ from the values of AF, again one can evaluate such terms as $\overline{SS}$, $\overline{GS}$ or $\overline{GG}$ from the terms $\overline{ss}$, $\overline{gs}$, or $\overline{gg}$. Note that the terms $\overline{SS}$, $\overline{GS}$ and $\overline{GG}$, like their lower-case counterparts and like the older $A\mathfrak{F}$, all have the dimensions of area; they will be referred to as *total-interchange area* terms. Note also that, whereas a direct-interchange area specific to two particular zones can be evaluated from knowledge of these two zones alone, the total-interchange area applicable to the same two zones will require knowledge of all zones that they can "see," either directly or by wall reflection.

It is plain that the interchange area between any two zones in the enclosure cannot be a function of temperature as long as the physical properties of the system (emissivities and absorptivities) are independent of temperature. With this limitation, one is justified in evaluating the interchange-area terms at any convenient temperature, and the result will be completely general. The problem of evaluating these terms is simplified if one assigns a value of absolute zero to the temperature of *every surface and gas zone except* ONE, as a consequence of which the emissive powers of every zone except one are all zero. This necessitates an imagined energy withdrawal from all zones, including the gas zones, by means unspecified but not interfering with transmission. Furthermore, one can assign a temperature to the one emitting zone that will make its black emissive power 1; i.e., so that $\mu^2\sigma T^4$ is 1. As a result of maintaining this temperature at the single surface or gas zone, there will be a radiant flux at and toward every surface in the system, and at and away from it as well, owing solely to original emission from the one zone and to the multiple reflections within the enclosure. In a black system this reflected flux would be equal to zero. The terminology to describe this outgoing flux density will be R, with a presubscript designating the original source of the energy and a final subscript the reflecting surface. Thus if gas zone g_1 were the only emitter in the system, the flux densities leaving surfaces $s_1, s_2, \cdots$ would be indicated by ${}_{g_1}R_{s_1}, {}_{g_1}R_{s_2}, \cdots$.

$$
\begin{aligned}
(\overline{s_1s_1}\cdot {}_{g_i}R_{s_1} + \overline{s_1s_2}\cdot {}_{g_i}R_{s_2} + \overline{s_1s_3}\cdot {}_{g_i}R_{s_3} + \cdots \overline{g_is_1})\rho_{s_1} &= A_{s_1}\cdot {}_{g_i}R_{s_1}\\
(\overline{s_1s_2}\cdot {}_{g_i}R_{s_1} + \overline{s_2s_2}\cdot {}_{g_i}R_{s_2} + \overline{s_2s_3}\cdot {}_{g_i}R_{s_3} + \cdots \overline{g_is_2})\rho_{s_2} &= A_{s_2}\cdot {}_{g_i}R_{s_2}\\
(\overline{s_1s_3}\cdot {}_{g_i}R_{s_1} + \overline{s_2s_3}\cdot {}_{g_i}R_{s_2} + \overline{s_3s_3}\cdot {}_{g_i}R_{s_3} + \cdots \overline{g_is_3})\rho_{s_3} &= A_{s_3}\cdot {}_{g_i}R_{s_3}\\
\vdots \quad\quad \vdots \quad\quad \vdots \quad\quad \vdots\ \vdots \quad\quad \vdots
\end{aligned}
\tag{17}
$$

Similarly, if surface s_1 were the only original emitter, the flux density leaving surfaces $s_2, s_3 \cdots$ would be ${}_{s_1}R_{s_2}, {}_{s_1}R_{s_3}, \cdots$ but the flux density leaving surface s_1 would be equal to ${}_{s_1}R_{s_1}$, owing to reflections, plus ϵ_{s_1} to allow for original emission from the surface.

1. Original Emitter Is a Gas Zone

If, for example, gas zone g_i is the sole original emitter, then the total radiant flux at and away from any surface such as s_j in the system is designated as ${}_{g_i}R_{s_j}\cdot A_{s_j}$. Since this is the reflected flux, multiplication by the ratio of absorptivity (equal to emissivity) of the surface to the reflectivity of the surface (the complement of absorptivity) yields the rate of energy absorption at the surface; and since the value of $\mu^2\sigma T^4$ of the original emitter was made equal to unity, this must by definition be identical with the desired total-interchange area $\overline{G_iS_j}$; or

$$
\overline{G_iS_j} = \overline{S_jG_i} = {}_{g_i}R_{s_j}\cdot\frac{A_{s_j}\epsilon_{s_j}}{\rho_{s_j}} \tag{16}
$$

where the reflectivity $1 - \alpha_{s_j}$ has been designated by the single term ρ_{s_j} because it will appear so often. The problem of finding $\overline{G_iS_j}$ has thus been reduced to one of determining the reflected flux ${}_{g_i}R_{s_j}$. To do that one must solve the system of simultaneous equations resulting from writing a radiant energy balance on each surface. The total rate of energy impingement on surface s_i is equal to the contributions from all the surfaces in the system, including itself, plus the energy it receives directly from the single gas zone which is the original emitter. If the sum of all these terms is then multiplied by the surface reflectivity, the result, which is the reflected flux, must be equal to ${}_{g_i}R_{s_i}\cdot A_{s_i}$. This summation can be carried out for every surface in the system, yielding a set of linear equations, one for each surface, as follows:

These may be expressed more compactly as

$$
\begin{aligned}
\sum_j \overline{s_1s_j}\cdot {}_{g_i}R_{s_j} - \frac{A_{s_1}\cdot {}_{g_i}R_{s_1}}{\rho_{s_1}} &= -\overline{g_is_1}\\
\sum_j \overline{s_2s_j}\cdot {}_{g_i}R_{s_j} - \frac{A_{s_2}\cdot {}_{g_i}R_{s_2}}{\rho_{s_2}} &= -\overline{g_is_2}
\end{aligned}
\tag{17a}
$$

The solution for any one of the unknowns, ${}_{g_i}R_{s_j}$, may be expressed in determinant form as

$$
{}_{g_i}R_{s_j} = \frac{{}_{g_i}D_{s_j}}{D} \tag{18}
$$

where the determinant D in the denominator is given by

$$
D = \begin{vmatrix}
\overline{s_1s_1} - \dfrac{A_{s_1}}{\rho_{s_1}} & \overline{s_1s_2} & \overline{s_1s_3} & \cdots\\
\overline{s_1s_2} & \overline{s_2s_2} - \dfrac{A_{s_2}}{\rho_{s_2}} & \overline{s_2s_3} & \cdots\\
\overline{s_1s_3} & \overline{s_2s_3} & \overline{s_3s_3} - \dfrac{A_{s_3}}{\rho_{s_3}} & \cdots\\
\vdots & \vdots & \vdots &
\end{vmatrix}
\tag{19}
$$

and ${}_{g_i}D_{s_j}$ is formed from D by replacing its s_j column (the one having j common to the subscripts of all elements) by the terms $-\overline{g_is_1}$, $-\overline{g_is_2}$, $-\overline{g_is_3}$, $\cdots$. It is to be noted that the value of D is independent of which gas volume is the original emitter, although the value of ${}_{g_i}D_{s_j}$ is not.

Returning now to the expression for the term $\overline{G_iS_j}$ in Equation (16) and substituting the value of ${}_{g_i}R_{s_j}$ from Equation (18), one obtains as the general expression for $\overline{G_iS_j}$ or $\overline{S_jG_i}$,

$$
\overline{G_iS_j} \equiv \overline{S_jG_i} = \frac{A_{s_j}\epsilon_{s_j}}{\rho_{s_j}}\cdot\frac{{}_{g_i}D_{s_j}}{D} \tag{20}
$$

From the value of the reflected flux density at the various surfaces it is also possible to calculate the total-interchange area between any two gas cubes. If gas zone g_m is the original emitter, then the total reception at any other gas zone such as zone g_n is equal to $\overline{g_mg_n}$, the direct radiation from g_m to g_n, plus the sum of the products of the reflected flux at each surface in the system multiplied by the fraction of that flux which reaches, and is absorbed by, gas zone g_n. Again, since the black-body emission from zone

g_m has been set at 1, this sum represents the desired $\overline{G_mG_n}$; or

$$\overline{G_mG_n} = \overline{g_mg_n} + \sum_i ({}_{g_m}R_{s_i})(\overline{s_ig_n}) \quad (21)$$

2. Original Emitter Is a Surface Zone

In order to obtain the one remaining kind of total-interchange area, that between two surfaces, it is convenient to assign a temperature to one of the surface zones that will permit its blackbody emission to become equal to 1 and to let all other surfaces as well as all gas zones be at absolute zero. One can again write energy balances on each surface in the system, the only changes being that there will be no direct radiation from the gas and that the surface that is the original emitter will send out, in addition to the reflected-flux term, an amount of energy per unit area equal to its emissivity. The set of resultant equations for this case, when surface s_1 is the sole original emitter, is

$$\begin{aligned}
&(\overline{s_1s_1}({}_{s_1}R_{s_1} + \epsilon_{s_1}) + \overline{s_1s_2}\cdot{}_{s_1}R_{s_2} + \overline{s_1s_3} \\
&\quad \cdot{}_{s_1}R_{s_3} + \cdots)\rho_{s_1} = A_{s_1}\cdot{}_{s_1}R_{s_1} \\
&(\overline{s_1s_2}({}_{s_1}R_{s_1} + \epsilon_{s_1}) + \overline{s_2s_2}\cdot{}_{s_1}R_{s_2} + \overline{s_2s_3} \\
&\quad \cdot{}_{s_1}R_{s_3} + \cdots)\rho_{s_2} = A_{s_2}\cdot{}_{s_1}R_{s_2} \quad (22) \\
&(\overline{s_1s_3}({}_{s_1}R_{s_1} + \epsilon_{s_1}) + \overline{s_2s_3}\cdot{}_{s_1}R_{s_2} + \overline{s_3s_3} \\
&\quad \cdot{}_{s_1}R_{s_3} + \cdots)\rho_{s_3} = A_{s_3}\cdot{}_{s_1}R_{s_3}
\end{aligned}$$

[This will be recognized as identical, except for nomenclature, to the system of equations covering the published case (5) of a multiple-surface-zone–single-gas-zone system.] The solution for any one of the unknowns ${}_{s_i}R_{s_1}$ is

$${}_{s_i}R_{s_1} = \frac{{}_{s_i}D_{s_1}}{D} \quad (23)$$

where D is the same as the expression obtained earlier and given in Equation (19) and ${}_{s_i}D_{s_j}$ is obtained by substituting into the s_i column of D the terms $-\epsilon_{s_i}\cdot\overline{s_is_1}$, $-\epsilon_{s_i}\cdot\overline{s_is_2}$, $-\epsilon_{s_i}\cdot\overline{s_is_3}$ $\cdots$.

If this value of the reflected-flux density is multiplied by the area of surface s_j and then by the ratio of the absorptivity to the reflectivity, one obtains the absorption rate at surface s_i due to original emission from surface s_i. This is equal to the desired quantity $\overline{S_iS_j}$, since the black emissive power of the original emitter was made equal to 1; or

$$\overline{S_iS_j} = \frac{A_{s_j}\epsilon_{s_j}}{\rho_{s_j}}\cdot\frac{{}_{s_i}D_{s_j}}{D} \equiv \frac{A_{s_i}\epsilon_{s_i}}{\rho_{s_i}}\cdot\frac{{}_{s_j}D_{s_i}}{D} = \overline{S_iS_j}\,^* \quad (24)$$

*Easier to use but the equivalent of this formulation is the statement that

$$\overline{S_iS_j} = \frac{A_{s_j}\epsilon_{s_j}}{\rho_{s_j}}\cdot\frac{A_{s_i}\epsilon_{s_i}}{\rho_{s_i}}\cdot\frac{D'_{s_is_j}}{D}$$

where $D'_{s_is_j}$ is the cofactor of row s_i and column s_j, defined as $(-1)^{(i+j}$ times the minor of D formed by crossing out the s_i row and s_j column of D. This is correct except when $i = j$, for which case

$$\overline{S_iS_i} = \frac{A_{s_i}\epsilon_{s_i}}{\rho_{s_i}}\left(\epsilon_{s_i} + \frac{A_{s_i}\epsilon_{s_i}}{\rho_{s_i}}\right)\frac{D'_{s_is_i}}{D}.$$

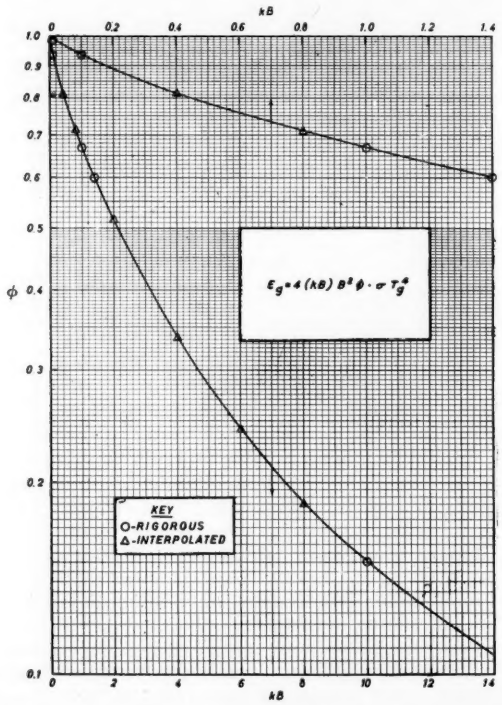

Fig. 1. Escape factor ϕ for emission from a cube of edge B filled with gas of absorption coefficient k.

Two important consequences of the definitions of these three kinds of total-interchange areas, analogous to Equations (13) and (15), are

$$\sum_i \overline{S_iS_i} + \sum_i \overline{S_iG_i} = \epsilon_{s_i}\cdot A_{s_i} \quad (25)$$

$$\sum_j \overline{G_iG_j} + \sum_j \overline{G_iS_j} = 4kV_{g_i} \quad (26)$$

In the most general case, the order of the determinants to be evaluated is equal to the number of surfaces present; the total number of sets of them to be evaluated as a consequence of letting each gas zone and surface zone be original emitters is equal to the total number of zones, gas and surface, in the enclosure; each set involves the evaluation of a number of determinants equal to the total number of surface zones in the system, and, in addition, one must evaluate the common-denominator determinant D once. An alternative procedure for the solution of sets of equations like (17) and (22) would be the use of the Crout Method (2) or of high-speed computing machines.

ALLOWANCE FOR A REAL GAS

A real gas, in contrast to the hypothetical uniformly absorbing gray gas used in the preceding derivations, exhibits a variation in absorption coefficient with wave length, which affects the validity of the method presented in several ways.

1. The total emissivity or absorptivity of the gas does not conform to the Beer's-Law exponential expression which characterizes monochromatic or gray-gas radiation and therefore does not approach 1 as a limit as the path length is increased.

2. Since by Planck's Law the wavelength range of interest depends on temperature, total gas emissivity is temperature dependent.

3. Gas absorptivity also depends on temperature.

4. Space variations in composition of the gas may cause local variations in its absorptivity and emissivity.

It has been shown (5) that, since the variation, with path length x, of the emissivity or absorptivity of a real gas is representable by the weighted sum of a number of e functions

$$\sum_i a_i(1 - e^{-k_ix}), \quad \text{with} \quad \sum a_i = 1,$$

it follows that the contribution of the real gas to radiant flux in an enclosure is the weighted sum of the independent contributions of several gray gases of different absorption coefficients k_i, weighted in proportion to the coefficients a_i. It has also been shown (5) that for one-gas-zone systems the calculated values of radiant flux are generally of adequate numerical accuracy when based on the assumption that the real gas is replaceable by but two "gray" gases one of which has an absorption coefficient k

and a weighting factor a and the other an absorption coefficient of 0 (i.e., a "clear" gas) and a weighting factor of $1 - a$. (These values of k and a, however, are not to be considered intrinsic properties of the gas; they must be fitted to the problem at hand.) For the case of a gas composed of a single gray and a clear component the total emissivity and absorptivity are related to the path length x by

$$\epsilon_x = a(1 - e^{-kx}) \tag{27}$$

and the unattenuated emission per unit volume is changed from $4k(\mu^2\sigma T^4)$ to $4ka(\mu^2\sigma T^4)$. If one fits the exponential above to the actual emissivity–vs.–path-length curve for a real gas at three path lengths—namely, zero path length, a path length equal to the primary path length L for the system (for which emissivity equals ϵ_L), and a path length twice this value (for which emissivity equals ϵ_{2L})—it may be shown (*5*) that a and kL are given by the relations

$$a = \frac{(\epsilon_L)^2}{2\epsilon_L - \epsilon_{2L}} \tag{28}$$

and

$$kL = \ln \frac{\epsilon_L}{\epsilon_{2L} - \epsilon_L}$$

$$= -\ln (1 - \epsilon_L/a) \tag{29}$$

If because of high diathermancy of the gas and/or high wall reflectivity it is desirable to fit the ϵ-x curve at 0 and L but at nL instead of $2L$, it can readily be shown that instead of (28), a is obtained from the relation

$$1 - \epsilon_{nL}/a = (1 - \epsilon_L/a)^n \tag{30}$$

and kL is obtained as before from relation (29). For the case of $n = 3$, (30) yields

$$a = \frac{2\epsilon_L}{3 - \sqrt{4(\epsilon_{3L}/\epsilon_L) - 3}} \tag{31}$$

As a consequence of this method of handling a real gas the total-interchange areas to be used become

$$\overline{SS} = a[\overline{SS}]_k + (1 - a)[\overline{SS}]_{k=0} \tag{32}$$

$$\overline{GS} = a[\overline{GS}]_k \tag{33}$$

$$\overline{GG} = a[\overline{GG}]_k \tag{34}$$

Total gas emissivity is temperature dependent, primarily because of the Planck's Law shift with temperature in the wave lengths of importance, secondarily because the absorption coefficients of the gas are themselves dependent on temperature. The numerical effect of this variation can be expressed, in conformity with the treatment of section 1 just preceding, as an effect on a and k. For the particular case of gas radiation due only to water vapor and carbon dioxide at equal partial pressures, it is found that over the temperature range of 1,000° to 3,500°R. (1) k is constant to within $\pm 4\%$ at values of PL below 0.4 foot-atmosphere and to within $\pm 30\%$ at a value of 1 ft.-atmosphere and (2) a decreases by about a factor of 2 at all values of $\sum PL$ up to 1 ft.-atmosphere when the temperature is increased 3.5-fold, or decreases 20 to 30% for a temperature change of 1,000°F. The variation in kL is tolerable, particularly at low values of $\sum PL$; the variation in a is less acceptable and stands as a source of error in use of the method on a furnace with large space variation in gas temperature. Greatest weight should be given to the a of that part of the system responsible for the major heat transfer. It should be emphasized here that choice of a and k to conform to conditions in that part of the enclosure which contributes most of the heat transfer will yield a solution the range of error of which is but a small fraction of the range of error in a and k mentioned above.

In principle, it is possible to go one step further toward a rigorous solution. When the total-interchange-area terms from a given zone, say g_1, to each of the others in the system are evaluated with a k based on the temperature of that zone, the error introduced cannot be large, as indicated by the following. The interchange with adjacent zones will be nearly correct since their temperature and hence their k will not be very far from the values of zone g_1; the interchange area with a zone very far away and consequently at a considerably different temperature will be in error, but because the term itself is so small one can tolerate a very substantial error in it. It would be possible to go through the procedure of evaluating total-interchange areas, letting each zone in turn be the original emitter in the system, and evaluating each set of areas at the k of the emitting zone. One result of such a technique would be that $\overline{G_1G_2}$ would be different from $\overline{G_2G_1}$ since the two are based on k's evaluated at T_{g_1} and T_{g_2}, respectively. To carry out such a procedure it would be necessary first to guess all the temperatures in the system and then, after a first solution to the problem, to revise the estimates of temperature and begin all over if the original assumptions were very much in error. Furthermore, the amount of work required to calculate the total-interchange areas would be increased considerably since the determinant D in Equations (18), (20), (23), and (24) would have to be completely reevaluated as each zone in turn became the original emitter. Although in principle one could more closely approach a rigorous solution by this technique, the labor involved would be prohibitive; and in engineering use one would generally introduce the approximation that gas emission and absorption properties can be evaluated at a single mean temperature.

When the mean surface temperature is either very high or very low compared with the gas temperature, one of the two processes, gas emission to the surface or gas absorption of surface emission, dominates the interchange. The use of an a and k corresponding to the dominant mechanism then yields numerically satisfactory results. If, for example, the surface is relatively cold the method will allow incorrectly for absorption, by the gas, of original surface emission, but the effect on the net flux is unimportant; and correct allowance will be made for self-absorption in the gas due to wall reflections. The surface satisfies this condition when its emissive power is that of a black surface at less than two-thirds the absolute gas temperature.

Gas absorptivity depends primarily on the temperature of the emitter, secondarily on that of the gas, because absorption coefficients depend somewhat on temperature. Except where gas and surface temperatures are the same, gas absorptivity of surface radiation and gas emissivity are different. By the very nature of the calculational technique being developed, however, one is forced into using for the entire system a single pair of mean values for a and k which will be able to account for both emission and absorption at all the temperature levels of importance in the enclosure. The error so introduced can be minimized by some such procedure as the following.

Although interchange between a uniform-temperature gas mass and surrounding black walls at a uniform temperature actually involves the difference between gas emission and gas absorption, it may be satisfactorily approximated by a simpler expression when the surface temperature is no less than two-thirds the gas temperature. That expression (*5*) is

$$q_{g \rightleftharpoons s} = \epsilon_{g,T_{avg}} \cdot K \cdot \sigma(T_g^4 - T_s^4) \tag{35}$$

where $\epsilon_{g,T_{avg}}$ is the gas emissivity evaluated at the arithmetic mean of the gas and surface temperatures and where

$$K = \frac{4 + d + b - c}{4} \tag{36}$$

For evaluating K, d and b are the fractional changes in gas emissivity per unit fractional change in PL and T_g, respectively (i.e., $\partial \ln \epsilon_g / \partial \ln PL$ and $\partial \ln \epsilon_g / \partial \ln T_g$), and c is an empirical constant (*4*, *5*) used in evaluating absorptivity from emissivity, equal to 0.65 for carbon dioxide and 0.45 for water vapor.

For a gray rather than black-walled system it may be shown (Appendix 4) that the term $\epsilon_{g,T_{avg}} K$ of Equation (35) is replaced by the infinite series

$$\epsilon_s^2 \sum_{n=1}^{\infty} \rho_s^{n-1} K \epsilon_{g,nL,T_{avg}}$$

This is identical with the result obtained when the method of this paper is applied to the single-gas-zone single-wall-zone

case, provided a single pair of values of a and k is used corresponding to an effective gas emissivity $K\ \epsilon_{g,T_{avg}}$ rather than ϵ_g. Accordingly, a single value for emissivity and absorptivity, equal to $K\ \epsilon_{g,T_{avg}}$ [where $T_{avg} = (T_s + T_g)/2$] and evaluated at the two path lengths necessary to determine a and k, may be used to represent satisfactorily both emission and absorption. Choice of representative mean temperatures T_g and T_s to use in these relations remains a problem. For gases containing carbon dioxide and water in equal proportions, a 200°F. error in choice of T_{avg} produces a 10 to 20% error in $K\epsilon_g$. It is recommended that for any furnace enclosure in which the gas temperature varies enough to make a choice of representative temperature doubtful, a preliminary solution of the problem be carried out by means of the one-gas–zone technique already available (5) and that the resulting temperature be used for T_g.

Limited allowance for the effect of local variations in concentration of the absorbing or emitting components of the gas may be made. Appendix 5 presents an approximation for that case in which the fluctuation in concentration produces local changes only in k and not in a.

ENTHALPY FLUX, CONVECTIVE FLUX, AND STORAGE

The only remaining terms to be evaluated for use in the total-energy balance on each zone are the nonradiation terms, enthalpy flux, convective flux and, when conditions are not steady in time, energy storage. If detailed knowledge of the gas composition, the direction of flow, and the molal flow rate G_m per unit area is available for every point in the enclosure, the net energy transferred across a boundary between any two gas zones may be evaluated. It is

$$\int_A G_{m_n}(H_s + H_c)\, dA \qquad (37)$$

where G_{m_n} is the component of G_m normal to dA, and H_s and H_c are the molal sensible enthalpy and the molal chemical enthalpy of the stream, both evaluated at the temperature of the zone from which the gas flows.

Similarly, the *one-way* convective flux to or from a gas or surface zone may be written as

$$\int_A h_c T\, dA \qquad (38)$$

where the temperature to be used (gas or surface) depends on the source of the energy and h_c is the convection coefficient. For transport between gas and surface, values of h_c are given by McAdams (6); for transport between adjacent gas zones (when significant compared with transport by the mean or bulk flow) an estimate of the coefficient may be made from the eddy diffusivities in pipes and jets (3, 7).

The energy storage rate in a zone is its heat capacity C_s or C_g times $\dot{T}$, the rate of temperature rise.

Since all the radiation terms in the energy balances are given as multiples of T^4, it is desirable to linearize the equations in T^4 by forcing the convection and enthalpy-flux terms into a fourth-power law. A new coefficient may be defined such that when multiplied by σT^4 (hereafter termed W for simplicity) it will yield the one-way flux between any two zones. If the enthalpy flux and convective flux coefficients are denoted by η and γ respectively, with a first subscript representing the energy-source zone and a second one the energy-sink zone, they become

$$\eta_{g_1 g_i} = \frac{\int_A G_{m_n}(H_s + H_c)_{T_{g_i}}\, dA}{W_{g_1}} \qquad (39)$$

$$\gamma_{g_1 g_i} = \frac{\int_A h_c T_{g_1}\, dA}{W_{g_1}} \qquad (40)$$

and

$$\gamma_{s_1 g_i} = \frac{\int_A h_c T_{s_1}\, dA}{W_{s_1}} \qquad (41)$$

where A is the area common to zones 1 and i and G_{m_n} is the normal flow, from zone 1 to zone i, through that area.

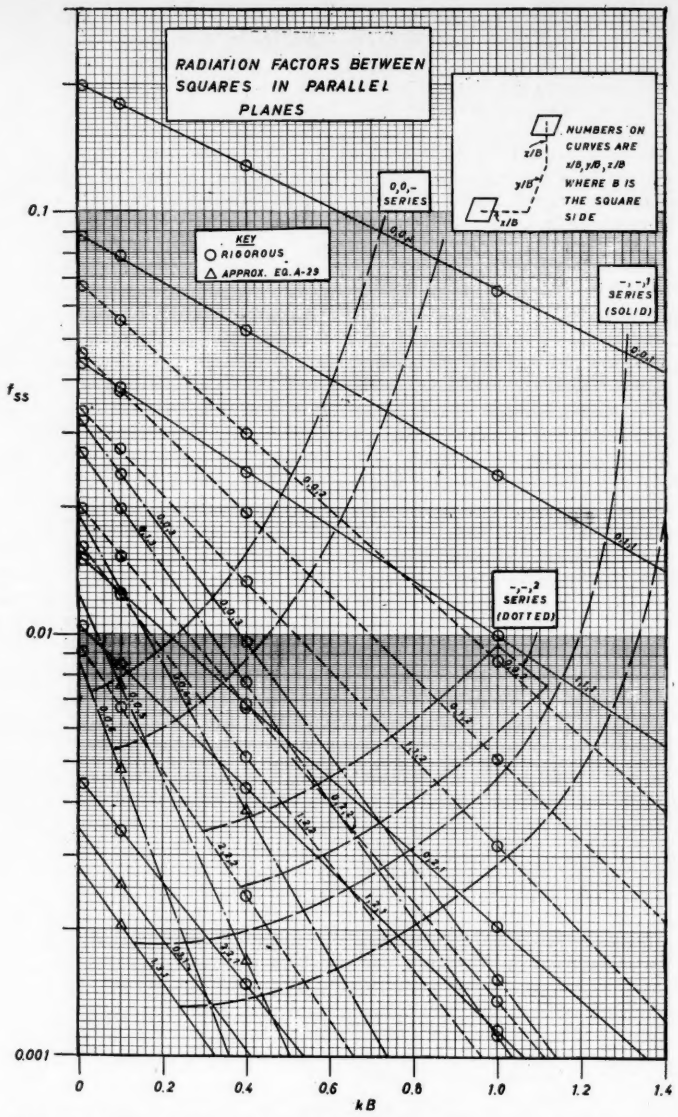

Fig. 2. Reception factor f_{ss} between squares of side B in perpendicular planes (f_{ss} = direct-view factor × transmittance).

Terms $\eta_{g_1 s_i}$ will appear only when a surface s_i sharing an area with g_1 contains ports through which gas flows, causing enthalpy flux out of the system. The coefficients η and γ have the dimensions of area.

FORMULATION OF ENERGY BALANCES

With the convention that a positive q represents flux to an element in question, the energy interchange between gas zone g_1 and all other zones (g_2, g_3, $\cdots$ g_i, s_1, s_2, $\cdots$ s_j, those having a common boundary with g_1; g_{10}, g_{11}, $\cdots$, s_{10}, s_{11}, $\cdots$ those not touching g_1) will take the form

$$W_{g_1}(\overline{G_1G_1} - 4kaV_{g_1} - \sum_i \gamma_{g_1 g_i} - \sum_j \gamma_{g_1 s_j} - \sum_i \eta_{g_1 g_i} - \sum_j \eta_{g_1 s_j}) + W_{g_2}(\overline{G_2G_1} + \gamma_{g_2 g_1} + \eta_{g_2 g_1}) + W_{g_3}(\overline{G_3G_1} + \gamma_{g_3 g_1} + \eta_{g_3 g_1}) + \cdots + W_{g_{10}}(\overline{G_{10}G_1}) + W_{g_{11}}(\overline{G_{11}G_1}) + \cdots + W_{s_1}(\overline{S_1G_1} + \gamma_{s_1 g_1}) + W_{s_2}(\overline{S_2G_1} + \gamma_{s_2 g_1}) + \cdots + W_{s_{10}}(S_{10}G_1) + W_{s_{11}}(S_{11}G_1) + \cdots + \dot{M}(H_c + H_s)_{in} - C_{g_1}\dot{T}_{g_1} = 0 \quad (42)$$

In this expression $\sum_i \gamma_{g_1 g_i}$ and $\sum_j \gamma_{g_1 s_j}$ represent the one-way convection from zone g_1 to every zone with which it shares an area; $\sum_i \eta_{g_1 g_i}$, however, represents the sum of enthalpy fluxes only for those zones g_i into which gas flows *from* g_1. Where gas flow is *into* g_1 from g_i, the enthalpy flux term, which will be $\eta_{g_i g_1}$, will appear as part of the coefficient of W_{g_i}. For simplification of notation for use in a later step, the following substitute notation will be used:

$$\sum_i \gamma_{g_1 g_i} + \sum_j \gamma_{g_1 s_j} = \gamma_{g_1} \quad (43)$$

and

$$\sum_i \eta_{g_1 g_i} + \sum_j \eta_{g_1 s_j} = \eta_{g_1} \quad (44)$$

The next-to-the last term of Equation (42) is present only where one of the bounding surfaces of zone g_1 contains ports through which there enters, at a molal flow rate $\dot{M}$ from outside the system, some gas and fuel having a molal sensible-plus-chemical enthalpy, $(H_c + H_s)_{in}$. The last term is absent in steady state problems and insignificant compared with the others in any case where g represents gas. However, g might represent the glass in a problem of glass heating, and the energy-storage term is then significant.

Similarly, a balance on any surface zone s_1 representing the interchange between it and all other zones (g_1, g_2, $\cdots$, those having a common boundary with s_1; g_{10}, g_{11}, $\cdots$, those not touching s_1; and s_2, s_3, $\cdots$) takes the form

$$W_{g_1}(\overline{G_1S_1} + \gamma_{g_1 s_1}) + W_{g_2}(\overline{G_2S_1} + \gamma_{g_2 s_1}) + \cdots + W_{g_{10}}(\overline{G_{10}S_1}) + W_{g_{11}}(\overline{G_{11}S_1}) + \cdots + W_{s_1}(\overline{S_1S_1} - \epsilon_{s_1}A_{s_1} - \sum_i \gamma_{s_1 g_i}) + W_{s_2}(\overline{S_2S_1}) + W_{s_3}(\overline{S_3S_1}) + \cdots - q_{s_1} - C_{s_1}\dot{T}_{s_1} = 0 \quad (45)$$

where the next-to-last term q_{s_1} represents the net outward heat flux through the wall in question. It is to be remembered that for a true heat sink of known temperature this wall flux will be an unknown quantity; for a well-insulated refractory surface the wall flux will be 0 but the temperature will be unknown. For a billet being heated in batch operation q_{s_1} will be 0 but $C_{s_1}\dot{T}$ will not; if the operation is continuous and in dynamic equilibrium, either of the terms may be used to describe the transfer. (See later.) Again, to simplify nomenclature the term $\sum_i \gamma_{s_1 g_i}$ will be represented by γ_{s_1}.

To aid in handling the solution of the system of energy balances of which Equations (42) and (45) are representative, the coefficients on W's may be arranged in a matrix, appearing in Table 1. Each row contains the coefficients of W's in a single energy balance, the rows from top to bottom corresponding to balances on g_1, g_2 $\cdots$, s_1, s_2 $\cdots$ in sequence. The coefficients are arranged

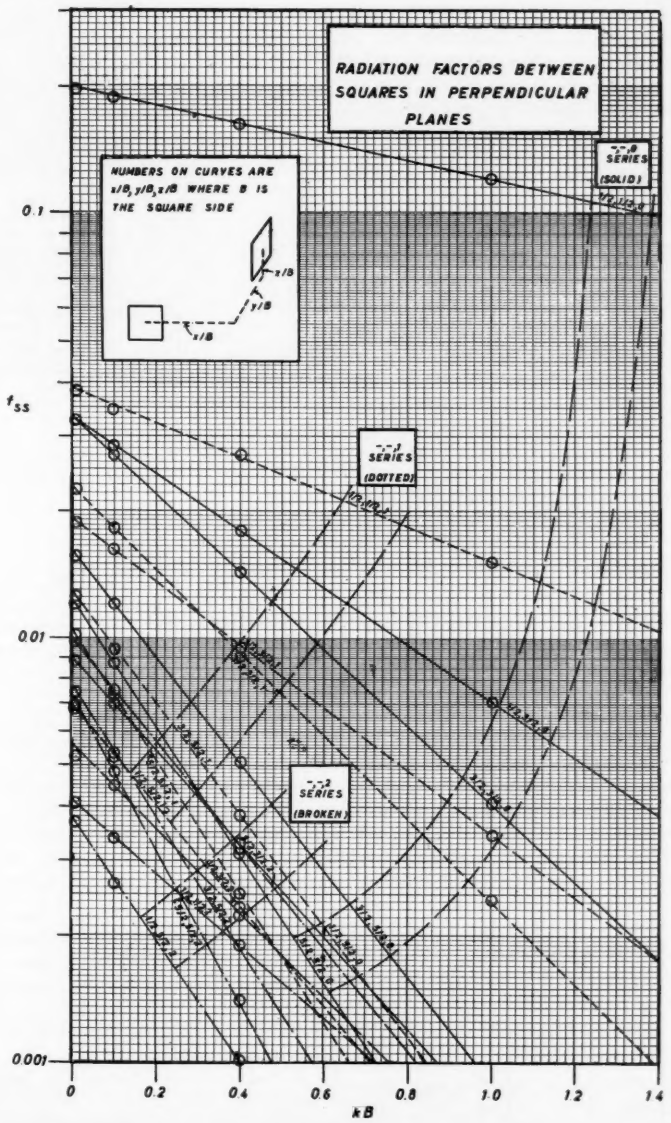

Fig. 3. Reception factor f_{ss} between squares of side B in perpendicular planes (f_{ss} = direct-view factor × transmittance).

in columnar form to make coefficients on $W_{g_1}, W_{g_2} \cdots W_{s_1}, W_{s_2}$ appear in sequence, left to right. Recapitulating, the energy balance on any gas zone is formed by summing the products formed by multiplying the terms in a row by their column headings and equating the result to the quantity $-\dot{M}(H_c + H_s)_{in} + C_g\dot{T}_g$ (either or both of which may be 0); the energy balance on any surface zone is formed by similar product summation for the row in question and equating of the result to $q_s + C_s\dot{T}$.

Before the solution of these equations is considered, it is necessary to examine the possible meanings, in different furnace chambers, of such terms as q_{s_i} appearing in the balance on zone s_i. There are three cases:

1. The temperature T_{s_i} is known and q_{s_i} unknown, as in the case of a surface zone representing a screen of water- or oil-cooled tubes. For this case W_{s_i} is known. If there are g gas zones and s surface zones of which u are in this category, there are still $g + s$ equations and as many unknowns, but there are only $g + s - u$ unknown temperatures and u unknown q's; and one needs to solve simultaneously only $g + s - u$ equations, followed by substitution in the others, to find the q's.

2. Both the temperature T_{s_i} and the flux q_{s_i} are unknown—the case of heat loss through a thin or poorly insulated refractory wall. A solution requires sufficient knowledge of the wall to evaluate q_{s_i} in the form $A_{s_i}U_{s_i}(T_{s_i} - T_0)$, where U_{s_i} is the over-all coefficient of heat transfer, inner wall surface to outside air at T_0. For simplicity in using this relation as a part of the system of fourth-power equations, one writes

$$q_{s_i} = A_{s_i}U_{s_i}(T_{s_i} - T_0)$$

$$= \left(\frac{A_{s_i}U_{s_i}}{\sigma T_{s_i}^{\ 3}}\right)W_{s_i} - A_{s_i}U_{s_i}T_0 \qquad (46)$$

Since q_{s_i} was the sole term on the right side of the energy balance formed from row s_i of the matrix (Table 1), the first term on the right side of (46) is transposed and the coefficient in parentheses incorporated, with sign changed, into the term in the W_{s_i} column of row s_i, leaving $-A_{s_i}U_{s_i}T_0$ as a known quantity on the right.

3. The temperature T_{s_i} and flux q_{s_i} are unknown, but related by an enthalpy balance—the case of a continuous furnace with stock, forming zone s_i, entering with hourly heat capacity $\dot{w}C_p$ from zone s_j or from outside the system with a specified temperature. For this case

$$q_{s_i} = \dot{w}C_p(T_{s_i} - T_{s_j})$$

$$\equiv \left[\frac{\dot{w}C_p}{\sigma T_{s_i}^{\ 3}}\right]W_{s_i} - \left[\frac{\dot{w}C_p}{\sigma T_{s_j}^{\ 3}}\right]W_{s_j} \quad (47)$$

As before, the coefficients in brackets are to be incorporated, with their signs changed, into the W_{s_i} and W_{s_j} columns of s_i; and the right-hand side of the energy balance is 0. Terms of the energy balance on s_j must be similarly modified.

4. Hybrids can exist, for example billets on water-cooled skids, involving the mechanisms of both classes (*b*) + (*c*); their treatment along the lines above is obvious.

Unless computers are available for handling higher order determinants, it is not recommended that a determinant technique be used to solve for the unknown temperatures for two reasons:

1. The various coefficients have profoundly different magnitudes because of the poor "view" that some zones have of other remote ones, in consequence of which one or two terms in any one of the energy balances may be of overriding importance.

2. Some of the terms in the "known" coefficients of Table 1 are in fact unknown because they have been obtained by a forced linearization and must therefore be estimated and changed when found not to conform to the temperatures obtained from the solution.

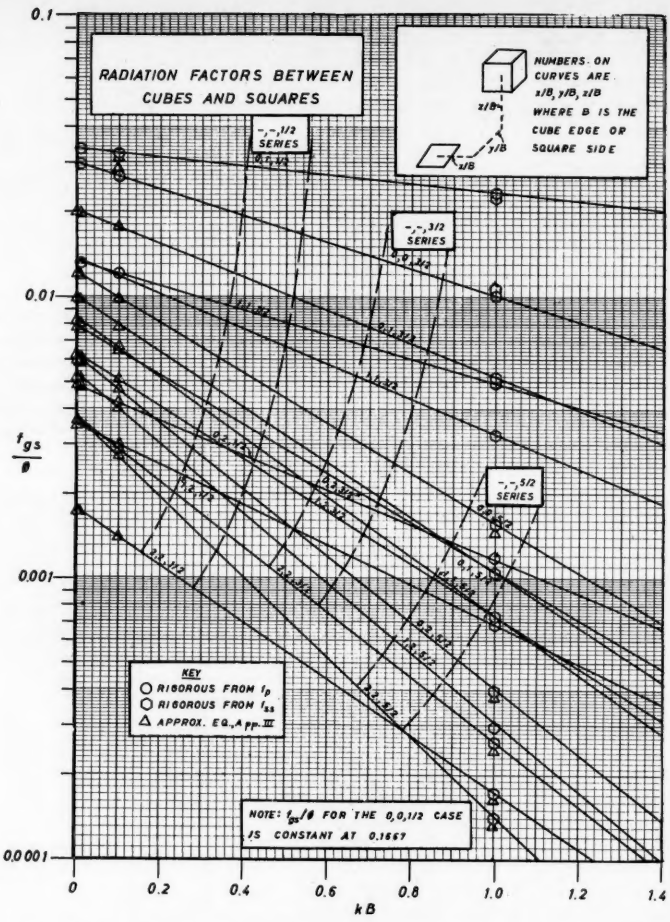

Fig. 4. Reception factor f_{gs} from cube to square, both of sides B (f_{gs} = direct-view factor × transmittance; ϕ from Figure 1).

On the basis of experience in handling numerical solutions the best procedure is to guess all the temperatures (or W's), to insert all but the most important one of the guesses into the first equation and solve for one unknown W, to use this answer and the remaining guesses except for one in the next equation, etc. For those cases tried, the solution converged quite rapidly.

CONCLUSION

A method for predicting radiant heat interchange in enclosures where allowance is to be made for gas-temperature variation has been presented. This includes a set of reception factors permitting evaluation of any exchange problem the geometry of which is represented in cartesian coordinates.

The new technique is capable of solving far more complex problems than could previously have been handled. Since the

radiation processes occurring within an enclosure are extremely complicated, the technique presented here which tries to take into account some of those complexities has turned out to be complicated itself. Plainly, however, there are problems the numerical solution of which is of sufficient importance to justify the considerable time required. One important engineering application of the new method is its use on a particular model or class of furnaces in comparison with various engineering shortcuts, to determine the range over which one of them may be relied upon.

APPENDIXES

1. EVALUATION OF ϕ

The rate of emission from an isothermal gas cube may be built up from the simpler case of the radiant interchange between a small-volume element and a plane area. Consider a differential volume of gas located at a distance X measured along the normal through one corner of a rectangle as in Figure 7. The total emission from the differential volume over the total solid angle of 4π is equal to $4k \cdot dV \cdot W$, and the energy received by a differential area on the plane is this times the fractional solid angle, reduced to allow for absorption by the intervening gray gas.

Radiation to differential plane area

$$= 4k \cdot dV \cdot W \cdot e^{-kr} \frac{d\omega}{4\pi} \qquad \text{(A1)}$$

Division by the emission from the volume and integration over the total solid angle subtended by the rectangle at dV gives the fraction of energy emitted from the differential volume that reaches the plane; this will be termed f_p. Express $d\omega$ in cylindrical coordinates as $\sin\psi \, d\psi \, \Delta\theta$ or $-\Delta\theta \, d(\cos\psi)$. Then

$$f_p = \frac{1}{4\pi} \int_{\cos\psi=1/\sqrt{1+(\alpha/X)^2+(\beta/X)^2}}^{\cos\psi=1} \Delta\theta \cdot e^{-kX/\cos\psi} \, d(\cos\psi), \qquad \text{(A2)}$$

where $\Delta\theta$ is the difference of the limiting values of θ associated with the curved-surface element lying at a constant angular position off the axis of X. Numerical values of f_p for a wide range of values of α/X, β/X, and kX have been obtained by graphical integration (*1*).

The factor ϕ, defined as the fraction of the energy originating within a cube of edge B which escapes through the boundaries, is therefore the integral of the sum of a maximum of 24 f_p terms (fraction of energy from infinitesimal volume source reaching walls) integrated over the volume and then divided by the volume, or

$$\phi = \frac{\int_v f_p \cdot dx \, dy \, dz}{B^3} = \int_0^1 \int_0^1 \int_0^1 f_p \cdot d\frac{x}{B} \, d\frac{y}{B} \, d\frac{z}{B} \qquad \text{(A3)}$$

Figure 1 was obtained by triple graphical integrations of Equation (A3).

2. EVALUATION OF RECEPTION FACTORS

The derivation of the equations and details of the graphical integrations for evaluation of the reception factors between any two zones in the enclosure will not be given here, but are available in reference *1*.

Use of nomenclature as shown in Figure 8 and of the same type of reasoning as in the derivation in Appendix 1 yields the factor between two squares of surface, each of side B, lying in either perpendicular or parallel planes:

$$f_{ss}(\text{parallel}) = \frac{1}{\pi} \int_{x_1} \int_{y_1} \int_{x_2} \int_{y_2} \cdot e^{-kB(r/B)} \cdot \frac{(\Delta z/B)^2}{(r/B)^4} \cdot d\left(\frac{x_1}{B}\right) d\left(\frac{y_1}{B}\right) d\left(\frac{x_2}{B}\right) d\left(\frac{y_2}{B}\right) \qquad \text{(A4)}$$

$$f_{ss}(\text{perpendicular}) = \frac{1}{\pi} \int_{x_1} \int_{z_1} \int_{y_2} \int_{z_2} \cdot e^{-kB(r/B)} \cdot \frac{(\Delta x/B)(\Delta y/B)}{(r/B)^4} \cdot d\left(\frac{x_1}{B}\right) d\left(\frac{z_1}{B}\right) d\left(\frac{y_2}{B}\right) d\left(\frac{z_2}{B}\right) \qquad \text{(A5)}$$

where

$$r/B = \left[\left(\frac{x_2 - x_1}{B}\right)^2 + \left(\frac{y_2 - y_1}{B}\right)^2 + \left(\frac{z_2 - z_1}{B}\right)^2\right]^{1/2} \qquad \text{(A6)}$$

Similarly, for interchange between two gas cubes, with nomenclature as given in Figure 9 and with r/B from equation (A6), the factor is given by

$$f_{gg} = \frac{kB}{4\pi} \int_{x_1} \int_{y_1} \int_{z_1} \int_{x_2} \int_{y_2} \int_{z_2} \frac{e^{-kB(r/B)}}{(r/B)^2} \cdot d\left(\frac{x_1}{B}\right) d\left(\frac{y_1}{B}\right) d\left(\frac{z_1}{B}\right) d\left(\frac{x_2}{B}\right) d\left(\frac{y_2}{B}\right) d\left(\frac{z_2}{B}\right) \qquad \text{(A7)}$$

The remaining type of interchange—gas to surface—may be obtained from the f_p plots described in Appendix 1. The fraction of the radiation originating in a gas cube which reaches a surface square is

$$f_{gs} = \frac{\int_v \sum f_p \cdot dx \, dy \, dz}{B^3} = \int_0^1 \int_0^1 \int_0^1 \sum f_p \cdot d\left(\frac{x}{B}\right) d\left(\frac{y}{B}\right) d\left(\frac{z}{B}\right) \qquad \text{(A8)}$$

where $\sum f_p$ represents the algebraic sum of four f_p factors yielding the fraction of the radiation from a differential volume element reaching the surface zone.

Multiple graphical integrations of Equations (A4), (A5), (A7), and (A8) yielded the working plots, Figures 2 through 5.

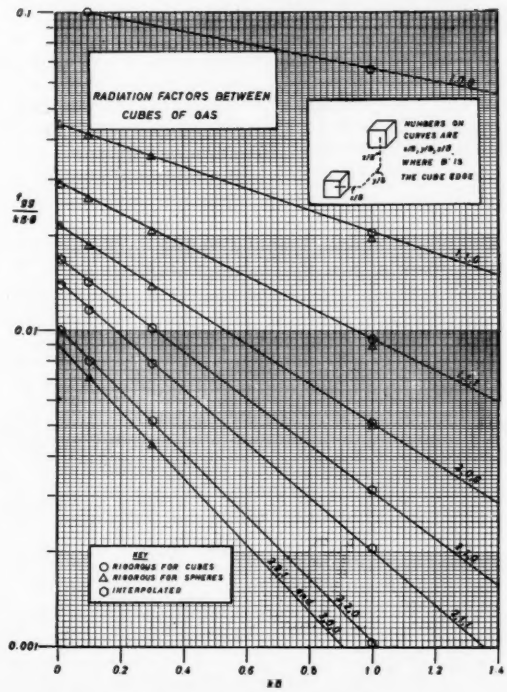

Fig. 5. Reception factor f_{gg} between cubes of side B (f_{gg} = direct-view factor × transmittance × absorptivity; ϕ from Figure 1).

3. LIMITING VALUES OF RECEPTION FACTORS AS r/B INCREASES

As the separating distance between the centers of any two elements becomes very large, so that the view and the path length for absorption are the same for all points in either zone, then the graphical integrations can be dispensed with. The reception factor may be evaluated as the product of the gas transmittance, equal to $e^{-kB(r_c/B)}$ where r_c/B is the center-to-center distance measured in terms of B, and a factor visualizable as the product of a direct-view factor and a fractional absorption in the receiver if a gas. Table 2 summarizes these limiting values.

4. INTERCHANGE BETWEEN GAS AND GRAY WALLS

Consider a gas uniform in temperature and surrounded by gray walls of uniform temperature. Surface absorption of gas emission and gas-absorption of surface emission will each be the sum of an infinite series. It has been shown (*4*) that the net flux may be written

$$q/A]_{g\rightleftharpoons s} = \epsilon_s{}^2 W_g \sum_{n=1}^{\infty} \rho_s{}^{n-1} \epsilon_{g,nL} - \epsilon_s{}^2 W_s \sum_{n=1}^{\infty} \rho_s{}^{n-1} \alpha_{gs,nL} \qquad \text{(A9)}$$

In general, the series summation is made numerically, by use of gas-radiation charts. The members of these two series may be paired to replace (A9) by

$$q/A]_{g\rightleftharpoons s} = \epsilon_s{}^2 \sum_{n=1}^{\infty} \rho_s{}^{n-1} (\epsilon_{g,nL} W_g - \alpha_{gs,nL} W_s) \qquad \text{(A10)}$$

If the gas emissivity for path length nL is assumed expressible in the form $a(1 - e^{-knL})$ and absorptivity is obtainable from emissivity by the relation (*5*) $\alpha_{gs,nL} = \epsilon_{g,nLT_s/T_g,T_s}(T_g/T_s)^{\epsilon}$ and if emissivity is proportional, over the temperature range T_g to T_s, to the b power of temperature, it has been shown (*1*) that the terms in parentheses may be written

$$K\epsilon_{g,nL,T_{avg}}(W_g - W_s)$$

where

$$K = \frac{4 + b - c - \left(\frac{a}{\epsilon_{g,L}} - 1\right) \ln\left(1 - \frac{\epsilon_{g,L}}{a}\right)}{4} \qquad \text{(A11)}$$

It is to be noted that if emissivity is assumed given by $a(1 - e^{-kL})$, then from the definition of d, K in (A11) is the same as K in Equation (36).

The series in (A10) may now be summed

$$q/A]_{g\rightleftharpoons s} = \epsilon_s{}^2 (W_g - W_s) \sum_{n=1}^{\infty} \rho_s{}^{n-1} (K\epsilon_{g,nL,T_{avg}})$$

If the effective emissivity $K\epsilon_{g,nL}$ is expressible in the form $a(1 - e^{-knL})$, then the foregoing becomes

$$q/A]_{g\rightleftharpoons s} = \epsilon_s{}^2 (W_g - W_s) \sum_{n=1}^{\infty} \rho_s{}^{n-1} a(1 - e^{-knL})$$

$$= \epsilon_s{}^2 (W_g - W_s) a \left(\frac{1}{1-\rho_s} - \frac{e^{-kL}}{1-\rho_s e^{-kL}}\right)$$

and since for gray surfaces $1 - \rho_s = \epsilon_s$,

$$q/A]_{g\rightleftharpoons s} = (W_g - W_s) a \frac{1}{\frac{1}{(\epsilon_{g,T_s}/a)} + \frac{1}{\epsilon_s} - 1} \qquad \text{(A12)}$$

This is the very relation obtainable by use of the method of this paper [or the older method (*5*) which is identical to it for the one-gas-zone case], provided that ϵ_g is replaced by $K\epsilon_g$.

5. LOCAL VARIATIONS IN CONCENTRATION OF ABSORBENT

When the concentrations of the absorbing components of the gas vary locally without causing the absorption characteristics or the proportions of the various components to change, allowance can be made for these variations. Knowledge must be available however, concerning the relation between concentration and k. The variation of $\epsilon_{g,L}$ with L, generally expressed graphically, must be available for a known uniform concentration of absorber; and the values of a and k obtained from it, by substituting into (28) and (29) the values of ϵ_g at L and $2L$, must be the same as those obtained at another concentration of absorber, after due allowance for the concentration ratio. In other words the values of a and k_{std}, where k_{std} is k adjusted to a standard concentration of absorber, must not vary. If those conditions are met or a reasonable compromise equivalent to meeting them is accepted, the following argument is applicable.

The transmittance of radiation through a path r with constant k is e^{-kr}; when k varies with r, it is $e^{-k_{avg}r}$, where k_{avg} is given by

$$k_{avg} = \frac{\int_0^r k\, dr}{r} \qquad \text{(A13)}$$

When gas cube 1 is radiating to gas cube 2 and their center-to-center distance of separation r is large compared with the side B of each, their interchange area is given by

$$\overline{g_1 g_2} = 4k_1 B^3 e^{-k_{avg}r} k_2 B^3 / \pi r^2 \qquad \text{(A14)}$$

whereas the corresponding relation based on a fixed $k(= k_{avg})$ is

$$\overline{g_1 g_2}]_{k_{avg}} = 4k_{avg}{}^2 B^6 e^{-k_{avg}r} / \pi r^2 \qquad \text{(A15)}$$

Although the assumptions that emission from g_1 is associated with a fixed k_1 and absorption at g_2 is associated with a fixed k_2 are no longer valid as the center-to-center separating distance approaches B, the use of the ratio of the right-hand sides of (A14) to (A15) to correct the value of $g_1 g_2]_{k_{avg}}$, as read from Figure 5, should not lead to much error. Then

$$\overline{g_1 g_2}_{variable\ k} = \overline{g_1 g_2}]_{k_{avg}} \left(\frac{k_1 k_2}{k_{avg}{}^2}\right) \qquad \text{(A16)}$$

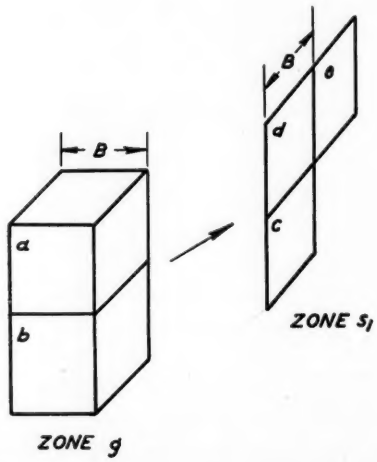

Fig. 6. Build-up of reception factors for zones from those for unit squares and cubes.

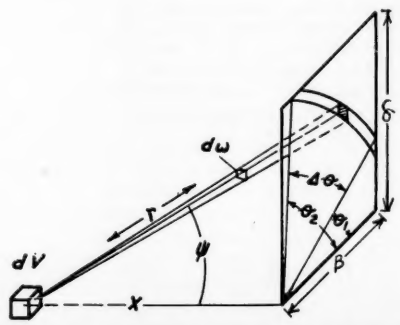

Fig. 7. Radiation from a differential-volume element to a plane.

TABLE 1. MATRIX FORMED FROM COEFFICIENTS ON W'S IN THE ENERGY BALANCES

From energy balance on	Coefficients on W_{g_1}	W_{g_2}	W_{s_1}	W_{s_2}
g_1	$(\overline{G_1G_1}-\gamma_{g_1}-\eta_{g_1}-4kaV_{g_1})$	$(\overline{G_2G_1}+\gamma_{g_2g_1}+\eta_{g_2g_1})$	$(\overline{S_1G_1}+\gamma_{s_1g_1})$	$(\overline{S_2G_1}+\gamma_{s_2g_1})$
g_2	$(\overline{G_1G_2}+\gamma_{g_1g_2}+\eta_{g_1g_2})$	$(\overline{G_2G_2}-\gamma_{g_2}-\eta_{g_2}-4kaV_{g_2})$	$(\overline{S_1G_2}+\gamma_{s_1g_2})$	$(\overline{S_2G_2}+\gamma_{s_2g_2})$
$\vdots$	$\vdots$	$\vdots$	$\vdots$	$\vdots$
s_1	$(\overline{G_1S_1}+\gamma_{g_1s_1})$	$(\overline{G_2S_1}+\gamma_{g_2s_1})$	$(\overline{S_1S_1}-\gamma_{s_1}-\epsilon_{s_1}A_{s_1})$	$(\overline{S_2S_1})$
s_2	$(\overline{G_1S_2}+\gamma_{g_1s_2})$	$(\overline{G_2S_2}+\gamma_{g_2s_2})$	$(\overline{S_1S_2})$	$(\overline{S_2S_2}-\gamma_{s_2}-\epsilon_{s_2}A_{s_2})$
$\vdots$	$\vdots$	$\vdots$	$\vdots$	$\vdots$

Similar reasoning to the above leads to the recommendation that k_{avg} should be determined as the integrated mean of k along the path connecting the zone centers, from the value of k_1 at the emitting zone to k_2 at the absorbing zone, and that the interchange areas *ss*, *sg*, *gs*, and *gg* should be determined as though k were constant at k_{avg} and should then be corrected by the factors 1, k_2/k_{avg}, k_1/k_{avg}, and k_1k_2/k_{avg}^2, respectively. This procedure permits allowance for combustion products of higher concentration in the center of the combustion chamber than near the walls.

TABLE 2

LIMITING VALUES OF RECEPTION FACTORS

f_{ss}(parallel)
$= e^{-kB(r_c/B)}(\Delta z/B)^2/\pi(r_c/B)^4$

f_{ss}(perpendicular)
$= e^{-kB(r_c/B)}(\Delta x/B)(\Delta y/B)/\pi(r_c/B)^4$

$f_{gs} = e^{-kB(r_c/B)}(\Delta z/B)/4\pi(r_c/B)^3$

$f_{sg} = e^{-kB(r_c/B)}kB(\Delta z/B)/\pi(r_c/B)^3$

$f_{gg} = e^{-kB(r_c/B)}kB/4\pi(r_c/B)^2$

ACKNOWLEDGMENT

This work was based in part on a thesis by E. S. Cohen submitted in 1955 to the Massachusetts Institute of Technology for the ScD. degree. Mr. Cohen wishes to acknowledge support for this investigation by Pittsburgh Consolidation Coal Company through a fellowship grant and later by Project SQUID under sponsorship of the Office of Naval Research, Office of Ordnance Research and Office of Scientific Research (Contract N6ori-105, T.O.III).

NOTATION

A = area of a surface, sq. ft.

a = weighting factor, dimensionless

B = cube edge or square side, ft.

b = $\partial \ln \epsilon_g / \partial \ln T_g$, dimensionless

C_p = heat capacity, B.t.u./(lb.)(°F.)

c = exponent on temperature ratio in obtaining α_g from ϵ_g, dimensionless

D = basic determinant for system of simultaneous equations used to obtain total interchange factors

${}_{g_i}D_{s_j}$ = determinant formed by replacing the s_j column of D by a column of g_i functions

${}_{s_i}D_{s_j}$ = determinant formed by replacing the s_j column of D by a column of s_i functions

${}_{s_i}D'_{s_j}$ = minor of D formed by crossing out the s_i row and s_j column of D

d = $\partial \ln \epsilon_g / \partial \ln (PL)$, dimensionless

E = radiation-emission rate, energy per unit time

F = view factor = fraction of radiation from one surface zone intercepted by another surface zone in the presence of a nonabsorbing medium, dimensionless

$\mathfrak{F}$ = over-all interchange factor, $\mathfrak{F}_{1g}$ ($\mathfrak{F}_{12}$) = radiation reaching gas (surface A_2) due to original emission from A_1 only, but including assistance given by reflection at all surfaces, expressed as a ratio to σT_1^4, dimensionless

f_p = fraction of the energy from a differential volume element absorbed by a black plane of dimensions α and β when the volume lies on a normal through one corner of the plane and at a distance X from it, dimensionless

f = reception factor = fraction of radiation originating in one zone which reaches and is absorbed by another zone in a black-walled enclosure, dimensionless

G_m = molal flow rate per unit area, moles per hr. per sq. ft.; G_{m_n} is component of G_m normal to a given area.

$\overline{GG}$ = total interchange area between any two gas zones including reflections at all surfaces, sq. ft.; $\overline{G_1G_2}$ ($\equiv \overline{G_2G_1}$) is equal to $q_{g_1g_2}/W_{g_1}$ or $q_{g_2g_1}/W_{g_2}$

$\overline{GS}$ = total interchange area between any gas and surface zone including reflections at all surfaces, sq. ft.; $\overline{G_1S_1}$ ($\equiv \overline{S_1G_1}$) is equal to $q_{g_1s_1}/W_{g_1}$ or $q_{s_1g_1}/W_{s_1}$

g = gas zone with a numerical subscript to designate the particular zone under consideration

$\overline{gg}$ = direct interchange area between any two gas zones, sq. ft.; $\overline{g_1g_2}$ ($\equiv \overline{g_2g_1}$) is equal to $(q_{g_1g_2})_{direct}/W_{g_1}$ or $(q_{g_2g_1})_{direct}/W_{g_2}$

$\overline{gs}$ = direct interchange area between any gas and surface zone, sq. ft.; $\overline{g_1s_1}$ ($\equiv \overline{s_1g_1}$) is equal to $(q_{g_1s_1})_{direct}/W_{g_1}$ or $(q_{s_1g_1})_{direct}/W_{s_1}$

H_c = molal chemical enthalpy, B.t.u./mole

H_s = molal sensible enthalpy, B.t.u./mole

h_c = convective coefficient of heat transfer, B.t.u./(hr.) (sq. ft.)/(°F.)

i, j = subscripts to represent any gas or surface zone

K = correction factors by which to multiply $\epsilon_{T_{avg}}$, dimensionless

k = absorption coefficient of a gas, ft.$^{-1}$

L = mean beam length for gas radiation, ft.

$\dot{M}$ = molal flow rate into system, moles/hr.

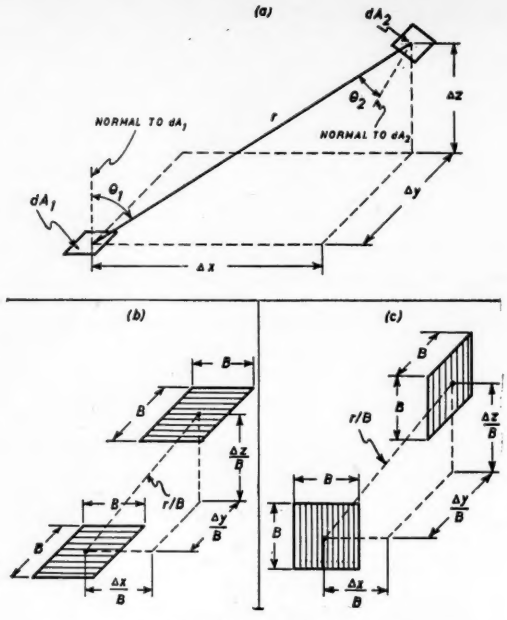

Fig. 8. Geometry of interchange between squares.

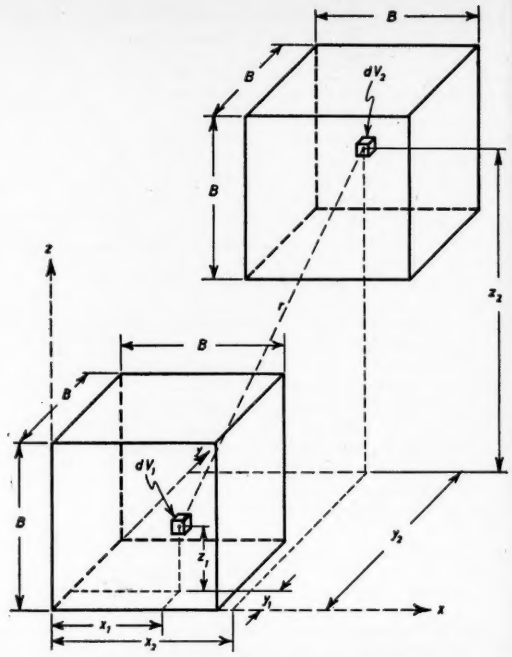

Fig. 9. Geometry of interchange between cubes.

m, n = subscripts to represent any two zones

n = a subscript to represent the number of passages through gas

P = pressure, atm.

q = heat transfer rate, B.t.u./hr.; $q_{s_i g_j}$ (or any other pair of subscripts) is the one-way energy transfer from the ith surface zone to the jth gas zone; q_s is the net heat transferred through wall s

R = relative flux density, dimensionless; ${}_{g_i}R_{s_j}$ (or any other pair of subscripts), flux density away from the jth surface zone, due solely to radiation originating within the ith gas zone, and expressed as a ratio to W_{s_i}

r = linear distance between two elements, ft.

$\overline{SG}$ = total interchange area between any surface and gas zone including reflections at all surfaces, sq. ft.; S_1G_1 ($\equiv \overline{G_1S_1}$) is equal to $q_{s_1g_1}/W_{s_1}$ or $q_{g_1s_1}/W_{g_1}$

$\overline{SS}$ = total interchange area between any two surface zones including reflections at all surfaces, sq. ft.; $\overline{S_1S_2}$ ($\equiv \overline{S_2S_1}$) is equal to $q_{s_1s_2}/W_{s_1}$ or $q_{s_2s_1}/W_{s_2}$

s = surface zone with a numerical subscript to designate the particular zone under consideration

$\overline{sg}$ = direct interchange area between any surface and gas zone, sq. ft.; $\overline{s_1g_1}$ ($\equiv \overline{g_1s_1}$) is equal to $(q_{s_1g_1})_{direct}/W_{s_1}$ or $(q_{g_1s_1})_{direct}/W_{g_1}$

$\overline{ss}$ = direct interchange area between any two surface zones, sq. ft.; $\overline{s_1s_2}$ ($\equiv \overline{s_2s_1}$) is equal to $(q_{s_1s_2})_{direct}/W_{s_1}$ or $(q_{s_2s_1})_{direct}/W_{s_2}$

T = temperature, °R.; T_g, of a gas zone; T_s, of a surface zone; T_0, of system surroundings; T_{avg}, arithmetic mean of two temperatures

U_s = over-all coefficient of heat transfer, inner surface of wall s to surroundings at T_0, B.t.u./(hr.)(sq. ft./°R.)

u = number of zones of known temperature, dimensionless

V = gas volume, cu. ft.

W = rate of emission from unit area of black body at temperature indicated by subscript, B.t.u./(hr.)(sq. ft.)

$\dot{w}$ = weight flow rate, lb./hr.

X = normal distance between a differential radiating volume element and a plane, ft.

x, y, z = linear dimensions along the three coordinate axes, ft.

Greek Letters

α = absorptivity, dimensionless

γ = convective flux coefficient, sq. ft.

Δ = a difference

ϵ = emissivity, dimensionless

η = enthalpy flux coefficient, sq. ft.

θ = angle, radius

μ = refractive index, dimensionless

ρ = reflectivity, dimensionless

σ = Stefan-Boltzmann constant = 0.1713×10^{-8} B.t.u./(hr.)(sq. ft./°R.^{4})

τ = gas transmissivity, dimensionless

ϕ = escape factor for radiation from a cube of gas (ratio of energy leaving boundaries to energy originating within volume), dimensionless

ψ = angle, radians

ω = solid angle, steradians

LITERATURE CITATIONS

1. Cohen, E. S., Sc.D. thesis, Mass. Inst., Technol., Cambridge (1955).
2. Crout, P. D., *Trans. Am.E.E.E.*, **60**, 1235 (1941).
3. Forstall, W., Jr., and A. H. Shapiro, *Proj. Meteor Report* 39, Mass. Inst. Technol., Cambridge (July, 1949).
4. Hottel, H. C., and R. B. Egbert, *Trans. Am. Soc. Mech. Engrs.*, **63**, 297 (1941).
5. Hottel, H. C., in W. H. McAdams, Heat Transmission, 3 ed., McGraw-Hill Book Company, Inc., New York (1954).
6. McAdams, W. H., "Heat Transmission," 3 ed., McGraw-Hill Book Company, Inc., New York (1954).
7. Towle, W. L., Sc.D. thesis, Mass. Inst. Chem. Engrs. (1937).

Manuscript submitted May, 1957; paper accepted September 3, 1957.

Heat Transfer Between Fluidized-solids Beds and Boundary Surfaces—Correlation of Data

LEONARD WENDER and GEORGE T. COOPER

The M. W. Kellogg Company, New York, New York

A broad empirical study of nine independent sets of data on fluidized-bed heat transfer is presented, with correlation of the data in two groups. A wide range of the many variables is covered, and some data on commercial units are included. Data for external (i.e., walls of the fluidizing vessel) and internal (i.e., tubes in the bed) heat transfer surfaces are correlated graphically. The correlations indicate the importance of heat transport by the mobile particles and of unsteady state conduction in the gas.

The problem of determining heat transfer coefficients between beds of fluidized solids and boundary surfaces (either the walls of the fluidizing vessel or tubes immersed in the bed) has attracted the attention of numerous investigators in recent years. Papers presenting data on such coefficients have been those of Bartholomew and Katz (*3*), Dow and Jakob (*7*), Mickley and Trilling (*21*), Toomey and Johnstone (*26*), Baerg, Klassen, and Gishler (*2*), Leva, Weintraub, and Grummer (*16*), Leva (*15*), Olin and Dean (*23*), Mickley and Fairbanks (*20*), Van Heerden, Nobel, and Van Krevelen (*29, 30*), Pritzlaff (*24*), Brazelton (*4*), Levenspiel and Walton (*18, 19*), Simon (*25*), Miller and Logwinuk (*22*), Jolley (*11*), Campbell and Rumford (*5*), Agarwal and Storrow (*1*), and Vreedenberg (*31, 32*).

Review papers or papers presenting special limited data have been those of Gamson (*8*), Van Heerden, Nobel, and Van Krevelen (*27, 28*), Leva and Grummer (*14*), Wen and Leva (*35*), and Gilliland (*9*). Papers dealing with heat transfer between the solid particles and the gas stream are those of Kettenring, Manderfield, and Smith (*12*), Walton, Olson and Levenspiel (*33*), and Wamsley and Johanson (*34*). Koble, Ademino, Bartkus, and Corrigan (*13*) studied dense-phase transport, and dilute phase transport was investigated by Pritzlaff (*24*). Carr and Amundson (*6*) presented a mathematical study.

Unpublished data were also available to the authors on commercial fluid-hydroformer–catalyst regenerators built by The M. W. Kellogg Company.

Of all the papers listed above, only one was a general correlation attempt, using more than one set of data to establish a correlation. That was the paper of Wen and Leva. Of course, many of the authors listed presented correlations for their own data, but none of these limited correlations appeared to be able to encompass many other data. The lack of theoretical understanding of mechanism and of general correlation work has left the problem of predicting fluidized-bed heat transfer coefficients in a chaotic state. The situation was well summarized by Van Heerden (*28*), who reviewed the picture and for comparison tabulated some of the proposed correlation equations. Using these to predict coefficients for four hypothetical cases, he found the predicted values to cover an enormous range—248-fold for one of the cases. The correlations proposed here, while empirical, do indicate that order can be brought into the situation, and it is hoped that these results will encourage other workers in the field to continue so that the problem of fluidized-bed heat transfer may be fully understood.

METHOD OF ATTACK

Of the data listed above, not all were used in this work. Some were not used because of lack of reporting of variables found to be necessary, and others because of time limitations. Among those used, some were not fully worked up because of time limitations; however, the substantial numbers of runs which were fully worked up are representative of the data in those cases. Data which were completely worked up are those of Bartholomew and Katz, of Dow and Jakob, of Mickley and Trilling, of Toomey and Johnstone, and of Baerg, Klassen, and Gishler. [In the last case, pressure drops for fraction solids calculation were supplied (*10*) to the authors for most, but not all, runs.] Those largely but incompletely covered are the data of Leva, Weintraub, and Grummer, of Mickley and Fairbanks, and of Olin and Dean. (The extensive data of Van Heerden, Nobel, and Van Krevelen were not worked up because of lack of values of bed density or fraction solids.)

Owing to the general lack of quantitative understanding of mechanism, it was decided to use an empirical approach in which the data would be permitted to "tell their story" and which would involve a minimum of preconceived notions as to the variables involved. Dimensional analysis was thus rejected. A laborious procedure of successive cross plotting to evaluate the effect of each variable—as it was found to exert an effect—was chosen, to be used as the data allowed. The over-all result was something of a "brute force" attack on the problem, but this was felt to be necessary in order

first to establish whether the various data could be hammered into some sort of cohesion before any very elegant refinements were attempted.

Study was limited to heat transfer between a bed and heat transfer surfaces (as against transfer between the solid particles and the gas). Continuous vertical transport was not studied.

CORRELATION OF EXTERNAL HEAT TRANSFER SURFACE DATA

High L_H/D_T Data as Start, Effect of Fraction Solids

Preliminary consideration was limited to data on external heat transfer surface. By this is meant operation with heat transferred between the bed and the walls of the fluidizing vessel. (It was later found that transfer between the bed and internal tubes requires a separate correlation.)

Van Heerden, et al. (*27, 28*) showed that a bed-height (L_B) effect reported by Dow and Jakob is in reality a heated-length (L_H) effect and one in which coefficients decrease and then level off to a constant value as L_H increases. Figure 1 shows Van Heerden's curve of h vs. L_H. It was evident that a good start would be had with data at a high and constant L_H/D_T, preferably above 5, the point at which Van Heerden's curve, converted to h vs. L_H/D_T, leveled off. In this manner a complex L_H/D_T effect would not be present to obscure the effect of other variables, and the wide L_H/D_T range data of Dow and Jakob could later be used to study this factor.

The data of Bartholomew and Katz suited this requirement well. This was a study of heat transfer from the walls of a 4-in. pipe to sand, calcium carbonate, and aluminum powder, respectively, fluidized with air. L_H/D_T was kept constant at 7.5 and the work covered a wide range of air velocity, particle size, and fraction solids.

An arbitrary decision was made (subject to change if found necessary) to start with h in the Nusselt number hD_p/k_g, or Nu_p and with mass velocity G in the Reynolds number D_pG/μ, or Re_p. (Some authors used G/G_{mf} instead of Re_p, but the latter was considered more convenient.) Curves of Nu_p vs. Re_p for sand-air data of Bartholomew and Katz, such as in Figure 2, showed separation according to average particle size D_p. They also showed maxima, due presumably to increased particle motion causing h to increase with G, with this factor being offset at high velocities by reduced solids concentration. The introduction of fraction solids, $1 - \epsilon$, seemed a profitable approach, and from Bartholomew and Katz data, as curves of $1 - \epsilon$ vs. Re_p at constant D_p, a cross plot was made, at constant Re_p, of Nu_p vs. $1 - \epsilon$ (Figure 3). (These data are for runs at 400°F. wall temperature. Their data at 600°F. wall

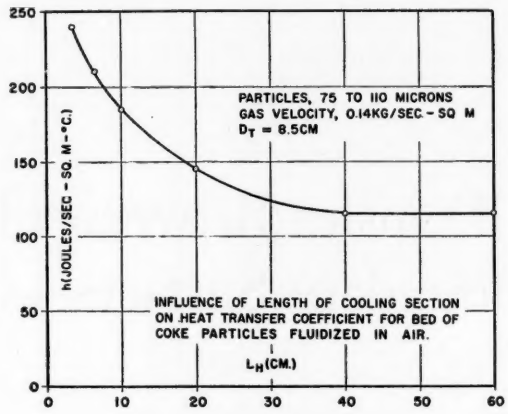

Fig. 1. Data of Van Heerden.

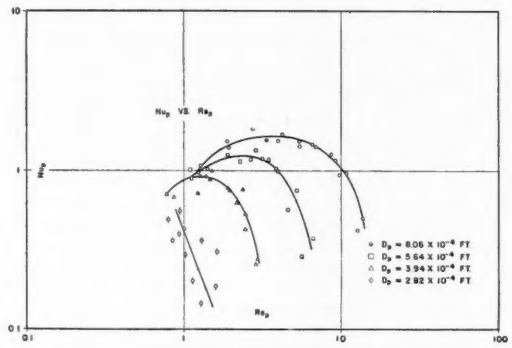

Fig. 2. Bartholomew and Katz sand-air data for narrow-size fractions; 400°F. wall temperature.

temperature are discussed below.) The points, which include both narrow and wide D_p ranges, lie on a straight line of slope 1.0, indicating proportionality of Nu_p to $1 - \epsilon$. A plot of $Nu_p/(1 - \epsilon)$ was then found to tie all these data of Figure 2 together on one smooth curve, with no maximum and no separation according to D_p (Figure 4). The group $Nu_p/(1 - \epsilon)$, plotted against Re_p, apparently takes care of the effects of D_p, G, and $1 - \epsilon$.

A composite plot of $Nu_p/(1 - \epsilon)$ vs. Re_p over an L_H/D_T range of 7 to 36, for the data of other authors as well as Bartholomew and Katz, showed a smooth curve with some spreading due to physical-properties variations for different systems, but no discernible effect of L_H/D_T. It was concluded that $L_H/D_T > 7$ was safe for physical-properties study, being in the region where L_H/D_T is high enough to be without effect.

Physical Properties, the Group $c_s\rho_p/c_g\rho_g$

Data of Bartholomew and Katz at 600°F. wall temperature were found to plot a bit high, relative to 400°F. wall temperature data, on a $Nu_p/(1 - \epsilon)$ vs. Re_p curve. The former data were at higher bed temperatures, causing some difference in gas properties. Vreedenberg (*31*) had suggested use of the ratio of gas density to particle density ρ_g/ρ_p as a multiplier on the coefficient, and it was found that this factor promoted an excellent line-up of the high- and low-temperature data of Bartholomew and Katz.

Attention was then turned to the data of Leva, Weintraub, and Grummer (*16*), who covered a wide range of physical properties. [Their reported coefficients were based on area corresponding to bed height at incipient fluidization L_{mf}, and ΔT values were determined by using values of bed temperature T_B integrated over the length L_{mf}. Their data were recalculated to obtain coefficients based on heated length L_H. In addition, their reported gas-inlet temperatures were in error, and their data were therefore recalculated to a basis of 80°F. gas-inlet temperature, which was believed to have been approximately correct (*17*).] Their runs at $L_H/D_T > 7$ were plotted as $Nu_p/(1 - \epsilon)$ and $Nu_p/[(1 - \epsilon)(\rho_p/\rho_g)]$ vs. Re_p, the latter showing a distinct advantage. However, their helium data (high gas-heat capacity c_g) deviated, indicating the need for inclusion of heat capacity, it being noted that use of a gas-to-solid heat-capacity ratio c_g/c_s as a direct multiplier on Nu_p would bring these data into line with the others.

The combined-properties group $c_s\rho_p/c_g\rho_g$ was used by Dow and Jakob and by Van Heerden, Nobel, and Van Krevelen, and its use here as $Nu_p/[(1 - \epsilon)(c_s\rho_p/c_g\rho_g)]$ was indicated. A cross plot of $Nu_p/(1 - \epsilon)$ vs. $c_s\rho_p/c_g\rho_g$, at constant Re_p, was prepared (Figure 5) from curves of $Nu_p(1 - \epsilon)$ vs. Re_p for

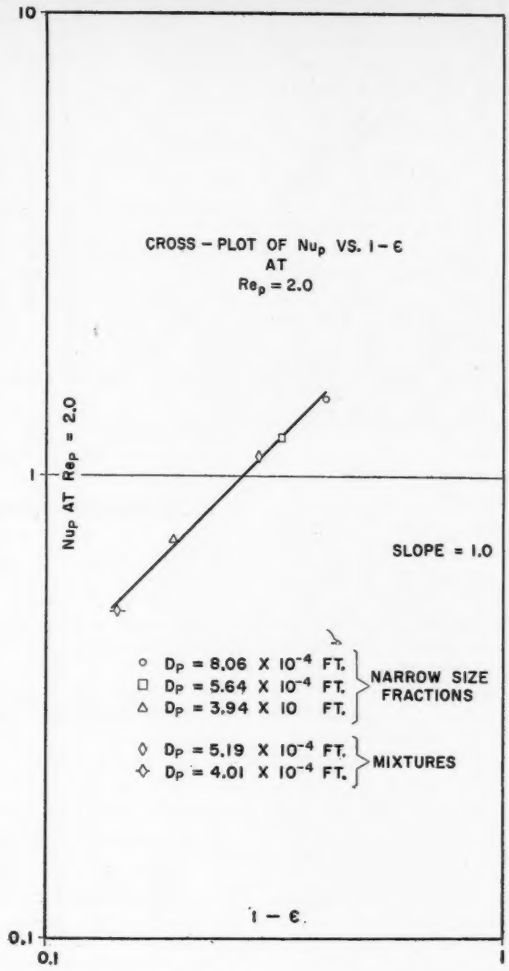

Fig. 3. Bartholomew and Katz sand-air data; 400°F. wall temperature.

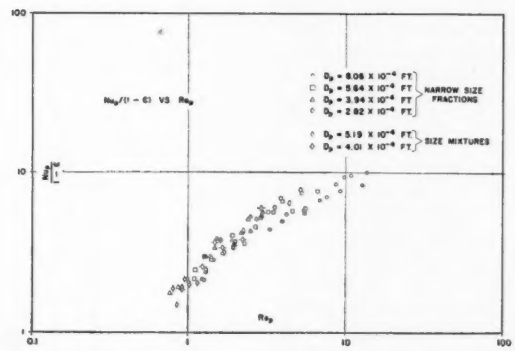

Fig. 4. Bartholomew and Katz sand-air data; 400°F. wall temperature.

constant system properties, using data at $L_H/D_T > 7$ of Leva, et al., and others. (See Table 1.) The points can be represented adequately by a line of slope 1.0, an indication of the applicability of $Nu_p/(1 - \epsilon)$ proportional to $c_s\rho_p/c_g\rho_g$. (Note: the subscript p was used in ρ_p to define this term specifically as particle density, including intraparticle voids when present, whereas c_s represents heat capacity of the solid.)

It was concluded that a correlation could be obtained by plotting $Nu_p/[(1 - \epsilon)(c_s\rho_p/c_g\rho_g)]$ vs. Re_p. For convenience, the correlation group $Nu_p/[(1 - \epsilon)(c_s\rho_p/c_g\rho_g)]$ is designated as y. Figure 6 shows y vs. Re_p for data at $L_H/D_T > 7$ from the four sources worked up.

Quantitative Treatment of L_H/D_T Effect

Extension to $L_H/D_T < 7$

Some of the data of Leva, Weintraub, and Grummer and of Toomey and Johnstone, and all the data of Dow and Jakob are at L_H/D_T less than 7. The Dow and Jakob data cover a wide range of L_H/D_T and are useful for evaluating its place in the correlation.

The Van Heerden curve, with h decreasing with L_H and then leveling off to a constant value, suggested use of a "dying-away" or "decaying" function of the form $h = h_0 + h_0Be^{-CL_H}$, where h_0 is the constant value reached by h at high L_H, rather than the simple 0.65 power function used by Dow and Jakob. As a test, the data of Van Heerden's L_H study shown in Figure 1 were redrawn as a semilog plot of $h/h_0 - 1$ vs. L_H, with $h_0 = 115$ joules/(sec.)(sq. meter/°C.). A straight line was obtained, which confirmed applicability of this function.

Application was then made to the Dow and Jakob data as follows. Over the Re_p range involved, the Dow and Jakob data show $Nu_p/(1 - \epsilon)$ proportional to $(Re_p)^{0.8}$, as reported by them. These data were worked up as $y/(Re_p)^{0.8}$, this combined function representing their data transposed to a Re_p of 1 for study of L_H effect. E designates y at $Re_p = 1$; and for Dow and Jakob, $E = y/(Re_p)^{0.8}$. (Cross plotting from lines of constant L_H/D_T could also have been used.) Comparison of plots of E vs. L_H and E vs. L_H/D_T for their coke data, obtained in 2- and 3-in. units, confirmed need for L_H as L_H/D_T. Separation of their Aerocat cracking catalyst, coke, and iron-powder data (all fluidized with air) when plotted as E vs. L_H/D_T indicated need for some additional properties term with L_H/D_T. Cross plots were made of L_H/D_T, at constant E, vs. ρ_p/ρ_g, c_s/c_g, and $c_s\rho_p/c_g\rho_g$. On the basis (admittedly sketchy) of obtaining a straight line of slope 1.1 on the c_s/c_g plot, it was decided to use the L_H/D_T group as $(L_H/D_T)/(c_s/c_g)$, here designated ϕ. (Van Heerden explains the variation of h with L_H as due

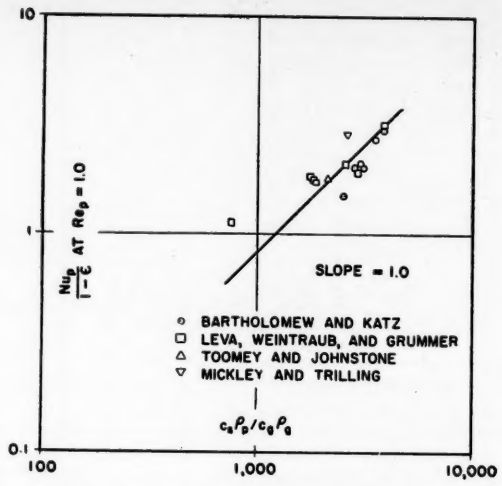

Fig. 5. Physical-properties cross plot for external surface; from data at $L_H/D_T > 7$.

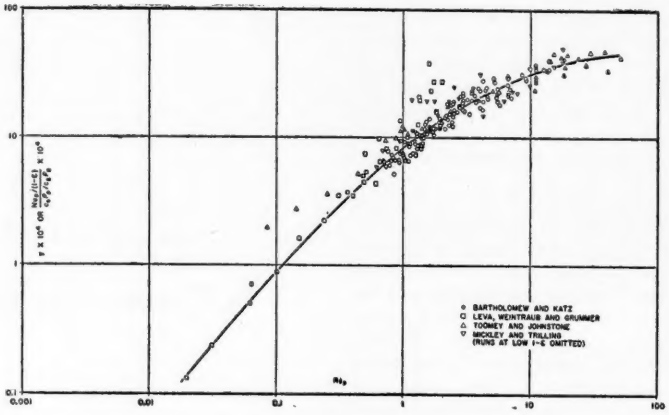

Fig. 6. Plot of y vs. Re_p for external heat transfer surface at $L_H/D_T > 7$.

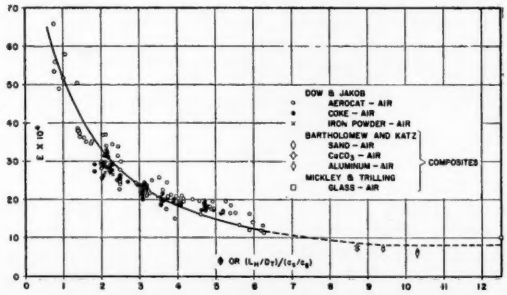

Fig. 7. E vs. ϕ for external surface.

to gradual establishment of a stationary temperature gradient in the downward-moving surface layer commonly observed at the wall of a fluidized bed. If so, then thermal properties may very well be involved.) Figure 7 shows E vs. ϕ for the Dow and Jakob data (individual runs) and for other data (composite values from cross plotting). (Data of Leva, Weintraub, and Grummer inexplicably show no L_H effect and are omitted in Figure 7.) It can be seen that Dow and Jakob data on Aerocat, coke, and iron powder fall together and that they extrapolate reasonably well to the high ϕ data of other workers. This tie-in of several authors' results was most encouraging.

A semilog plot of $E/E_0 - 1$ vs. ϕ was used for evaluation of constants B and C in the decaying function $y = y_0(1 + Be^{-C\phi})$. Rearranging and writing for use of E gives $E/E_0 - 1 = Be^{-C\phi}$. (The subscript 0 refers to the region of high L_H/D_T, where h is constant.) Selection of a proper value of E_0 was necessary in order to prepare this graph. Since Figure 6 represents data in the region where the L_H effect has essentially vanished, the value of y_0 at $Re_p = 1$ can be estimated from this graph. Inspection of Figure 6 yields 8.0×10^{-4} as a suitable value of y_0 at $Re_p = 1$, or E_0. In Figure 7 the Dow and Jakob data are shown satisfactorily extrapolated to this value of E_0. From the semilog plot of $E/E_0 - 1$ vs. ϕ, B and C were obtained as 7.5 and 0.44 respectively. The L_H-group correction factor becomes $1 + 7.5e^{-0.44\phi}$. Calling this F makes the final correlation group, then,

$$\frac{hD_p/[k_g(1-\epsilon)(c_s\rho_p/c_g\rho_g)]}{1 + 7.5e^{-0.44(L_H/D_T)/(c_s/c_g)}} \quad \text{or} \quad \frac{y}{F}$$

Figure 8, y/F vs. Re_p, shows the data of Dow and Jakob; of Bartholomew and Katz; of Leva, Weintraub, and Grummer; of Mickley and Trilling; and of Toomey and Johnstone (approximate bed heights estimated from inspection of individual section pressure drops for their sectionalized apparatus and may include dilute phase above dense bed) and is presented as a correlation for the case of external heat transfer surface. The average deviation is 22.1% for the 429 points. The low ϕ data of Leva et al. deviate the most seriously of the points plotted. Major deviations of the low-bed-density runs of Mickley and Trilling are not shown, but are discussed later.

CORRELATION OF INTERNAL HEAT TRANSFER SURFACE DATA

Physical Properties

Data which have been worked up for the case of internal heat transfer surface are those of Mickley and Fairbanks; Olin and Dean; Baerg, Klassen, and Gishler; Toomey and Johnstone; Mickley and Trilling; and Kellogg-built commercial fluid-hydroformer-catalyst-regenerator bed coolers. These data did not check out with the y correlation, and need for a separate correlation was apparent.

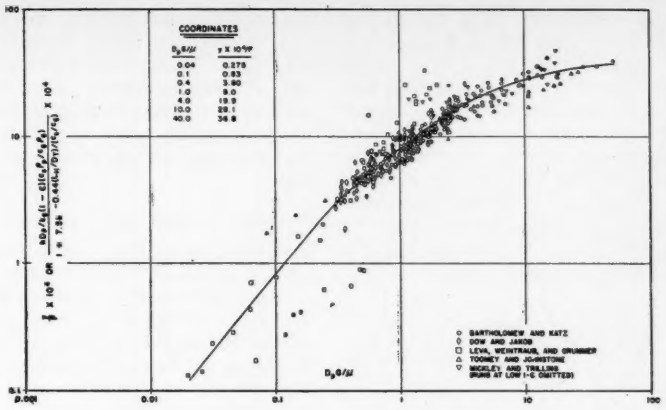

Fig. 8. The y correlation for external heat transfer surface.

Owing to lack of suitable data covering a wide range of fraction solids, proportionality of Nu_p to $1 - \epsilon$ was assumed on the basis of its having been established for the external surface case. (Some confirmatory evidence has since become available on the commercial units.) No L/D effect was observed for the internal surface data although L_B/D_T ranged ninefold and L_H/D_T fifteenfold.

Physical-properties effects were evaluated from the excellent data of Mickley and Fairbanks, who covered a wide range of gas properties. Their data when plotted as $Nu_p/(1 - \epsilon)$ vs. Re_p showed a family of lines for the different systems used. (See Table 2 for a summary of physical-properties terms.) Cross plotting of $Nu_p/(1 - \epsilon)$, at constant Re_p vs. $c_s\rho_p/c_g\rho_g$ yielded no correlation; however, trial-and-error log-paper plotting of $Nu_p/[(1 - \epsilon)(c_s/c_g)^n]$ vs. ρ_p/ρ_g with various values of n yielded a good line-up of points when $n = 0.80$, the slope of the line being 0.66. This indicated suitability of $Nu_p/[(1 - \epsilon)(c_s c_g)^{0.80}(\rho_p/\rho_g)^{0.66}]$. However, the helium and dichlorodifluoromethane (Freon 12) points did not line up with the others, an indication of a need for some additional group which has essentially the same value for all the other gases but which has markedly different values for helium and dichlorodifluoromethane. Inspection of properties (Table 2) showed

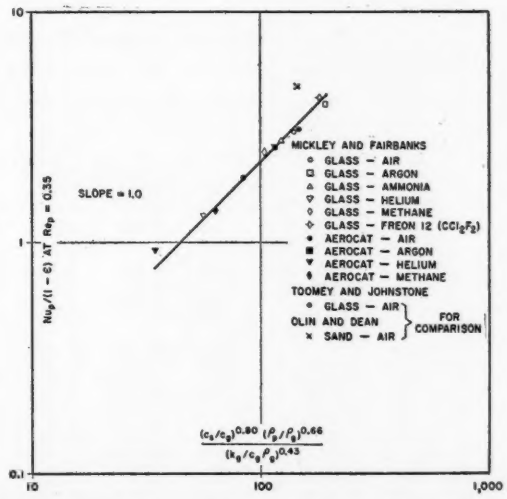

Fig. 9. Physical-properties cross plot for internal surface.

thermal diffusivity $k_g/c_g\rho_g$ to fit this requirement. A log plot of $Nu_p/[(1-\epsilon)(c_s/c_g)^{0.80}(\rho_p/\rho_g)^{0.66}]$ vs. $k_g/c_g\rho_g$ caused helium and dichlorodifluoromethane data to line up with the others on a slope of -0.43. (Kinematic viscosity μ/ρ_g behaves essentially the same, since values of Prandtl number vary little.) Figure 9 shows $Nu_p/(1-\epsilon)$ plotted against the combined-properties group $(c_s/c_g)^{0.80}(\rho_p/\rho_g)^{0.66}/(k_g/c_g\rho_g)^{0.43}$. Accordingly, the final-correlation group becomes

$$\frac{hD_p}{k_g(1-\epsilon)}\frac{\left(\frac{k_g}{c_g\rho_g}\right)^{0.43}}{\left(\frac{c_s}{c_g}\right)^{0.80}\left(\frac{\rho_p}{\rho_g}\right)^{0.66}} \quad \text{or} \quad z$$

This is not dimensionless, $k_g/c_g\rho_g$ having net units of square feet per hour. For convenience, the entire group is labeled z.

When plotted against Re_p, the z group showed tight correlation of the data of Mickley and Fairbanks (Figure 10) and a general correlation of these data with those of Olin and Dean; Toomey and Johnstone; Baerg, Klassen, and Gishler; and Mickley and Trilling. However, these data are all for axial tube location, and data of Kellogg-built commercial fluid-hydroformer–catalyst regenerators having multiple cooling tubes located between shell axis and shell wall plotted somewhat high.

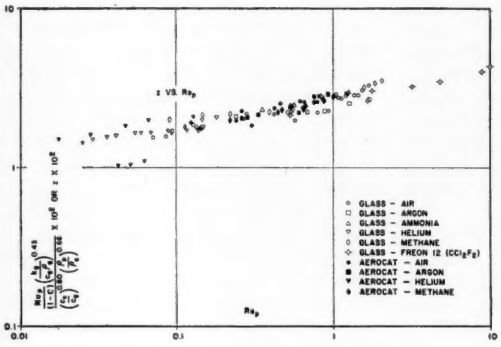

Fig. 10. Data of Mickley and Fairbanks.

Correction for Nonaxial-tube Location

It was recalled that Vreedenberg (*31*) studied the effect of tube location, using a vertical tube at three locations (including axial) at constant operating conditions. His results are shown in Figure 11 as h/h_{axial} vs. R_t/R_T, the ratio of radial-tube distance from the center line to the radius of the shell. The effect of tube location is substantial. The ratio h/h_{axial} was designated as a correction factor C_R for nonaxial tube location and the z correlation was modified to z/C_R vs. Re_p. (Of course, for all axial-tube data $C_R = 1$.) Figure 12 shows the final correlation and includes the data mentioned above plus six points calculated from operating data on three commercial fluid-hydroformer–catalyst–regenerator bed coolers which, with use of the C_R factor, now fall in with the axial-tube data. These commercial units represent a substantial scale-up relative to the laboratory units used by those workers from whose data the z correlation was developed.

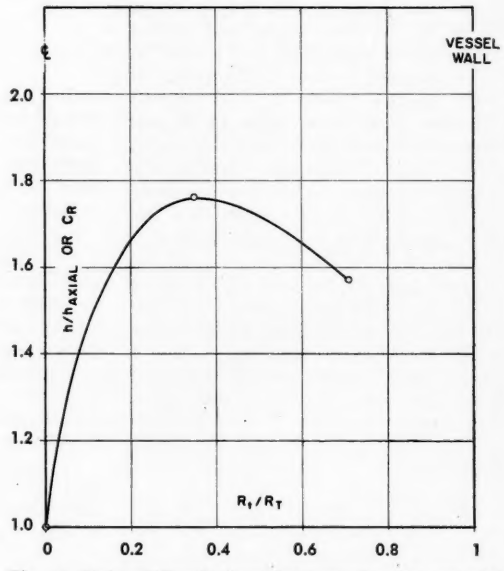

Fig. 11. Data of Vreedenberg for correction for nonaxial tube location in case of internal (inserted) surface.

TABLE 1

TERMS FOR EXTERNAL HEAT-TRANSFER SURFACE,

$L_H/D_T > 7.0$

$Nu_p/(1-\epsilon)$ at $Re_p = 1.0$ as a Function of Physical Properties

Source	Solid	Gas	Identification	ρ_p	ρ_g	c_s	c_g	$c_s\rho_p/c_g\rho_g$	k_g	$k_g/c_g\rho_g$, sq. ft./hr.	$\frac{Nu_p}{1-\epsilon}$ at $Re_p = 1.0$	$\frac{hD_p}{(1-\epsilon)c_s\rho_p}$ at $Re_p = 1.0$
3	Sand	Air	600°F. Wall	165	0.038	0.20	0.25	3,500	0.0268	2.83	2.72	0.00221
3	Sand	Air	400°F. Wall	165	0.047	0.20	0.25	2,800	0.0225	1.91	2.02	0.00138
3	$CaCO_3$	Air	600°F. Wall	167	0.038	0.214	0.25	3,800	0.0268	2.83	3.00	0.00225
3	$CaCO_3$	Air	400°F. Wall	167	0.047	0.214	0.25	3,000	0.0225	1.91	2.10	0.00132
3	Aluminum	Air	600°F. Wall	160	0.038	0.182	0.25	3,100	0.0268	2.83	2.01	0.00185
3	Aluminum	Air	400°F. Wall	160	0.047	0.182	0.25	2,500	0.0225	1.91	1.50	0.00116
21	Glass •	Air	$c_s\rho_p/c_g\rho_g$ = 2,600	153	0.047	0.20	0.25	2,600	0.0234	1.99	2.85	0.00218
26	Glass	Air		175	0.067	0.20	0.25	2,100	0.0180	1.07	1.80	0.000928
16	Sand	Air	Run 28	165	0.0734	0.20	0.25	1,800	0.0216	1.18	1.72	0.00113
16	Sand	Air	Run 57	165	0.0514	0.20	0.25	2,570	0.0216	1.68	2.10	0.00138
16	Sand	CO_2	Run 5	165	0.1845	0.20	0.235	764	0.0170	0.392	1.12	0.000576
16	Sand	CO_2	Run 4	165	0.0775	0.20	0.235	1,810	0.0170	0.935	1.72	0.00109
16	Sand	Helium	Run 56	165	0.0069	0.20	1.24	3,860	0.108	12.6	3.2*	0.0104*
16	Iron catalyst	Air	Run 39	312	0.135	0.193	0.25	1,770	0.0216	0.641	1.80	0.000645
16	Iron catalyst	Air	Run 46	312	0.0818	0.193	0.25	2,920	0.0216	1.05	1.91	0.000685

*Extrapolated value. Curve of $Nu_p/(1-\epsilon)$ vs. Re_p extrapolated to have same slope at $Re_p = 1$ as the other curves of Leva, et. al.

The equation of the straight line of Figure 12 is

$$\left(\frac{hD_p/k_g}{1-\epsilon}\right)\left(\frac{k_g}{c_g\rho_g}\right)^{0.43} = 0.033C_R\left(\frac{D_pG}{\mu}\right)^{0.23}\left(\frac{c_s}{c_g}\right)^{0.80}\left(\frac{\rho_p}{\rho_g}\right)^{0.66}$$

with C_R being read from Figure 11. The group $k_g/c_g\rho_g$ has net units of square feet per hour. This is presented as the correlation for internal heat transfer surface. Average deviation for the 323 points plotted is 19.5%.

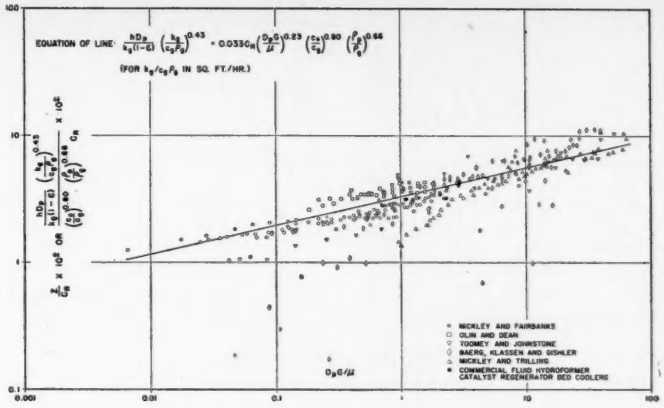

Fig. 12. The z correlation for internal heat transfer surface.

DISCUSSION OF THE CORRELATIONS

Major Deviations

Data of Mickley and Trilling, for their external surface units, show large deviations from the y correlation at low values of $1-\epsilon$, points sweeping sharply upward as vertical "tails," separated according to D_p. (See Figure 13.) These runs, which are at high velocities and which were omitted in the y correlation are believed to involve continuous vertical transport rather than true fluidized beds, with a different mechanism controlling. Even though they had disengaging sections atop their fluidization columns, some small external recycle was reported from their cyclone separators to a feed column and then to the bottoms of the fluidizing columns. In addition, inspection of their data will indicate several instances where, for a given D_p, markedly different values of ρ_b or $1-\epsilon$ were observed for runs at the same air velocity. Whereas for a fluidized bed ρ_b or $1-\epsilon$ is a unique function of gas flow rate, the behavior mentioned above is characteristic of vertical transport, where ρ_b or $1-\epsilon$ is also dependent upon the solids feed rate.

Low velocity runs of Baerg, Klassen, and Gishler deviate sharply on the z correlation, as seen in Figure 12, with separation according to particle size. The explanation is not clear. It may be due to the coordinated downward flow of particles at the wall of their internal axial heater reported by them at low velocities. Apparently at higher velocities increased side mixing causes the data to bend over and line up together within themselves and with the other data of Figure 12.

No L_H/D_T effect was observed in the external-surface data of Leva, Weintraub, and Grummer, although data of Van Heerden, et al. and of Dow and Jakob show such an effect. For this reason, the validity of the y/F correlation (Figure 8) at values of L_H/D_T less than 7 (i.e., $F > 1$) is uncertain. Somewhere below this point entrance effects, not yet rigidly defined, become prominent. The data of Dow and Jakob can be described by an expression such as developed herein; the conditions of Leva and coworkers in some way obviated an entrance effect. Of course no such qualification need be attached to the y correlation of Figure 6, which is limited to $L_H/D_T \geqq 7$.

It should be noted that only the low L_H/D_T air data of Leva et al. deviate from the y/F curve, application of the F factor causing them to plot low. Their helium data were at a high c_g, causing ϕ $(= L_Hc_g/D_Tc_s)$ to be high even at low L_H/D_T and thereby giving F equal to unity and no deviation. The low L_H/D_T air data of Leva et al. were not used in drawing the lower end of Figure 8; the curve was drawn through the helium points. (This low Re_p region is determined by the data of Leva et al., which ranged down to far lower Re_p values than did other data.)

Indications of Mechanism and General Discussion

With the use of fraction solids as $Nu_p/(1-\epsilon)$, no effect was found of particle shape or particle-size distribution. Data for various shapes and D_p ranges fall in together. Of course, reliable prediction of $1-\epsilon$ values may require these factors, but use of $1-\epsilon$ as a correlating variable apparently relieves the heat transfer problem of this burden. Indeed, experimental values of $1-\epsilon$ for a particular solid can be determined quickly and easily, when required, relative to the experimental determination of heat transfer coefficients. [Fraction

TABLE 2

TERMS FOR INTERNAL HEAT TRANSFER SURFACE

$Nu_p/(1-\epsilon)$ at $Re_p = 0.35$ as a Function of Average Physical Properties

Source	Solid	Gas	ρ_p	ρ_g	c_s	c_g	k_g	$k_g/c_g\rho_g$ sq. ft./hr.	$\frac{Nu_p}{1-\epsilon}$ at $Re_p = 0.35$
20	Glass	CCl_2F_2	153	0.30	0.20	0.15	0.0061	0.136	4.2
20	Glass	Argon	153	0.11	0.20	0.125	0.011	0.800	3.95
20	Glass	Air	153	0.071	0.20	0.25	0.016	0.900	3.00
20	Glass	Ammonia	153	0.042	0.20	0.52	0.015	0.685	2.75
20	Glass	Methane	153	0.041	0.20	0.55	0.021	0.935	2.45
20	Glass	Helium	153	0.011	0.20	1.24	0.088	6.45	1.31
20	Aerocat (Cracking Cat.)	Argon	49	0.11	0.276	0.125	0.011	0.800	2.60
20	Aerocat (Cracking Cat.)	Air	49	0.071	0.276	0.25	0.016	0.900	1.91
20	Aerocat (Cracking Cat.)	Methane	49	0.041	0.276	0.55	0.021	0.935	1.39
20	Aerocat (Cracking Cat.)	Helium	49	0.011	0.276	1.24	0.088	6.45	0.92
26	Glass	Air	175	0.067	0.20	0.25	0.018	1.07	3.1
23	Sand	Air	165	0.062	0.20	0.25	0.0175	1.13	4.7

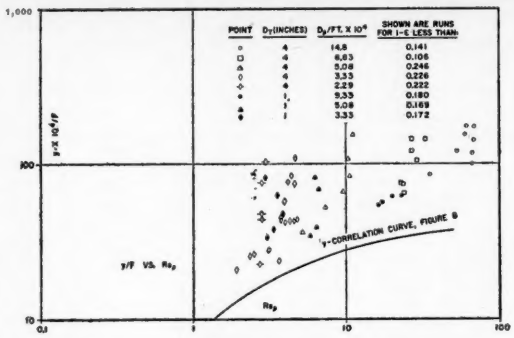

Fig. 13. Low $1 - \epsilon$ data of Mickley and Trilling (external surface) showing deviations from y correlation.

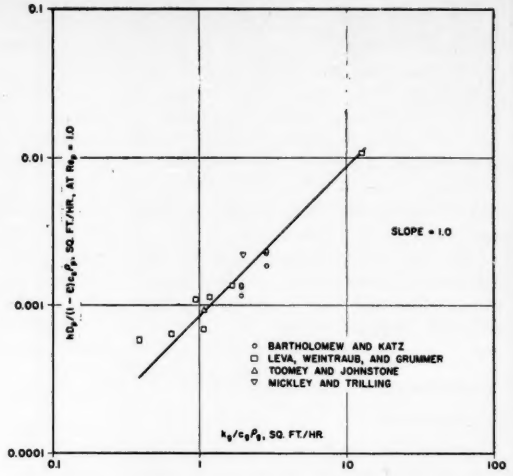

Fig. 14. Effect of gas properties on external surface heat transfer; from data at $L_H/D_T > 7$.

solids is proportional to bed density by the simple relation $\rho_b = (1 - \epsilon)\rho_p$ for gas fluidization.]

In the case of the external surface correlation, an important role for heat transport by the solid particles, as proposed by Van Heerden, Nobel, and Van Krevelen (*27*), is indicated by the dependence upon the heat-carrying capacity of the solids, $(1 - \epsilon)\ c_s\rho_p$. Writing the y correlation group as $hD_p/[(1 - \epsilon)c_s\rho_p(k_g/c_g\rho_g)]$ shows the dependence of h upon the gas thermal diffusivity in addition to dependence upon $(1 - \epsilon)\ c_s\rho_p$. The effect of gas properties as $k_g/c_g\rho_g$ is seen in Figure 14, a modification Figure 5. Here $k_g/c_g\rho_g$ is split out of the y group and plotted against $hD_p/[(1 - \epsilon)c_s\rho_p]$. The appearance of gas thermal diffusivity indicated that unsteady state conduction in the gas is important. It will be noted also that if the physical-properties terms in the y correlation group are rearranged to $k_g[(1 - \epsilon)c_s\rho_p/c_g\rho_g]$ it is as if the gas thermal conductivity in the Nusselt number were being magnified by the ratio $(1 - \epsilon)c_s\rho_p/c_g\rho_g$. The product might be interpreted as an "effective thermal conductivity" for the mobile particle suspension. This "effective thermal conductivity" should vary from a low value near the vessel wall (quiescent down flow of particles at the wall visually observed by several workers) to a very high value in the bulk of the bed [cf. high eddy conductivities reported by Gilliland (*21*)], and the group $k_g[(1 - \epsilon)c_s\rho_p/c_g\rho_g]$ may represent some mean value. With typical values (characteristic of many of the runs in the y correlation) of 0.35 for $1 - \epsilon$, 0.20 for c_s, 165 for ρ_p, 0.025 for k_g, 0.25 for c_g, and 0.050 for ρ_g, a value of 23 for the group $k_g[(1 - \epsilon)c_s\rho_p/c_g\rho_g]$ is obtained as an indication of order of magnitude of effective thermal conductivity.

As far as dependence of h upon D_p in the y correlation is concerned, it is difficult to characterize, since $1 - \epsilon$ is also dependent on D_p. Inspection of the y correlation curve (Figure 8) indicates that at low Re_p the ratio $h/(1 - \epsilon)$ or the coefficient "per unit fraction solids" increases with increasing D_p, becoming independent of D_p at intermediate Re_p values where the slope of the curve is about one, and then decreasing with decreasing D_p at high Re_p values. This behavior may explain contradictions in the literature regarding effect of D_p.

The inclusion of c_s/c_g with L_H/D_T in the external-surface L_H group ϕ is a point that requires verification. More data on physical-properties studies are needed to check this inclusion, as against a revision of the direct proportionality of $Nu_p/(1 - \epsilon)$ to $c_s\rho_p/c_g\rho_g$ to relieve the L_H/D_T group of carrying some physical properties with it. Again, Van Heerden's explanation for the L_H effect suggests possible inclusion of thermal properties with L_H/D_T.

In the case of the z correlation for internal-surface data, the complexity of the group, with separation of the ρ_p/ρ_g and c_s/c_g terms, makes analysis difficult. The importance of thermal diffusivity of the gas indicates unsteady state conduction in the gas as a major factor. Lesser variation with Reynolds number is probably due to more side mixing in the bed than at the vessel wall. Dependence of $h/(1 - \epsilon)$ upon D_p is seen to be simply $h/(1 - \epsilon) \propto D_p^{-0.77}$, showing decrease of $h/(1 - \epsilon)$ with increasing D_p in the case of internal surface. Inspection of the z correlation equation will also show ρ_g to drop out when gas mass velocity G is replaced by linear velocity as $u_g\rho_g$.

It must be remembered, of course, that the z function was established by the work of only one group (Mickley and Fairbanks) and that the other internal surface data tied in with it. There appears to be some evidence of discrepancies at low gas velocities ($G/G_{mf} < 2$).

CONCLUSION

For the first time, correlations of the data from as many as eight literature sources, plus commercial units, are reported for heat transfer to beds of fluidized solids. The correlations are

1. For external heat transfer surface, a curve (Figure 8) of the dimensionless y/F group

$$\frac{hD_p/[k_g(1 - \epsilon)(c_s\rho_p/c_g\rho_g)]}{1 + 7.5e^{-0.44(L_H/D_T)/(c_s/c_g)}}$$

vs. D_pG/μ, with five data sets included.

Table 3

Ranges of Variables Covered

	External surface y correlation	Internal surface z correlation
D_p(ft. × 10^4)	1.62–27.8	1.33–28.8
c_s	0.117–0.276	0.20–0.316
ρ_p	52–328	49–179
$1 - \epsilon$	0.050–0.564	0.055–0.603
c_g	0.235–1.24	0.125–1.24
ρ_g	0.0069–0.185	0.011–0.485
μ(centipoises)	0.0193–0.0290	0.0105–0.0382
k_g	0.0165–0.108	0.0061–0.088
D_T(ft.)	0.083–0.394	0.24–6.33
L_H(ft.)	0.142–3.33	0.33–17.5
L_B(ft.)	0.142–8.33	0.83–26.6
h	3.3–174	10.0–181

2. For internal heat transfer surface, a straight-line plot (Figure 12) of the dimensional z/C_R group

$$\frac{\dfrac{hD_p}{k_g}\left(\dfrac{k_g}{c_g\rho_g}\right)^{0.43}}{(1 - \epsilon)C_R\left(\dfrac{c_s}{c_g}\right)^{0.80}\left(\dfrac{\rho_p}{\rho_g}\right)^{0.66}}$$

vs. D_pG/μ, with six data sets included. The equation of this correlation is

$$\frac{hD_p}{k_g(1-\epsilon)}\left(\frac{k_g}{c_g\rho_g}\right)^{0.43} = 0.033C_R\left(\frac{D_pG}{\mu}\right)^{0.23}\left(\frac{c_s}{c_g}\right)^{0.80}\left(\frac{\rho_p}{\rho_g}\right)^{0.66}$$

C_R, the correlation for nonaxial tube location, is read from Figure 11.

While empirical, these correlations offer a means of predicting coefficients until better understanding of mechanism enables sounder theoretical methods to be evolved. A total of 752 runs is included, with average deviations of 22.1% for the 429 runs in the y correlation for external surface and 19.5% for the 323 runs in the z correlation for internal surface. These are considered to be fairly good, in view of the number and variety of experimental studies correlated. The inclusion of data on commercial units, in the z correlation, is particularly encouraging. Table 3 summarizes the ranges of variables covered.

Over all, the most important conclusion is that order can indeed be brought into what had previously appeared to be a chaotic situation.

ACKNOWLEDGMENT

The authors wish to thank The M. W. Kellogg Company for permission to publish this paper and W. E. Lobo and G. T. Skaperdas for their helpful guidance.

NOTATION

B = an arbitrary constant

c_g = heat capacity of the fluidizing gas, B.t.u./(lb.)(°F.)

c_s = heat capacity of solid being fluidized, B.t.u./(lb.)(°F.)

C = an arbitrary constant

C_R = correction for nonaxial-tube location, for cases of internal heat transfer surface

D_p = average particle diameter, ft.

D_T = diameter of fluidization vessel, ft.

e = base of natural logarithms

E = the group y at a Reynolds number of 1

E_0 = the group y_0 at a Reynolds number of 1

F = heated-length correction factor, $1 + 7.5e^{-0.44\phi}$, for external surface correlation

G = superficial mass velocity of gas, lb./(sec.)(sq. ft.) or lb./(hr.)(sq. ft.)

G_{mf} = minimum fluidizing mass velocity, lb./(sec.)(sq. ft.) or lb./(hr.)(sq. ft.)

h = heat transfer coefficient for transfer between bed and heating or cooling surface, B.t.u./(hr.)(sq. ft./°F.)

h_0 = constant value of external surface h at high values of heated-length group ϕ, B.t.u./(hr.)(sq. ft./°F.)

k_g = thermal conductivity of the fluidizing gas, B.t.u./(hr.)(sq. ft.)(°F./ft.)

L_B = bed height, ft.

L_H = length of heat transfer surface, ft.

L_{mf} = bed height at incipient fluidization or height of freshly settled bed, ft.

n = an arbitrary constant

Nu_p = Nusselt number, hD_p/k_g, based on average particle diameter

Pr = Prandtl number, $c_g\mu/k_g$

Re_p = Reynolds number, D_pG/μ, based on average particle diameter

R_t = radial distance of tubes from axis of shell, ft.

R_T = radius of shell or fluidizing vessel, ft.

u_g = superficial linear velocity of gas, ft./sec. or ft./hr.

y = dimensionless correlation group $hD_p/[k_g(1-\epsilon)(c_s\rho_p/c_g\rho_g)]$ for external heat transfer surface

y_0 = constant value of y at high values of heated-length group ϕ, i.e., the group y based on h_0

z = dimensional-correlation group $(hD_p/k_g)(k_g/c_g\rho_g)^{0.43}/[(1-\epsilon)(c_s/c_g)^{0.80}(\rho_p/\rho_g)^{0.66}]$ for internal heat transfer surface

Greek Letters

ϵ = fraction voids (extraparticle) in fluidized bed

$1-\epsilon$ = fraction solids in fluidized bed

ρ_b = average fluidized-bed density, lb./cu. ft.

ρ_g = density of fluidizing gas, lb./cu. ft.

ρ_p = particle density, lb./cu. ft., including internal voids for porous particles; equal to mass of particle/volume of particle

ϕ = dimensionless heated-length group $(L_H/D_T)/(c_s/c_g)$ for external heat transfer surface

μ = viscosity of the fluidizing gas, centipoises, lb./(sec.)(ft.), lb./(hr.)(ft.)

LITERATURE CITED

1. Agarwal, O. P., and J. A. Storrow, *Chem. & Ind.*, p. 321 (1951).
2. Baerg, A., J. Klassen, and P. E. Gishler, *Can. J. Research*, **28F**, 287 (1950).
3. Bartholomew, R. N., and D. L. Katz, *Chem. Eng. Progr. Symposium Ser.* No. 4, **48**, 3 (1952); also Bartholomew, R. N., Ph.D. thesis, Univ. Mich., Ann Arbor (1950).
4. Brazelton, W. T., Ph.D. thesis, Northwestern Univ., Evanston, Ill. (1951).
5. Campbell, J. R., and F. Rumford, *J. Soc. Chem. Ind.*, **69**, 373 (1950).
6. Carr, N. L., and N. R. Amundson, *Ind. Eng. Chem.*, **43**, 1856 (1951).
7. Dow, W. M., and Max Jakob, *Chem. Eng. Progr.*, **47**, 637 (1951).
8. Gamson, B. W., *Chem. Eng. Progr.*, **47**, 19 (1951).
9. Gilliland, E. R., paper presented at A.I.Ch.E. New Jersey Section Meeting (May 5, 1953).
10. Gishler, P. E., personal communication (Aug. 17, 1953).
11. Jolley, L. J., *Fuel*, **28**, 114 (1949).
12. Kettenring, K. N., E. L. Manderfield, and J. M. Smith, *Chem. Eng. Progr.*, **46**, 139 (1950).
13. Koble, R. A., J. N. Ademino, E. P. Bartkus, and T. E. Corrigan, *Chem. Eng.*, p. 174 (September, 1951).
14. Leva, Max and M. Grummer, *Chem. Eng. Progr.*, **48**, 307 (1952).
15. Leva, Max, paper presented at the General Discussion of Heat Transfer, Inst. Mech. Engrs., London (Sept. 11–13, 1951).
16. Leva, Max, M. Weintraub, and M. Grummer, *Chem. Eng. Progr.*, **45**, 563 (1949).
17. Leva, Max, communication to W. J. Danziger of The M. W. Kellogg Co.
18. Levenspiel, Octave, and J. S. Walton, *Chem. Eng. Progr. Symposium Ser.* No. 9, **50**, 1 (1954); also Octave Levenspiel, Ph.D. thesis, Oregon State College, Corvallis (1952).
19. Levenspiel, Octave and J. S. Walton, "Proc. of Heat Transfer and Fluid Mechanics Institute," p. 139, *Am. Soc. of Mech. Engrs.* (May, 1949).
20. Mickley, H. S., and D. F. Fairbanks, *A.I.Ch.E. Journal*, **1**, 374 (1955); also Fairbanks, D. F., Sc.D. thesis, Mass. Inst. Technol., Cambridge (1953).
21. Mickley, H. S., and C. A. Trilling, *Ind. Eng. Chem.*, **41**, 1135 (1949).
22. Miller, C. O., and A. K. Logwinuk, *ibid.*, **43**, 1220 (1951); also, Logwinuk, A. K., Ph.D. thesis, Case Inst. Technol., Cleveland, Ohio (1948).
23. Olin, H. L., and O. C. Dean, *The Petroleum Engineer*, p. C-23 (March, 1953); also Dean, O. C., Ph.D. thesis, Univ. Iowa, Ames (1952).
24. Pritzlaff, A. H., Jr., Ph.D. thesis, Northwestern Univ., Evanston, Ill. (1951).
25. Simon, R. H., Ph.D. thesis, Oregon State College, Corvallis (1948).
26. Toomey, R. D., and H. F. Johnstone, *Chem. Eng. Progr. Symposium Ser.* No. 5, **49**, 51 (1953); also Toomey, R. D., Ph.D. thesis, Univ. of Illinois, Urbana (1950).
27. Van Heerden, C., A. P. P. Nobel, and D. W. Van Krevelen, *Ind. Eng. Chem.*, **45**, 1237 (1953).
28. Van Heerden, C., *J. Appl. Chem.*, **2**, Supplementary Issue No. 1, S-7 (1952).
29. ———, A. P. P. Nobel, and D. W. Van Krevelen, paper presented at the General Discussion of Heat Transfer, Inst. Mech. Engrs., London (Sept. 11–13, 1951).
30. ———, *Chem. Eng. Sci.*, **1**, 51 (1951).
31. Vreedenberg, H. A., *J. Appl. Chem.*, **2**, Supplementary Issue No. 1, S-26 (1952).
32. Vreedenberg, H. A., paper presented at the General Discussion of Heat Transfer, Inst. Mech. Engrs., London (Sept. 11–13, 1951).
33. Walton, J. S., R. L. Olson, and Octave Levenspiel, *Ind. Eng. Chem.*, **44**, 1474 (1952).
34. Wamsley, W. E., and L. N. Johanson, *Chem. Eng. Progr.*, **50**, 347 (1954).
35. Wen, C. Y., and Max Leva, *A.I.Ch.E. Journal*, **2**, 482 (1956).

Manuscript submitted May, 1957; revision received September 3, 1957; paper accepted September 9, 1957.

Entrapment of Gas in the Spreading of a Liquid Over a Rough Surface

S. G. BANKOFF

Rose Polytechnic Institute, Terre Haute, Indiana

Conditions for the incomplete displacement of gas from the valley between two parallel ridges by a liquid-drop front advancing over the ridges are calculated. The significant parameters are found to be the liquid density, surface tension, contact angle, and geometry of the ridges. The solution may be obtained analytically or, more conveniently, graphically. Surface roughnesses are divided into four classes, one of which can stably switch from liquid—to gas—fill, and another vice versa. This may account for some of the hysteresis effects reported in bubble nucleation. It is pointed out that surfaces consisting predominately of cavities are more likely to follow these considerations than grooved surfaces, owing to displacement of gas by advance of liquid along the grooves. An example important in boiling and cavitation theory is worked out, and qualitative agreement with the literature is shown.

In 1953 Bartell and Shepard (*2*) reported the results of an interesting series of experiments on the wetting of rough paraffin surfaces. The surfaces were machined in two directions to give pyramidal asperities of known height h and inclination to the horizontal ϕ, and the advancing and receding contact angles of large drops of various liquids on these surfaces were measured. In all cases the advancing contact angle increased with increasing ϕ. With liquids which wet the surface poorly, such as water, the hysteresis of the contact angle was almost exactly equal to the inclination ϕ. With liquids of better wetting power, such as methanol, the situation became complicated by the fact that flow through the valleys, as well as over the tops of the asperities, was an important mode of advance and recession; however, the results in general support the conclusion that would be expected from the application of Young's equation (*10*) on a microscopic scale, i.e., that the static contact angle at any point of the triple interface is a constant. The increase in advancing contact angle with increase of ϕ can be attributed to the fact that the triple interface usually comes to rest on the rear (viewed from the direction of advance) faces of the asperities, since this usually requires less contortion of the free liquid surface, and hence more nearly satisfies the minimum energy requirements.

Of equal interest was Bartell and Shepard's observation that the degree of air entrapment depended primarily on the steepness of the asperities and secondarily on their height. Large-scale entrapment was apparent in several cases where $\phi = 60$ deg. They proposed the hypothesis that the advancing liquid front contacts the forward face of the next asperity before displacing all the air from the crevice between and that the advance then proceeds from this new point of contact. The importance of this phenomenon is made apparent when it is realized that in practically all cases of ebullition, cavitation, and effervescence the appearance of bubbles is nucleated and controlled by minute quantities of gas, usually entrapped on solid surfaces. Each of these crevices where the advancing liquid front fails to displace the gaseous phase completely may therefore be a nucleus for bubble formation. Bartell and Shepard did not go into the conditions for entrapment quantitatively, and it is the purpose of this paper to set quantitative criteria for entrapment and displacement of gases from surface roughnesses. The mechanism considered by Bartell and Shepard, namely the advancement of the liquid across a valley, is alone considered. It is hoped that the advance of the liquid front along a valley will be considered at a later time. In addition to valleys, entrapment of gases in holes is also considered.

FREE LIQUID SURFACE

Before the surface geometry is considered, it is necessary to obtain the equation of the free surface of a semiinfinite sheet of liquid advancing unidirectionally. The two-dimensional problem is chosen to simplify the calculation, and since the orientation of the sheet is not specified, this does not limit the generality. The horizontal asymptote to the free liquid surface is chosen as the X axis. The location of the vertical Z axis is fixed by the condition that $X = 0$ when $Z = -2B^{1/2}$, where

$$B = \frac{\gamma}{(\rho_L - \rho_G)g} \tag{1}$$

In this case γ is surface tension, ρ_L and ρ_G are the densities of liquid and gas, and g is the local acceleration due to gravity. Since one principal radius of curvature of the liquid surface is everywhere infinite, the Gibbs (*5*) condition for equilibrium of a curved interface reduces to

$$Z = \frac{-B}{R} \tag{2}$$

where R is the radius of curvature. The solution of this problem yields (*1*) for a sheet advancing to the left

$$X = B^{1/2}\left[\log\left(+\sqrt{\frac{4B}{Z^2} - 1} - \frac{2B^{1/2}}{Z}\right) - 2\sqrt{B - \frac{Z^2}{4}}\right] \tag{3}$$

The signs in front of the square-root terms would be reversed for a sheet advancing to the right. The valuable result is obtained that, for a particular liquid at a particular temperature, a single curve describes all possible surface configurations, regardless of contact angle at the solid surface, since B is the only parameter in Equation (3).

SURFACE GROOVES

Now the advance of this semiinfinite liquid sheet normally across a groove, or valley is considered. It should be noted that a system of long grooves constitutes the most common type of gross surface roughness of metals, since almost all metal-forming operations, such as machining, drawing, extruding, polishing, and even pressing, will give a grooved surface. In regard to grooves with a V-shaped profile, such that the angle of inclination of the groove walls with the horizontal is ϕ (Figure 1), the conditions for entrapment may be quite simply stated:

$$\theta > 180° - 2\phi \tag{4}$$

This implies that no gas can be entrapped

if the liquid wets the solid perfectly ($\theta = 0$). Likewise, every deep groove with vertical walls will have trapped gas, according to this mechanism. It should be emphasized at this point that we are considering displacement of gas only by travel of liquid across the grooves, and not by some other mechanism, such as travel along the grooves.

It is of interest to consider the displacement of liquid from the grooves by gas (Figure 2). It is assumed that the walls of the groove are perfectly smooth, and so by a microscopic force balance, there is no hysteresis of the contact angle. If the curvature of the liquid surface within these small cavities is neglected, the condition that the advancing gas-liquid interface fails to displace the liquid completely is

$$2\phi > \theta \qquad (5)$$

This makes it possible to divide grooves in a particular system into four classes: (1) those that obey the first inequality, but not the second, (2) those that obey the second, but not the first, (3) those that obey both, and (4) those that obey neither. These will be examined in more detail.

The first class will exist when the liquid wets the solid poorly ($\theta \geq 90$ deg.) and when the grooves are gradually sloped ($\phi < 45$ deg.). Gas will be trapped in these shallow grooves, and even if the groove is filled with liquid, it can be completely displaced by gas. This would favor a maximum number of nucleation sites for cavitation or boiling from the surface.

The second class will exist when the liquid wets the solid well ($\theta \ll 90$ deg.) and ϕ is not nearly zero. Liquid will always eventually fill these grooves. It follows that the addition of wetting agents, sometimes used to obtain smaller bubble-release volumes in boiling, may have an unfavorable effect in reducing the number of effective nucleation sites.

The third class will exist when θ is not nearly zero, and $\phi \gg 45$ deg. Similarly, the fourth class will exist when θ is not nearly zero, and $\phi \ll 45$ deg. All very steep-walled grooves will be in the third class, from which complete displacement of either liquid or gas, once filled, is not possible. All very shallow grooves will be in the fourth class, in which entrapment is not possible.

The existence of the first and second classes of grooves, in which it is possible to switch stably from liquid to gas filled, and vice versa, may account for hysteresis phenomena observed by several investigators (*4, 9, 6*) in boiling heat transfer.

The problem becomes more complex when rounded grooves are considered. From Figure 3 it will be seen that the liquid contact angle must be considerably greater than 90 deg. in order to entrap gas if the groove is semicircular in cross section. It will be practically impossible to trap gas if the cross-sectional arc is less than a semicircle.

If the groove has any arbitrary geometry, Equation (2) must be used in either an analytical or graphical solution, the graphical solution usually being the easier method. As an example, one may wish to find the width of a groove with vertical walls which will always entrap gas when water at 100°C. is spreading over the surface with a contact angle of 60 deg. This problem is of importance in boiling heat transfer. The solution, which is given graphically in Figure 4, shows that a relatively wide groove will still entrap gas. Once again, however, only this mechanism is here being considered.

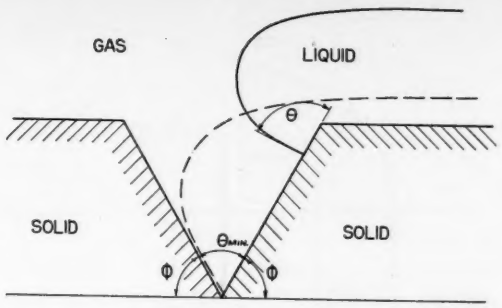

Fig. 1. Conditions for the entrapment of gas in the advance of a semiinfinite liquid sheet across a groove.

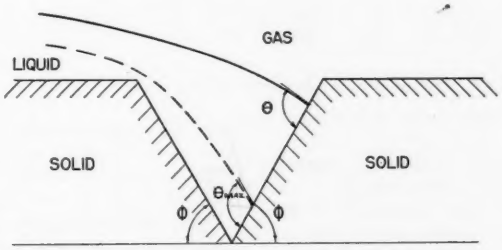

Fig. 2. Conditions for the entrapment of liquid in the recession of a semiinfinite liquid sheet across a groove.

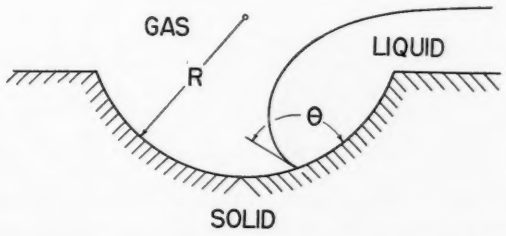

Fig. 3. Advance of a semiinfinite sheet of liquid across a rounded groove.

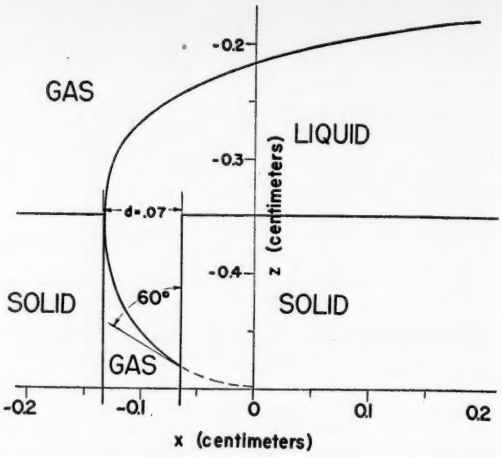

Fig. 4. Solution of problem of width of rectangular groove which will always entrap gas in the advance of a semiinfinite sheet of liquid (θ = 60 deg.).

CAVITIES

Conical cavities will obey approximately the same considerations as V-shaped grooves, and cylindrical or rectangular cavities approximately the same as rectangular grooves. In fact, it is more likely that the postulated mechanism will be the determining factor in gas entrapment and therefore that these considerations will be valid, for cavities rather than for long grooves, where advance of the liquid along the grooves is an important consideration.

DISCUSSION

It is of interest to compare this theory with the large quantity of experimental data available on superheating and tensile strength of liquids. From the preceding example, the critical width of the vertical groove for the entrapment of gas in a system with water boiling at 1 atm. is about 0.07 cm. Hence the radius of curvature of the entrapped gas bubble would be about half this figure, or 0.04 cm., if such grooves exist on the surface. This would represent an extremely rough surface. Most experimenters have dealt with much smoother surfaces and have obtained critical nuclei radii, calculated from the Gibbs equation, several orders of magnitude smaller. It should also be noted that the elements of surface roughness should be cavities, rather than grooves, for the mechanism of gas entrapment by the advance of a liquid front to be controlling. As pointed out previously, most polished or machined surfaces do not obey this condition.

Two rather diverse investigations involving the cavity type of surface have been found in the literature. Jakob and Fritz (*7*) compared ebullition of water from a horizontal heating plate fitted with smooth (chromium plated and polished) surfaces and also a "screen" surface, fitted with square cavities, with lengths, depths, and spacings of about 0.025 cm. On the basis of the change of slope of the curve of heat flux vs. temperature excess, it is estimated that bubbles began forming in sizable quantities on the screen surface at a temperature excess of about 1°C. This corresponds to a critical bubble radius of about 0.0035 cm., about one-fourth the maximum that could be expected from the cavity dimensions. From the previous discussion it is seen that the liquid would probably displace some of the gas from each cavity; moreover, the thermal resistance of the entrapped gas is relatively large, thereby tending to increase the necessary temperature excess. In view of these uncertainties, this is a reasonably good order-of-magnitude check with the theory. Bubble initiation superheats of about 4° and 9°C. were found respectively for freshly formed sand-blasted and smooth surfaces, corresponding to bubble radii of about 9×10^{-4} and 4×10^{-4} cm. On any of these surfaces being allowed to remain in contact with water for a number of hours, the temperature excess required to initiate ebullition appeared to be unchanged; however, the temperature excess for a given flux was increased, possibly because some of the larger cavities had stably switched from gas-fill to liquid-fill, as described above. On allowing the surfaces to lie in contact with air again, the previous temperature excesses were restored.

Kermeen, McGraw, and Parkin (*8*) studied the inception of cavitation on various surfaces of revolution in water-tunnel experiments. Using an anodized aluminum surface, which may be considered to be a cavity type of surface, they found incipient cavitation to occur at local pressures 80 to 90 mm. Hg below the vapor pressure of water. This corresponds to a critical bubble radius of about 0.014 cm., considerably larger than the radii of 10^{-5} cm. and smaller observed in various measurements of the tensile strength of pure liquids by static, dynamic, and acoustic methods (*3*).

CONCLUSIONS

1. A quantitative procedure is given for determining whether a surface cavity of known shape and size will entrap gas or vapor in contact with a given liquid with a specified contact angle.

2. Four classes of cavities are shown to exist: those which are always liquid or gas filled; those in which complete displacement of gas by liquid is possible, but not vice versa; and those in which complete displacement of liquid by gas or vapor is possible, but not vice versa. The existence of the last two classes may account for some hysteresis effects in ebullition.

3. The primary roughness elements of most surfaces are grooves, which are relatively poor vapor traps and hence are relatively ineffective in initiating ebullition or cavitation. Two examples of the cavity type of surface, resulting in fracture of the liquid under low stresses, are adduced.

ACKNOWLEDGMENT

This work was supported by a grant from the Research Corporation. A portion of it was performed during a period of summer employment at Argonne National Laboratory.

LITERATURE CITED

1. Bankoff, S. G., *J. Phys. Chem.*, **60**, 952 (1956).
2. Bartell, F. E., and J. W. Shepard, *op. cit.*, **57**, 211, 457 (1953).
3. Blake, F. G., Jr., NR-014-903 TM9 (June, 1949).
4. Corty, Clyde, Ph.D. thesis, Univ. Mich., Ann Arbor (1951).
5. Gibbs, J. W., "Scientific Papers," vol. 1, p. 282, Yale Univ. Press, New Haven (1948).
6. Hajjar, A. J., M.S. thesis, Rose Polytechnic Institute, Terre Haute, Ind. (1955).
7. Jakob, Max, and W. Fritz, *Forsch. Gebiete Ingenieurw.*, **2**, 435 (1931).
8. Kermeen, R. W., J. T. McGraw, and B. R. Parkin, *Trans. Am. Soc. Mech. Engrs.*, **77**, 533 (1955).
9. Van Camp, W. M., Ph.D. thesis, Purdue Univ., West Lafayette, Ind. (1952).
10. Young, T., *Phil. Trans.*, **96A**, 65 (1805).

Manuscript submitted April 25, 1956; paper accepted December 21, 1956, but author requested delay in publication. Paper released December, 1957.

Distribution of Eddy Viscosity and Mixing Length in Smooth Tubes

R. R. ROTHFUS, D. H. ARCHER, and K. G. SIKCHI

Carnegie Institute of Technology, Pittsburgh, Pennsylvania

Profiles of eddy viscosity and Prandtl mixing length in fluids flowing steadily and isothermally in smooth tubes have been calculated from the velocity data of several investigators for Reynolds numbers between 1.2×10^3 and 3.2×10^6. In the transition range unusually high values of eddy viscosity and mixing length are obtained in some portions of the stream. In the fully turbulent range the effect of Reynolds number is small and the mixing length tends toward zero at the center of the tube. The parameters for turbulent flow between parallel plates have been correlated through the concept of an equivalent tube. The results are of importance in designing equipment for heat and mass transfer and mixing.

When dealing with processing equipment, one often finds it necessary or highly desirable to be able to predict the rate of heat, mass, or momentum transfer at a particular point in a moving fluid. In general, this requires some knowledge of the relationship between the designated flux and the corresponding potential gradient at the spot in question. If the flow is truly viscous, a direct solution for the desired rate of transfer is sometimes possible. When the flow is turbulent to any extent, however, empirical information is ultimately necessary, even in ducts having simple cross-sectional shapes.

Progress in predicting mixing phenomena as well as local rates of heat and mass transfer has not been so rapid as might be expected. One of the principal reasons for this seems to be the lack of sufficient consistent information about eddy viscosities in elementary conduits such as smooth tubes of circular cross section. In spite of the relatively large number of velocity distributions available in the literature, there have been but few attempts to translate these into profiles of eddy viscosities or mixing lengths. In particular, the effect of Reynolds number on the radial distribution of these parameters has not been demonstrated adequately.

It is the purpose of this paper to present explicit correlations of eddy viscosities and Prandtl mixing lengths for the steady isothermal flow of constant-density fluids in smooth tubes. The effect of Reynolds number on the radial distribution of the two quantities has been calculated for both the transition and fully turbulent ranges of flow. The supporting data have been smoothed and made internally consistent in order to increase the ultimate utility of the calculated results.

BASIS OF CORRELATION

The steady, isothermal flow of a constant-density fluid through a long, straight tube of circular cross section will be considered, with u representing the mean temporal fluid velocity at the radial distance y from the tube wall and τg_0 the corresponding value of the mean local shearing stress. Following the procedure used by Murphree (*5*), the shearing stress for such a case of flow may be written in terms of the eddy viscosity ϵ as

$$\tau g_0 = (\mu + \epsilon) \frac{du}{dy} \qquad (1)$$

The shearing stress might also be expressed in terms of the Prandtl mixing length (*9*). As shown by Schlichting (*12*), the relationship between the eddy viscosity and the mixing length l is

$$\epsilon = \rho l^2 \left(\frac{du}{dy}\right) \qquad (2)$$

If the fluid motion at the point under consideration is entirely viscous, the eddy viscosity and mixing length are zero.

Regardless of the prevailing type of flow, the local shearing stress varies linearly with the distance from the wall of the tube (*13*). Thus, if $\tau_0 g_0$ represents

Kamal G. Sikchi is at Amraoti (M.P.), Bombay State, India.

the shearing stress at the wall and r_0 the tube radius,

$$\tau g_0 = \tau_0 g_0 \left(1 - \frac{y}{r_0}\right) \qquad (3)$$

Since the skin friction $\tau_0 g_0$ can be obtained readily from pressure-drop correlations, the cited equations permit calculation of the eddy viscosity and mixing length from experimental velocity distributions.

In the present work it has been found convenient to correlate the results in terms of two dimensionless groups, E and L, defined as follows:

$$E = \frac{\epsilon}{r_0 u_* \rho} \left(\frac{u_m}{V}\right)_p \qquad (4)$$

and

$$L = \frac{l}{r_0} \left(\frac{u_m}{V}\right)_p \qquad (5)$$

The symbol u_* denotes the friction velocity $\sqrt{\tau_0 g_0/\rho}$ The groups E and L have the same form as those used by Nikuradse (*6*) and others, except for the introduction of the velocity ratio $(u_m/V)_p$. The latter ratio was used by Rothfus and Monrad (*11*) in modifying the usual u^+, y^+ correlation of velocity distribution in order to remove the effect of Reynolds number in the fully turbulent range. They found that the relationship between the new parameters

$$U^+ = \frac{u}{u_*} \left(\frac{V}{u_m}\right)_p \qquad (6)$$

and

$$Y^+ = \frac{y u_* \rho}{\mu} \left(\frac{u_m}{V}\right)_p \qquad (7)$$

could be adequately represented by a single curve at Reynolds numbers greater than 3,000 in smooth tubes. It was also shown that the same correlation could be used for flow between parallel plates if $(V/u_m)_p$ were taken to be that in a tube having the same radius as the half clearance between the plates and operating at the same friction velocity u_*, with a fluid of the same kinematic viscosity μ/ρ as that between the plates.

In terms of the U^+ and Y^+ parameters, Equations (1) and (2) take the forms

$$E = \frac{(Y_m^+ - Y^+)}{(Y_m^+)^2 (dU^+/dY^+)} - \frac{1}{Y_m^+} \left(\frac{u_m}{V}\right)_p^2 \qquad (8)$$

and

$$L = \left[\frac{E}{Y_m^+ (dU^+/dY^+)}\right]^{1/2} \qquad (9)$$

The symbol Y_m^+ denotes the maximum (i.e., center-line) value of the modified friction distance parameter Y^+.

At very high Reynolds numbers the velocity distribution in the main stream can be represented approximately by an equation of the form

$$U^+ = A + B \ln Y^+ \qquad (10)$$

where A and B are constants. Under such conditions the effect of the viscous term in Equation (8) is negligible and Equations (8) and (9) reduce to the simple relationships

$$E = \frac{1}{B} \left(\frac{y}{r_0}\right)\left(1 - \frac{y}{r_0}\right) \qquad (11)$$

and

$$L = \frac{1}{B} \left(\frac{y}{r_0}\right) \sqrt{1 - \frac{y}{r_0}} \qquad (12)$$

To the extent that Equation (10) is correct, therefore, E and L should prove to be independent of Reynolds number; the maximum value of E should be obtained at $y/r_0 = 0.50$ and that of L at $y/r_0 = 0.67$. Since the logarithmic velocity distribution cannot be valid at the center of the stream or close to the wall of the tube, even at high Reynolds numbers, these conclusions can be taken only as rough approximations. They do, however, afford a starting point for any attempt to describe the behavior of the dimensionless groups E and L in the lower ranges of Reynolds number.

At high Reynolds numbers the thickness of the buffer layer and laminar film (if any such film exists) is a very small part of the distance from the center of the stream to the wall. For practical purposes the main-stream behavior can be taken to apply over the entire cross section of the fluid. At lower Reynolds numbers the buffer layer and laminar film are thicker. Therefore, the eddy viscosity and mixing length can be expected to be zero or very small for a measurable distance from the wall. In view of this, it is probable that the maximum point in the profile of E or L shifts toward the center of the stream as the Reynolds number is decreased through the lower turbulent and transition ranges of flow.

SOURCES OF VELOCITY DATA

It is apparent that accurate values of the velocity gradient must be available before the eddy viscosity and Prandtl mixing length can be computed satisfactorily from experimental velocity data. Suitable gradients can be obtained only when the velocity profile is established by numerous points of sufficiently high precision. This requirement makes it necessary to reject the results of several investigations which could profitably be included if velocity distribution alone were the subject of primary concern.

The velocity data of Nikuradse (*6*) and of Senecal and Rothfus (*14*) can be used for smooth tubes and those of Sage and coworkers (*1, 7, 8*) for flow between parallel plates. The Reynolds-number range included is 600 to 3,240,000 for tubes and 6,960 to 53,400 for parallel plates. The notable smooth-tube data of Deissler (*2*) can be used to establish velocity profiles but have not been presented in a form adaptable to the calculation of velocity gradients.

Nikuradse has presented profiles of the total effective viscosity as well as of a Prandtl type of mixing length calculated by means of the equation

$$l = u_* \sqrt{1 - y/r_0}/(du/dy) \qquad (13)$$

His tables contain several numerical errors, however, and his velocity gradients near the center of the tube appear to lack satisfactory precision. The graphs of mixing length against position in the stream indicate a consistent increase of l/r_0 with increasing y/r_0 at constant Reynolds number in the turbulent range.

Sage and coworkers (*8*) have calculated eddy-viscosity profiles from their excellent velocity data for flow between broad, parallel plates. The velocity distributions for tubes and parallel plates have been found to coincide under the conditions imposed by Rothfus and Monrad as noted in a previous paragraph. By virtue of Equations (8) and (9), therefore, the corresponding profiles of E and L must also be coincident on this basis. The data for parallel plates can thus be used in establishing the eddy-viscosity and mixing-length profiles for tubes as well.

The literature contains no explicit information about the characteristics of the eddy viscosity and mixing length in the range of laminar-turbulent transition. The velocity data of Senecal and Rothfus, however, provide the raw material necessary for the calculation of these profiles at tube Reynolds numbers up to 4,000.

COMPUTATIONS AND RESULTS

In both the transition and turbulent ranges of flow, the eddy viscosity and mixing length parameters were calculated by means of Equations (8) and (9) respectively. The technique used in establishing the proper value of the gradient dU^+/dY^+ was dependent on the precision of the experimental information available in the Reynolds number range under consideration.

The Transition Range

In the transition range, at Reynolds numbers from 1,200 to 4,000, the velocity data of Senecal and Rothfus were first plotted as curves of U^+ against Reynolds number at constant values of y/r_0 ($= Y^+/Y_m^+$). Cross plots of U^+ against y/r_0 at constant values of the Reynolds number were then constructed and the curves on both diagrams were adjusted to achieve smoothness, consistency, and the best agreement with the data. Figure 1 shows the final form of the velocity correlation.

The gradient (dU^+/dY^+) was obtained

from the derivative $dU^+/d(y/r_0)$, since by definition

$$\frac{dU^+}{dY^+} = \frac{1}{Y_m{}^+} \frac{dU^+}{d(y/r_0)} \qquad (14)$$

Values of U^+ were read from Figure 1 at even increments of 0.1 y/r_0 and difference tables were constructed from which values of $dU^+/d(y/r_0)$ were calculated numerically. Any one of three interpolation formulas, two by Newton and one by Stirling, was used in these calculations. The choice of a formula depended on its applicability in the particular range of y/r_0 being investigated. In regions of the stream where more than one formula could be used equally well, the average value of the gradient obtained by the various means was computed. The quantity E was then calculated by the use of Equations (8) and (14) for each point in the cross section at which the gradient had been determined. These values were smoothed with respect to both radial position and Reynolds number in a manner similar to that described for the velocity distribution data. The consistent, smoothed results for Reynolds numbers between 1,600 and 4,000 are shown in Figure 2. Corresponding values of L, calculated by means of Equation (9), are shown in Figure 4.

The Turbulent Range

In the fully turbulent range, at Reynolds numbers between 4,000 and 3,240,000, values of the eddy viscosity parameter E were calculated largely from the velocity data of Nikuradse. The parallel-plate velocity data of Sage and his coworkers were taken to be equivalent to smooth-tube data on the basis proposed by Rothfus and Monrad. Upon appropriate transformation, values of E obtained from Sage's data were used to supplement those calculated from Nikuradse's results.

Nikuradse presented values of the velocity gradient du/dy but did not clearly indicate his method of obtaining the derivative. His tabulated results scattered sufficiently, however, to suggest that his method was not precise or that the velocity data were not smoothed before the derivatives were calculated. For more reliable values of the velocity gradient from Nikuradse's data, the following graphs were drawn at each Reynolds number investigated by him:

in the range

$$0.3 < y/r_0 < 1.0, \ln u \text{ against } (y/r_0)$$

in the range

$$0.02 < y/r_0 < 0.3, \quad u \text{ against } (y/r_0)$$

Straight lines representing the data as closely as possible were drawn on both diagrams. Curves of residual velocity showing the deviation of the data from the two straight lines as a function of radial position were than drawn and smoothed. The slopes of these curves were measured by means of a prismatic tangent meter. The value of the derivative $du/d(y/r_0)$ at a particular y/r_0 was then obtained by adding the slope of the residual curve to the slope of the appropriate straight line. The gradient du/dy followed directly. The values of du/dy thus obtained were checked by means of difference tables as previously described

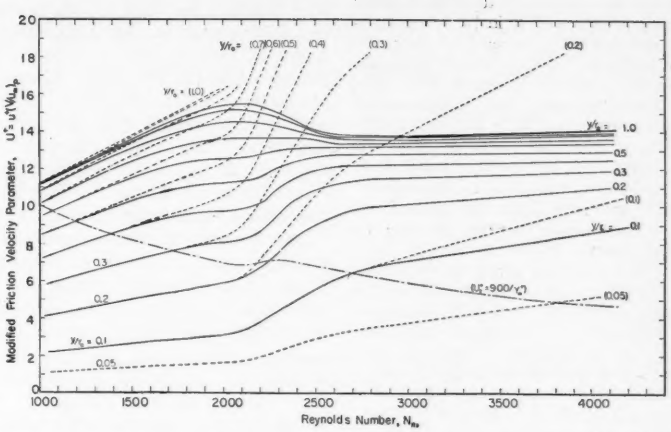

Fig. 1. Correlation of local velocities for transition flow in smooth tubes; dotted lines are calculated from viscous-flow equation (15).

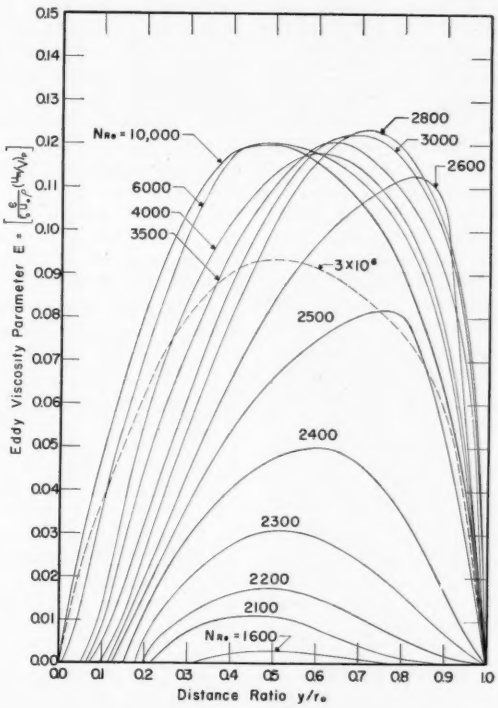

Fig. 2. Effect of Reynolds number on the radial distribution of the eddy-viscosity parameter E in the transition flow range.

for the transition region, and excellent agreement was noted.

In order to show the precision of the results and the nature of Reynolds-number dependence, values of E in both the transition and turbulent ranges of flow are plotted in Figure 3 as functions of Reynolds number at constant values of y/r_0. The solid lines represent the recommended correlation, smoothed with respect to both Reynolds number and radial position. In the placement of the recommended lines due consideration was given to the value of dU^+/dY^+ derivable from the generalized U^+, Y^+ correlation through the use of difference tables. Figure 3 can be used directly as a working graph at Reynolds numbers above 4,000. The nature of the correlation, however, makes it advisable to use Figure 2 in the transition range. For purposes of comparison, Figure 2 also contains curves showing the radial distribution of the eddy viscosity group at Reynolds numbers of 6×10^3, 1×10^4 and 3×10^6.

Figure 4 shows values of the mixing-length group L, calculated by means of Equation (9), for several Reynolds numbers in the transition range. The radial distribution at a Reynolds number of 3×10^6 is also included. In every case the lines correspond to the recommended values of E shown in Figures 2 and 3. To show a comparison with Nikuradse's data, points representing the average of his results for Reynolds numbers above 100,000 are included in Figure 4.

The values of the velocity ratio $(V/u_m)_p$ which were used in computing E and L are shown in Table 1. Obtained directly from experimental data, these represent the results of several reliable investigations (*3, 4, 6, 14, 15*).

DISCUSSION OF RESULTS

Figure 3 shows that the radial distribution of the eddy viscosity group E is not entirely independent of Reynolds number in the higher turbulent range. At Reynolds numbers greater than 100,000, however, the variation is small for y/r_0 values from 0.3 to 0.7. It is apparent that the effect of the $(V/u_m)_p$ ratio in the eddy viscosity group is to minimize the effect of Reynolds number in the central portion of the stream, where y/r_0 is greater than 0.7. At the same time values of E close to the wall are maintained reasonably independent of Reynolds number, the variation at $y/r_0 = 0.1$ being in the neighborhood of 10% over the range $10^5 < N_{Re} < 3 \times 10^6$.

Since viscous effects are negligible at high Reynolds numbers, the small variation of E with Reynolds number must be the result of a Reynolds-number effect on the U^+, Y^+ velocity correlation. This effect is imperceptible in the velocity distribution itself but is magnified when local gradients are taken. Even though the U^+, Y^+ correlation is not unique, no part of the main stream shows much effect of Reynolds number on E and L in the upper turbulent range of flow.

Nikuradse correlated eddy viscosities and mixing lengths in terms of the dimensionless groups $(\mu + \epsilon)/r_0 u_* \rho$ and l/r_0 respectively. The latter group was obtained from Equation (13) and therefore involves the mixing length defined by that equation. At high Reynolds numbers, where the contribution of viscous shear is negligible, Nikuradse's groups are almost independent of Reynolds number except near the center of the tube, where they increase with increased Reynolds number to a greater extent than do E and L. This simply reflects the small rotation of the lines in Figure 3 resulting from inclusion of the velocity ratio $(V/u_m)_p$ in the ordinate E.

The most striking departure from Nikuradse's conclusions is evident in the radial distribution of the mixing-length parameter near the center of the stream. His published results indicate that values of l/r_0 calculated from Equation (13) increase with distance from the wall all the way to the center of the tube. Careful reevaluation of his data, however, has led to the conclusion that the mixing-length parameter goes through a maximum point and tends strongly toward zero where the center of the stream is approached, as shown in Figure 4. The fact that the velocity gradients calculated in the present work are more consistent than Nikuradse's lends support to this conclusion. In the last analysis, however, it remains for more precise measurements of local velocities to furnish the basis for a firm judgement. It should be noted that the Prandtl and von Karman logarithmic velocity distributions predict zero mixing length at the center of the tube. Since both theories also indicate a finite velocity gradient at the center, they cannot be considered valid in the latter vicinity; however, they do predict qualitatively the relation between l/r_0 and y/r_0 which has been calculated from experimental data obtained in the central portions of smooth tubes.

At Reynolds numbers less than 10,000, there is a decided effect of Reynolds number on the magnitude and radial distribution of the parameters E and L. The nature of the variation is illustrated in Figures 2, 3, and 4. The values of E over the cross section of the tube increase rapidly as Reynolds number is increased above 1,600. At a Reynolds number of between 3,000 and 10,000, depending on the value of y/r_0, E reaches a maximum and then decreases with a further increase of N_{Re}. This behavior of E in the transition and lower turbulent-flow regions cannot with certainty be interpreted in terms of existing theories of turbulence.

The effect of laminar-film thickness in the transition zone is clearly indicated in Figures 2 and 4. The radial distributions of the eddy viscosity and mixing-length parameters are set out a greater and greater distance from the wall as the film thickens with decreased Reynolds number.

It is notable also that the points of maximum eddy viscosity and mixing length shift toward the center of the stream in the transition range. Particularly in the case of the mixing length, this is accompanied by an increase in the magnitude of the parameter L. Thus the central region of the tube in transition flow becomes a zone of large-scale mixing. Dye studies (*10*) indicate that the flow in this region may be sinuous at one instant and part of a large disturbance eddy at another. In either case, however, relatively long segments of the dye filament move as units without appreciable rapid small-scale diffusion; but it should be recognized that these low-frequency transient effects influence the film thickness, eddy viscosity, and mixing length in the transition range. The values indicated in the cited graphs are time averages and are therefore dependent on the frequency with which strong disturbance eddies are cast off and move downstream.

Figure 1 can be used as a working correlation of local velocities in the transition range of flow. This type of correlation aids interpolation, as it eliminates the crossing over of neighboring lines. The graph illustrates the complexity of correlation in the transition region and emphasizes the fact that in transition flow the functional relation between U^+ and Y^+ depends on the value of Reynolds number—unlike the relation in turbulent flow, where the relation between U^+ and Y^+ is virtually independent of Reynolds number.

The dashed lines in Figure 1 indicate the velocity distribution calculated by the equation

$$U^+ = \frac{Y_m^+}{2}\left(\frac{V}{u_m}\right)_p^2\left[\frac{Y^+}{Y_m^+}\left(1 - \frac{Y^+}{2Y_m^+}\right)\right]$$

$$= \frac{1}{2} N_{Re}\sqrt{\frac{f}{2}}\left(\frac{V}{u_m}\right)_p\left[\frac{y}{r_0}\left(1 - \frac{y}{2r_0}\right)\right] \quad (15)$$

This expression can be obtained from Equation (8) by assuming that $E = 0$ and integrating at a given Reynolds number from the tube wall, where U^+ and Y^+ are zero, to any arbitrary point in the fluid stream where $Y^+ = (y/r_0)(Y_m^+)$ and $U^+ = U^+$. In the calculations the actual values of f and $(V/u_m)_p$ for smooth tubes at the given Reynolds number were used. A U^+ calculated from Equation (15) should be the correct one in the regions adjacent to the wall, where the assumption that $E = 0$ is reasonably accurate. The profiles calculated by Equation (15) aid in interpreting the experimentally determined velocity distribution in the transition range. Since the actual profiles depart so gradually from the viscous distributions in the lower transition zone, it is difficult to establish the laminar-film thickness very precisely. But it does appear, however, that the modified friction velocity parameter U_f^+ taken at the edge of the laminar film is

related to the center-line value Y_m^+ of the modified friction distance parameter through the expression

$$U_f^+ Y_m^+ = 900 \qquad (16)$$

within the limits of observation. Dye studies by Prengle and Rothfus (*10*) and pressure-drop data by Senecal and Rothfus (*14*) have yielded a value of about 1,200 for the constant in the last equation. In both cases the experimental technique might be expected to produce somewhat higher values than those obtained from velocity measurements. The agreement can therefore be considered satisfactory in view of the various uncertainties involved. Since the flow within the laminar layer is parabolic, the radial distance from the center of the stream to the edge of the laminar film r_f can be obtained from Equation (16) and is given by the relationship

$$1 - \left(\frac{r_f}{r_0}\right)^2 = \frac{14{,}400}{(N_{Re}\sqrt{f})^2} \qquad (17)$$

Prengle and Rothfus report a value of 19,600 for the constant on the right-hand side of the equation.

It is apparent from Figure 1 that the divergence of the actual velocity profiles from the viscous-flow extrapolations become less pronounced at very small values of y/r_0. This suggests that a higher Reynolds numbers where the laminar film, if any, is extremely thin, velocity measurements become poor indicators of the film thickness. Instead, it can be predicted that such measurements should lead to the notion that a much thicker film exists than is actually the case, since the effects of weak eddies in the buffer layer next to the film will not be picked up by ordinary means. Consequently, it is not surprising that velocity data seem to indicate that the modified friction distance parameter Y_f^+ at the edge of the apparent film is approximately constant

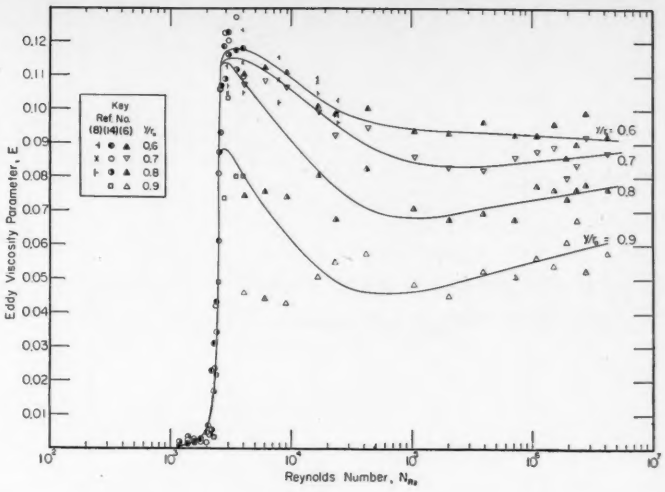

Fig. 3*a*.

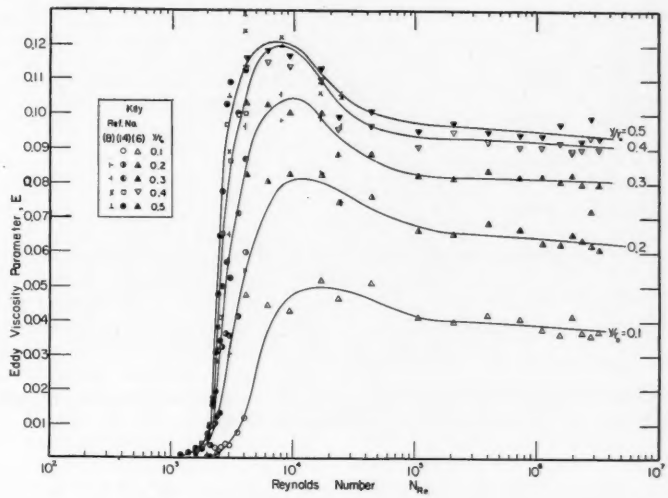

Fig. 3*b*.

Fig. 3. Effect of Reynolds number on the eddy-viscosity parameter *E* at fixed position in the stream.

TABLE 1

THE RATIO OF BULK AVERAGE TO MAXIMUM VELOCITIES IN SMOOTH TUBES

N_{Re}	$(V/u_m)_p$	N_{Re}	$(V/u_m)_p$
2,000	0.500	8,000	0.774
2,100	0.502	9,000	0.778
2,200	0.567	10,000	0.780
2,300	0.604	15,000	0.792
2,400	0.636	20,000	0.798
2,500	0.667	25,000	0.803
2,600	0.685	30,000	0.808
2,700	0.697	40,000	0.812
2,800	0.705	50,000	0.818
2,900	0.710	60,000	0.822
3,000	0.717	80,000	0.826
3,250	0.724	1×10^5	0.830
3,500	0.731	2×10^5	0.841
3,750	0.738	4×10^5	0.852
4,000	0.744	6×10^5	0.857
4,500	0.752	1×10^6	0.864
5,000	0.758	2×10^6	0.872
6,000	0.765	3×10^6	0.877
7,000	0.770		

and independent of Reynolds number at Reynolds numbers above, say, 10,000.

The eddy viscosity and mixing-length parameters used in Figures 2, 3, and 4 were chosen because they yield relationships which are essentially independent of Reynolds number in the higher turbulent range and are relatively easy to interpolate. To aid in the placing of the recommended lines on these graphs, the generalized diagram of U^+ against Y^+ was used as a guide in the middle range of y/r_0 values. Since the assumption of a unique U^+, Y^+ relationship is only a rough approximation near the wall and at the center of the stream, the slope of the generalized U^+, Y^+ curve is not sufficiently accurate to be of much help in these zones.

In the lower turbulent range it is apparent that the recommended curves in Figure 3 do not coincide with Nikuradse's data near the center of the tube. It is believed that the data of Senecal and Rothfus are more reliable than Nikuradse's in this region. The recommended lines have, therefore, been drawn to progress smoothly to Senecal's values at the upper limit of the transition region.

The parallel-plate data of Sage and his coworkers were found to be in excellent agreement with tube data on the equivalent basis suggested by Rothfus and Monrad. This result was to be expected in view of the excellent agreement in velocity data obtained on U^+, Y^+ coordinates. The correspondence of eddy viscosities, however, constitutes a more stringent check on the postulated equivalence of tubes and parallel plates.

Isakoff and Drew (*3*) have measured velocity profiles for mercury flowing

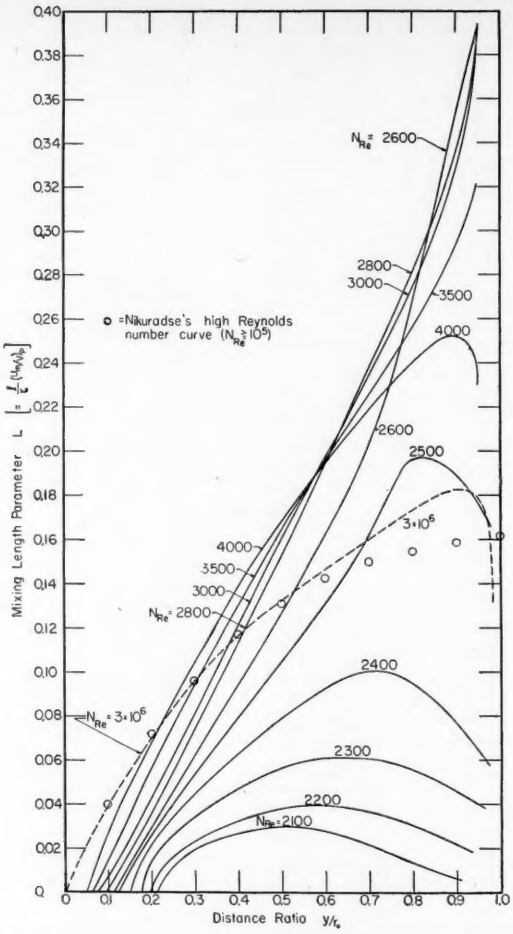

Fig. 4. Effect of Reynolds number on the radial distribution of the mixing-length parameter L in the transition flow range.

through smooth tubes at ten different Reynolds numbers in the range of 125,000 to 500,000. They present a graph which shows a calculated eddy momentum diffusivity ratio $(\epsilon/\rho)/(\epsilon/\rho)_{max} = E/E_{max}$ as a function of y/r_0. They were unable to detect a variation of this ratio with Reynolds number in the range of their investigation. Their calculated values of E/E_{max} agree with those presented in Figure 3 with an accuracy of $\pm 7\%$ except in the center of the tube, where the Isakoff and Drew calculations are about 15% greater than the results presented here. Since Isakoff and Drew state that their diffusivity data scatter by as much as $\pm 10\%$, it can be concluded that there is substantial agreement between their work and the results presented here. Furthermore they conclude that $(\epsilon/\rho)_{max}$ varies as the 0.83 power of the Reynolds number. Figure 3 predicts that for a given fluid $(\epsilon/\rho)_{max}$ will vary with about the 0.9 power of the Reynolds number over the range of Reynolds numbers investigated by Isakoff and Drew.

NOTATION

A, B = constants

E = eddy viscosity parameter $\epsilon/r_0 u_* \rho \ (u_m/V)_p$, dimensionless

f = fanning friction factor, dimensionless

g_0 = conversion factor, 32.2 $\frac{\text{(lb. mass)(ft.)}}{\text{(lb. force)(sec.}^2\text{)}}$

l = Prandtl mixing length, ft.

L = Prandtl mixing-length parameter $(l/r_0)(u_m/V)_p$, dimensionless

N_{Re} = Reynolds number for flow in a tube $2r_0V\rho/\mu$, dimensionless

r = distance to a point measured from the tube axis, ft.

r_f = distance from the tube axis to the edge of the laminar film, ft.

r_0 = tube radius, ft.

u_m = maximum flow velocity within the tube, ft./sec.

$(u_m/V)_p$ = ratio of the maximum to the average flow velocity in a smooth tube, dimensionless

u_* = friction velocity parameter $\sqrt{\tau_0 g_0/\rho}$, ft./sec.

u^+ = velocity parameter u/u_*, dimensionless

U^+ = modified velocity parameter $u^+ (V/u_m)_p$, dimensionless

V = average flow velocity within a tube, ft./sec.

x = distance measured along the tube axis, ft.

y = distance measured in a radial direction from the tube wall $(r_0 - r)$, ft.

y^+ = distance parameter $yu_*\rho/\mu$, dimensionless

Y^+ = modified dimensionless distance parameter $(u_m/V)_p \ y^+$, dimensionless

Y_m^+ = maximum value of Y^+ in a tube $(r_0 u_* \rho/\mu) \ (u_m/V)_p$, dimensionless

Greek Letters

ϵ = eddy viscosity, lb. mass/(ft.)(sec.)

μ = coefficient of viscosity, lb. mass/(ft.)(sec.)

ρ = fluid density, lb. mass/cu. ft.

τ = shear stress at any point in the tube, lb. force/sq. ft.

τ_0 = shear stress at the tube wall, lb. force/sq. ft.

LITERATURE CITED

1. Corcoran, W. H., F. Page, Jr., W. G. Schlinger, and B. H. Sage, *Ind. Eng. Chem.*, **44**, 410 (1952).
2. Diessler, R. G., *Trans. Am. Soc. Mech. Engrs.*, **73**, 101 (1951).
3. Isakoff, S. E., and T. B. Drew, "Proc. General Discussion on Heat Transfer," Institution of Mechanical Engineers, London (1951).
4. Klimaszewski, I. C., M.S. thesis, Carnegie Inst. Technol., Pittsburgh (1950).
5. Murphree, E. V., *Ind. Eng. Chem.*, **24**, 726 (1932).
6. Nikuradse, J., *V.D.I. Forschungsheft*, **356**, 1 (1932).
7. Page, F., Jr., W. H. Corcoran, W. G. Schlinger, and B. H. Sage, *Ind. Eng. Chem.*, **44**, 419 (1952).
8. Page, F., Jr., W. G. Schlinger, D. K. Breaux, and B. H. Sage, *Ind. Eng. Chem.*, **44**, 424 (1952).
9. Prandtl, L., *Z. angew. Math. u. Mech.*, **5**, 137 (1925).
10. Prengle, R. S., and R. R. Rothfus, *Ind. Eng. Chem.*, **47**, 379 (1955).
11. Rothfus, R. R., and C. C. Monrad, *ibid.*, 1144.
12. Schlichting, Hermann, "Boundary Layer Theory," p. 387, McGraw-Hill Book Company, Inc., New York (1955).
13. *Ibid.*, p. 400.
14. Senecal, V. E., and R. R. Rothfus, *Chem. Eng. Progr.*, **49**, 533 (1953).
15. Stanton, T. E., and J. R. Pannell, *Trans. Roy. Soc. (London)*, **A214**, 199 (1916).

Manuscript submitted February, 1957; revision received August 26, 1957; paper accepted September 20, 1957.

Control of Flow Distribution by Mixing Headers

SEYMOUR C. HYMAN, ALAN R. GRUBER, and LEON JOSEPH

Nuclear Development Corporation of America, White Plains, New York

The coolant flow distribution among parallel passages in a nuclear reactor (or boiler or heat exchanger) can be very sensitive to variations in heat input, channel dimensions, etc. In a previous paper this flow sensitivity was defined in terms of certain partial derivatives, which were related by analytical expressions to fluid properties and operating characteristics. Flow sensitivity contributes largely to potential malfunction, reduced efficiency, or failures. The use of valves and orifices was quantitatively evaluated for supercritical water in the earlier paper. The scope of this paper is to consider the utility of mixing headers. These mixing chambers are located along the flow passage as a common receiver for parallel flow from many channels. The headers, in turn, supply subsequent lengths of heated passages in parallel. Analytical expressions are derived for the effect of headers on flow, outlet-fluid enthalpy, and channel-wall temperatures. The limiting cases of minimum and complete mixing in the headers are considered and numerical results for water at supercritical pressures are given to show the marked increase in stability obtained by use of intermediate mixing headers.

Severe flow maldistributions can occur in nuclear reactors in which the coolant decreases appreciably in density or where the physical properties of the coolant are sharply temperature dependent. In such cases small variations in heat flux—either from tube to tube or with time—can cause significant fluctuations in flow, which, in turn, can materially reduce heat transfer efficiency or, in extreme cases, even result in tube burnout. In any case, strong flow variations are unfavorable since they make the heat exchange process difficult to control.

The flow distribution of expansible fluids among parallel heated channels was treated in a previous paper (*1*) in which the variation of flow with heat flux was evaluated in terms of *flow sensitivities*, which are functions of the physical properties of the coolant and such parameters as inlet and outlet temperature, heat flux, hydraulic diameter, and tube length. The paper also discussed the reduction of flow sensitivity through the use of valves and orifices.

The current paper deals with the control of flow sensitivity (and the resultant flow maldistributions) through the use of subdivided tubes jointed to intermediate flow-mixing headers which permit the equalization of temperatures and pressures across the tube bank. Blending the flows from all tubes in the intermediate headers reduces flow sensitivity by preventing the accumulation of adverse effects along the entire length of an abnormally powered tube.

Ideally, equalization of both temperature and pressure should be accomplished in the mixing headers to obtain the maximum reduction in flow sensitivity. In practice, however, the necessity for compactness limits the size of the headers, thereby making thorough lateral temperature equalization difficult. In recognition of this practical difficulty, flow-sensitivity relationships have been derived below for the case in which there is no thermal equalization in the intermediate header, as well as for the case in which perfect thermal equalization is obtained. All derivations pertain to a tube bundle with a single mixing chamber located midway along the flow path. For both cases considered, expressions are also obtained for the variation of outlet temperature and tube-wall temperature with variations in heat flux.

As an illustration of the reduction in sensitivity that can be effected, the flow, outlet-temperature, and wall-temperature sensitivities have been computed for a divided and undivided tube for a typical case in which water at supercritical pressure undergoes an eightfold expansion from inlet to outlet. A comparison of these results shows that even under the overly pessimistic assumption of complete absence of thermal mixing in the header, the flow in a divided tube is still substantially less sensitive to heat flux than the flow in the comparable undivided tube. However, the large reduction in sensitivity that can be obtained in a divided tube by perfect mixing in the intermediate header furnishes incentive for a careful study of the design of efficient mixing headers of compact size.

THEORETICAL DEVELOPMENT

Flow Sensitivity of a Divided Tube

No Temperature Mixing in Intermediate Header. In this case, the intermediate header is assumed to produce pressure equilization only.

The flow through a tube between constant pressure headers will vary with the average heat flux and the fluid inlet temperature.

$$dG = \left(\frac{\partial G}{\partial Q}\right)_{T_{in},\Delta p} dQ + \left(\frac{\partial G}{\partial T_{in}}\right)_{Q,\Delta p} dT_{in} \qquad (1)$$

$$\left(\frac{dG/G}{dQ/Q}\right)_{\Delta p} = \left(\frac{\partial G/G}{\partial Q/Q}\right)_{T_{in},\Delta p} + \left(\frac{\partial G/G}{\partial T_{in}}\right)_{Q,\Delta p}\left(\frac{dT_{in}}{dQ/Q}\right)_{\Delta p} \qquad (2)$$

A tube heat balance yields

$$\Delta h = h_0 - h_{in} = \frac{4LQ}{GD} \qquad (3)$$

Differentiation at constant inlet enthalpy gives

$$\left(\frac{dh_0}{dQ}\right)_{\Delta p, T_{in}} = \frac{4L}{GD} + \frac{4LQ}{G^2D}\left(\frac{dG}{dQ}\right)_{\Delta p, T_{in}} \qquad (4)$$

Substituting (3) into (4) and multiplying by Q gives

$$\left(\frac{dh_0}{dQ/Q}\right)_{\Delta p, T_{in}} = \Delta h\left[1 - \left(\frac{dG/G}{dQ/Q}\right)_{\Delta p, T_{in}}\right] \quad (5)$$

Under the assumption of no temperature equalization in the header, the inlet temperature of the second half will change with the heat-flux variation of the first half of the tube. If the two halves of the tube have the same fractional change in average heat flux, then no distinguishing notation is needed on this change.

$$\left(\frac{dT_{in}}{dQ/Q}\right)_{2/2, \Delta p} = \left(\frac{dT_0}{dQ/Q}\right)_{1/2, \Delta p, T_{in}} \quad (6)$$

Rearranging and substituting (5) gives

$$\left(\frac{dT_0}{dQ/Q}\right)_{1/2, \Delta p, T_{in}} = \left(\frac{dh_0}{dQ/Q}\right)_{1/2, \Delta p, T_{in}} \left(\frac{dT}{dh}\right)_{1/2,0}$$

$$= \frac{\Delta h_{1/2}}{(C_p)_{1/2,0}}\left[1 - \left(\frac{dG/G}{dQ/Q}\right)_{1/2, \Delta p, T_{in}}\right] \quad (7)$$

where

$$(C_p)_{1/2,0} = \left(\frac{dh}{dT}\right)_{1/2,0}$$

Substituting (6) and (7) into (2), written for the second half, gives

$$\left(\frac{dG/G}{dQ/Q}\right)_{2/2, \Delta p} = \left(\frac{\partial G/G}{\partial Q/Q}\right)_{2/2, \Delta p, T_{in}} + \left(\frac{\partial G/G}{\partial T_{in}}\right)_{2/2, \Delta p, Q} \frac{\Delta h_{1/2}}{(C_p)_{1/2,0}} \cdot \left[1 - \left(\frac{dG/G}{dQ/Q}\right)_{1/2, \Delta p, T_{in}}\right] \quad (8)$$

The cyclic properties of partial derivatives are such that

$$\left(\frac{\partial G/G}{\partial T_{in}}\right)_{\Delta p, Q} = -\left(\frac{\partial G/G}{\partial Q/Q}\right)_{\Delta p, T_{in}} \left(\frac{\partial Q/Q}{\partial T_{in}}\right)_{\Delta p, G} \quad (9)$$

One can write

$$\left(\frac{\partial Q/Q}{\partial T_{in}}\right)_{\Delta p, G} = \left(\frac{\partial Q/Q}{\partial \Delta h}\right)_{\Delta p, G} \left(\frac{\partial \Delta h}{\partial T_{in}}\right)_{\Delta p, G} \quad (10)$$

Differentiating (3) at constant G gives

$$\left(\frac{\partial \Delta h}{\partial Q/Q}\right)_{\Delta p, G} = \frac{4LQ}{GD} = \Delta h \quad (11)$$

Substituting (9), (10), and (11) into (8) and recalling that the divided tube is assumed to undergo the same heat-flux variation in both halves, so that $\Delta h_{1/2} = \Delta h_{2/2}$, one gets

$$\left(\frac{dG/G}{dQ/Q}\right)_{2/2, \Delta p} = \left(\frac{\partial G/G}{\partial Q/Q}\right)_{2/2, \Delta p, T_{in}} \cdot \left\{1 - \frac{1}{(C_p)_{1/2,0}}\left(\frac{\partial \Delta h}{\partial T_{in}}\right)_{2/2, \Delta p, G} \cdot \left[1 - \left(\frac{\partial G/G}{\partial Q/Q}\right)_{1/2, p, T_{in}}\right]\right\} \quad (12)$$

Equation (12) gives the means of calculating the fractional change in flow per fractional change in heat flux (flow sensitivity). For the case of pressure equalization, but no temperature equalization, the flow sensitivity of the second half is influenced by that of the first half.

Complete Temperature Mixing in Intermediate Header. If the stream entering the header from the first half of the perverse tube can be completely mixed with a relatively large flow from other tubes, the unstabilizing effect is dissipated before the stream passes on to the second half. In this case both halves operate at fixed inlet temperatures. Equation (1) reduces to

$$\left(\frac{dG/G}{dQ/Q}\right)_{\Delta p, T_{in}} = \left(\frac{\partial G/G}{\partial Q/Q}\right)_{\Delta p, T_{in}} \quad (13)$$

The flow sensitivities for each half of the tube can be evaluated from the following expressions:

$$\left(\frac{dG/G}{dQ/Q}\right)_{1/2, \Delta p, T_{in}} = -\frac{\left(\frac{\partial \Delta p/\Delta p}{\partial Q/Q}\right)_{1/2, G, T_{in}}}{\left(\frac{\partial \Delta p/\Delta p}{\partial G/G}\right)_{1/2, Q, T_{in}}} \quad (14)$$

$$\left(\frac{dG/G}{dQ/Q}\right)_{2/2, \Delta p, T_{in}} = -\frac{\left(\frac{\partial \Delta p/\Delta p}{\partial Q/Q}\right)_{2/2, G, T_{in}}}{\left(\frac{\partial \Delta p/\Delta p}{\partial G/G}\right)_{2/2, Q, T_{in}}} \quad (15)$$

A comparison of (12) and (13) shows that for the second half of the tube the flow sensitivity with incomplete mixing is a multiple of the flow sensitivity with complete mixing.

If the design permits a regular variation of heat flux with tube position in the bundle, rather than just an occasional abnormality, perfect mixing in the intermediate header would still result in a fixed inlet enthalpy for the second half of the tube bundle.

A single flow sensitivity cannot describe flow variations in a divided tube; consequently the flow sensitivities of divided and undivided tubes operating under the same conditions, cannot be compared directly. The outlet enthalpy and the wall-temperature sensitivities, however, are of prime importance and are strongly dependent on flow sensitivity. These sensitivities are directly comparable for divided and undivided tubes and furnish a basis for critical comparison of the divided and undivided tubes for a particular design.

Outlet Enthalpy Sensitivity of a Divided Tube

No Temperature Mixing in Intermediate Header. From Equations (3), (4), and (5) rewritten without the restriction of constant inlet enthalpy one gets

$$\left(\frac{dh_0}{dQ/Q}\right)_{\Delta p} - \left(\frac{dh_{in}}{dQ/Q}\right)_{\Delta p} = \Delta h\left[1 - \left(\frac{dG/G}{dQ/Q}\right)_{\Delta p}\right] \quad (16)$$

For the second half of a tube without intermediate thermal mixing

$$\left(\frac{dh_{in}}{dQ/Q}\right)_{2/2, \Delta p} = \left(\frac{dh_0}{dQ/Q}\right)_{1/2, \Delta p, T_{in}} \quad (17)$$

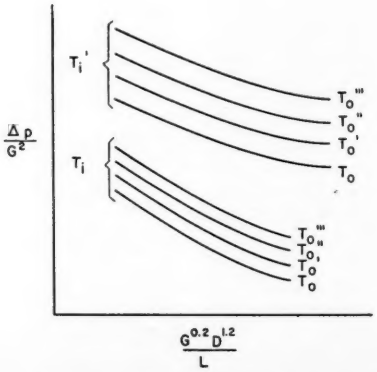

Fig. 1. Generalized pressure-drop chart.

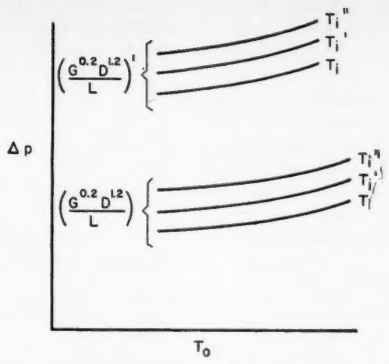

Fig. 2. Cross plot used in computation of flow sensitivity by Equation (12).

Writing Equation (16) for the second half and substituting (17) and (5) into it gives

$$\left(\frac{dh_0}{dQ/Q}\right)_{2/2,\Delta p} = \Delta h_{2/2}\left[1 - \left(\frac{dG/G}{dQ/Q}\right)_{2/2,\Delta p}\right] + \Delta h_{1/2}\left[1 - \left(\frac{dG/G}{dQ/Q}\right)_{1/2,\Delta p,T_{in}}\right] \quad (18)$$

By prior assumption, the enthalpy rise is the same in both halves of the tube, and so

$$\left(\frac{dh_0/\Delta h}{dQ/Q}\right)_{2/2,\Delta p} = 2\left[1 - \frac{\left(\frac{dG/G}{dQ/Q}\right)_{1/2,\Delta p,T_{in}} + \left(\frac{dG/G}{dQ/Q}\right)_{2/2,\Delta p}}{2}\right] \quad (19)$$

For an undivided tube the comparable equation is

$$\left(\frac{dh_0/\Delta h}{dQ/Q}\right)_{\Delta p} = \left[1 - \left(\frac{dG/G}{dQ/Q}\right)_{\Delta p}\right] \quad (20)$$

For this case the outlet enthalpy sensitivity of the divided tube can therefore be compared with that of an undivided tube by use of the arithmetic average of the flow sensitivities in the two halves.

Complete Temperature Mixing in Intermediate Header. If the second half of a tube receives completely mixed flow, its inlet enthalpy will not vary and Equation (16) reduces to

$$\left(\frac{dh_0/\Delta h}{dQ/Q}\right)_{2/2,\Delta p,T_{in}} = \left[1 - \left(\frac{dG/G}{dQ/Q}\right)_{2/2,\Delta p,T_{in}}\right] \quad (21)$$

Wall-temperature Sensitivity of a Divided Tube

No Temperature Mixing in Intermediate Header. The wall temperature at a point is a function of the average heat flux, the mass velocity, and the bulk temperature of the fluid. The variation in wall temperature may be expressed as

$$\frac{dT_w}{dQ} = \left(\frac{\partial T_w}{\partial G}\right)_{Q,T_b}\left(\frac{dG}{dQ}\right) + \left(\frac{\partial T_w}{\partial Q}\right)_{G,T_b} + \left(\frac{\partial T_w}{\partial T_b}\right)_{Q,G}\left(\frac{dT_b}{dQ}\right) \quad (22)$$

In turn, the variation in bulk temperature can be related to the heat flux, flow rate, and inlet temperature as

$$\left(\frac{dT_b}{dQ}\right)_{2/2} = \left(\frac{\partial T_b}{\partial Q}\right)_{G,2/2,T_d} + \left(\frac{\partial T_b}{\partial G}\right)_{Q,2/2,T_d}\left(\frac{dG}{dQ}\right)_{2/2} + \left(\frac{\partial T_b}{\partial T_d}\right)_{G,Q,2/2}\left(\frac{dT_d}{dQ}\right)_{2/2} \quad (23)$$

Rewriting Equation (3) for the section from point of division to the location of maximum wall temperature yields

$$h_b - h_d = \frac{4QL_{db}}{GD} = \Delta h_{db} \quad (24)$$

Differentiating at constant G and also at constant Q gives

$$\left(\frac{\partial h_b}{\partial Q/Q}\right)_{G,2/2,T_d} = \Delta h_{db} = C_{p,b}\left(\frac{\partial T_b}{\partial Q/Q}\right)_{G,2/2,T_d} \quad (25)$$

$$\left(\frac{\partial h_b}{\partial G/G}\right)_{Q,2/2,T_d} = -\Delta h_{db} = C_{p,b}\left(\frac{\partial T_b}{\partial G/G}\right)_{Q,2/2,T_d} \quad (26)$$

$$\left(\frac{\partial T_b}{\partial T_d}\right)_{G,Q,2/2} = \frac{C_{p,d}}{C_{p,b}}\left(\frac{\partial h_b}{\partial h_d}\right)_{G,Q,2/2} = \frac{C_{p,d}}{C_{p,b}} \quad (27)$$

Because of the earlier assumption that both halves of the tube experience the same heat fluxes and through Equation (5),

$$\left(\frac{\partial T_d}{\partial Q/Q}\right)_{2/2} = \left(\frac{\partial T_d}{\partial Q/Q}\right)_{1/2} = \frac{1}{C_{p,d}}\left(\frac{\partial h_d}{\partial Q/Q}\right) = \frac{\Delta h_{id}}{C_{p,d}}\left[1 - \left(\frac{dG/G}{dQ/Q}\right)_{\Delta p,1/2}\right] \quad (28)$$

Substituting (25), (26), (27), and (28) into (23) gives

$$\left(\frac{dT_b}{dQ/Q}\right)_{\Delta p,2/2} = \frac{\Delta h_{db}}{C_{p,b}}\left[1 - \left(\frac{dG/G}{dQ/Q}\right)_{\Delta p,2/2}\right] + \frac{\Delta h_{id}}{C_{p,b}}\left[1 - \left(\frac{dG/G}{dQ/Q}\right)_{\Delta p,1/2}\right] \quad (29)$$

Finally, substitution of (29) into (22) gives

$$\left(\frac{dT_w}{dQ/Q}\right)_{2/2,\Delta p} = \left(\frac{\partial T_w}{\partial Q/Q}\right)_{G,T_b} + \left(\frac{\partial T_w}{\partial G/G}\right)_{Q,T_b}\left(\frac{dG/G}{dQ/Q}\right)_{2/2,\Delta p} + \left(\frac{\partial T_w}{\partial T_b}\right)_{Q,G}\frac{1}{C_{p,b}} \cdot \left\{\Delta h_{db}\left[1 - \left(\frac{dG/G}{dQ/Q}\right)_{\Delta p,2/2}\right] + \Delta h_{id}\left[1 - \left(\frac{dG/G}{dQ/Q}\right)_{p,1/2}\right]\right\} \quad (30)$$

When the maximum wall temperature is at the outlet, Equation (19) can be used directly with Equation (22) to produce the same result as in Equation (30).

Complete Temperature Mixing in Intermediate Header. In the case of constant inlet enthalpy for the second half of the tube, Equation (23) reduces to

$$\left(\frac{dT_b}{dQ/Q}\right)_{2/2} = \left(\frac{\partial T_b}{\partial Q}\right)_{G,2/2,T_d} + \left(\frac{\partial T_b}{\partial G}\right)_{Q,2/2,T_d}\left(\frac{dG}{dQ}\right)_{2/2} \quad (31)$$

and Equation (30) becomes

$$\left(\frac{dT_w}{dQ/Q}\right)_{2/2,\Delta p,T_{in}} = \left(\frac{\partial T_w}{\partial Q/Q}\right)_{G,T_b} + \left(\frac{\partial T_w}{\partial G/G}\right)_{Q,T_b}\left(\frac{dG/G}{dQ/Q}\right)_{2/2,\Delta p,T_{in}} + \left(\frac{\partial T_w}{\partial T_b}\right)_{Q,G}\left(\frac{\Delta h_{db}}{C_{p,b}}\right) \cdot \left[1 - \left(\frac{dG/G}{dQ/Q}\right)_{2/2,\Delta p,T_{in}}\right] \quad (32)$$

Examination of Equation (32) shows how efficient intermediate mixing reduces wall-temperature sensitivity, as evidenced by the reduced value of flow sensitivity appearing in the second and third terms as well as by the elimination of the effect of the flow sensitivity of the first half of the tube.

METHOD OF CALCULATION

For fluids that have physical properties varying greatly with temperature, the flow losses must be calculated point to point along the heated tube. For a short length containing fluid of fixed physical properties, the Fanning equation can be written

$$\frac{\Delta p}{G^2} = \frac{0.092\mu^{0.2}}{\rho g_c} \cdot \frac{L}{G^{0.2}D^{1.2}} \quad (33)$$

Pressure drops due to acceleration, and entrance and exit effects will depend on the physical properties at ends of the tube divisions.

By point-to-point calculations, integrated for the tube length, it is possible to construct charts of $\Delta p/G^2$ plotted vs. $G^{0.2}D^{1.2}/L$ with families of curves of various outlet temperatures for each inlet temperature. Figure 1 is an example of these plots, which can be made for the whole tube as well as for each half.

Next, one can plot the pressure drop against the value of the heat flux (corresponding then to a particular outlet temperature) at fixed values of $G^{0.2}D^{1.2}/L$ and inlet temperature. The slopes of these lines give the value $(\partial\Delta p/\partial Q)_{G,T_{in}}$. In a similar fashion, $(\partial\Delta p/\partial G)_{Q,T_{in}}$ is obtained.

The partial differential

$$(\partial\Delta h/\partial T_{in})_{\Delta p,G,2/2}$$

needed for Equation (12) is evaluated in the following manner. For fixed values of $(G^{0.2}D^{1.2}/L)$, the values of $\Delta p_{2/2}$ are plotted against $T_{0,2/2}$ in a family of $T_{in,2/2}$ curves (Figure 2). A horizontal line on this plot represents the condition of constant $\Delta p_{2/2}$ and $G_{2/2}$ and intersects the various $T_{in,2/2}$ lines at different values of $T_{0,2/2}$. The values of $T_{0,2/2}$ and $T_{in,2/2}$ at these intersections are converted to values of $\Delta h_{2/2}$ and plotted vs. $T_{in,2/2}$. The slopes of these lines give $(\partial\Delta h/\partial T_{in})_{\Delta p,G,2/2}$.

The usual correlations show film coefficients of heat transfer to be functions of physical properties and of $(G^{0.8}/D^{0.2})$. The ratio of heat flux to film coefficient is equal to the difference between wall temperature and bulk temperature. It is possible to plot $(QD^{0.2}/G^{0.8})$ vs. bulk temperature as a family of curves with wall temperature as parameter. From such a plot are obtained the wall-temperature derivatives needed in some of the foregoing equations.

CALCULATED RESULTS FOR A SUPERCRITICAL WATER BOILER

The material presented above is illustrated by a case that is typical of the results obtained in a series of calculations on water at supercritical pressures, heated in parallel tubes of nominally identical heat input, and flowing in tubes which are connected to common headers. It might be noted that the temperatures and pressures of the example are similar to those of a large central-station supercritical-pressure boiler planned for a utility company (*2*). This boiler has one-pass flow instead of recirculation as in most large boilers and would be subject to problems of flow sensitivity. Dimensions, flow rates, and heat flux are assumed arbitrarily at reasonable values and do not reflect the values for any industrial power plant or any nuclear reactor.

The Typical Case

The physical conditions, flow rate, and heat input are given in Table 1. The headers are assumed large enough to allow calculations on the basis of loss of one half of a velocity head at tube entrance and one velocity head at the tube outlet. It is assumed that the pressure drop between the headers is small compared to 5,000 lb./sq. in. The relevant properties of water have been indicated in an earlier paper (*1*). It should be noted that the water undergoes eightfold expansion in being heated from 515° to 1,150°F.

For the example of Table 1, it is found that the maximum temperature of the tube heating surface is 1,370°F. and the pressure drop is 44.9 lb./sq. in. Heat transfer coefficients and friction factors were evaluated according to calculations of Goldmann (*3*). For present purposes the Goldmann predictions give results substantially the same as do the method of Deissler (*4*) or the usual isothermal-turbulent-flow formulas used with properties based on mean film temperatures.

Table 1

p	5,000 lb./sq. in.
T_i	515 °F.
T_0	1,150 °F.
Q	3×10^5 B.t.u./(hr.)(sq. ft.)
G	1.8×10^6 lb./(hr.)(sq. ft.)
D	0.0416 ft.
L	62 ft.

The results of calculation are shown in Table 2, wherein the effectiveness of an intermediate header in reducing flow-sensitivity outlet enthalpy, temperature sensitivity, and tube-wall temperature sensitivity can readily be seen.

Table 2

		Second half of divided tube	
	Undivided tube	No temperature mixing	Complete temperature mixing
$\left(\frac{dG/G}{dQ/Q}\right)_{\Delta p}$	−3.75	−1.70	−0.59
$\left(\frac{dh_0/\Delta h}{dQ/Q}\right)_{\Delta p}$	4.75	2.70	1.59
$\left(\frac{dT_0}{dQ/Q}\right)_{\Delta p}$	6,700°F.	2,700°F.	1,100°F.
$\left(\frac{dT_w}{dQ/Q}\right)_{\Delta p}$	8,000°F.	5,800°F.	3,000°F.

ACKNOWLEDGMENT

The work reported here draws on ideas and results of related studies by several other staff members of Nuclear Development Corporation of America, notably Kurt Goldmann, R. C. Ross, and N. R. Adolph. Elaine Scheer and Gloria Sullivan performed the computations from which these results were taken.

NOTATION

- D = equivalent diameter of heated passage or tube, ft.
- G = mass velocity, lb. mass/(hr.) (sq. ft.)
- Δh = difference in enthalpy between two locations, B.t.u./lb. mass
- L = length of heated passage, ft.
- p = pressure, lb. force/sq. ft.
- Δp = difference in pressure between two locations, lb. force/sq. ft.
- Q = average heat flux along heated passage, B.t.u./(hr.)(sq. ft.)
- T = temperature, °F.

Subscripts

- b = bulk
- d = point of division of tube length
- in = inlet
- o = outlet
- $1/2$ = first half
- $2/2$ = second half

LITERATURE CITED

1. Gruber, A. R., and S. C. Hyman, *A.I.Ch.E. Journal*, **2**, 199 (1956).
2. *Electrical World*, p. 72 (June 29, 1953.).
3. Goldmann, Kurt, *Chem. Eng. Progr. Symposium Series* No. 11, **50**, 105 (1954).
4. Deissler, R. G., *Trans. Am. Soc. Mech. Engrs.*, **76**, 73 (1954).

Manuscript submitted May, 1957; revision received July 12, 1957; paper accepted July 30, 1957.

Convective Heat Transfer from High-temperature Air Inside a Tube

HERBERT E. ZELLNIK and STUART W. CHURCHILL

University of Michigan, Ann Arbor, Michigan

Local rates of convective heat transfer from air at high temperature to a cold wall were measured in the inlet region of a circular tube. Air entered the tube with a flat velocity and temperature profile at temperatures from 480° to 2,000°F. and flow rates corresponding to Reynolds numbers from 4,500 to 22,500. The inner surface of the 1.0-in. I.D. tube was maintained at approximately 100°F. by water cooling. Local rates of heat transfer were determined at 1.5, 4, 7, and 10 tube diameters from the entrance by measuring the radial temperature profile in thermally isolated, annular sections of the tube wall.

The local rate data for all gas temperatures are well represented by previous correlations for small temperature differences if the gas properties are evaluated at the bulk temperature rather than at the film temperature. The data agree well with the data of previous investigators wherever the experimental ranges overlap.

Convective heat transfer to and from gases flowing in tubes has been investigated extensively, but primarily in long tubes at ambient conditions. The generally accepted correlations are therefore subject to such limitations. Current interest in the extension of the temperature range of many engineering operations and in compact heat exchangers suggests the experimental extension and the reevaluation of these correlations.

Excellent summaries of previous work may be found in McAdams (*1*) and Groeber, et al. (*2*), The most definitive data for the local rate of heat transfer in the inlet region are those of Boelter, et al. (*3*). The analytical results of Deissler (*4*) based upon an empirical equation for the eddy diffusivity agree well with these data (*3*). The only extensive data for convection in tubes at extreme temperatures are those of Humble, et al. (*5*), on air heated at tube-wall temperatures up to 2,950°F. Limited data were also obtained for heat extraction at air temperatures up to 1,040°F. The length of the tube was varied but in increments too long for the derivation of local rates. The data deviated significantly from low-temperature correlations and for theoretically proposed equations for large temperature differences (*6*).

This investigation was undertaken to evaluate the effect of increasing air temperatures on the *local* rate of heat transfer in the inlet region. A uniform wall temperature, turbulent flow, and a flat velocity profile at the inlet were chosen as boundary conditions.

EXPERIMENTAL APPARATUS AND PROCEDURE

The apparatus was designed to provide gas at temperatures up to 2,500°F. and flow rates up to 25 std. cu. ft./min. and to measure local rates of heat transfer to a cold wall in the entrance section of a circular

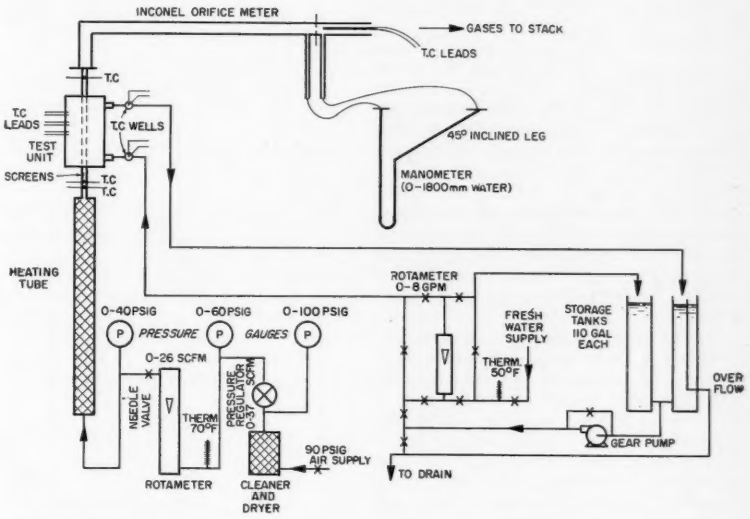

↗ **Fig. 1. Schematic diagram of equipment.**

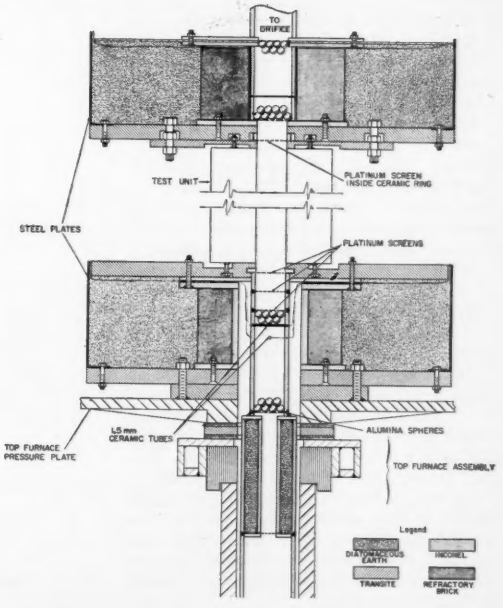

Fig. 2. Detail of adiabatic sections and top furnace assembly. →

H. E. Zellnik is at present with Union Carbide Nuclear Company, New York, New York.

tube. Compressed air was passed through a cleaner and dehumidifier, then through a rotameter at regulated pressure, and was heated in passage through a packed tube in an electric resistance furnace. The temperature of the air entering the test section was measured in a packed adiabatic tube at the furnace outlet. Hot-wire–anemometer measurements showed that a negligible intensity of turbulence and a flat velocity profile at the inlet to the test section were established by three 52-mesh platinum screens when the air was not heated. It is assumed that similar conditions existed in the heated gas at the same Reynolds number. The test section consisted of a 1.0-in. I.D. by 1.8-in. O.D. by 11.25-in.-long water-cooled Inconel tube. The air leaving the test section passed through another adiabatic packed tube in which the exit temperature was measured and then through an orifice. The orifice was installed because of leakage of gas in passage through the furnace. A sketch of the apparatus is shown in Figure 1 and details of the adiabatic sections appear in Figure 2.

The temperatures of the gas and packing were assumed to be equal near the outlet and inlet respectively of the inlet and outlet packed adiabatic tubes. The temperature of the packing, which consisted of ¼-in. alumina spheres, was measured with butt-welded 28 gauge Chromel-Alumel thermocouples in a singly perforated ceramic tube as shown. Since the tube can "see" only packing at essentially the same temperature, the error due to radiation is negligible. The theoretical and experimental basis for this method of determining the gas temperature is discussed in further detail in reference 7.

Details of the test section are indicated in Figure 3. Thirty-six-gauge, coated, butt-welded Chromel-constantan thermocouples were induction-welded at the bottom of 20-mil holes at three radii in each of four thermally isolated annular sectors of the Inconel tube. The thermocouple junctions were precisely located at the end of the experimental work by slicing the tube near the couples and X-raying. The midpoints of the annular sectors were 1.5, 4, 7, and 10 in. from the inlet of the heated tube. The insulating slots and the holes were filled with a silicon resin after insertion of the thermocouples, and the test object was baked at 500°F. The tube was enclosed in a brass shell for cooling and was insulated from the adjacent adiabatic sections by transite sheets and asbestos gaskets. Cooling-water temperatures were measured with Chromel-constantan thermocouples in wells in the inlet and outlet piping, and the flow rate was measured with a rotameter.

Runs were made at gas inlet temperatures of approximately 500, 1,000, 1,500, and 2,000°F. and at flow rates corresponding to bulk Reynolds numbers of approximately 5,000, 7,500, 10,000, 12,000, 15,000, and 20,000; flow rates corresponding to a Reynolds number of 20,000 at 1,500°F. and of 15,000 at 2,000°F. were not attainable owing to limitations of the pressure-regulating and flow-measuring instruments. Surface temperatures ranged from 73 to 208°F. from run to run but were uniform within ±2% of the absolute temperature from station to station. Only illustrative data are presented herein. The detailed data are presented in both graphical and tabular form in reference 8.

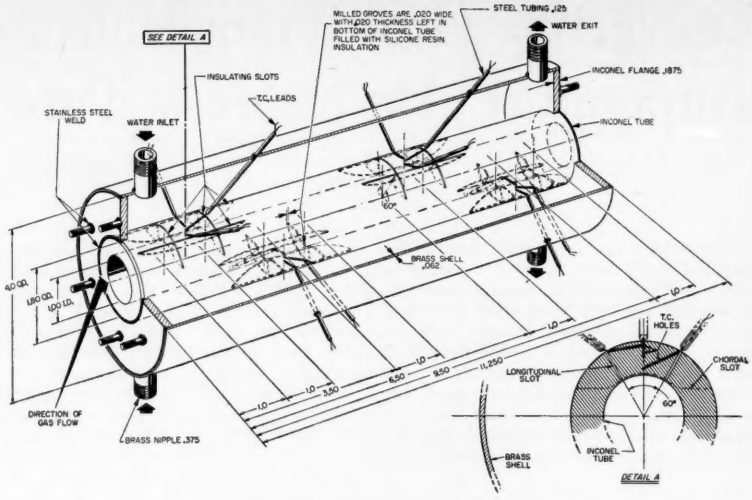

Fig. 3. Detail of test section.

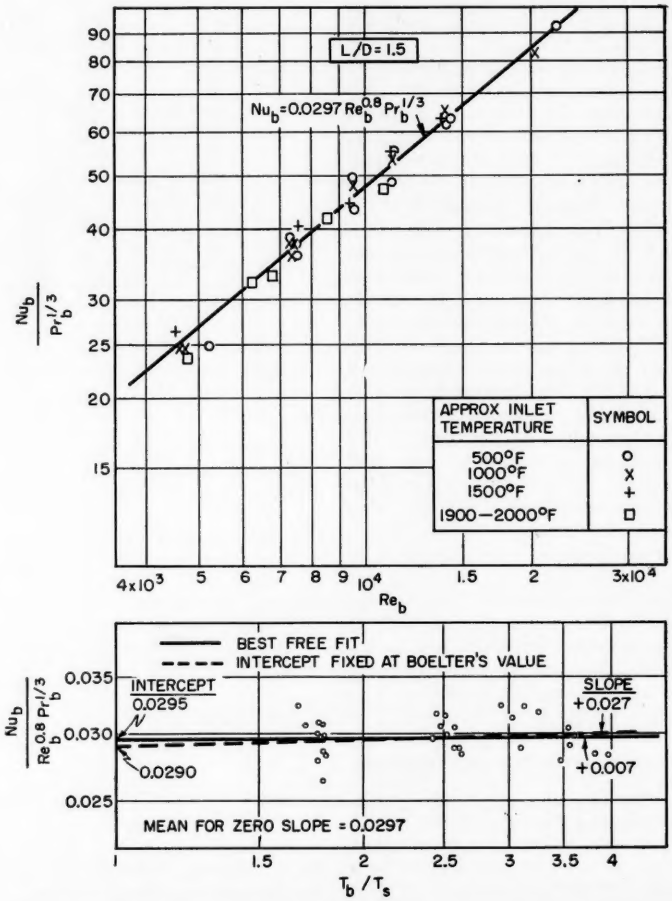

Fig. 4. Correlation of heat transfer data for $L/D = 1.5$; properties evaluated at bulk temperature.

DETERMINATION OF THE RATE FROM THE DATA

For steady state, constant conductivity, and negligible angular and longitudinal gradients in a hollow cylinder the equation for conduction reduces to

$$\frac{1}{r}\frac{d}{dr}\left(r\frac{dT}{dr}\right) = 0 \qquad (1)$$

and a solution can be written in terms of known temperatures at any two points (T_1, r_1) and (T_2, r_2)

$$\frac{T - T_1}{T_2 - T_1} = \frac{\ln r/r_1}{\ln r_2/r_1} \qquad (2)$$

The surface temperature can be calculated from Equation (2) or found graphically by extrapolation of a straight line through two or more points on a plot of T vs. $\ln r$.

The heat flux through the wall is found in terms of two of the measured wall temperatures or in terms of the surface temperatures determined from all three measured temperatures:

$$q_s = \frac{k_m}{r_s}\frac{(T_2 - T_1)}{\ln r_1/r_2} = \frac{k_m}{r_s}\frac{(T_s - T_o)}{\ln r_o/r_s} \qquad (3)$$

The convective heat transfer coefficient is obtained by subtracting the radiant flux to the wall from the measured flux

$$h = \frac{q_s - q_r}{T_b - T_s} \qquad (4)$$

The radiant flux between the platinum screens at the ends of the test section and points on the surface was calculated by use of the interchange factors computed by Hamilton and Morgan (*9*). This correction reached a maximum of 8% of the total flux at a gas temperature of 2,000°F. and an L/D of 1.5.

The gas temperature at any L/D could be computed from either the inlet temperature or outlet temperature and the integrated convective flux to the wall. However, the inlet and outlet thermocouples demonstrated some inconsistency, which is to be expected at the conditions at which they were used. Consequently a linear variation of gas temperature between the measured temperatures was assumed to minimize the uncertainty introduced by an error in either thermocouple reading. The maximum uncertainty introduced in the heat transfer coefficients by this decision was 2%.

CORRELATION OF RATE DATA

The experimental data for each of the four stations were correlated separately in terms of the empirical equation

$$\frac{hD}{k} = A\left(\frac{C_p\mu}{k}\right)^{1/3}\left(\frac{DG}{\mu}\right)^{0.8}\left(\frac{T_b}{T_s}\right)^m \qquad (5)$$

The form of Equation (5) and the exponents for the Prandtl and Reynolds numbers were chosen on the basis of previous investigations for small temperature differences. The Prandtl number was not varied significantly in this investigation and, as will be shown, the effect of Reynolds number over the fivefold range of this investigation appears to be adequately represented by the 0.8 power.

The representation of the data by Equation (5) was investigated with the viscosity and thermal conductivity evaluated at the bulk, film, and surface temperatures. Since Keenan and Kay (*10*) give values for both the thermal conductivity and the viscosity of air, these values were used rather than the more recent values of Hilsenrath (*11*) for the viscosity, which agree up to 800°F. but are 2% lower at 2,000°F. Since Hilsenrath reported a variation in $(C_p\mu/k)^{1/3}$ only from 0.879 to 0.891 for the entire range of this experimental work, a mean value of 0.885 was used. Evaluation of the properties at the bulk temperature was found to give the best fit.

Specifically Equation (5) was rearranged in the form

$$\ln \frac{(hD/k)}{(C_p\mu/k)^{1/3}(DG/\mu)^{0.8}} = \ln A + m \ln\left(\frac{T_b}{T_s}\right) \qquad (6)$$

and A and/or m were determined by least squares for three cases:

1. The best free fit, equivalent to the best straight line through a plot of log $(hD/k)/(C_p\mu/k)^{1/3}(DG/\mu)^{0.8}$ vs. log (T_b/T_s).
2. Fixed A. The best value of m was found with A equal to 0.023 (h/h_m). The ratio of the local coefficient to the asymptotic coefficient for large L/D was computed from the results of Boelter, et al. (*3*) for a flat velocity profile at the inlet and is included in Table 1. This representation is equivalent to the best straight line through the chosen value of A on the previously discussed plot and forces extrapolation of the correlation to the low-temperature results of Boelter as T_b/T_s approaches unity.
3. Zero exponent for temperature ratio. The best value of A was found for $m = 0$. This is equivalent to the best straight line of zero slope on the previously discussed plot.

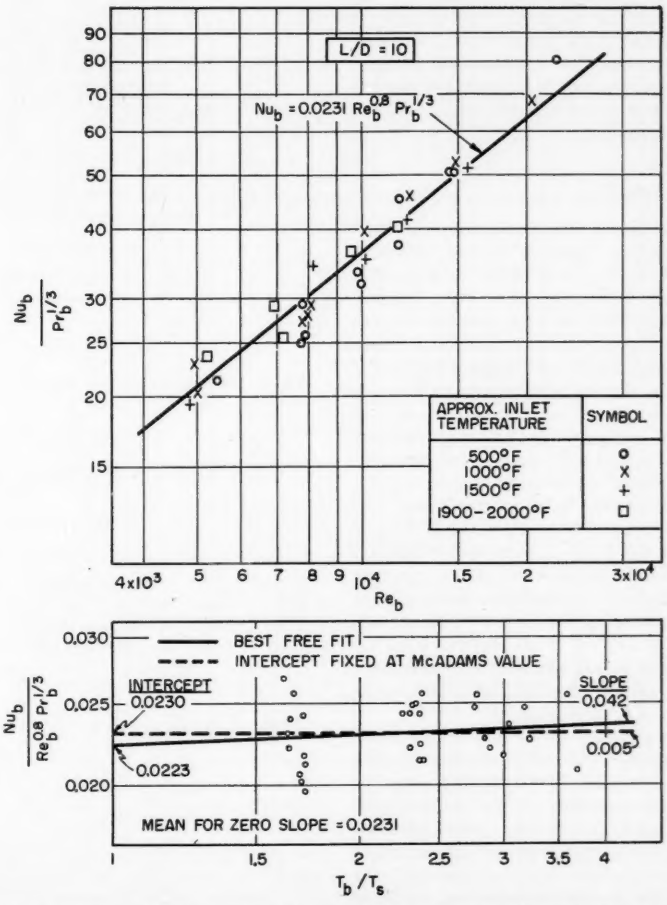

Fig. 5. Correlation of heat transfer data for L/D = 10; properties evaluated at bulk temperature.

The correlation procedure is illustrated for L/D of 1.5 and 10.0 in the lower graph in Figures 4 and 5 and the results are summarized for all four stations in Table 1. The standard deviations in log $(hD/k)/(C_p\mu/k)^{1/3}(DG/\mu)^{0.8}$ are not significantly greater for the third case than for the free fit. Therefore the correlation

$$\frac{hD}{k_b} = A\left(\frac{C_p\mu}{k}\right)^{1/3}\left(\frac{DG}{\mu_b}\right)^{0.8} \qquad (7)$$

with A given under case 3 in Table 1 is recommended in terms of simplicity. The limited results of Humble, et al, (*5*) for cooling air were also reported to show no dependence on temperature when expressed in terms of bulk temperature.

The lowest graph of Figures 4 and 5 exaggerates the deviations. The upper graph indicates the representation of the data for L/D of 1.5 and 10.0 by Equation (7) in more customary form. The data are plotted in terms of the local bulk temperature at L/D of 1.5 and 10.0 respectively but for simplicity are coded in terms of the inlet temperature ($L/D = 0$). The scatter with respect to gas temperature appears to be random and the arbitrary choice of an exponent of 0.8 for the Reynolds number appears satisfactory. The representations obtained for the other two intermediate stations are quite comparable to the representation in Figures 4 and 5 and therefore are not reproduced here.

DISCUSSION

That the correlation is independent of the surface temperature is probably fortuitous. The data of this investigation and that of Humble, et al. were obtained at nearly ambient and constant surface temperatures. Correlation of future data for a high fixed bulk temperature and a variable surface temperature will probably require explicit inclusion of the surface temperature or of properties dependent upon the surface temperature. The present correlation should not be inferred to hold for these conditions.

The constants A and m for a free fit and m for fixed A were also evaluated with the properties evaluated at the film and surface temperature. Some of the results for L/D of 1.5 and 10.0 are compared in Table 2. The dependence on the temperature ratio is seen to increase as the properties are evaluated at successively lower temperatures.

The viscosity of air is approximately proportional to $T^{0.68}$ and the thermal conductivity of $T^{0.85}$ over the range of this investigation (*8*, *9*). Accordingly, Equation (5) can be rearranged as follows in terms of properties evaluated at the surface temperature and the coefficient A_b and exponent m_b, obtained in terms of properties evaluated at the bulk temperature.

$$\frac{hD}{k_s} = A_b\left(\frac{C_p\mu}{k}\right)^{1/3} \cdot \left(\frac{DG}{\mu_s}\right)^{0.8}\left(\frac{T_b}{T_s}\right)^{0.31+m_b} \qquad (8)$$

The net coefficient in Equation (8) is obviously the same as in Equation (5) and the net exponent is increased by $0.85 - (0.8)(0.68) = 0.31$. These values are in reasonable agreement with the results shown in Table 2 in which the actual variation in properties rather than the power representation was utilized. The correlation obtained in terms of surface temperature is thus equivalent to

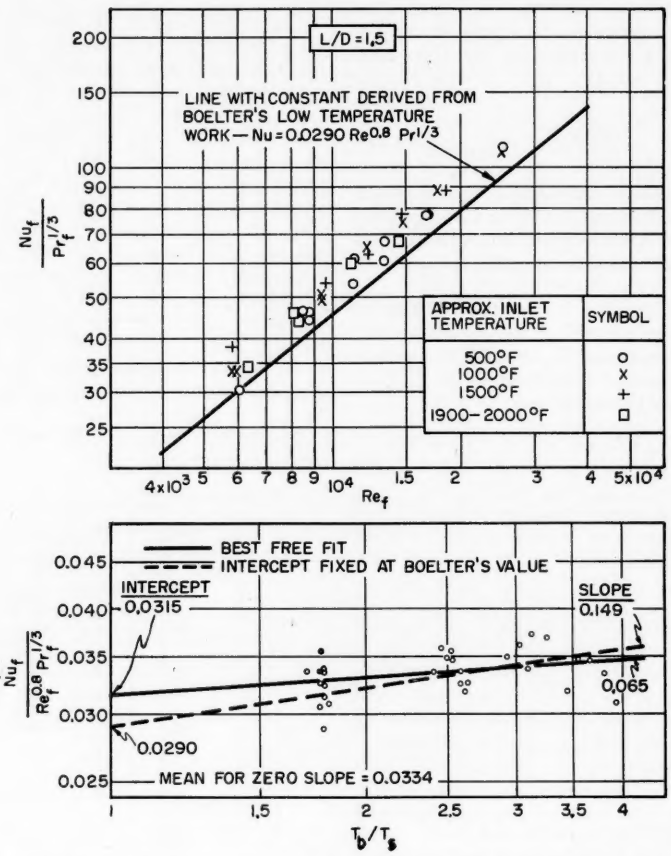

Fig. 6. Correlation of heat transfer data for $L/D = 1.5$; properties evaluated at film temperature.

TABLE 1. EVALUATION OF CONSTANTS IN EQUATION (5), PROPERTIES EVALUATED AT BULK TEMPERATURE

		Best free fit			Fixed A			$m = 0$	
L/D	h/h_∞ (*3*)	A	m	σ, %	A	m	σ, %	A	σ, %
1.5	1.26	0.0295	+0.007	6.3	0.0290	+0.027	7.8	0.0297	7.8
4.0	1.09	0.0264	−0.026	7.8	0.0251	+0.026	10.2	0.0257	7.8
7.0	1.03	0.0237	−0.003	7.2	0.0237	+0.002	7.8	0.0236	7.2
10.0	1.00	0.0223	+0.042	6.3	0.0230	+0.005	6.8	0.0231	7.8

TABLE 2. EVALUATION OF CONSTANTS IN EQUATION (5) FOR DIFFERENT REFERENCE TEMPERATURES

		Best free fit		Fixed A		$m = 0$
L/D	Reference temperature	A	m	A	m	A
1.5	Bulk	0.0295	0.007	0.0290	0.027	0.0297
	Film	0.0315	0.065	0.0290	0.149	0.0334
	Surface	0.0288	0.337	0.0290	0.332	
10.0	Bulk	0.0223	0.042	0.0230	0.005	0.0231
	Film	0.0228	0.135	0.0230	0.122	0.0255

that obtained in terms of bulk temperatures, insofar as the variation of properties can be represented as a power of the absolute temperature.

There is no such equivalence for the correlation obtained in terms of the film temperature. With a free fit the coefficient A is strikingly higher; i.e., the correlation does not extrapolate satisfactorily to the low-temperature results of Boelter, et al. (3). With $m = 0$ and with a fixed intercept to force extrapolation to the low temperature results, a poor representation is obtained, as illustrated in Figures 6 and 7. Coefficients which differ about 13% from those of Boelter are obtained. This difference appears to be greater than the uncertainties in the data of Boelter and of this investigation and a null hypothesis test indicates that it is statistically significant. The correlation based on bulk temperature is therefore recommended unless a temperature ratio is included. Even if a temperature ratio with the corresponding exponent indicated in Table 2 is included in the correlation, the bulk or surface temperature appears to be a more satisfactory reference temperature than the film temperature.

The mean and probable error for all thirty data points at each of the four stations are compared with the correlation of Boelter, et al. in Figure 8. The agreement is excellent even though dividing the ordinate by $(DG/\mu_b)^{0.8}$ accentuates the deviations, as is apparent in the two portions of Figure 4. It should be noted that Figure 8 is general for all flow rates and air temperatures insofar as Equation (7) holds; whereas T_b/T_s becomes a parameter when h/h_∞ or $(hD/k_b)/(hD/k_b)_\infty$ is plotted vs. L/D.

The local heat transfer coefficient itself at $L/D = 1.5$ is plotted in Figure 9 to emphasize the very real increase which takes place with increasing air temperature. Since $(hD/k_b)/(DG/\mu_b)^{0.8}$ does not increase with the bulk air temperature, h must be approximately proportional to $k_b/\mu_b^{0.8}$ and hence to $T_b^{0.31}$.

All previous investigators have found that by $L/D = 10.0$, hD/k attains essentially its asymptotic value for long tubes with constant wall temperature. Hence the results obtained and conclusions drawn for $L/D = 10.0$ appear to be applicable for a mean hD/k in a long tube.

The prediction of Deissler (6) that the data for cooling could be generalized in terms of the properties at the film temperature or at $0.4T_b + 0.6T_s$ does not appear to be compatible with the results of this investigation. However, as emphasized by Deissler, this prediction was based on the assumption that both the viscosity and the thermal conductivity were proportional to $T^{0.68}$. Recalculation of the experimental hD/k in terms of

$$k = k_a(T/T_a)^{0.68} \qquad (9)$$

rather than in terms of the values given by Keenan and Kaye (10) was found to yield values of hD/k in excellent agreement with the predictions of Deissler. This emphasizes the dependence of the correlations and the conclusions of this investigation upon the validity of current values for the physical properties.

The results of this investigation for cooling air ($T_b/T_s > 1$) are compared with those of Humble, et al. (5) for heating air ($T_b/T_s < 1$) in Figure 10. The lines represent the correlations obtained with the properties evaluated at the bulk, film, and surface temperatures. The discontinuity in the slope of the lines at $T_b/T_s = 1.0$ is undoubtedly an artificiality resulting from separate correlation of the data for heating and cooling,

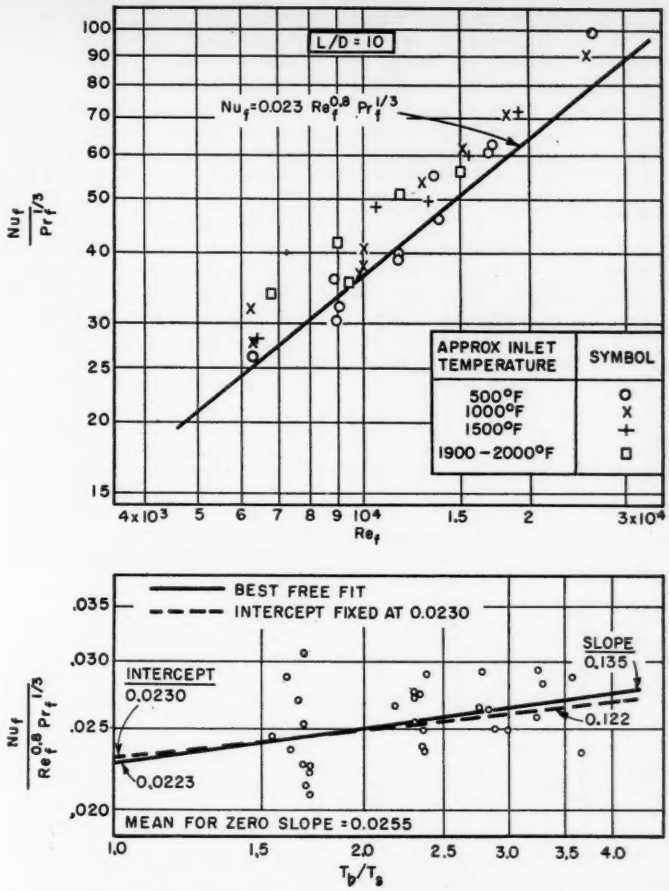

Fig. 7. Correlation of heat transfer data for $L/D = 10$; properties evaluated at film temperature.

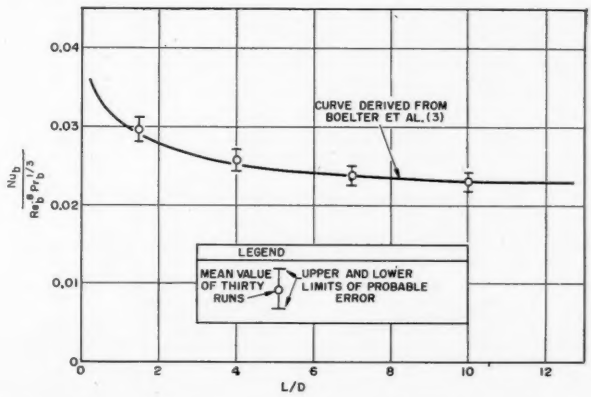

Fig. 8. Summary of local heat transfer rate data for high air temperatures.

but it does indicate that a power function of the temperature ratio is inadequate to represent the effect of property variation for both heating and cooling of gases in tubes, as contrasted with the success of Douglas and Churchill (*12*) for the flow of gas over cylinders.

CONCLUSIONS

The local and the over-all rate of heat extraction from air in turbulent flow in tubes can be predicted from previous correlations for low-temperature differences provided that the viscosity and the thermal conductivity are evaluated at the bulk temperature. An equivalent but less convenient correlation can be obtained by evaluation of these properties at the surface temperature and inclusion of $(T_b/T_s)^{0.33}$ as a factor in the correlation. These conclusions are dependent upon the validity of current values for the thermal conductivity and viscosity of air. Although this investigation was limited to air, similar results are to be expected for other gases for which the temperature dependence of physical properties parallels that of air. Previous investigations of gaseous convection appear to justify the generalized form in which the data are correlated.

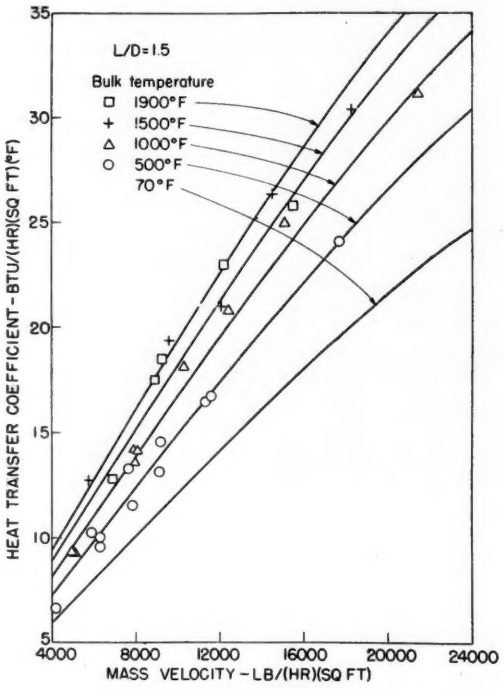

Fig. 9. Local heat transfer coefficients at $L/D = 1.5$.

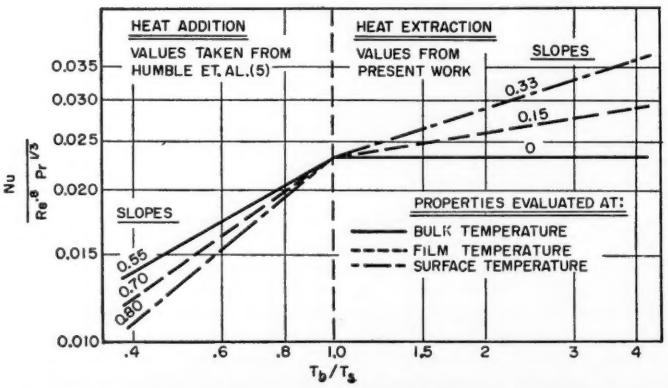

Fig. 10. The effect of temperature level on heating and cooling.

The results are in contrast with correlations for heat addition in which the ratio of the surface to the bulk temperature has been found to be a parameter no matter which single temperature is chosen for evaluation of the gas properties.

NOTATION

A = coefficient
C_b = heat capacity, B.t.u./(lb.)(°F.)
D = diameter, ft.
G = mass velocity, lb./(hr.)(sq. ft.)
h = heat transfer coefficient, B.t.u./(hr.)(sq. ft.)(°F.)
k = thermal conductivity, B.t.u./(hr.)(ft.)(°F.)
L = tube length, ft.
m = exponent
Nu = hD/k
Pr = $C_p\mu/k$
q = heat flux, B.t.u./(hr.)(sq. ft.)
r = radial distance, ft.
Re = DG/μ
μ = viscosity, lb./(hr.)(ft.)
σ = standard deviation, %

Subscripts

a = ambient
b = bulk or mixed mean
m = metal
o = outside tube
r = radiant
s = inside surface
1 = any position
2 = any position
∞ = asymptotic value as $L/D \rightarrow \infty$

LITERATURE CITED

1. McAdams, W. H., "Heat Transmission," 3 ed., McGraw-Hill Book Company, Inc., New York (1954).
2. Groeber, Heinrich, Sigmund Erk, and Ulrich Grigull, "Die Grundgesetz der Warmeubertragung," 3 ed., Springer Verlag, Berlin (1955).
3. Boelter, L. M. K., G. Young, and H. W. Iversen, *Natl. Advisory Comm. Aeronaut. Tech. Note* 1451 (July, 1948).
4. Deissler, R. G., *Trans. Am. Soc. Mech. Engrs.*, **77**, 1221 (1957).
5. Humble, L. V., W. H. Lowdermilk, and L. G. Desmon, *Natl. Advisory Comm. Aeronaut. Rept.* 1020 (1951).
6. Deissler, R. G., *Natl. Advisory Comm. Aeronaut. Tech. Note* 2242 (December, 1950).
7. Churchill, S. W., Ph.D. thesis, Univ. Mich., Ann Arbor (1952).
8. Zellnik, H. E., Ph.D. thesis, Univ. Mich., Ann Arbor (1956).
9. Hamilton, D. C., and W. R. Morgan, *Natl. Advisory Comm. Aeronaut. Tech. Note*, 2836 (December, 1952).
10. Keenan, J. H., and G. W. C. Kaye, "Thermodynamic Properties of Air," John Wiley and Sons, New York (1945).
11. Hilsenrath, Joseph, et al., *Natl. Bur. Standards Circular* 564 (Nov. 1, 1955).
12. Douglas, W. J. M., and S. W. Churchill, *Chem. Eng. Progr. Symposium Ser.* No. 18, **52**, p. 23 (1956).

Manuscript submitted May, 1957, paper accepted September 9, 1957.

Heat Transfer from Superheated Vapors to a Horizontal Tube

GAREN BALEKJIAN and DONALD L. KATZ

University of Michigan, Ann Arbor, Michigan

Experimental data are reported for condensing Freon-114 (tetrafluorodichloroethane) and steam at several pressures. The condition of the vapors ranged from saturation to 180°F. of superheat. The condensing tube containing embedded thermocouples was 3/4 in. in diameter and 3 ft. long. Visual observation showed that steam condensed by dropwise condensation in part. Increase of superheat in the vapor at constant pressure caused a lowering of the tube-wall temperature, which was indicative of a lowering of the surface temperature of the condensate. The lowering of the condensate-surface temperature below the saturation temperature was computed from the experimental tube-wall temperatures, the heat flux, and Nusselt's equation for the condensate-film resistance. The lowering of the condensate-surface temperature is correlated with degree of superheat. An interfacial coefficient of heat transfer between the superheated vapor and the condensate surface is reported based on the computed surface temperatures. Schrage's analysis and equations for relating mass and heat transfer with conditions at an interface were simplified and used to correlate the experimental condensing load with the degree of superheat.

The condensation of superheated vapors is frequently encountered in industry, for instance in vapor leaving compressors. A superheated vapor in contact with a surface at temperatures below the dew point of the vapor will form a condensate film on the cold surface. The heat extracted from the vapor passes through the liquid film much as in the condensation of saturated vapors. The difference in the condensation of superheated vapors from the process for saturated vapors lies in the removal of the superheat from the vapor at an extremely short distance from the condensate surface and in the effect that this process has on the temperature of the liquid at the vapor-liquid interface. The proper design of a superheated vapor condenser requires the formulation of a theory whereby the behavior of superheated vapors may be predicted for a wide range of pressures and superheats in order to anticipate the peculiar condenser condition when the tube surface is no longer wetted with a liquid film.

The classical work of Nusselt (*21*) presents theoretical equations for the condensation of vapors on different surfaces. The derivation of these equations and a detailed discussion of the experimental data on this subject is available in several references (*8, 9, 11, 13, 14, 17, 18,* and *20*). The effect of condensate-film turbulence on the condensate-film coefficient is observed by Kirkbride (*16*). Other factors such as vapor velocity and its effect on the turbulence of the condensate film and literature related to them are reviewed in reference *23*.

The condensation of superheated vapors is discussed in the original work of Nusselt (*21*). The integrated equations for the condensate-film thickness on a vertical plate and the corresponding condensing load are presented in references *14* and *20*. Using an approximation of the analytical results, Stender (*26*) and Merkel (*19*) predict an increase of up to 37% in the heat flux due to superheat (*20*). Katz et al. (*15*) report the results of their studies for superheated Freon-12 condensing on the outside of horizontal plain and finned tubes. No effect of superheat as compared with saturated vapors is observed for the range of pressure of 103 to 172 lb./sq. in. abs. and the maximum superheat of 122.5°F. Nusselt's derivation of an equation applied to superheated vapors gives an equation similar to that for saturated vapors where the factor $(-\Delta H)$ represents the total heat removed in condensing the superheated vapors. This equation predicts a small increase in heat flux due to superheat. Conventional design of superheated vapor condensers is based on the condensate film coefficient predicted by this method.

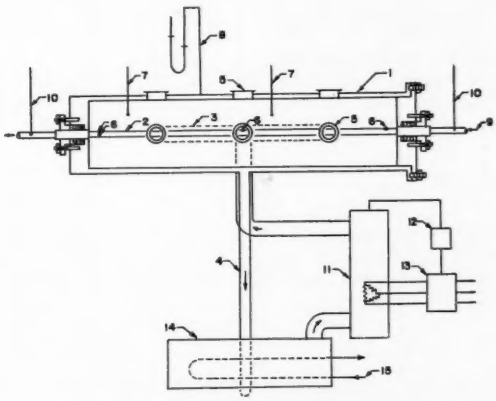

Fig. 1. Experimental apparatus.

Garen Balekjian is at present with C. F. Braun and Company, Alhambra, California.

INTERPHASE TRANSFER THEORY

Condensation of superheated vapors involves the transfer of mass and energy across the vapor-liquid film. The statistical behavior of molecules predicted from the kinetic theory of gases is useful in relating the temperature and pressure conditions of the system with the rate of mass and energy transfer. The work of Schrage (*24*) presents the basic equations applicable to condensation and vaporization phenomena. The following relationship is derived for the rate of interphase transfer and the prevailing temperature and pressure conditions:

$$m_s = h_f \sqrt{\frac{g_c M}{2\pi R T_s}} \left[P_s^* - P_g \left(\frac{T_s}{T_g} \right)^{1/2} \Gamma \right] \tag{1}$$

The variable Γ in Equation (1) is a correction factor involving the error integral and is evaluated as a function of

$$\phi_g = \sqrt{\frac{g_c M}{2RT_g}}\, u_g$$

Subscripts s and g refer to conditions at the vapor-liquid interface and the vapor region respectively. The condensation coefficient h_f, defined as the ratio of molecules condensed to the total number of molecules striking the surface, is assumed to be constant and independent of the molecular vector velocity. It is a function of the state of the surface and the kind of molecules involved. The derivation of Equation (1) does not assume equilibrium conditions at the interface. The maximum rate of evaporation or condensation is used in the derivation of Equation (1) and is defined as

$$m_e = h_f P_s^* \sqrt{\frac{g_c M}{2\pi R T_s}} \tag{2}$$

The use of Equation (1) to predict the deviation from equilibrium for actual cases is made difficult by the functional interdependence of m_s, m_e, h_f, Γ, and ϕ_g. Schrage defines ϕ_g by the following equation:

$$\phi_g = \frac{1}{2\pi^{1/2}} \frac{m_s}{m_e} \left(\frac{P_s^*}{P_g} \right) \left(\frac{T_g}{T_s} \right)^{1/2} \tag{3}$$

A modified form of Equation (1) is used extensively in the literature concerning interphase transfer phenomena:

$$m_s = h_f (P_s^* - P_g) \sqrt{\frac{g_c M}{2\pi R T_s}} \tag{4}$$

Equation (4) involves the assumption of interfacial equilibrium

$$\Gamma = 1.0, \left(\frac{T_s}{T_g} \right) = 1.0$$

Equations (2) and (4) are used by Alty and coworkers (*1* to *5*) for the experimental evaluation of the condensation

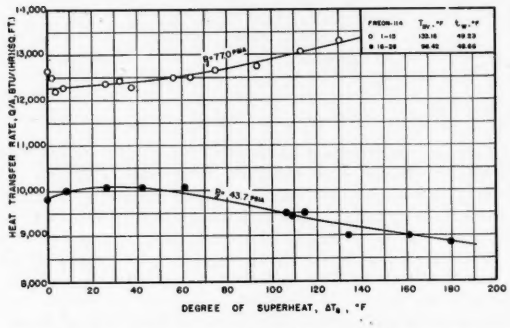

Fig. 2. Effect of superheat on heat flux for condensation of Freon-114.

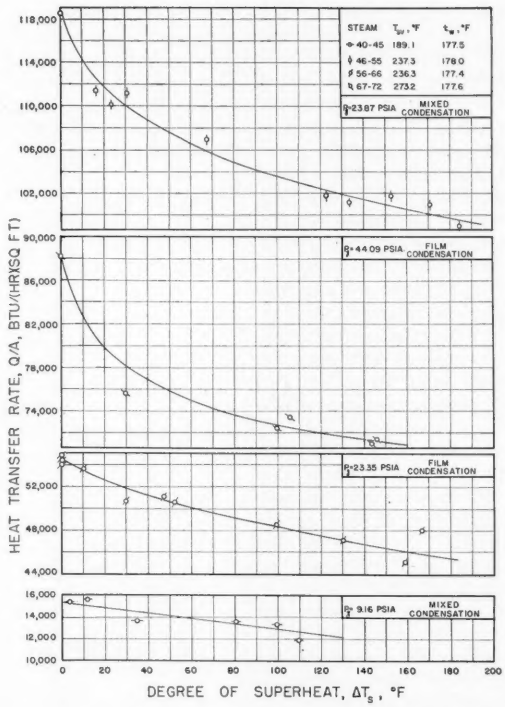

Fig. 3. Effect of superheat on heat flux for condensation of steam.

coefficient h_f for water, carbon tetrachloride, and several other liquids and solids. It is concluded that the condensation coefficient of polar compounds is relatively small, whereas that of nonpolar compounds is very close to unity. Prüger (*22*) has determined the condensation coefficient of water and carbon tetrachloride at atmospheric pressure. The values of h_f of 0.04 and unity for water and carbon tetrachloride respectively agree with those reported by Alty. A recent study (*12*) on the rate of condensation of water vapor under vacuum presents a correlation based on Equation (2).

The concept of the lowering of the condensate-surface temperature below that of the saturated vapor during the condensation of superheated steam is reported by Jakob (*13*), and a theoretical attempt to prove lowering of the condensate-surface temperature below the saturation temperature is made by Bosnjakovic (*7*).

Using the approximate Equation (4) along with the Clapeyron equation Silver (*25*) has defined an interfacial film coefficient for the evaluation of condensate subcooling during the condensation of saturated steam at low pressures. The interfacial film coefficient h_i based on $(T_{sv} - T_s)$ and $h_f = 0.036$ (*2*) is defined as

$$h_i = 778 h_f \sqrt{\frac{g_c M}{2\pi R T_s}} \frac{(-\Delta H)^2 \rho_L}{T} \qquad (5)$$

Equation (5) is used by Cornell (*10*) in a method recommended for the evaluation of the condensate surface temperature (T_s), the interfacial film coefficient (h_i), and the temperature drop across the interfacial film for the condensation of superheated steam. It is assumed that the vapor at the interface is at the saturation temperature and that the temperature drop through the interfacial film is of the same order as that for a saturated vapor.

EXPERIMENTAL APPARATUS

The experimental apparatus consists of a closed system for generating vapor, superheating it, condensing the superheated vapor, and returning condensate to the vapor generator. Figure 1 presents the flow diagram describing the experimental apparatus.

The essential feature of the apparatus is the horizontal condenser tube ¾ in. in outside diameter and 3 ft. long, housed in a 6-in. shell. The limited surface and large shell reduce the effects of vapor velocity and condensate splashing on shell-side heat transfer. Four thermocouples made from 30-gauge copper-constantan wires are installed circumferentially in the tube wall to measure the temperature. Two of these thermocouples are located at the water-outlet end of the experimental tube, one at the top and the other 90 deg. from the

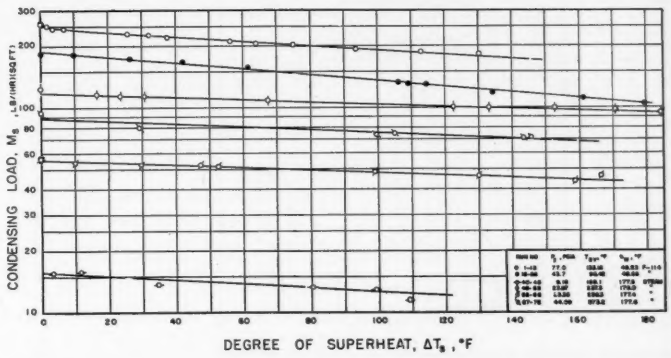

Fig. 4. Effect of superheat on condensing load for condensation of Freon-114 and steam.

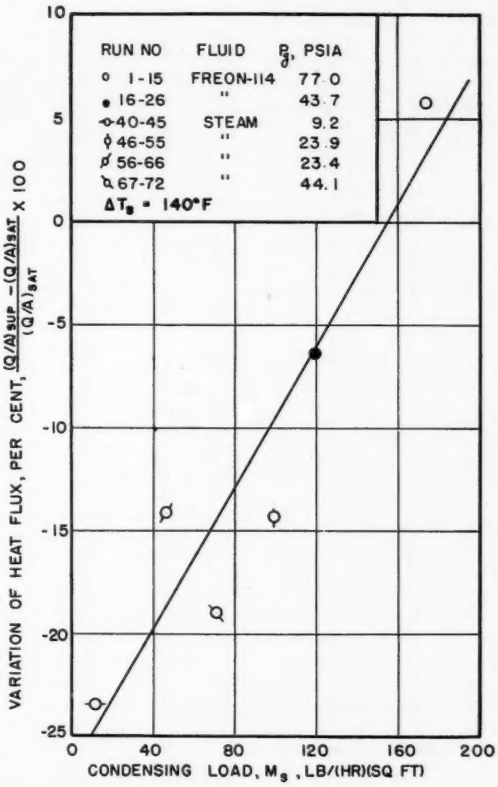

Fig. 5. Correlation of the effect of superheat on the heat flux with the condensing load.

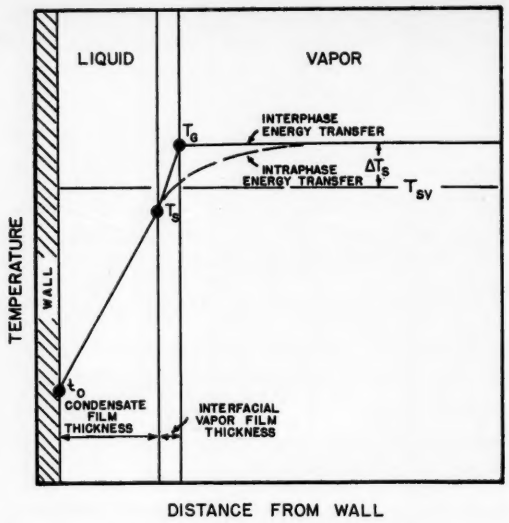

Fig. 6. Temperature profile for a condensing superheated vapor.

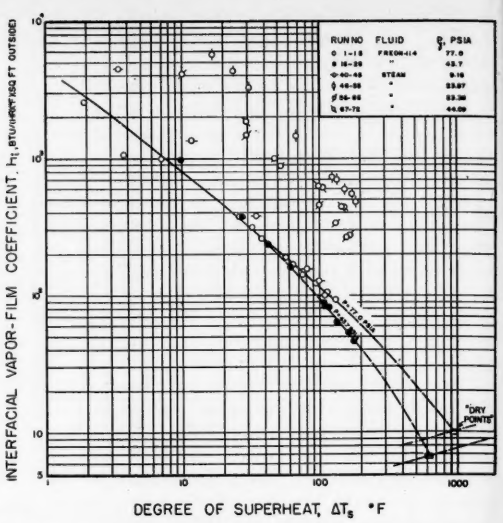

Fig. 7. Effect of superheat on interphase vapor-film coefficient h_i for condensation of Freon-114 and steam.

top position. The third and fourth thermocouples are at the middle and at the water-inlet end of the tube respectively, both at the top position. The end thermocouples are spaced $3\frac{1}{16}$ in. from the inner surface of the condenser headers, and the thermocouple at the center of the tube is spaced $15\frac{7}{32}$ in. from those at the ends. Water at a controlled temperature is circulated through the tube to extract the heat from the condensing vapor. The heat transfer rate is determined by the temperature rise of the water measured with mercury-in-glass thermometers and by the water flow rate indicated by a calibrated rotameter. Two iron-constantan thermocouples in the vapor space of the condenser indicate the temperature of the vapor. The degree of superheat in the vapor is automatically controlled by an electric superheater. The superheater and condenser are lagged heavily with insulation to reduce variation of the vapor temperature in the condenser.

Water and Freon-114 (tetrafluorodichloroethane) are selected for this study as two fluids with widely different properties. Freon-114 is chosen as the organic fluid because it has a suitable vapor pressure and generally gives stable film condensation. At the time steam was selected, it was expected that it would be made to condense by film; however, for most of the data on steam the condensation was a mixture of drop and film condensation. At a given condenser pressure the auxiliary equipment is arranged to provide hot water at a constant temperature and flow rate. The absence of noncondensables is indicated by the constant heat flux at steady state conditions, after the bleeding off of a portion of the condenser vapor.

The experimental data consist of the following measurements: condenser temperatures, condenser tube-wall temperatures, water flow rate, inlet and outlet water temperatures, condenser pressure, barometric pressure, and room temperature.

EXPERIMENTAL DATA

Condensation of Freon-114 is studied at two pressures of 77.0 and 43.7 lb./sq. in. abs. and different vapor superheats ranging from 0° to 180°F. Four sets of comparable data are obtained for steam at pressures of 9.2, 23.4, 23.9, and 44.1 lb./sq. in. abs. and maximum superheats varying from 109° to 184°F. Runs made at 23.4 and 44.1 lb./sq. in. abs. constitute data with primarily film condensation of steam.

The condensing-water flow rate varies for the different condenser pressures, the range being from 7 to 18 ft./sec. Water-temperature rise for the test runs varies from 1.9° to 11.6°F. Under these conditions the portion of the thermal resistance due to condensing water is 50% or less. The tube-wall thermocouples indicate a maximum temperature variation of 6.5°F. along the tube. A circumferential temperature variation is observed from the two thermocouples at the water-outlet end of the tube. The thermocouple at the top position indicates wall temperatures which are 0.5° to 2°F. higher than those of the thermocouple located 90 deg. from the top. The maximum variation of the vapor temperature from the two condenser thermocouples is 1° to 2°F. at the highest superheats investigated. Experimental data and calculated results are available in reference *6*.

The degree of superheat is defined as the difference between the temperature of the superheated vapor and the saturation temperature corresponding to the condenser pressure. The experimental heat fluxes are presented in Figure 2 for Freon-114 and in Figure 3 for steam. The general trend is a gradual decrease in the heat flux due to superheat. The effect of superheat on the heat flux varies for the various pressures. It is interesting to observe the trend indicated for the effect of superheat on the condensing load in order to interpret the over-all performance of superheated vapors. The calculated condensing loads are presented in Figure 4 on a semilogarithmic plot of the condensing load vs. the degree of superheat. In all cases the condensing load decreases gradually with the superheat. A comparison of Figures 2 and 3 with Figure 4 indicates that at the lowest condensing loads represented by the steam data at 9.2 lb./sq. in. abs. the reduction in heat flux at 140°F. superheat compared with the heat flux at saturation is a maximum of 23.4%. For intermediate condensing loads this reduction is 14.1 to 19.0%. For the higher condensing loads represented by the Freon-114 data at 43.7 lb./sq. in. abs. the reduction in the heat transfer rate is a minimum of 6.4% for the same degree of superheat. At the highest condensing loads with Freon-114 at 77.0 lb./sq. in. abs. the trend in the heat transfer rate is reversed and there is an increase of 5.8% in the heat flux.

These results indicate that the trend obtained for the effect of superheat on the heat-flux curve depends on the condensing load (Figure 5). This is due to the fact that an uncertain amount of desuperheating of the vapor occurs in the condenser because of the intimate contact of the subcooled condensate with the vapor surrounding it. The discrepancy shown in Figure 5 by some steam results is due primarily to the difference in the tube-side water-flow rates and the type of condensation obtained.

Interfacial Film Coefficients

The difficult measurement of the vapor and liquid temperatures at the interface as shown in Figure 6 is not feasible in this investigation. For the case of stable film condensation the condensate film coefficient is calculated for the saturated vapor from the Nusselt equation, the measured tube-surface temperature, and the condensing load. For Freon-114 the calculated condensate-film coefficient is 4.1% higher at 77.0 lb./sq. in. abs. and 17.5% lower at 43.7 lb./sq. in. abs. than the corresponding experimental value. The fair agreement between the two results indicates the possibility of calculating the condensate-surface

temperature for the results with superheated Freon-114 and steam. Assuming the available temperature drop between the superheated vapor and the condensate surface to occur at the vapor-liquid interface makes possible the calculation of the corresponding interfacial-film coefficient. The validity of this assumption is shown by the extent to which experimental results agree with the theory. The interfacial-temperature difference is calculated as

$$\Delta t_i = (T_g - T_s) \qquad (6)$$

The interfacial film coefficient is defined by the following equation:

$$h_i = \frac{Q}{A\Delta t_i} \qquad (7)$$

Actual thickness of the interfacial film (Figure 6) is very small, of the order of a molecular mean free path. Since the exact location and area of the interface are unknown, a good approximation for A in Equation (7) is the outside-tube–surface area.

Figure 7 presents the relationship between the calculated interfacial-film coefficients and the degree of superheat for Freon-114 and steam results. As the degree of superheat is increased, the condensing load decreases, the condensate-film coefficient increases, and the interfacial-film coefficient decreases. The interfacial-film coefficient is infinite for a saturated vapor. Up to a superheat of about 30°F. the effect of pressure on the interfacial-film coefficient of Freon-114 seems to be relatively small (Figure 7). The more pronounced spacing of the steam results is to be accounted for partly by the variable extent of the condensation by drops observed with steam.

Figure 7 is useful in predicting conditions of superheat in the region close to the "dry point." This region characterizes the superheated vapor temperatures at which the tube surface is dry and the outside film coefficient is represented by the interfacial film coefficient. In the region close to the "dry point" the outer-tube-surface temperature approaches the tube-side fluid temperature. It is reasonable to assume that under these conditions the interfacial-film coefficient is of the order of the combined natural convection and radiation coefficients. Dashed lines representing these calculated coefficients are shown in Figure 7.

Intersection of these lines with the extrapolated interfacial-film coefficients gives the calculated dry points. For Freon-114 at 43.7 and 77.0 lb./sq. in. abs. the dry point corresponds to a superheat of 625° and 925°F. respectively.

CORRELATION OF CONDENSING LOAD

The theory on interphase mass and energy transfer is used for the correlation of experimental and calculated results. The condensate-surface temperature calculated as described in the preceding section is presented as a function of the degree of superheat in Figure 8. The semilogarithmic plot indicates a straight-line relationship. Lines are drawn to represent the best trend indicated by the calculated points. The equations of these lines given in Figure 8 show the mean saturation temperature for all the runs in a given set corresponding to the mean condenser pressure. Saturation and condensate-surface temperatures used for the correlation of experimental heat transfer rates and condensing loads are obtained from the lines shown in Figure 8.

Direct application of Equation (1) for the correlation of results is complicated because of the correction factor Γ, as indicated earlier. This relationship is simplified by expressing Γ as a simple function of ϕ_g defined by Equation (3). Values of $(\Gamma - 1)$ are presented graphically for condensation ($\phi_g < 0$) and evaporation ($\phi_g > 0$) in reference *24* for the range $1.0 \geq |\phi_g| \geq 0.001$. The major portion of this graph corresponding to the range of $0.1 \geq |\phi_g| \geq 0.001$ is represented satisfactorily by a straight line with a slope of unity. The following equation approximates the calculated values of Γ for condensation with a maximum deviation of $\pm 4\%$:

$$\Gamma = 1 + 1.85\,|\phi_g| \qquad \text{for} \quad 0.1 \geq |\phi_g| \geq 0.001 \qquad (8)$$

On substitution for the absolute rate of evaporation (m_s) from Equation (2) into Equation (3), ϕ_g is expressed as

$$\phi_g = \frac{m_s}{2\pi^{1/2} h_f P_g} \sqrt{\frac{2\pi R T_s}{g_c M}} \left(\frac{T_g}{T_s}\right)^{1/2} \qquad (9)$$

Substituting for Γ in Equation (1) the linear function given by Equation (8) and solving for ϕ_g yields

$$\phi_g = \frac{1}{1.85}\left(\frac{P_s^*}{P_g}\right)\left(\frac{T_g}{T_s}\right)^{1/2} - \frac{m_s}{1.85 h_f P_g}\left(\frac{T_g}{T_s}\right)^{1/2}\sqrt{\frac{2\pi R T_s}{g_c M}} - \frac{1}{1.85} \qquad (10)$$

If Equations (9) and (10) are combined to eliminate ϕ_g, the following equation is derived for the condensation coefficient h_f:

$$h_f = \frac{1.52 m_s \sqrt{\dfrac{2\pi R T_s}{g_c M}}}{\left[P_s^* - P_g\left(\dfrac{T_s}{T_g}\right)^{1/2}\right]} \qquad (11)$$

Equation (11) is equivalent to Equation (1), discussed earlier, with the correction factor Γ replaced by its equivalent constant factor of 1.52. A relationship similar to Equation (11) is presented by Bosnjakovic (*7*) without the constant factor. On substitution for $\sqrt{2\pi R/g_c}$ Equation (11) is simplified to

$$h_f = \frac{m_s \sqrt{\dfrac{T_s}{M}}}{19{,}630\left[P_s^* - P_g\left(\dfrac{T_s}{T_g}\right)^{1/2}\right]} \qquad (12)$$

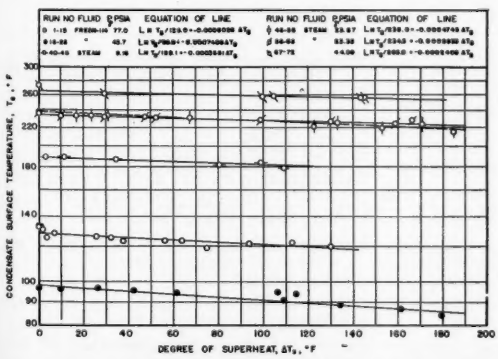

Fig. 8. Correlation of calculated condensate surface temperature with superheat for condensation of Freon-114 and steam.

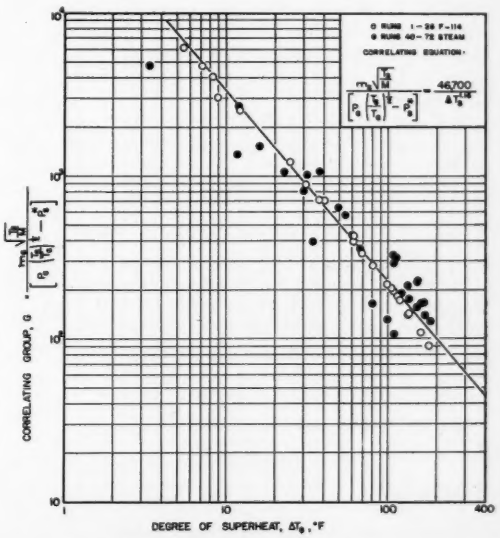

Fig. 9. Correlation of condensing load with superheat as a function of condensation coefficient.

where P_s^* and P_g are expressed in pounds force) per square inch absolute. The experimental and calculated results are used to calculate h_f from Equation (12) and ϕ_g from Equation (9). These calculations indicate values of ϕ_g of about 0.007 and justify the use of Equation (8) to eliminate Γ in Equation (1).

The correlating group defined as

$$G = \frac{m_s\sqrt{\frac{T_s}{M}}}{\left[P_g\left(\frac{T_s}{T_g}\right)^{1/2} - P_s^*\right]} \qquad (13)$$

is used for the correlation of the experimental condensing load and the calculated temperature and pressure conditions at the interface with the degree of superheat. The correlating group is plotted against the superheat in Figure 9. Of the two fluids Freon-114 indicates stable film condensation and is expected to give results which agree better with predictions from interphase theory. This is shown by the satisfactory grouping of the Freon-114 results about the line drawn to represent the best trend. It is interesting to note that the present correlation predicts conservative condensing loads for superheated steam condensing by film. The maximum deviation of the results is $+12$ and -20% for Freon-114 and $\pm 50\%$ for the steam results. The equation of the correlating line in Figure 9 is found to be

$$\frac{m_s\sqrt{\frac{T_s}{M}}}{\left[P_g\left(\frac{T_s}{T_g}\right)^{1/2} - P_s^*\right]} = \frac{46{,}700}{\Delta T_s^{\,1.16}} \qquad (14)$$

Combining Equations (12) and (14) shows the condensation coefficient to be unity at $T_s = 2$°F. Since the value of h_f cannot exceed unity, it may be deduced that for saturated Freon-114 vapor the value of the condensation coefficient is close to unity.

The use of Figure 9 or Equation (14) is recommended for applications involving the film condensation of a superheated vapor outside horizontal tubes. For the given pressure, degree of superheat, and tube-surface temperature, Nusselt's equation and Equation (14) are used to calculate the unknown condensate-surface temperature and the corresponding heat flux and condensing load. The correct value of the condensate surface temperature is that which gives the same calculated heat flux or condensing load from Nusselt's equation and Equation (14).

CONCLUSIONS

The present investigation reveals some important phenomena encountered during the condensation of superheated vapors. The effect of superheat in the absence of excessive splashing of the condensate is a lowering of the heat flux and condensing load and a depression of the condensate-surface temperature below that of the saturated vapor.

The general theory of interphase mass and energy transfer is applicable for the correlation of results obtained with film condensation of superheated vapors. For a thorough understanding of this subject the interfacial temperature and pressure conditions prevailing during the condensation of superheated vapors must be obtained accurately from direct or indirect experimental measurements.

ACKNOWLEDGMENT

This work was supported by a fellowship provided by the Continental Oil Company.

NOTATION

A = total outside area, sq. ft.

g_c = conversion factor, 4.17×10^8 (lb. mass)(ft.)/(lb. force)(sq. hr.)

G = correlating group involving m_s, M, T_s, T_g, P_s^*, and P_g

h_c = condensate film coefficient, B.t.u./(hr. °F. sq. ft. outside)

h_f = condensation coefficient, dimensionless

h_i = interfacial film coefficient, B.t.u./(hr. °F. sq. ft. outside)

$(-\Delta H)$ = total heat removed, latent heat for saturated vapor, B.t.u./lb.

m_e = absolute rate of evaporation, lb./(hr.)(sq. ft.)

m_s = condensing load, lb./(hr.)(sq. ft.)

M = molecular weight, lb. mass/lb. mole

P_g = pressure of gas phase, lb. (force)/sq. ft. abs., lb. (force)/sq. in. abs. in Equations (12) through (14)

P_s^* = equilibrium vapor pressure at T_s, lb. (force)/sq. ft. abs., lb. (force)/sq. in. abs. in Equations (12) through (14)

Q = total heat transferred, B.t.u./hr.

Q/A = heat flux, B.t.u./(hr.)(sq. ft. outside)

R = gas constant, 1,544 (ft.)(lb. force)/(lb. mole)(°R.)

Δt_i = temperature drop through interfacial film $(T_g - T_s)$, °F.

t_0 = outside tube-surface temperature, °F.

t_w = average tube side water temperature, °F.

T = average temperature between T_s and T_{sv}, °R.

T_g = superheated vapor temperature, °R.

T_s = condensate surface temperature, °R. (°F. in Figure 8)

T_{sv} = saturation temperature, °R (°F. in Figures 2, 3, and 4)

ΔT_s = degree of superheat, $(T_g - T_{sv})$, °F.

u_g = absolute mean molecular velocity representing rate of mass transfer

ρ_L = Liquid density, lb./cu. ft.

$\phi_g = \sqrt{\frac{g_c M}{2RT_g}}\, u_g$, variable defining Γ

Γ = correction factor, function of error integral

LITERATURE CITED

1. Alty, T., *Proc. Roy. Soc.* (*London*), **A131**, 554 (1931).
2. ———, *Phil. Mag.*, **15**, 83 (1933).
3. ———, *Proc. Roy. Soc.* (*London*), **A161**, 68 (1937).
4. ———, and C. A. Mackay, *ibid.*, **A149**, 104 (1935).
5. Alty, T., and F. H. Nicoll, *Can. J. Research*, **4**, 547 (1931).
6. Balekjian, Garen, Ph.D. thesis, Univ. Mich., Ann Arbor (1956).
7. Bosnjakovic, F., *Forsch. Gebiete Ingenieurw.*, **3**, 135 (1932).
8. Claassen, H., *Centr. Zukerind.*, **35**, 129 (1927).
9. ———, *Wärme*, **61**, 403 (1938).
10. Cornell, David, "Condensation of Superheated Vapors," Heat and Mass Transfer Seminar Report, Univ. Mich., Ann Arbor (1952).
11. Dobkin, G. I., *Teplosilovoe Khoz.*, **1**, 21 (1941); see *Chem. Abs.*, **37**, 4278.
12. Glbson, L. C., Ph.D. thesis, Univ. Wis. Madison (1952).
13. Jakob, Max, *Mech. Eng.*, **58**, 729 (1936).
14. ———, "Heat Transfer," vol. 1, John Wiley and Sons, New York (1953).
15. Katz, D. L., et al., *J. Am. Soc. Refrigerating Engrs.*, **53**, 315 (1947).
16. Kirkbride, C. G., *Trans. Am. Inst. Chem. Engrs.*, **30**, 170 (1933–34); *Ind. Eng. Chem.*, **26**, 425 (1934).
17. Lang, M., *Forsch. Gebiete Ingenieurw.*, **B5**, 212 (1934).
18. McAdams, W. H., "Heat Transmission," 2 ed., McGraw-Hill Book Company, Inc., New York (1942).
19. Merkel, F., "Die Grundlagen der Wärmeübertragung, "Steinkopff, Leipzig (1927).
20. Monrad, C. C., and W. L. Badger, *Trans. Am. Inst. Chem. Engrs.*, **24**, 84 (1930).
21. Nusselt, W., *Z. Ver. deut. Ing.*, **60**, 541, 569 (1916).
22. Prüger, W., *Z. Physik*, **115**, 202 (1940).
23. Rohsenow, W. M., J. H. Webber, and A. T. Ling, Preprint 54-A-145, *Am. Soc. Mech. Engrs.* (1954).
24. Schrage, R. W., "Interphase Mass Transfer," Columbia Univ. Press, New York (1953).
25. Silver, R. S., *Engineering*, **161**, 505 (1946).
26. Stender, W., *Z. Ver. deut. Ing.*, **69**, 905 (1925).

Manuscript received May 9, 1957; revision received Nov. 12, 1957; paper accepted Dec. 9, 1957.

A New Electric Analogue Model for Nonsteady State Flow Problems

IRVING FATT

California Research Corporation, La Habra, California

A new, simple electric analogue model is demonstrated which gives solutions, accurate within ten %, to problems in nonsteady state flow of heat, diffusion, and flow of liquids in porous media. The analogue consists essentially of a sandwich of electrical conducting paper, polyethylene or polyester sheeting, and metal foil. One- or two-dimensional problems can be treated. This analogue provides a medium with distributed resistance and capacitance rather than the finite steps of conventional analogues; therefore two-dimensional problems of complex shape can easily be modeled. The analogue is pulsed by a square wave generator and the transient potential response is displayed on a cathode-ray oscilloscope.

Problems in nonsteady state heat conduction, diffusion, and fluid flow through porous media are often encountered in engineering design and operations. When these problems arise for simple geometrical shapes, the solutions usually can be found in the literature. For irregular or complex geometrical shapes, solutions can be obtained only by analogue models or high-speed digital computers. Pachkis (*1*) and Bruce (*2*) have described electric analogue models which can solve these problems, but their models are complex and expensive. Recently the trend has been toward the use of digital computers for the solution of nonsteady state flow problems. Digital-computer solutions usually require machine programs that are difficult and expensive to devise. Both the digital-computer solutions and most electric analogue models have a disadvantage because they require the continuous body under study to be transformed to a finite mesh. The process of making a "lumped" mesh from a continuum may introduce serious errors if there are regions of rapidly converging or diverging stream lines.

This paper describes a new, simple, continuous electric analogue model that is equivalent to an infinitely fine mesh and that will give an approximate solution of many one- and two-dimensional nonsteady state problems. The analogue consists of electrical conducting paper, a thin sheet of dielectric material, and metal foil all sandwiched together to form a continuous resistance and capacitance analogue. In its simplest form this analogue can model only homogeneous systems. In a slightly more complex form, it can model systems in which there are regions of different diffusivity constants*. A continuous variation of diffusivity constant with distance can also be modeled if the continuous variation in the prototype is transformed to a stepwise variation in the model. Variation of the diffusivity constant with time or potential cannot be modeled.

The paper analogue and the method of measuring potential transients described in this paper can model systems in which a potential is instantaneously applied or removed from any boundary or point or in which the applied potential is a known function of time.

The analogue can be constructed and the data taken and analyzed in less than a working day. The accuracy, about 10% is usually sufficient for engineering purposes.

Present address: University of California, Berkeley, California.

*The term *diffusivity constant* refers to the coefficient in the nonsteady state flow equation and is not limited to the coefficient in the diffusion equation.

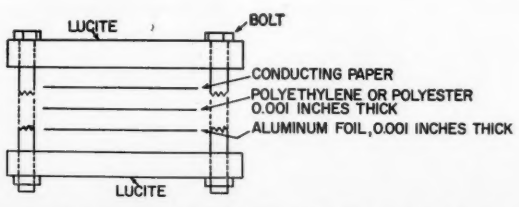

Fig. 1. Cross section of paper electric analogue model in exploded view. In actual model the bolts are drawn tight to force paper, polyethylene, and foil into contact.

PRINCIPLE OF ELECTRIC ANALOGUE MODELS

Problems in nonsteady state heat conduction, diffusion, and flow of liquids in porous media can be solved by an electric analogue model because all these phenomena are described by the same equation that governs flow of electricity in certain networks of resistors and capacitors.

The governing equation, usually called the heat equation, is in one dimension

$$\frac{\partial U}{\partial t} = \alpha \frac{\partial^2 U}{\partial x^2} \qquad (1)$$

and in two dimensions

$$\frac{\partial U}{\partial t} = \alpha\left(\frac{\partial^2 U}{\partial x^2} + \frac{\partial^2 U}{\partial y^2}\right) \qquad (2)$$

DESCRIPTION OF PAPER ANALOGUE MODEL

The electric analogue model to be described here is in principle the same as the models of Pachkis (*1*) and Bruce (*2*), but it uses different kinds of resistance and capacitance elements and a different method of measuring transient voltage.

The electric analogue model described in this paper is made of Western Union L 39 Teledeltos or Timefax electrical conducting paper, 0.001 in. thick polyethylene or polyester sheeting (the kind used for packaging perishable food), and metal foil. The conducting paper, dielectric sheeting, and foil are sandwiched between two Lucite plates to form an analogue with a distributed resistance and capacitance medium. A typical analogue constructed during this study was made of two pieces of ½- by 6- by 6-in. Lucite. Ten ¼-in. holes were drilled along the edge to take the ¼ by 20 machine bolts that held the elements of

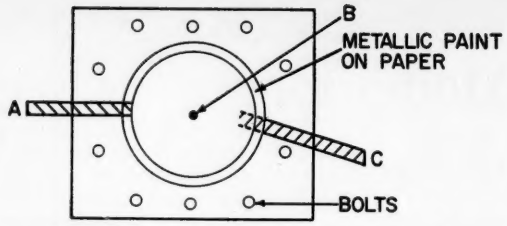

Fig. 2. Top view of paper analogue model of infinite cylinder. Point *A* is the lead to the outer edge, *B* is the lead to the center, and *C* is the lead to the ground plate.

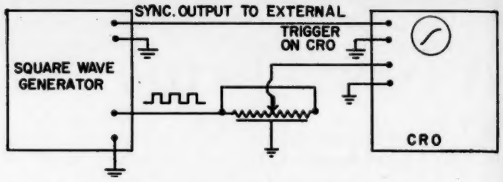

Fig. 3. Circuit diagram showing method of pulsing and measuring transient in paper analogue model.

the analogue in intimate contact. To be certain that there was uniform pressure on the entire surface of the conducting paper, dielectric sheeting, and foil combination, four *C* clamps were equally spaced around the center. A cross section of the analogue is shown in Figure 1. The top view of an analogue model representing a radial system is shown in Figure 2. Printed-circuit silver paint applied to the conducting paper acts as the electrode. Contact to the painted electrode is made by means of a strip of brass shim stock. The paint reduces to a negligible value the contact resistance between the paper and stock.

The resistance-capacitance product of the paper analogue model described above is so low that voltage build-up takes place in a few microseconds. The resistance of L 39 Teledeltos paper is 2,000 ohms/sq. in.; Timefax has a resistance of 6,000. The capacitance of the model is about 500 $\mu\mu$fd./sq. in., polyethylene or polyester 0.001 in. thick being used. If a model 1-in. wide and 3-in. long is pulsed at one end, the voltage at the other end will rise to 63% of the input voltage in about 4 μsec. when Teledeltos paper is used and in 12 μsec. when Timefax paper is used. The input pulse must be supplied by a high-speed switch or a square wave generator and the voltage build-up curve must be recorded photographically from a cathode-ray oscilloscope. An arrangement of this kind has been described by Lawson and McGuire (*3*).

The recently developed fast-rise-time oscilloscopes and the Polaroid oscilloscope camera make it convenient to obtain transient response directly. In the study reported here the analogue model was pulsed with a model 43A square wave generator manufactured by Electro-Mechanical Research, Incorporated, the transient response was displayed on a Tektronix model 545 oscilloscope, and the pattern on the oscilloscope was photographed with a Du Mont polaroid camera.

COMPARISON OF PAPER-ANALOGUE-MODEL SOLUTIONS TO ANALYTICAL SOLUTION

Paper analogue models were constructed to represent an infinite plate, an infinite square bar, and an infinite cylinder. A schematic sketch of the cylinder models is shown in Figure 2. Several models of each kind were made to determine the optimum size and combination of conductive paper and dielectric material. The infinite plate models were about 3 by 2 in., the square bar models were 2 to 4 in. on a side, and the cylinder models were 3 to 4 in. in diameter. The central contact was a 4–40 machine screw that was threaded through the upper Lucite plate and that made contact with the conducting paper through a small hole in the foil and dielectric. The potential at this contact, as a function of time, gave the central potential history of the model.

The circuit diagram showing the model, square wave generator, and oscilloscope is given in Figure 3. The square wave generator was operated at about 5,000 cycles/sec. This frequency is not critical. The only requirement is that there be sufficient time for the model to discharge between pulses. At 5,000 cycles/sec. the pulse length and discharge time are both 200 μsec. The model was essentially completely discharged after 20 μsec. The output impedance of the generator was 300 ohms (or less if an external resistor was shunted across the output), so that the model might discharge through the generator during the period between pulses.

The potential transient at the center of the model was picked up by a Tektronix P 450-L probe, which has an input capacitance of 2.5 $\mu\mu$fd. and an input resistance of 10 megohms. The high input impedance assured that the probe did not load the model. From the probe the signal was fed to the type 53/54K input unit of the Tektronix 545 oscilloscope. The fast rise time of this input unit, about 0.006 μsec., assured that the transient being measured was not distorted by the input amplifier characteristic.

The input to the model was displayed on the scope and photographed. The

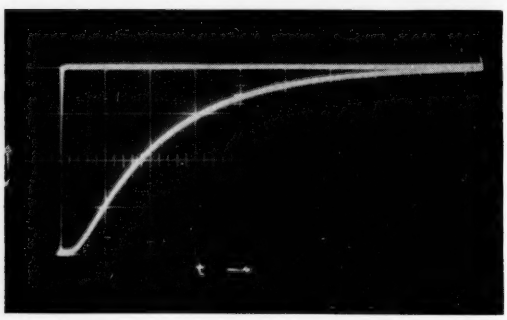

Fig. 4. Photoreproduction of trace displayed on oscilloscope. Both input impulse and transient are shown. Each large time division is 2 μsec. The maximum voltage is about 0.5 volt.

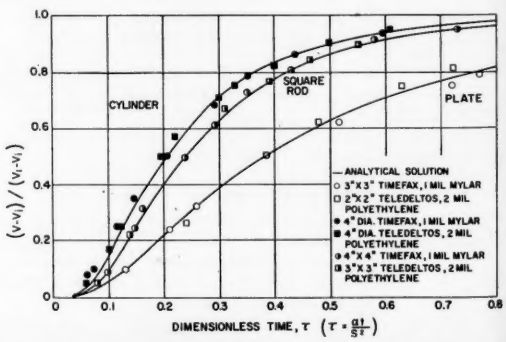

Fig. 5. Central potential history of several solids when the outer surface is suddenly raised from V_i to V_1. Lines are analytical solution; data points are from analogue model.

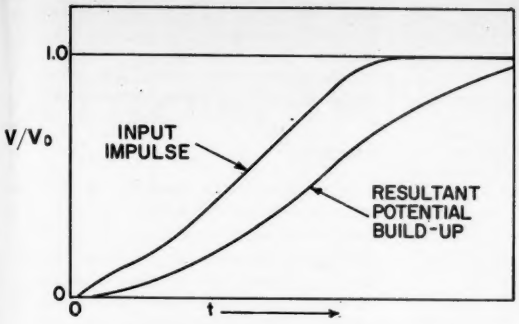

Fig. 6. Input impulse and resultant potential build-up curve.

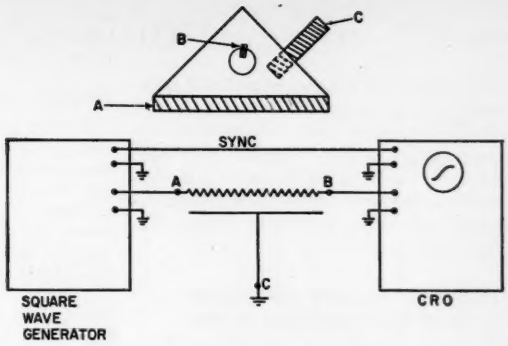

Fig. 7. Paper analogue model of insulated triangular bar and electrical circuit.

scope was then connected to the output and a second exposure was made on the same film. The result is shown in Figure 4. The grid is on a transparent plate that covers the scope. In Figure 4 each large division on the abscissa is 2.0 μsec.

The ordinate in Figure 4 is automatically normalized to unity by adjusting the input pulse height. The abscissa, however, is real time and must be converted to a dimensionless time in order to compare the model data with the analytical solution. The dimensionless time τ is given by $\tau = t/S^2RC$. In theory, R and C could be measured separately by standard measuring instruments. In practice, it was easier to calculate RC by comparing the model transient curve with the analytical solution for one model made of a given conducting paper and dielectric material. This value of RC was used to convert the real-time transient curve to a dimensionless time curve for all other models using the same conducting paper and dielectric. RC for Teledeltos paper and 0.002-in. polyethylene was 1.11×10^{-6} ohm farads/in.; for Teledeltos paper and 0.001-in. polyester (Mylar), RC was 2.20×10^{-6} ohm farads/in.; and for Timefax paper and 0.001-in. polyester, RC was 3.46×10^{-6} ohm farads/in.

Figure 5 shows the dimensionless central potential history as obtained by paper analogue models. RC was calculated for each conducting paper and dielectric combination by equating the model solution for an infinite plate at $(V - V_i)/(V_1 - V_i) = 0.50$ with the corresponding analytical solution as given by Jakob (*4*) or Schneider (*5*). The scatter of the model data points about the analytical curves is not much worse than that obtained by more complex analogue models (*5*, p. 353).

Timefax paper and 0.001-in.-thick Mylar polyester film gave models that had a potential build-up time at the center of about 10 μsec. This combination gave a transient curve that was least influenced by the oscilloscope input characteristics. On the other hand, it presented a highly capacitative load to the square wave generator with a resultant tendency to round off the corner of the input square wave. This rounding off was counteracted by shunting a resistor of from 20 to 100 ohms across the output of the square wave generator.

Teledeltos paper and 0.002-in.-thick polyethylene gave models that had potential build-up times of 1.5 to 2.5 μsec. The input characteristics of the scope, a 0.01-μsec. rise time, gave a slight distortion of the transient curve. However, this model did not significantly load the square wave generator. There seems to be little reason to believe any particular combination of paper and dielectric to be better than another.

SPECIAL APPLICATIONS OF PAPER ANALOGUE MODEL

Systems with Potential Gradient at Time Zero

The potential history of a system in which a potential is added to a potential gradient already existing at time zero is often desired. The potential history of such one-dimensional systems can be obtained from the paper analogue model if the original gradient is linear. In such cases it is necessary to add the nonsteady state solution obtained from an analogue, with no potential gradient at time zero, to the original gradient. A radial system can be treated in the same manner if the original gradient is linear with respect to the logarithm of the radius.

Systems with Zones of Different Diffusivity Constant

The paper analogue can be used to model systems in which there are regions of different diffusivity constant. For example, in a problem in fluid flow through a radial porous body in which there is a zone of reduced permeability around the central output hole, the diffusivity constant in the prototype is $k/\phi\beta\eta$, whereas in the analogue it is $1/RC$. In the zone of reduced permeability, therefore, $1/RC$ should be less than in the remainder of the analogue. The simplest way of reducing $1/RC$ in the analogue is to increase C. The analogue is therefore constructed with several thicknesses of polyethylene sheet as the dielectric over all the area except around the central output hole. In this area there is only one thickness of dielectric material. The ratio of permeability in the zone around the output hole to the permeability in the remainder of the system will be the ratio of the thickness of the dielectrics. If, for example, the prototype has a zone around the output hole one fifth as permeable as the remainder of the system, then one sheet of dielectric material is used for the area around the output and five sheets for the remainder.

Another situation that may arise is one in which the prototype has a diffusivity constant that is continuously variable with distance. The paper analogue can model such system if the continuous variation is converted to a stepwise variation. If, for example, a radial porous body has a continuously increasing permeability from the central hole to the outer edge, the paper analogue would be constructed so as to have the least thickness of dielectric material around the hole. The thickness of dielectric material would increase stepwise along a radius, thereby giving concentric rings which become thicker toward the outer boundary.

In any paper analogue models in which there is a stepwise change in thickness of the dielectric, it may be necessary to use a thin sheet of soft rubber under the metal foil in order to assure intimate contact of paper, dielectric, and foil at the step.

Calculation of Response to Any Arbitrary Input Function from the Response to an Instantaneous Pulse

If the potential build-up curve of any analogue is known for an instantaneous potential rise $A(t)$ at the input boundary, then the build-up curve $H(t)$ for the case when the potential rise is any arbitrary function of time $G(t)$ can be calculated by employing the superposition theorem given by

$$H(t) = \frac{d}{dt}\int_0^t G(t-\gamma)A(\gamma)\,d\gamma \qquad (3)$$

The integration can be carried out conveniently by numerical means for any specified value of time. Figure 6 shows an irregular input impulse and the resultant potential build-up for a model with transient response to a unit impulse typical of those responses shown in Figure 6.

EXAMPLES OF PROBLEMS THAT CAN BE SOLVED BY PAPER ANALOGUE MODELS

Several examples of engineering problems that can be solved by the paper analogue model are given below. The potential build-up curve is displayed on the oscilloscope and photographed as outlined previously.

Heat Flow

1. A long metal bar of triangular cross section with a circular hole running through the bar at the center is covered on two sides with insulating material. The surface of the center hole is also covered with insulation. The open side is placed at $t = 0$, on a hot plate of temperature T. The temperature at a point on the surface of the central hole as a function of time is desired. The initial temperature of the bar is uniform. The paper analogue and the electrical circuit are shown in Figure 7.

The RC product per unit area for the paper and dielectric material used for this analogue is calculated from a measurement on a suitable analogue whose solution is known, as described previously. The temperature build-up at B is calculated from RC and the potential transient at B.

Diffusion

A long hollow cylinder of a porous material is covered over part of its outer circumference by an impermeable layer. The cross section of this cylinder is shown in Figure 8. The cylinder is in a large vessel containing pure water. The porous material is saturated with pure water and the central hole is filled with pure water. At time $t = 0$ a salt solution is flowed through the central hole the salt concentration being kept constant in the hole. The problem is to find the salt concentration of the water in the outer vessel as a function of time. The paper analogue and the electrical circuit are shown in Figure 8. The condenser K represents the volume of the outer vessel and the capacity of K is calculated from the capacity of the analogue, the pore volume of the porous cylinder, and the volume of the outer vessel by the equation

$$\frac{\text{capacity of analogue}}{\text{capacity of } K} = \frac{\text{pore volume of porous cylinder}}{\text{volume of outer vessel}}$$

The capacity of the analogue is calculated from the RC product of an analogue of the same materials whose solution is known and from measured resistance from A to B.

The voltage build-up curve at point B is displayed on the oscilloscope. This gives V/V_∞ as a function of time at B. The salt concentration in the outer vessel at infinite time will be equal to the salt concentration of the solution flowing through the central hole. Therefore the salt concentration in the outer vessel at any time can be read directly, in fraction of the constant salt concentration in the central hole, from the potential build-up curve measured at B.

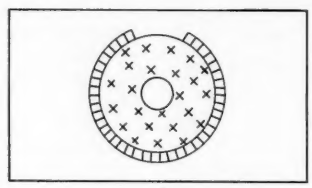

CROSS-SECTION OF RADIAL DIFFUSION SYSTEM

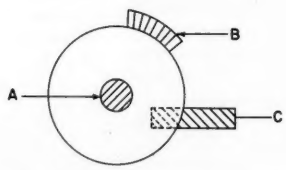

PAPER ANALOG MODEL FOR RADIAL DIFFUSION SYSTEM

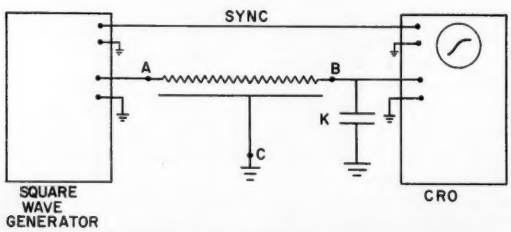

Fig. 8. Paper analogue model for radial diffusion.

SUMMARY

A simple electric analogue model has been devised for the solution of one- and two-dimensional nonsteady state flow problems. The model is composed of conducting paper, polyethylene or polyester sheeting, and metal foil. The model is pulsed by a square wave generator and the transient response is displayed on a cathode-ray oscilloscope.

Several problems are solved on the model and these solutions compared with the analytical solutions. The model gives results that do not deviate more than about 10% from the analytical solution. The method of applying the model to several nonsteady state flow problems is shown.

NOTATION

c = specific heat
C = specific capacity
D = diffusion coefficient
k = permeability
K = thermal conductivity
R = specific resistance
S = half thickness of plate or bar, or radius of cylinder
t = real time
T = temperature
U = temperature, concentration, pressure, or voltage
V = voltage
x = real distance
y = real distance

Greek Letters

α = diffusivity constant; $\alpha = K/C\rho$ for U = temperature, $\alpha = D$ for U = concentration, $\alpha = k/\phi\beta\eta$ for U = pressure, $\alpha = 1/RC$ for U = voltage
β = liquid compressibility
γ = an integrating variable
η = viscosity
ρ = density
τ = dimensionless time
ϕ = porosity

LITERATURE CITED

1. Pachkis, V., and H. D. Baker, *Trans. Amer. Soc. Mech. Engrs.*, **64**, 105 (1942).
2. Bruce, W. A., *Trans. Amer. Inst. Mining and Met. Engrs.*, **151**, 112 (1943).
3. Lawson, D. T., and J. H. McGuire, *Proc. Inst. Mech. Engrs.* (*London*) **A167**, 275 (1953).
4. Jakob, Max, "Heat Transfer," p. 266, John Wiley and Sons, New York (1949).
5. Schneider, P. J., "Conduction Heat Transfer," p. 249, Addison Wesley Publishing Co., Cambridge, Mass. (1955).

Manuscript received on July 29, 1957; revision received on November 18, 1957; paper accepted November 20, 1957.

A Graphical Method for Solution of Freezing Problems

P. A. LONGWELL

California Institute of Technology, Pasadena, California

Problems in heat conduction involving a moving boundary are encountered in the freezing of liquids and in other situations. Such problems are difficult to solve, and exact solutions are almost unknown. A graphical method for obtaining numerical solutions to problems of this type which can be described in terms of one space coordinate is derived and is demonstrated in two examples involving the freezing of liquids. The method, which does not require specialized knowledge or equipment, takes into account both sensible heats and latent heat.

The rates of solidification of liquids have been of interest to engineers for a long time, the freezing problem being encountered in the manufacture of ice, in the casting of metals, in the preparation of cast explosive loadings in ordnance plants, in the processing of frozen foods, and in other circumstances. The mathematical problem of unsteady diffusion of heat in solids has received a large amount of attention, as evidenced by extensive treatments (*2, 6*); however the special case of unsteady diffusion of heat involving a moving boundary, such as the problem of freezing, is intractable mathematically, and there is little published work to be found on this subject.

Neumann obtained a particular solution for freezing, or melting, in the semiinfinite region bounded by a plane. The solution, described by Carslaw and Jaeger (*2*) and Ingersoll et al. (*6*), neglects change of volume with freezing but takes into account differing thermal properties of the two phases. It applies for constant temperature initial and boundary conditions. Danckwerts (*4*) described solutions for a plane boundary similar to Neumann's but taking into account changes in volume. Lightfoot (*10*) treated solidification in the linear case by using the concept of moving sources. He assumed the thermal properties of the solid and of the liquid to be the same. Allen and Severn (*1*) used relaxation methods for numerical solution of the freezing problem in a semiinfinite medium with a plane boundary. Crank (*3*) recently gave methods for numerical solution of moving-boundary problems where the boundary is a plane. Pekeris and Slichter (*13*) described an approximate solution for ice formation on the outside of a cylinder when the liquid is initially at the freezing point. London and Seban (*11*) gave approximate solutions to the freezing problem for the slab, cylinder, and sphere. These solutions neglect the specific heats of the two phases, and in a later paper Seban and London (*16*) experimentally verified these solutions under conditions in which the neglect of specific heats was not serious. Fujita (*5*) described approximate analytic solutions for diffusion with a moving boundary for a semiinfinite medium and for the infinite cylinder for specific boundary conditions involving diffusion on only one side of the boundary. In the latter case the solution is apparently quite laborious. Keller and Ballard (*9*) treated the freezing of orange juice in cylindrical shape by using an effective thermometric conductivity which included the latent heat of fusion. They considered this treatment appropriate for orange juice since the juice does not have a definite freezing point.

EQUATIONS DESCRIBING FREEZING

Application of the principles of conservation of energy and of conservation of matter to a continuous phase having constant thermal conductivity and being held at constant pressure yields the following relationship, if kinetic and potential energies are neglected and if there are no distributed sources of energy:

$$K\nabla^2 t - u\cdot\nabla t = \frac{\partial t}{\partial \theta} \qquad (1)$$

Equation (1) includes the transport of energy by motion of the fluid.

If it is assumed that there is a definite interface between the solid and liquid phases and that the latent heat of fusion is liberated, or absorbed, at this interface, consideration of energy transfer at the interface leads to the equation

$$k_1(\nabla t_1)_i - k_2(\nabla t_2)_i = L\sigma_1 U \qquad (2)$$

If the phase change occurs at a definite temperature, the temperatures of both phases at the interface are described by

$$(t_1)_i = (t_2)_i = t_f \qquad (3)$$

If there is a change in volume accompanying the phase change, there is a hydrodynamic velocity of the liquid at the interface given by the equation

$$(u_2)_i = \left(1 - \frac{\sigma_1}{\sigma_2}\right)U \qquad (4)$$

A coordinate system fixed with respect to the solid phase is assumed.

If the specific weight of the liquid phase is assumed constant, the equation of continuity for the liquid phase reduces to the equation

$$\nabla\cdot u_2 = 0 \qquad (5)$$

The initial temperature distribution in each phase, the initial location of the interface, and the boundary conditions imposed must also be known in order to define the situation completely.

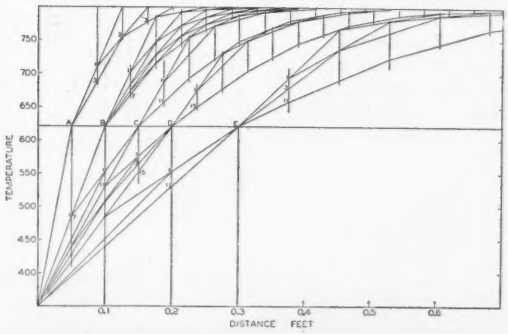

Fig. 1. Graphical construction for example 1.

DERIVATIONS FOR GRAPHICAL SOLUTION

The hydrodynamic velocity shown in Equation (1) and determined by Equations (4) and (5), and perhaps by certain boundary conditions, serves to complicate a problem which is already difficult. It is probably permissible, however, in the absence of forced convection to neglect hydrodynamic velocities, and they are so neglected in this paper. The magnitude of the error caused by this neglect can of course be estimated after solution of the simplified problem has been obtained.

With the neglect of hydrodynamic velocity, differential Equations (1) through (3) can be solved by graphical means when only one coordinate is involved. These graphical means are extensions of the method described by Schmidt (*14, 15*) for the investigation of transient linear heat conduction in solids. The case of linear flow of heat is considered first. Equation (1) becomes for the solid and liquid phases respectively,

$$\frac{\partial t_1}{\partial \theta} = \mathrm{K}_1 \frac{\partial^2 t_1}{\partial x^2} \quad 0 \leq x \leq X \qquad (6)$$

and

$$\frac{\partial t_2}{\partial \theta} = \mathrm{K}_2 \frac{\partial^2 t_2}{\partial x^2} \quad X \leq x \qquad (7)$$

Equation (2) for the linear case becomes

$$k_1\left(\frac{\partial t_1}{\partial x}\right)_i - k_2\left(\frac{\partial t_2}{\partial x}\right)_i = L\sigma_1 \frac{dX}{d\theta} \qquad (8)$$

When the boundaries are stationary, Equations (6) and (7) are easily solved by the conventional Schmidt graphical construction. This construction requires that the intervals in time and distance be related by the equation

$$(\Delta x)^2 = 2\mathrm{K}\Delta\theta \qquad (9)$$

and since the two phases have different thermometric conductivities, for equal time intervals the distance intervals for the two phases must be related by

$$\frac{\Delta x_1}{\Delta x_2} = \sqrt{\frac{\mathrm{K}_1}{\mathrm{K}_2}} \qquad (10)$$

However, one boundary for each of Equations (6) and (7) moves at a velocity determined by Equation (8). For this reason the solution to Equations (6), (7), and (8) is approximated by solving Equations (6) and (7) for a series of fixed boundaries which are changed at intervals controlled by Equation (8). Equation (8) may be written in finite-difference form as

$$k_1\left(\frac{\Delta t_1}{\Delta x_1}\right)_{i\ avg} - k_2\left(\frac{\Delta t_2}{\Delta x_2}\right)_{i\ avg} = L\sigma_1 \frac{\Delta X}{N\Delta\theta} \qquad (11)$$

in which $N\Delta\theta$ is the time necessary for the interface to move a distance ΔX. If the operation of averaging is included in Equation (11), it becomes

$$\sum_1^N \left[k_1\left(\frac{\Delta t_1}{\Delta x_1}\right)_i - k_2\left(\frac{\Delta t_2}{\Delta x_2}\right)_i\right] = L\sigma_1 \frac{\Delta X}{\Delta\theta} \qquad (12)$$

and since the increment in the interface position ΔX is taken equal to Δx_1, rearrangement of Equation (12) and use of Equations (9) and (10) lead to the relationship

$$\sum_1^N \left[\Delta t_1 - \frac{k_2}{k_1}\sqrt{\frac{\mathrm{K}_1}{\mathrm{K}_2}}\,\Delta t_2\right] = \frac{2L}{C_{p1}} \qquad (13)$$

which is the governing equation at the interface. The temperature increments in Equation (13) are measured over the interval next to the interface.

The time for the interface to move a distance ΔX is determined by moving the interface by a distance Δx_1 and then performing Schmidt constructions in each phase. The summation of the left side of Equation (13) is calculated after each time interval $\Delta\theta$, and N is determined by satisfaction of the equality.

Example 1 Linear Flow of Heat with Change of Phase

Since Neumann's solution (*2, 6*) is an exact solution if the hydrodynamic velocity is ignored, a graphical solution was made of a problem for which Neumann's solution applied, and the results of the two methods were compared. Furthermore, the situation chosen is one in which the sensible heats of each phase are of the same order as the latent heat of fusion, since approximations neglecting either sensible heats or latent heat should be least applicable in this case. The problem selected may be stated as follows:

A large volume of molten lead is initially at a uniform temperature of 800°F. A plane at $x = 0$ is suddenly cooled to 350°F. and held at this temperature. Determine the position of the liquid-solid interface as a function of time and determine the temperature distribution at a selected time.

The situation is described mathematically by Equations (6), (7), and (8) and the initial and boundary conditions:

$$t = 800°F. \quad \text{at} \quad 0 \leq x \leq \infty \quad \text{for} \quad \theta < 0 \qquad (14)$$

$$t = 350°F. \quad \text{at} \quad x = 0 \quad \text{for} \quad \theta > 0 \qquad (15)$$

and

$$t_1 = t_2 = 621°\mathrm{F}. \quad \text{at} \quad x = X \qquad (16)$$

The physical data used were obtained from the International Critical Tables (*7*) and temperature dependence of the properties was neglected. It was found that, of the total energy liberated in cooling lead from 800° to 350°F., approximately 23.7% is released in cooling the liquid to the freezing temperature of 621°F., 40.2% is released during freezing, and 36.1% is released in cooling the solid from 621° to 350°F.

Substituting numerical data in Equation (13) yields the following equation:

$$\sum_1^N (\Delta t_1 - 0.696\Delta t_2) = 601 \qquad (17)$$

To start a graphical solution Δx_1 was taken as 0.05 ft. By use of Equation (10) Δx_2 was found to be 0.038 ft. and Equation (9) gave $\Delta\theta$ as 5.69 sec. The construction is shown in Figure 1, and point A represents the position of the interface for the first calculation. Δt_1 was constant for this calculation at 271°F. and Δt_2 was determined by the graphical construction. Since temperature is determined graphically at the first interval from the interface only at odd values of N, the value of temperature to be used for even values of N must be arbitrarily decided. It is considered that use of the same temperature as determined for the previous odd value of N is appropriate here and that a better estimate of the average temperature gradient at the interface is obtained in this way than would be obtained by interpolation. Accordingly, for use in Equation (17) the temperatures at odd N were determined by the construction of Figure 1 and those at even N were taken as the same as at the preceding odd N. The numbers at points in Figure 1 correspond to N, and, in the case of point A, solution of Equation (17) gave $N = 2.83$, as shown in Table 1, which lists the solutions of Equation (17) for all intervals.

The position of the interface was then moved to point B of Figure 1 and graphical construction made as is shown in detail. The construction for subsequent positions of the interface is shown only in part because the lines came close together and would cause confusion in the small-scale reproduction. Constructions with the same increments in x were made for increments A through D, with the results shown in Table 1. Because the values of N necessary to solve Equation (17) were becoming large, the increment in x was doubled for point E, with the consequent quadrupling of the time interval $\Delta\theta$.

The detailed calculations for the solution at point C are shown in Table 2 to illustrate

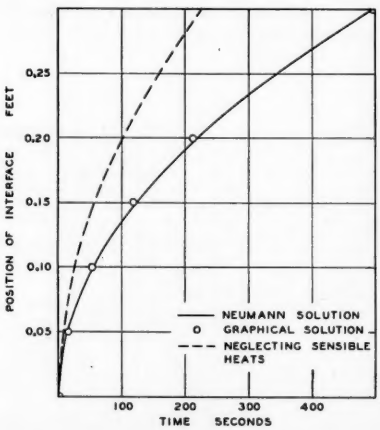

Fig. 2. Position of liquid-solid interface, example 1.

the method of determination of the values of N shown in Table 1.

The graphically determined position of the interface is shown in Figure 2 as a function of time, and the result of the analytical solution devised by Neumann (*2*) is also shown there. The agreement of the graphical solution with the analytical solution is good even though rather large intervals ΔX were used on the graphical solution. The dashed line represents the position of the interface calculated by neglecting the specific heats of the two phases (*11*). As would be expected for the chosen situation, large errors are introduced by neglect of the specific heats.

The distributions of temperature as determined by the graphical and by Neumann's analytical method were compared in Figure 3 for a time of 212 sec. after initiation of freezing. The graphical temperature distribution shown in Figure 3 was estimated by making arithmetic averages of the temperatures shown during the construction for point D of Figure 1, which corresponds to an elapsed time of 212 sec. The agreement of the temperatures determined by graphical means with those determined by Neumann's solution is close, in spite of the use in the graphical method of what appear to be rather crude approximations. The fact that the temperature gradients in the two phases at the interface appear to be the same in Figure 3 is fortuitous.

GRAPHICAL SOLUTION IN CYLINDRICAL SYMMETRY

In many applications involving freezing the geometry is such that the use of cylindrical coordinates is appropriate. If the phenomena considered are independent of angle and position along the axis, and if the hydrodynamic velocity is neglected, Equation (1) becomes the equations

$$K_1 \frac{1}{r}\frac{\partial}{\partial r}\left(r\frac{\partial t_1}{\partial r}\right) = \frac{\partial t_1}{\partial \theta} \qquad (18)$$

$$r_0 \geq r \geq R$$

and

$$K_2 \frac{1}{r}\frac{\partial}{\partial r}\left(r\frac{\partial t_2}{\partial r}\right) = \frac{\partial t_2}{\partial \theta} \quad r \leq R \qquad (19)$$

and Equation (2) may be expressed as

$$k_1\left(\frac{\partial t_1}{\partial r}\right)_i - k_2\left(\frac{\partial t_2}{\partial r}\right)_i = L\sigma_1 \frac{dR}{d\theta} \qquad (20)$$

Solution of Equations (18), (19), and (20) is possible if sufficient initial and boundary conditions are known.

Equations in cylindrical coordinates of the type shown in Equations (18) and (19) are conventionally (*8, 15*) solved for situations where the boundaries are fixed by a Schmidt-type graphical construction in which the radius is divided into equal increments Δr which satisfy the relationship

$$(\Delta r)^2 = 2K\Delta\theta \qquad (21)$$

The graphical construction is performed on a plot having ln r as the abscissa, with the intervals in ln r selected to correspond with radii satisfying Equation (21), This approximation is satisfactory for cylindrical shells and is used here. A modification of this method is used for the solid phase near the center of the cylinder.

For definiteness the outside phase is taken as solid. This assumption corresponds to the case of the freezing of a cylinder having an external radius r_0. A change of variable is made in accordance with the relationship

$$w = -\ln\left(\frac{r}{r_0}\right) \qquad (22)$$

Equations (18) and (19) may be solved for a series of fixed boundaries by graphical construction by use of w as defined in Equation (22) as the abscissa, and with the increments in w selected by use of

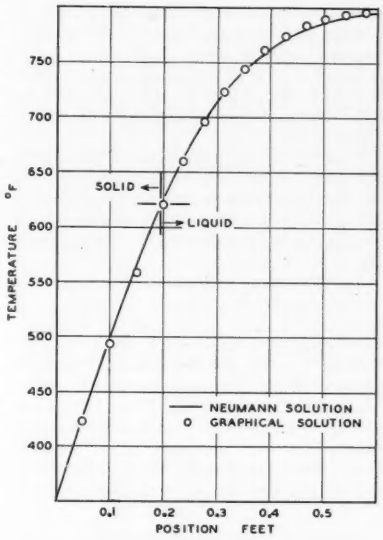

Fig. 3. Temperature distribution at 212 sec., example 1.

Equation (21). The time interval $\Delta\theta$ must be the same in both phases.

Use of Equation (22) in Equation (20) gives the equation

$$k_1\left(\frac{\partial t_1}{\partial w}\right)_i - k_2\left(\frac{\partial t_2}{\partial w}\right)_i = L\sigma_1 R^2 \frac{dW}{d\theta} \qquad (23)$$

when

$$W = -\ln\left(\frac{R}{r_0}\right) \qquad (24)$$

Equation (23) is written in finite difference form as

$$\sum_1^N \left[k_1\left(\frac{\Delta t_1}{\Delta w_1}\right)_i - k_2\left(\frac{\Delta t_2}{\Delta w_2}\right)_i\right] = L\sigma_1 R^2_{avg}\frac{\Delta W}{\Delta\theta} \qquad (25)$$

If the logarithmic mean radius (*12*) is used, the following equation applies:

$$R_{avg} = -\frac{\Delta R}{\Delta W} \qquad (26)$$

and substitution of Equation (26) in Equation (25) gives

$$\sum_1^N \left[k_1\left(\frac{\Delta t_1}{\Delta w_1}\right)_i - k_2\left(\frac{\Delta t_2}{\Delta w_2}\right)_i\right] = \frac{L\sigma_1(\Delta R)^2}{(\Delta W)(\Delta\theta)} \qquad (27)$$

as the equation to be satisfied at the interface between liquid and solid. Use of Equation (27) is similar to the use of Equation (13) for the linear case.

Example 2 Freezing in a Cylindrical System

The situation taken as an example of freezing in geometry having cylindrical symmetry is as follows.

Molten lead at an initially uniform temperature of 800°F. is contained in a cylindrical steel mold having an internal diameter of 4.0 in. and a wall thickness of ⅛ in. The mold is cooled externally by a fluid having a bulk temperature of 300°F. The heat transfer coefficient from this fluid to the mold may be taken as 300 B.t.u./(hr.)(sq. ft.)(°F.). Determine the position of the liquid-solid interface as a function of time after initiation of cooling and also determine the temperature distribution when the lead is almost totally frozen.

It was assumed that the height of the mold was large compared with the diameter, and so end effects could be neglected; hydrodynamic velocity was neglected also. The situation then is expressed mathematically by Equations (18), (19), and (20) and the initial conditions

$$t_2 = 800°\text{F.} \quad \text{at} \quad r_0 \geq r \geq 0 \quad \text{for} \quad \theta < 0 \qquad (28)$$

and

$$R = r_0 \quad \text{for} \quad \theta \leq 0 \qquad (29)$$

and the boundary conditions

$$\frac{\partial t}{\partial r} = 0 \quad \text{at} \quad r = 0 \qquad (30)$$

$$t_1 = t_2 = 621°\text{F.} \quad \text{for} \quad r = R \qquad (31)$$

and

$$\left(\frac{\partial t_1}{\partial r}\right)_{r=r_0} = \frac{t_s - t_0}{k_1\left[\frac{r_0}{hr_e} + \frac{r_0}{k_m}\ln\left(\frac{r_e}{r_0}\right)\right]} \qquad (32)$$

Equation (32) was derived by consideration of the external heat transfer. The specific heat of the steel mold was neglected, and the thermal flux from the lead was

equated to that passing through the steel mold and into the coolant fluid. Use of Equation (22) in Equation (32) gives the equation

$$\left(\frac{\partial t_1}{\partial w}\right)_{w=0} = \frac{t_0 - t_s}{k_1\left[\frac{1}{hr_e} + \frac{1}{k_m}\ln\left(\frac{r_e}{r_0}\right)\right]} \quad (33)$$

A time interval $\Delta\theta$ was selected in accordance with the relationship

$$\Delta\theta = \frac{r_0^2}{128K_1} \quad (34)$$

which corresponds to the time interval calculated from Equation (21) for eight equal divisions of radius in a solid cylinder. A time interval $\Delta\theta$ of 0.9864 sec. was calculated by use of Equation (34). Because the thermometric conductivities of the two phases are not equal, the radial intervals in the liquid phase must be recalculated for each new position of the liquid-solid interface by use of the formula

$$\Delta r_2 = \sqrt{\frac{K_2}{K_1}}\frac{r_0}{8} \quad (35)$$

The intervals Δw for the solid phase were calculated to correspond to intervals in the radius of one-eighth the internal radius of the mold.

The graphical construction is illustrated in Figure 4. Vertical lines at the values of w calculated for the solid phase are drawn in Figure 4 for temperatures less than the fusion temperature of 621°F. Vertical lines for temperatures greater than 621°F. are drawn as calculated by use of Equation (35) for the first four positions of the interface. Substitution of numerical data in Equation (33) gives as a boundary condition the equation

$$\left(\frac{\partial t}{\partial w}\right)_{w=0} = \frac{t_0 - 300}{0.3853} \quad (36)$$

This condition is satisfied by construction from a point located at 300°F. and a w of −0.3853, as shown in Figure 4.

Equation (27) may be rearranged to the form

$$C_1 + C_2\sum_1^N \Delta t_2 - \sum_1^N \Delta t_1 = 0 \quad (37)$$

The temperature increments used in Equation (37) are those for the increment in w closest to W, the interface position. The values of C_1 and C_2 in Equation (37) are shown in Table 3 for each step.

The graphical construction used in Figure 4 to solve Equation (37) is similar to that used for the linear semiinfinite case of Example 1 as shown in Figure 1. Only a portion of the construction lines is shown for each position of the interface in order to avoid confusion. The points from which values of Δt_1 and Δt_2 were read in Figure 4 are numbered to correspond to N in Equation (37), and values of Δt for even N were taken as the same as for the preceding odd N. The graphical construction for the liquid phase was done for the first four steps. Since the temperature of the liquid phase was quite close to the fusion temperature at the end of the fourth step, the sensible heat of the liquid was neglected for subsequent steps.

The construction was extended for one step beyond a radius ratio of 0.125 by methods which have not been published. It is possible to show that graphical solutions of the diffusion equation for solid cylinders are considerably improved in accuracy by taking the smaller radius of the innermost interval as equal to about 10 to 12% of the normal increment Δr rather than as zero. In the present case the innermost position was taken at a value of r/r_0 of 0.0133, corresponding to a w of 4.323. This position is not shown on Figure 4.

The values of N obtained and the times at which the interface was estimated to reach the indicated positions are shown in Table 3.

Figure 5 shows the position of the liquid-solid interface determined by this graphical solution as a function of time. The position calculated when the sensible heats of the two phases were neglected is also shown in Figure 5.

Temperature distributions for two positions of the liquid-solid interface are shown in Figure 6. The graphical temperatures were estimated by taking an arithmetic mean of the temperature indicated for each value of N without any interpolation between construction points. The dotted lines of Figure 6 show the logarithmic distribution which was obtained when sensible heats were neglected. The logarithmic distribution becomes a poor approximation to the temperature distribution in the solid phase as the liquid-solid interface approaches the center of the cylinder. The neglect of the sensible heat of the liquid phase implies that the liquid phase is always at the fusion temperature.

GRAPHICAL SOLUTION IN SPHERICAL SYMMETRY

Situations where the initial and boundary conditions possess spherical symmetry can be treated in spherical coordinates. If hydrodynamic velocities are neglected and temperature is a function only of the radial coordinate and time, Equation (1) has the form

$$\frac{\partial t}{\partial \theta} = \frac{K}{r^2}\frac{\partial}{\partial r}\left(r^2\frac{\partial t}{\partial r}\right) \quad (38)$$

and Equation (2) becomes

$$k_1\left(\frac{\partial t_1}{\partial r}\right)_i - k_2\left(\frac{\partial t_2}{\partial r}\right)_i = L\sigma_1\frac{dR}{d\theta} \quad (39)$$

Substitution of the variable w, defined by the equation

$$w = \frac{r_0}{r} \quad (40)$$

is made, and Equation (39) becomes

$$k_1\left(\frac{\partial t_1}{\partial w}\right)_i - k_2\left(\frac{\partial t_2}{\partial w}\right)_i = \frac{L\sigma_1 R^4}{r_0^2}\frac{dW}{d\theta} = \frac{L\sigma_1 r_0^2}{W^4}\frac{dW}{d\theta} \quad (41)$$

Equations of the type of Equation (38) are conventionally solved for stationary boundaries by a Schmidt-type construction, with the variable w as abscissa and with the increments corresponding to equal increments in radius (*8*, *15*). The graphical method can be extended to a series of fixed boundaries in the spherical case, as was done above for the cylindrical case. Equation (41), when expressed in finite difference form, becomes

$$\sum_1^N\left[k_1\left(\frac{\Delta t_1}{\Delta w_1}\right)_i - k_2\left(\frac{\Delta t_2}{\Delta w_2}\right)_i\right]$$

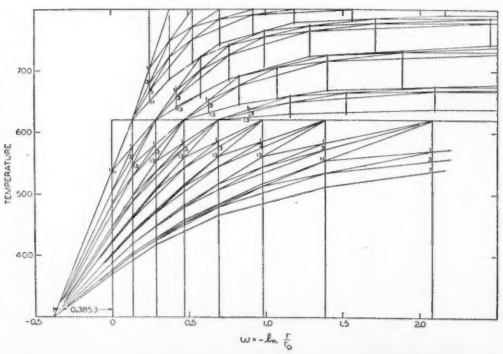

Fig. 4. Graphical construction for example 2.

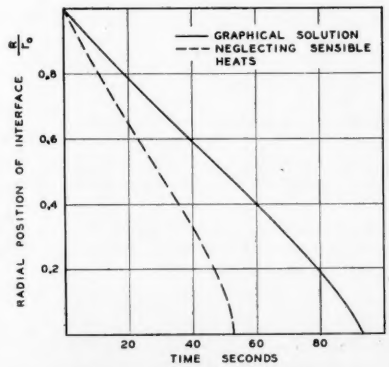

Fig. 5. Position of liquid-solid interface, example 2.

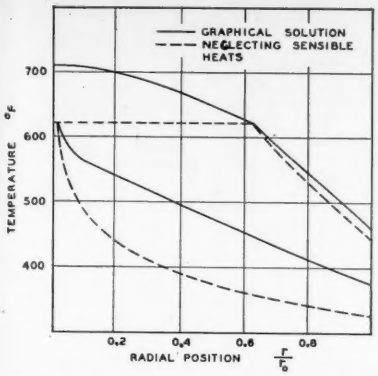

Fig. 6. Temperature distributions for two positions of interface, example 2.

TABLE 1. SOLUTIONS OF EQUATION (17) DETERMINED BY FIGURE 1

Interface position	X', ft.	Solution N	$\Delta\theta$, sec.	Time interval, sec.	Total elapsed time, sec.
A	0.05	2.82	5.69	16.0	16.0
B	0.10	6.63	5.69	37.7	53.7
C	0.15	11.47	5.69	65.3	119.0
D	0.20	16.35	5.69	93.0	212.0
E	0.30	12.46	22.76	283.6	495.6

TABLE 2. DETAILED SOLUTION OF EQUATION (17) FOR POINT C OF FIGURE 1

N	Δt_1, °F.	Δt_2, °F.	$0.696\Delta t_2$, °F.	Residual,* °F.
1	68	67	47	580
2	68	67	47	559
3	86	54	38	511
4	86	54	38	463
5	90	47	33	406
6	90	47	33	349
7	91	42	29	287
8	91	42	29	225
9	91	39	27	161
10	91	39	27	97
11	91	36	25	31
12	91	36	25	−35

Solution: $N = 11.47$

$$\text{Time increment} = 11.47 \times 5.69 = 65.3 \text{ sec.}$$

*Residual $= 601 + 0.696 \sum_1^N \Delta t_2 - \sum_1^N \Delta t_1$.

TABLE 3. CONSTANTS FOR AND SOLUTIONS OF EQUATION (37)

Step	$\frac{R}{r_0}$	Constants C_1	Constants C_2	Solution N	Total elapsed time, sec.
1	0.875	601	0.613	11.53	11.37
2	0.750	601	0.598	12.62	23.79
3	0.625	601	0.589	13.21	36.81
4	0.500	601	0.563	12.75	49.36
5	0.375	601	—	13.29	62.46
6	0.250	601	—	12.15	74.44
7	0.125	601	—	11.21	85.49
8	0.0133	480	—	7.16	92.55

$$= \frac{L\sigma_1 R_{avg}^4 \Delta W}{r_0^2 \Delta\theta}$$

$$= \frac{L\sigma_1 r_0^2 \Delta W}{\Delta\theta W_A^2 W_B^2} \qquad (42)$$

The geometric mean radius (*12*) is employed in Equation (42) since the geometry is spherical. Equation (42) is applied in the graphical solution for spherical symmetry in the manner that Equations (13) and (27) are used for linear and cylindrical cases respectively,

DISCUSSION

A procedure suitable for solution of moving-boundary problems such as are encountered with phase changes has been described and demonstrated. The method, which is graphical, does not require specialized equipment or difficult calculations and the time requirement is not large considering the relative complexity of the problem.

The derivations and the two examples chosen are for the freezing of a liquid; however the method of solution demonstrated should be suitable for other situations where the diffusion equation applies on each side of a moving boundary and the dependent variable has a constant value at the moving boundary.

While no mathematical proof is offered that a solution obtained by this method is indeed a good approximation to the exact solution, it is known that the Schmidt method of solution for fixed boundary problems is stable and does approach the exact solution as the size of the increments is reduced. It therefore appears that the graphical method demonstrated here should behave similarly, and certainly the results found in Example 1 agree very well with the exact solution even though the grid used was rather coarse.

NOTATION

C_1, C_2 = constants in Equation (37)
C_p = specific heat at constant pressure, B.t.u./(lb.)(°F.)
d = differential operator
h = heat transfer coefficient, B.t.u./(sq. ft.)(sec.)(°F.)
k = thermal conductivity, B.t.u./(ft.)(sec.)(°F.)
k_m = thermal conductivity of mold, B.t.u./(ft.)(sec.)(°F.)
L = latent heat of fusion, B.t.u./lb.
ln = natural logarithm
N = number of intervals
R = radius of liquid-solid interface, ft.
r = radius, ft.
r_0 = internal radius of mold, ft.
r_e = external radius of mold, ft.
t = temperature, °F.
t_f = fusion temperature, °F.
t_0 = temperature at internal surface of mold, °F.
t_a = bulk temperature of cooling medium, Example 2, °F.
U = vector velocity of liquid-solid interface, ft./sec.
u = vector hydrodynamic velocity, ft./sec.
W = value of w at liquid-solid interface, dimensionless
w = transformation variable, dimensionless
X = value of x at liquid-solid interface, ft.
x = Cartesian coordinate, ft.
Δ = increment in
θ = time, sec.
K = thermometric conductivity, sq. ft./sec.
$\sum$ = summation
σ = specific weight, lb./cu. ft.
∂ = partial differential operator
∇ = operator del of vector analysis
∇^2 = Laplacian operator of vector analysis
$\cdot$ = scalar product operator of vector analysis

Subscripts

1 = solid phase
2 = liquid phase
A, B = two sides of interval
avg = average
i = liquid-solid interface

LITERATURE CITED

1. Allen, D. N. De G., and R. T. Severn, *Quart. J. Mech. and App. Math.*, **5**, 447 (1952).
2. Carslaw, H. S., and J. C. Jaeger, "Conduction of Heat in Solids," Clarendon Press, Oxford (1947).
3. Crank, J., *Quart. J. Mech. and App. Math.*, **10**, 220 (1957).
4. Danckwerts, P. V., *Trans. Faraday Soc.*, **46**, 701 (1950).
5. Fujita, Hiroshi, *J. Chem. Phys.*, **21**, 700 (1953).
6. Ingersoll, L. R., Otto J. Zobel, and A. C. Ingersoll, "Heat Conduction," McGraw-Hill Book Company, Inc., New York (1948).
7. International Critical Tables, vols. 1 and 5, McGraw-Hill Book Company, Inc., New York (1926, 1929).
8. Jakob, Max, "Heat Transfer," vol. 1, John Wiley and Sons, Inc., New York (1949).
9. Keller, G. J., and J. H. Ballard, *Ind. Eng. Chem.*, **48**, 188 (1956).
10. Lightfoot, N. M. H., *Proc. London Math. Soc.* (2), **31**, 97 (1929).
11. London, A. L., and R. A. Seban, *Trans. Am. Soc. Mech. Engrs.*, **65**, 771 (1943).
12. McAdams, W. H., "Heat Transmission," 3 ed., McGraw-Hill Book Company, Inc., New York (1954).
13. Pekeris, C. L., and L. B. Slichter, *J. Appl. Phys.*, **10**, 135 (1939).
14. Schmidt, Ernst, "Festschrift zum Siebzigsten Geburtstag August Foeppls," p. 179, Julius Springer, Berlin (1924).
15. Schmidt, Ernst, *Forsch. Gebiete Ingenieurw.*, **13**, 177 (1942).
16. Seban, R. A., and A. L. London, *Trans. Am. Soc. Mech. Engrs.*, **67**, 39 (1945).

Manuscript submitted March 5, 1957; paper accepted July 3, 1957.

Film Boiling from Vertical Tubes

Y. Y. HSU and J. W. WESTWATER

University of Illinois, Urbana, Illinois

Heat transfer measurements were made with vertical stainless steel bayonet tubes, 3/8 to 3/4 in. O.D., with lengths from 2.6 to 6.5 in. The heat source was steam. The boiling film ΔT ranged from 154° to 314°F. for three organic liquids and from 547° to 788°F. for nitrogen, all at 1 atm. No forced convection was used. Benzene, carbon tetrachloride, and nitrogen on the longer tubes had h values two or three times greater than predicted by the Bromley equation; however, the Reynolds numbers were found to exceed 2,000. Nitrogen on the 2.6-in. length obeyed the equation; the Reynolds numbers were less than 2,000. Methanol is an anomaly; although the Reynolds numbers were less than 2,000, the flow was proved by photography to be turbulent and the h values were much higher than predicted for viscous flow. A correlation is given which fits all the data except for methanol. It shows that a vertical orientation is superior to the horizontal for liquids boiling outside tubes.

Film boiling is typified by the existence of a vapor film coating the heat transfer surface. The film hinders heat transfer, and the resulting heat flux is usually small compared with the values observed during nucleate boiling. With most industrial processes for vaporizing liquids, film boiling is avoided. However, when large temperature differences are encountered, such as when an ordinary liquid contacts a very hot solid or when steam is used to heat liquids with low boiling points, film boiling may occur.

The object of this investigation was to study film boiling outside vertical tubes. As no prior data for film boiling from vertical surfaces in the absence of forced flow are available, it was desirable to obtain experimental data and to make a comparison with the theoretical equation of Bromley.

THEORETICAL EQUATION OF BROMLEY

Film boiling has received much less attention than nucleate boiling; yet the film-type phenomenon appears to be more susceptible to attack from the theoretical viewpoint. The analogy between film boiling and film condensation was apparent to many of the early writers on boiling, but Bromley (*2*) in 1950 was the first to present a formal derivation of an equation for film boiling. The derivation is similar to Nusselt's derivation (*9*) for film condensation, with the substitution of a vapor film for a liquid film. Fos a horizontal tube the equation for film boiling is

$$h = C_1\left[\frac{k^3\rho_v(\rho_L - \rho_v)g\lambda'}{\mu D\Delta T}\right]^{1/4} \qquad (1)$$

The physical properties k, ρ_v, and μ are taken at the mean temperature of the vapos film, $\frac{1}{2}(T_S + T_L)$. The symbol λ' represents the latent heat of vaporization plus the sensible heat of the vapor. Originally this was taken as $\lambda' = \lambda + \frac{1}{2}C_p\ \Delta T$. Later it was shown that a better fit with data occurs if one uses $\lambda' = (\lambda + 0.4C_p\ \Delta T)^2/\lambda$, and the theoretical reason for this was given (*4*). Recently it was shown (*11*) that a more accurate expression for λ' employs 0.34 instead of 0.4. The disagreement here is minor, and 0.4 was used in the present work.

Two values for the coefficient C_1 may be derived. If the liquid is imagined to be stationary, C_1 is 0.512; if the liquid moves with the same velocity as the vapor, C_1 is 0.724. The mean of these values, 0.62, gives the best fit to Bromley's data and is the value he recommends.

Bromley made runs at atmospheric pressure with seven liquids, using horizontal tubes with diameters between $\frac{3}{16}$ and $\frac{1}{2}$ in. His values agreed within about 10% of the predictions of Equation (1) (with $C_1 = 0.62$.) There is no question as to the applicability of this equation to horizontal tubes of intermediate diameter; however, the equation must not be used blindly when the diameter is very small or very large. For very small diameters, the film thickness and the cylinder diameter are comparable, and therefore the data for hot wires, such as given by Nukiyama (*8*), McAdams and coworkers (*6*), and others show greater heat fluxes than predicted. For very large diameters Equation (1) predicts vanishingly small values of h. Banchero and coworkers (*1*) propose a modified form of Equation (1) which was selected empirically so as to give realistic values of h for values of D near $\frac{3}{4}$ in.

For vertical tubes or vertical plates, the theoretical expression for film boiling (*2*) is given by Equation (2):

$$h = C_2\left[\frac{k^3\rho_v(\rho_L - \rho_v)g\lambda'}{\mu L\Delta T}\right]^{1/4} \qquad (2)$$

Although the value of C_2 was not stated by Bromley, it can be easily derived. If the liquid is stagnant, C_2 has a theoretical value of 0.667; if the liquid moves with

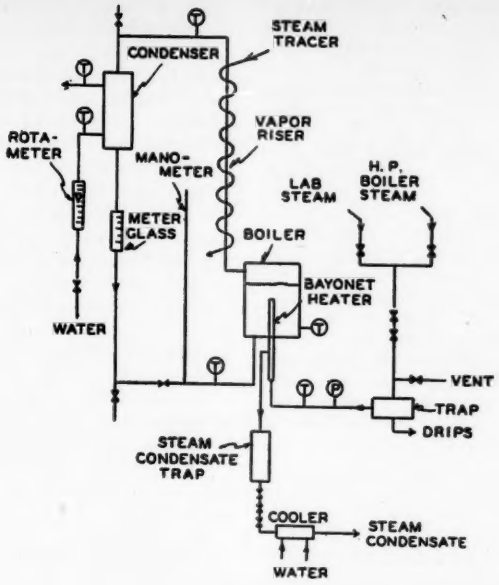

Fig. 1. Sketch of boiling equipment.

the same velocity as the vapor, C_2 is 0.943. No prior data have been published to show whether Equation (2) is valid.

A number of assumptions are necessary in the derivation of Equation (2). Most of these seem reasonable, for example: (*a*) a continuous film of vapor separates the liquid from the solid heat source; (*b*) the vapor motion upward is caused by buoyancy and is opposed by drag at the solid surface and perhaps by additional drag at the liquid; (*c*) kinetic energy of the vapor is not important; (*d*) the liquid is at its boiling point throughout; (*e*) the solid surface is at a uniform temperature; (*f*) radiation heat transfer is negligible or will be accounted for by means of a radiation term, such as shown by Bromley (*2*); (*g*) forced convection in the liquid is negligible or will be handled by means of a correlation like that shown by Bromley and coworkers (*4*); (*h*) the vapor flow is viscous. This last assumption, however, seems questionable for a vertical surface. The length of the flow path for the vapor film is much greater for a vertical tube than for a horizontal one. The largest tube used by Bromley had a diameter of ½-in.; thus the flow path, half the circumference, was 0.8 in. For Banchero et al. the greatest flow path was 1.2 in. For vertical tubes, however, the flow path is the tube length, which is usually much greater than 1.2 in. A long flow path results in a thick film. A thick film could be unstable, turbulence could develop, and Equation (2) could fail.

TEST LIQUIDS

The present tests were conducted with methanol, benzene, carbon tetrachloride, and nitrogen, each boiling at atmospheric pressure, the range in boiling points being from −321° to +176°F. Steam, the source of heat, was available as hot as 475°F. The temperature drop across the vapor film of the test liquids was varied from 154° to 788°F. The choice of liquids offered a wide range in physical properties: latent heat of vaporization from 86 to 474 B.t.u./lb., vapor-heat capacity from 0.09 to 0.46 B.t.u./(lb.)(°F.), vapor density from 0.06 to 0.31 lb./(cu. ft.), liquid density from 49 to 99 lb./(cu. ft.), and vapor thermal conductivity from 0.005 to 0.016 B.t.u./(hr.)(ft./°F.).

Great care was taken to exclude impurities from the test liquids. The organic liquids were reagent grade and before each run were purified by distillation in a column with reflux. When stored, the organic liquids were kept in glass containers with glass stoppers. The stored liquids were in contact with silica gel so as to keep them free from water. The liquid nitrogen was obtained directly from the university liquid-air–fractionation plant, the purity varying from 95 to 99+% nitrogen, with the remainder being oxygen.

VERTICAL HEATING TUBE

The experimental apparatus is illustrated in Figure 1. Each test liquid was boiled outside a single vertical tube, with no forced convection. The effective tube length was 2.60, 4.38, 4.63, 5.0, 5.38, and 6.5 in. Three outside diameters were used, ⅜, ½, and ¾ in. Each tube was made of copper or 18-gauge stainless steel and had at the top a flat plug sealed in place with silver solder. As the tip area did not exceed 5% of the side area for any test, for convenience the tip area was omitted from the heat-flux calculations. Each heater tube was actually the outside tube of a bayonet heater. Steam flowed upward in a ¼- or a $\frac{5}{16}$-in. O.D. inner tube and then downward in the annulus.

For pressures less than 100 lb./sq. in. gauge the source of steam was the laboratory supply; for pressures between 100 and 500 lb./sq. in. a special steam generator was used. The steam pressure in the heater tube was adjusted by means of a pressure controller connected to the generator (which was electrically heated with a maximum input of 39,000 B.t.u./hr.) and also by means of two needle valves in series near the heater. During each run the steam pressure was held to within 1 lb./sq. in.

The heating tube was located in a stainless steel, rectangular boiler which measured 11 by 8 by 4 in. Flat Pyrex-glass windows were located front and back during runs with the organic liquids. Approximately 1.5 gal. of liquid was placed in the boiler for each run. The top of the heater was immersed to a depth of several inches at the start and was adjusted so as to be 2.0 in. at the time data were recorded. Prior tests (*7*) had shown that depths of immersion varying from zero (liquid level at the top of the tube) to several inches do not affect the results. Banchero and coworkers (*1*) also had found that liquid levels between 1 and 6 in. gave the same results for tests with a horizontal tube. The vapors which formed during the present tests passed up a 1-in. pipe 5.5 ft. long. In this riser the vapors were superheated by means of a steam tracer located outside the pipe, so that condensation of test vapors in the riser was prevented and a potential source of error eliminated. The vapors subsequently passed downward to a condenser, and the condensate was metered by a graduated glass tube in the vertical liquid line below the condenser. After a valve downstream was closed, the time for 80 ml. of condensate to collect in the glass was measured. Then the valve was opened and the liquid could be either returned to the boiler or removed from the apparatus. The closed- and open-loop arrangements both were used with the organic liquids in film boiling. Either gave good results as shown by heat balances.

The uncertainty in h, due to heat unaccounted for, averaged 9.6% for methanol. This was considered satisfactory; so only the heat output was recorded for benzene and carbon tetrachloride. On the other hand, past experience had shown that the closed loop was preferable during nucleate boiling, and with it the heat input (found by metering the steam condensate) was found routinely to be very close to the heat output (found by metering the boil-up rate and measuring heat losses during a dry run).

For liquid nitrogen an open loop was always used. With nitrogen some modifications of the apparatus were employed so as to minimize heat leakage from the surroundings. The boiler, for instance, was fitted with double walls, the outer part being the metal container described above and the inner part a smaller concentric

container made of Plexiglas sheeting. Liquid nitrogen was in the inner boiler only. Nitrogen vapors passed through a 2-in. gap between the two boilers and then entered the riser described above. Thus heat which leaked in from the surroundings was absorbed by the leaving vapor instead of by the boiling liquid. Each window on the boiler was also of double-wall construction, consisting of two $\frac{1}{16}$-in. sheets of Plexiglas with dry air sealed in a $\frac{1}{8}$-in. gap between. Nitrogen vapor from the boiler was allowed to flow through sufficient piping until it had warmed to roughly 70°F.; then it was metered with a calibrated rotameter and was discharged to the room. Complete heat balances were made for all runs with nitrogen. The uncertainty in h, due to heat unaccounted for, averaged 23.7%.

The windows, the boiler, and the important flow lines were covered with from 3 to 6 in. of insulation during runs, but before certain runs the windows were uncovered to allow still photographs and motion pictures to be obtained. The photographic techniques have been described previously (*12*).

The gasket material for the windows was neoprene for the organic liquids and paraffin-impregnated yarn for the nitrogen. Replacement was necessary every two or three weeks. In the packing gland which sealed the heating tube in the boiler, a combination of Teflon, asbestos, and neoprene was used. The test liquids contacted the Teflon only.

PROCEDURE

Before each run the heater surface was polished with a commercial polishing agent and the heater was rinsed and dried. Little attention was needed to keep the surface smooth and lustrous, in contrast to past experience with liquids in nucleate boiling, when (*10*, *12*) contamination of the tubes was a persistent problem.

When the boiler windows had been closed, the test liquid was added and heating was started. After a warm-up of about 1 hr. the readings became steady and data were recorded. For runs with nitrogen it was important to remove all water and stagnant steam from the heater tube before the test liquid was put into the boiler, to prevent the formation of ice, which would prevent the flow of steam later. In addition, in order to conserve liquid nitrogen, the boiler was cooled with dry ice for about an hour before nitrogen was introduced.

Observations of the steam pressure and the boiling temperature of the boiling liquid provided values of the over-all temperature-difference driving force. The temperature drop through the metal wall was calculated from a knowledge of the heat flux, that through the steam film by the assumption of a steam-film coefficient of 3,000 B.t.u./(hr.)(sq. ft./°F.). When film-type boiling is occurring, these two ΔT corrections are quite small compared with the boiling-side ΔT. Thus a precise value of the steam-film coefficient is of no importance. In no case was the boiling-side ΔT less than 95% of the over-all ΔT. There was no need to use the resistance-thermometer technique (*10*) to measure directly the metal temperature.

RESULTS

The results are shown in Figures 2 to 5, plotted in the form used by Bromley for horizontal tubes.* It is evident that the Bromley type of theoretical equation for vertical tubes has poor accuracy for all tests except that of nitrogen boiling on the shortest length used, 2.6 in. Excluding this case, the heat transfer rates were definitely greater than the predicted values. The h values for benzene average 120% higher than the theoretical ones predicted from the equation based on a moving-liquid boundary; h for carbon tetrachloride is about 150% high, nitrogen on the longer tube is about 40% high, and methanol is about 60% high.

*Tabular material has been deposited as document 5496 with the American Document Institute, Photoduplication Service, Library of Congress, Washington 25, D. C., and may be obtained for $2.50 for photoprints or $1.75 for 35-mm. microfilm.

The test results are shown again in Figure 6, plotted in the manner suggested by Colburn (*5*) for film-type condensation on vertical surfaces. The two lines having negative slopes are exactly equivalent to Equation (2) when its coefficient C_2 is given values of 0.943 and 0.667. The transformation from Equation (2) to the form shown in Figure 6 is straightforward. The abscissa in Figure 6 corresponds to the Reynolds number at the top of the tube, defined as $4W/(\pi D\mu)$. For nitrogen on the shortest tube, the Reynolds number is less than 1,400. Thus the flow was probably viscous and for this reason the results obtained are consistent with Equation (2).

The Reynolds numbers for carbon tetrachloride, benzene, and nitrogen on the longer tube lie between 2,100 and 4,800. Without a doubt in such cases the flow is turbulent, and Equation (2) cannot apply.

The solid curve having a positive slope in Figure 6 corresponds to Equation (3):

$$h\left[\frac{\mu^2}{k^3\rho_v(\rho_L-\rho_v)g}\right]^{1/3} = \frac{\left(\frac{4W}{\pi D\mu}\right)}{22\left(\frac{C_P\mu}{k}\right)^{-1/3}\left[\left(\frac{4W}{\pi D\mu}\right)^{0.8}-364\right]+12{,}800} \qquad (3)$$

This equation was derived originally by Colburn (*5*) for condensation on a vertical surface with the liquid flow being viscous for part of the flow path and turbulent for the rest of the way. For the viscous region the expression $Y = 1.47\ Re^{-1/3}$ [exactly equivalent to Equation (2) with $C_2 = 0.943$] was assumed to hold. For the turbulent region the expression $Y = 0.056\ Re^{0.2}\ (C_P\mu/k)^{1/3}$ was assumed to hold. This last expression is Colburn's correlation involving the Reynolds number, Prandtl number, and a modified Stanton number. The dividing point between viscous and turbulent flow was assumed to occur at a Reynolds number of 1,600. The value of h in Equation (3) is a true integrated average over both flow regimes. In Colburn's original equation the physical properties refer to the liquid phase; in Equation (3) they refer to the vapor phase except for the one density factor. The Prandtl number used for graphing Equation (3) in Figure 6 was unity, the true Prandtl numbers for the materials tested being between 0.5 and 1.1.

For all Reynolds numbers greater than about 2,000, Equation (3) gives much better predictions than does the Bromley type of equation. Furthermore, the trend of the data agree with Equation (3) but not with the Bromley equation. The data are still somewhat high, by about 40% on the average.

If the best correlation is desired, theory must be abandoned, and a single straight line may be drawn on Figure 6 which passes through all data except methanol. The equation for this correlation, line

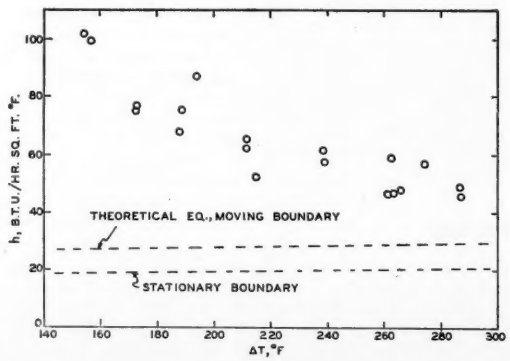

Fig. 2. Film boiling of benzene from a vertical tube, 1/2-in. O.D., 4.63 in. long, at 1 atm.

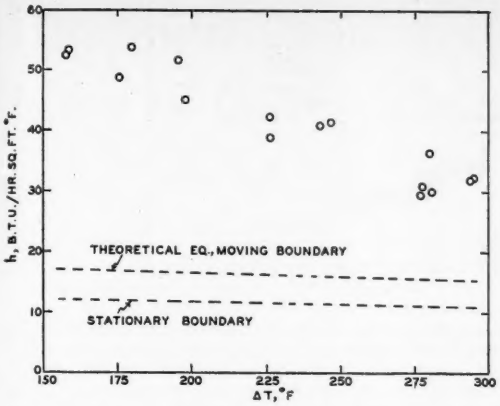

Fig. 3. Film boiling of carbon tetrachloride from a vertical tube, 1/2-in. O.D., 4.63 in. long, at 1 atm.

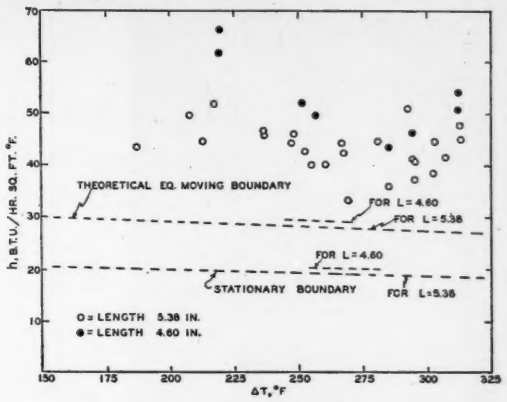

Fig. 4. Film boiling of methanol from vertical tubes, 3/8-in. O.D., 5.38 in. long and 1/2-in. O.D., 4.60 in. long, at 1 atm.

$A\ B$, is Equation (4):

$$h\left[\frac{\mu^2}{k^3\rho_v(\rho_L - \rho_v)g}\right]^{1/3} = 0.0020\left[\frac{4W}{\pi D\mu}\right]^{0.60} \quad (4)$$

This equation applies for Reynolds numbers from 800 to 5,000. The average absolute error in h is but 14%, and the worst error is 36%.

VERTICAL vs. HORIZONTAL TUBES

Comparison of Equation (4) with Equation (1) shows that film boiling outside a vertical tube is superior to boiling outside a horizontal tube for all practical lengths, at least in the range of diameters for which data are available, The expression for the break-even length is complex, involving the physical properties of the fluid as well as the ΔT and the diameter. For 1/4-in. tubes, at atmospheric pressure, all lengths greater than about 1.2 in. favor the vertical orientation for the liquids reported here. For larger diameters the break-even length is shorter than this. Therefore, if equipment is designed for film boiling outside tubes, the tubes should be vertical if possible. This rule is contrary to the practice fos film-type condensation, during which horizontal tubes are usually better than vertical ones. There is no assurance that this film-boiling rule will hold if the horizontal tubes have diameters large enough to cause turbulent flow.

ANOMALOUS BEHAVIOR OF METHANOL

Methanol in film boiling outside vertical tubes is an anomaly, the data lying in the range of Reynolds number from 840 to 1,430. In spite of this the actual flows were not viscous. High-speed motion pictures (4,000 frames/sec.) illustrated the flow pattern, which was similar to that shown by other test liquids at high Reynolds numbers. For example, Figure 7 is a high-speed still photograph (10^{-6} sec. exposure) of benzene at a ΔT of 287°F. and a theoretical maximum Reynolds number of 3,000. Methanol in the motion pictures has an appearance just like this. The tube is surrounded by vapor, and no solid-liquid contact exists. The vapor flows in waves, and the liquid-vapor interface is greatly disturbed.

Methanol behaves normally in horizontal tubes. Still photographs and motion pictures (*12*) show a viscous-flow pattern on a horizontal tube during film boiling in which small ripples cause a slight disturbance of the liquid-vapor interface, but the disturbance is not enough to affect the heat transfer. With the vertical tubes, however, the interface is deformed greatly and the heat transfer is definitely affected.

Numerous attempts were made to photograph nitrogen boiling on the short tube to see whether it exhibited a true viscous flow. Unfortunately, this project had to be abandoned before satisfactory pictures had been obtained. The lighting problems resulting from the use of double windows were very troublesome, and the scattering of light, by traces of fog that formed continuously on the outer window, was also a problem which was not overcome.

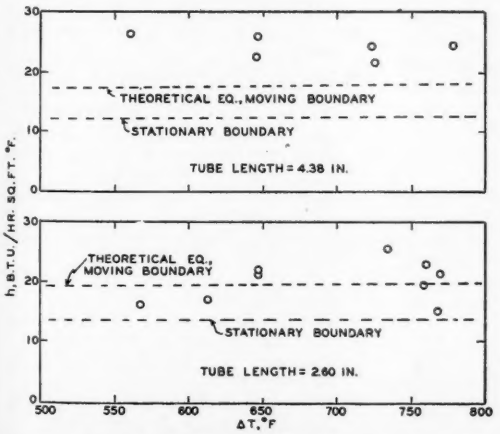

Fig. 5. Film boiling of nitrogen from vertical tubes, 1/2-in. O.D., 2.60 in. and 4.38 in. long, at 1 atm.

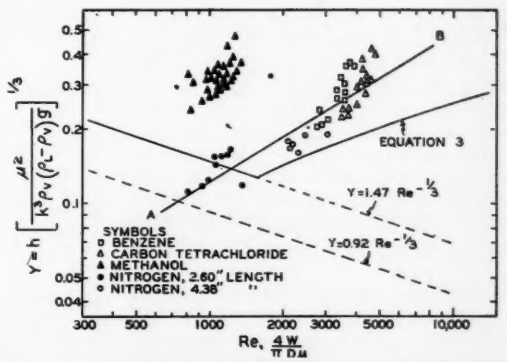

Fig. 6. Film boiling from vertical tubes as affected by Reynolds number.

Fig. 7. Film boiling of benzene on a vertical tube, 1/2-in. O.D., ΔT = 287°F.; Reynolds number at top = 3,000.

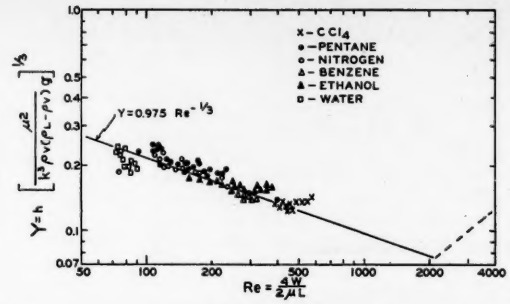

Fig. 8. Bromley's data for film boiling from horizontal tubes, 0.188- to 0.468-in. O.D., at 1 atm.

Film boiling outside horizontal tubes may be represented in terms of a Reynolds number, although other workers have not chosen to do so, Bromley's data are shown in Figure 8. The range of Reynolds number is from 70 to 600, the flow is viscous, and the data fit the line nicely. The equation of the line is exactly equivalent to Equation (1), with C_1 = 0.62.

CRITERIA FOR FILM BOILING

One of two perplexing problems which future scientists must solve concerning the criteria for film boiling is the question: what is the minimum ΔT needed to cause stable film boiling? Here *stable* means that the equations based on the concept of heat conduction across a vapor film will apply. Probably this value is a function of pressure. We do not know whether it should be the same for horizontal and vertical surfaces. Bromley found that his horizontal tubes had stable film boiling at the lowest values of ΔT reported in his paper. These minimum values for 1 atm. are nitrogen = 300°F., pentane = 310°F., ethanol = 350°F., benzene = 415°F., carbon tetrachloride = 600°F., and water = 700°F. The equation for horizontal tubes probably applies at even lower temperature differences. Data for methanol (*10, 12*) outside horizontal tubes show that the Bromley equation is accurate (within 2%) at a ΔT of 180°F.; however, at a ΔT of 160°F. it is of poor accuracy, and at a ΔT of 147°F. it predicts a value of h which is but one-third the correct value. Banchero and coworkers (*1*) found that film boiling of oxygen at 14.3 lb./sq. in. abs. was stable at a ΔT of 240°F. on a 0.069-in. horizontal tube and also at a ΔT of 100°F. at 487 lb./sq. in. abs.

The second important question is indirectly related to the first: what conditions are required so that the vapor-liquid interface will be smooth during film boiling? This question cannot be answered in simple terms of a limiting Reynolds number, as is illustrated by the data in Figure 6 and by the motion pictures. It is likely that the interfacial tension between the liquid and vapor must be important, but this value does not appear in any equations in this paper. The flow situation is complex: vapor flows upward in an annular space, and the inner boundary is fixed but the outer boundary is liquid at the saturation temperature. Under certain circumstances the liquid-vapor interface will be smooth. Under other conditions the vapor drag will cause the interface to break into waves, just as wind causes waves on the ocean. But the boiling case is more difficult, because the amount of flowing vapor increases steadily along the flow path. At present this flow problem has not been solved.

ACKNOWLEDGMENT

Valuable assistance was given by C. D. Nelson and B. J. Sutker, and financial support was provided by the National Science Foundation. A research assistantship was furnished to Mr. Hsu by the University of Illinois Engineering Experiment Station.

NOTATION

C_1, C_2 = constants, determined by boundary conditions
C_P = heat capacity of vapor, B.t.u./(lb.)(°F.)
D = outside diameter of tube, ft.
g = gravity constant, ft./hr.²
h = individual heat transfer coefficient averaged over entire tube, B.t.u./(hr.)(sq. ft./°F.)
k = thermal conductivity of vapor, B.t.u./(hr.)(ft./°F.)
L = tube length, ft.
Re = Reynolds number, $4W/(\pi D\mu)$ for vertical tubes, $4W/(2L\mu)$ for horizontal tubes, dimensionless
T_L = boiling point of liquid, °F.
T_S = surface temperature of heat source, °F.
ΔT = temperature difference, $T_S - T_L$
W = maximum vapor flow rate, lb./hr.
Y = dimensionless, group, $h[\mu^2/(k^3\rho_v\{\rho_L - \rho_v\}g)]^{1/3}$
λ = latent heat of vaporization, B.t.u./lb.
λ' = latent heat plus sensible heat content of vapor, B.t.u./lb.
μ = viscosity of vapor, lb./(ft.)(hr.)
ρ_L, ρ_v = density of liquid and vapor, lb./cu. ft.

LITERATURE CITED

1. Banchero, J. T., G. E. Barker, and R. H. Boll, *Chem. Eng. Progr. Symposium Ser.* No. 17, **51**, 21 (1955).
2. Bromley, L. A., *Chem. Eng. Progr.*, **46**, 221 (1950).
3. ———, *Ind. Eng. Chem.*, **44**, 2966 (1952).
4. ———, N. R. Leroy, and J. A. Robbers, *ibid.*, **45**, 2639 (1953).
5. Colburn, A. P., *ibid.*, **26**, 432 (1934).
6. McAdams, W. H., J. N. Addoms, P. M. Rinaldo, and R. S. Day, *Chem. Eng. Progr.*, **44**, 639 (1948).
7. Nelson, C. D., M.S. thesis, Univ. Ill., Urbana (1955).
8. Nukiyama, Shiro, *Soc. Mech. Engrs. (Japan)*, **37**, 367 (1934).
9. Nusselt, W. Z., *Z. Ver. deut. Ing.*, **60**, 541, 569 (1916).
10. Perkins, A. S., and J. W. Westwater, *A.I.Ch.E. Journal*, **2**, 471 (1956).
11. Rohsenow, W. M., *Trans. A.S.M.E.*, **78**, 1645 (1956).
12. Westwater, J. W., and J. G. Santangelo, *Ind. Eng. Chem.*, **47**, 1605 (1955).

Manuscript submitted May 1, 1957; revision received October 25, 1957; paper accepted October 28, 1957.

Heat and Momentum Transfer in the Flow of Gases Through Packed Beds

MARVIN B. GLASER and GEORGE THODOS

The Technological Institute, Northwestern University, Evanston, Illinois

Heat and momentum transfer studies have been made for the flow of gases through fixed beds consisting of randomly packed, solid metallic particles. The experimental technique employed in these studies made possible for the first time the procurement of gas-film heat transfer data under steady state conditions and in the absence of mass transfer effects. Electric current passed through the metallic particles of the bed created within the particles a steady generation of heat, which was continuously removed by gases flowing through the bed. Several direct temperature measurements of both gases and solids within the bed made possible the direct calculation of the heat transfer coefficient for the gas film to produce the Colburn heat transfer factor j_h, which has been found to correlate with the modified Reynolds number, $Re_h = \sqrt{A_p}G/[\mu(1 - \epsilon)\varphi]$. The shape factor φ was established in these studies for cubes and cylinders and was found to be identical to their respective sphericities.

Pressure-drop measurements produced a friction factor f_k of the Blake type, which yielded separate curves for each shape when correlated with the modified Reynolds number Re_m. No simple relationship was found to exist between the heat transfer and friction factors. A single correlation of the pressure-drop data was obtained for the modulus $f_k\varphi^n$ when correlated with a Reynolds number of the type $Re_m = \sqrt{A_p}G/[\mu(1 - \epsilon)]$. The exponent n varies with the particle shape.

Experimental runs have been carried out for 3/16, 1/4, 5/16-in. spheres, 1/4 and 3/8-in. cubes, and regular cylinders using hydrogen and carbon dioxide to extend the range of molecular weights beyond that of air, used for the majority of these runs. A particle-size, column-diameter effect was found to exist for both heat and momentum transfer. This effect becomes significant in the low Reynolds region.

Investigations dealing with the flow of heat between granular solids and flowing gases have been associated with simultaneous mass transfer or have been involved with unsteady state conditions (*1, 2, 3, 9, 11* to *16*). The heat transfer correlations produced from mass transfer studies involved the vaporization of a liquid from a solid surface, and as a result the heat transfer data were obtained indirectly. Thus Gamson et al. (*9*) and Taecker and Hougen (*15*) vaporized water from porous catalyst carriers and, by assuming adiabatic conditions, were able to establish the gas and particle temperatures with a humidity chart. Satterfield, Resnick, and Wentworth (*13*) decomposed hydrogen peroxide in the presence of metallic spheres to obtain simultaneous mass and heat transfer data. Heat transfer coefficients for the gas film were produced from measured sphere temperatures, and the calculated heat generated on the catalyst surface was assumed to transfer completely to the flowing gas.

Early attempts to establish independent heat transfer mechanisms associated in the flow of gases through granular particles were of the unsteady state type as described by Schumann (*14*) and Furnas (*8*). The interpretation of these results in terms of an average heat transfer coefficient was difficult because of the prevailing transient conditions and mathematical complexity of the problems.

The correlation of pressure-drop data for the flow of gases through porous media, which first considered the inclusion of the void volume effect, was proposed in 1922 by Blake (*4*) from dimensional-analysis considerations. Further developments resolved the total momentum transfer encountered into kinetic- and viscous-energy contributions. Using these concepts, Ergun (*7*) presented the pressure-drop expression

$$\frac{g_c \Delta P}{L} \frac{D_p}{Gu} \frac{\epsilon^3}{1 - \epsilon} = f_k \qquad (1)$$

where f_k is a function of the modified Reynolds number, $Re' = D_p G/[\mu(1 - \epsilon)]$. In Equation (1) f_k represents the ratio of total-energy losses to kinetic-energy losses. A review of the literature points to the fact that this pressure-drop relation produces a dependable correlation with experimental data.

Colburn (*6*) derived and experimentally verified a similarity between heat, mass, and momentum transfer for the flow of fluids through circular conduits; however, the possible existence of such an analogy for the flow of fluids through granular beds has been highly controversial.

The present investigation has been initiated primarily to establish heat transfer coefficients for gases flowing through a fixed bed of randomly packed granular particles in the absence of mass transfer effects and under steady state conditions. As a secondary consequence, the simultaneous pressure-drop information would permit a reevaluation of the possibility of the existence of an analogy between heat and momentum transfer.

EXPERIMENTAL EQUIPMENT AND PROCEDURE

The experimental unit was designed to produce uniform heat generation within a granular bed consisting of metallic particles for which heat removal was accomplished by the flow of gases. Radial heat transfer was eliminated in order to ensure accuracy in the measurement of heat generated. Simultaneous pressure-drop measurements were made with an inclined-draft gauge.

A schematic diagram of the equipment is presented in Figure 1, which includes the column containing the packed bed. This column with its auxiliaries is shown in Figure 2. Compressed air from the building supply was regulated and passed through a filter for the removal of entrained oil and water prior to metering through Fischer-Porter flowmeters connected in parallel. In a similar fashion carbon dioxide and hydrogen furnished from high-pressure gas cylinders were pressure regulated and passed through the flowmeters. After being metered, the gas was introduced into the column to remove from the fixed bed the heat which was generated by the passage of electric current through the metallic particles of the bed. The electric current for heating the bed was provided from a specially designed

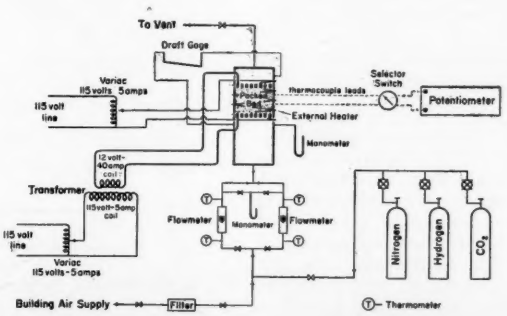

Fig. 1. Schematic diagram of experimental unit.

Marvin B. Glaser is at present with the Esso Research and Engineering Company, Linden, New Jersey.

high-amperage, low-voltage transformer, which has a primary rating of 115 volts, 5 amp. and a secondary rating of 12 volts, 40 amp. Current to the transformer was controlled with a conventional 115-volt, 5-amp. variac. The heated gases after leaving the column were vented to the atmosphere.

Figure 2 presents the details of the vertical column which was prepared from a transite pipe having an inside diameter of 2 in. Transite was selected because of its excellent electrical and thermal insulating properties and its machineability. The column consisted of three distinct sections. The bottom section, 9 in. in length, contained a 6-in. section packed with ball bearings, which served to calm and distribute the gas flow evenly into the heat transfer section. The lower column section also contained pressure taps and one of the heavy copper leads which contacted the heat transfer section. Similarly, pressure taps and another heavy copper lead were contained in the upper column section, which was 3 in. long. The middle section, 4 in. long, contained the packed bed of metallic particles, supported between perforated stainless steel plates $\frac{1}{16}$ in. thick, which served as the electrodes of the bed. These three separate component sections were assembled by superimposition. When pressure was applied between the calming section and the upper section, the packing in the middle section became fixed. The necessary pressure was supplied to the bed by four steel compression rods, which spanned the full length of the column between two steel flanges.

When the column was assembled, the two copper leads contacted the perforated-plate electrodes to permit the flow of electric current through the bed. Thus the resistance of the metallic bed was responsible for the generation of heat within the solid particles. The application of proper pressures on the compression rods permitted the even distribution of electric current through the bed in order to ensure uniform heating. Through these means the total bed resistance could be varied from 1 to 5 ohms. It is probable that a large portion of the total heat was generated at the points of particle contact; however, a uniform particle temperature was obtained because of the high thermal conductivities of the metals used and the multiplicity of contact points per particle.

External heat was supplied to the heat transfer section in order to eliminate radial temperature gradients within the bed. This was accomplished by means of a $\frac{1}{8}$-in. nichrome strip heater, which was wrapped around the heat transfer section of the column. Two iron-constantan thermocouples were embedded in the heat transfer wall and spaced on a common radius so that one thermocouple was located near the inside radius and the other was near the outside. Adiabatic conditions were realized when these two thermocouples indicated the same temperature.

Iron-constantan thermocouples of 24 B and S gauge thickness and covered with glass and asbestos insulation were used to measure particle and gas temperatures within the bed. A total of twelve thermocouples were located in each bed and were connected to a Brown single-point electronic potentiometer which had a 4.5-sec. full-dial response. This potentiometer was connected to three multipoint thermocouple switches. The thermocouple leads were brought into the bed through small holes drilled in the column wall. After the lead wires had been inserted, the holes were sealed with litharge. Some thermocouples were permanently attached to the particle surfaces by drilling a small hole through a major diameter and inserting the thermocouple wire through this hole until the couple junction reached a point just below the opposite surface, whereupon it was fastened in place with a drop of solder. Generally, two or three thermocouples were placed in a cross-sectional area of the bed at different radial distances in order to check the uniformity of heat generation.

The rest of the thermocouples were placed between the interstices of the bed and forced against the surface of the solid particles. These unfastened thermocouples were then positioned in the void spaces of the bed by means of the following sensitive procedure to ensure proper placement. After the entire bed was in place, electric current was passed through it for the generation of heat. Gas was then allowed to flow through the bed. When equilibrium conditions had been attained, the temperatures indicated by all thermocouples in any given cross section were found to record approximately the same temperatures, varying at most by 0.5°F. The unattached thermocouples were moved gently by applying a slight pull on the lead wires until their indicated temperature suddenly dropped. At this position the thermocouple junction was assumed to be surrounded completely by gas, the temperature of which could be directly measured. The thermocouple was then frozen in this position with the application of litharge to the lead-wire wall-entry hole. The radial position of this thermocouple was indicated from designated markings on the lead wires.

This procedure enabled the procurement of solid and gas temperatures for different cross sections of the bed and thus established the longitudinal temperature profiles for the entire bed length. These temperature profiles made possible the calculation of point heat transfer coefficients, thus eliminating the influence of end effects caused by the perforated-plate electrodes.

Three types of metallic packings, consisting of spheres, cubes, and regular cylinders, were investigated. The properties of these packings and the various beds used are presented in Table 1. All spheres were commercial ball bearings ground to rigid specifications. The cubes and cylinders were prepared by cutting steel rods into the desired size particles. Tolerances for the cubes and cylinders were limited to ±0.003 in.

Seven randomly packed beds were investigated with reference to shape, size, and void volume. The void volume of each bed was determined in *situ* by placing the required number of particles to fill the heat transfer section of the column included between the two electrodes. The total solid volume of the particles was established from the number and the calculated volume of the particles. Each bed was prepared by dropping particles individually into the column. When the desired level had been reached, particles containing fixed thermocouples were carefully positioned before the further additio(of packing. Air, hydrogen,

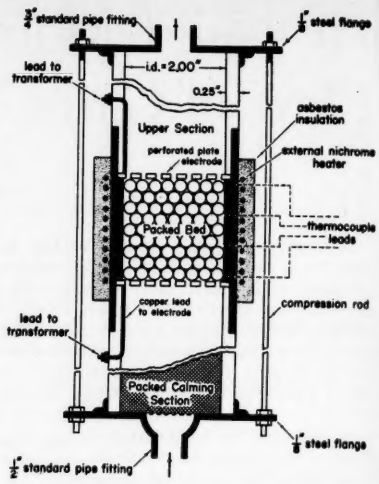

Fig. 2. Detailed sketch of transite column.

and carbon dioxide were the gases employed with each bed and were used in order to cover the range of molecular weights for the common gases.

A number of preliminary tests were performed on each bed in order to determine the uniformity of internal heat generation. First, current was supplied to the bed with no gas flow, and the temperatures of all particles equipped with thermocouples were examined after a short heating period and were found to be constant within 0.5°F. A

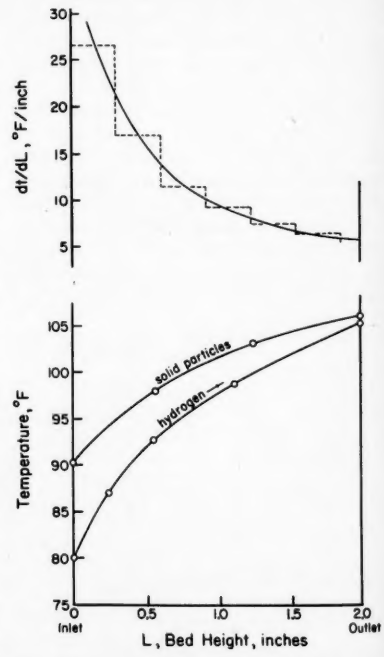

Fig. 3. Longitudinal temperature profiles for the flow of hydrogen through packed spheres and resulting gas temperature gradient (run 63-1/4-in. spheres).

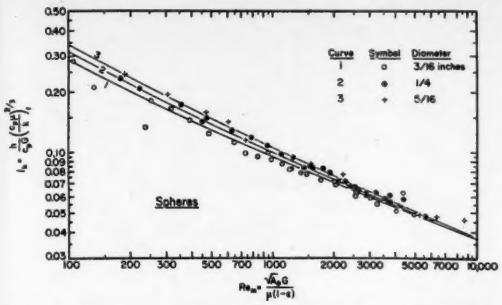

Fig. 4. Heat transfer factors for packed beds of spheres.

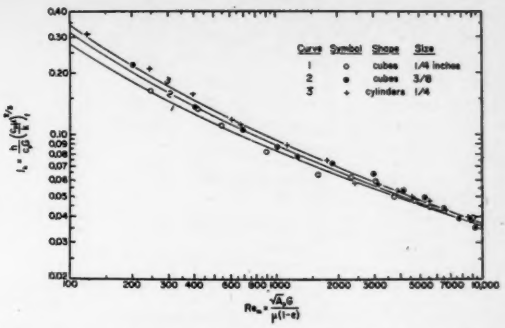

Fig. 5. Heat transfer factors for packed beds of cubes and cylinders.

total time of approximately 10 sec. was required to obtain all these readings. The passage of the electric current through the bed did not influence the performance of the thermocouples, as the galvanometer of the potentiometer does not respond sufficiently to the 60-cycle current of the magnitude used to heat the bed. Air was then passed through the bed at a constant rate, and the temperatures of the particles in any cross section were found to be essentially constant; for nearly all runs they averaged within 1° to 2°F. of each other. Therefore, an average of the solid temperatures in a given cross section was used to represent the temperature of the particles in that cross section.

Steady state conditions were realized for each run. One hundred and eighteen runs, which included simultaneous heat and momentum transfer, were made, and 65 additional runs were conducted for the purpose of securing a more extensive background for pressure-drop measurements (*10*). In order to minimize radiation effects, the temperature differential between the inlet and outlet gas was limited to 50°F., and the maximum particle temperature was not allowed to exceed 150°F. For the hydrogen runs the entire system was first purged with nitrogen in order to eliminate any hazard of an air-hydrogen explosion, which could be caused by an electric spark.

INTERPRETATION OF HEAT TRANSFER DATA

The method used to calculate the local heat transfer coefficient for the gas film involved the consideration of a differential height of bed dL. Since heat is being generated within the particles and is completely transferred to the flowing gas at the steady rate q, a heat balance over the differential segment shows that

$$q = wc_p\,dt = h_g a(S\,dL)(T - t) \qquad (2)$$

The local heat transfer coefficient h_g is obtained by rearranging Equation (2) into the form

$$h_g = \frac{c_p G}{a(T - t)}\left(\frac{dt}{dL}\right) \qquad (3)$$

A typical plot of longitudinal gas- and solid-temperature profiles is presented in Figure 3 for run 63. A graphical differentiation of the gas-temperature profile by means of the chord-area method produced the gas-temperature gradient dt/dL, presented in Figure 3. For a fixed point within the bed the values $T - t$ and dt/dL were obtained directly to produce the local heat transfer coefficient h_g from Equation (3). In general, coefficients were evaluated at four equidistant points ranging from ¼ to 1¼ in. from the bed entrance. A variation of approximately ±5% was noted for the calculated local heat transfer coefficient for each bed. An arithmetic average of the local coefficients was used to obtain an average coefficient for the entire bed.

Heat transfer factors defined by Colburn (*5*) as

$$j_h = \frac{h}{c_p G}\left(\frac{c_p\mu}{k}\right)_f^{2/3} \qquad (4)$$

were calculated from the average coefficients and average film properties. A summary of these calculated values and properties is presented in Table 2 for the 5/16-in. spheres only. The complete listing of the results presented in Table 2 for all the seven different beds of Table 1 are available elsewhere (*10*). The calculated values of j_h are plotted in Figures 4 and 5 against a Reynolds number of the type $Re_m = \sqrt{A_p}G/[\mu(1 - \epsilon)]$, where $\sqrt{A_p}$ expresses a linear dimension characteristic of the particle.

An inspection of Figures 4 and 5 shows that the data for each individual bed produce good correlations; however, these correlations are distinct within themselves and depend on particle shape and size. Lack of a generalized correlation for the three sizes of spheres is apparent in Figure 4, in which the effect of particle size is found to be most significant in the region of low Reynolds number. Similar behavior is shown in Figure 5 for two sizes of cubes. It is also apparent from Figures 4 and 5 that no correlation exists between spheres, cubes, and cylinders of the same size.

The lack of a single correlation for different sizes of the same type of packing is attributed to a ratio of particle size to column diameter. These ratios, expressed as D_p/D_r, become for the three sizes of spheres 0.10, 0.133, 0.167 and extend beyond the recommended limit for packed columns of 0.125.

The absence of a single correlation for different particle shapes is due to the unavailability of a fraction of the entire particle surface area which results from particle-area contacts. For spheres, particle contacts are point contacts; whereas for shapes such as cubes and cylinders, the contacts may involve significant areas. In order to take into account the actual surface involved in the transfer of heat and mass, the shape factor φ, representing the fraction of the total participating surface, has been developed to introduce φ into the modified Reynolds number as follows. By definition

$$Re = \frac{G}{(a\varphi)\mu} \qquad (4)$$

where the product $a\varphi$ represents the participating transfer area. For spheres, cubes, and regular cylinders, it can be shown that

$$a = \frac{6}{D_p}(1 - \epsilon) \qquad (5)$$

where D_p represents a characteristic particle dimension. Eliminating a from Equation (4) yields the Reynolds number

$$Re = \frac{D_p G}{6(1 - \epsilon)\varphi\mu} \qquad (6)$$

Furthermore, the surface area of a particle A_p can be expressed in terms of D_p as $A_p = KD_p^2$ where K is a constant depending on the particle geometry. When the quantity $D_p = \sqrt{A_p/K}$ is substituted, a Reynolds number can be expressed in terms of these variables as

$$Re_h = \frac{\sqrt{A_p}G}{\mu(1 - \epsilon)\varphi} \qquad (7)$$

For spheres the shape factor φ has been

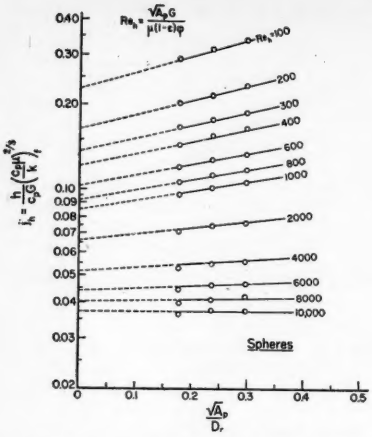

Fig. 6. Relationships of heat transfer factor with equivalent particle-size, column-diameter ratio for spheres.

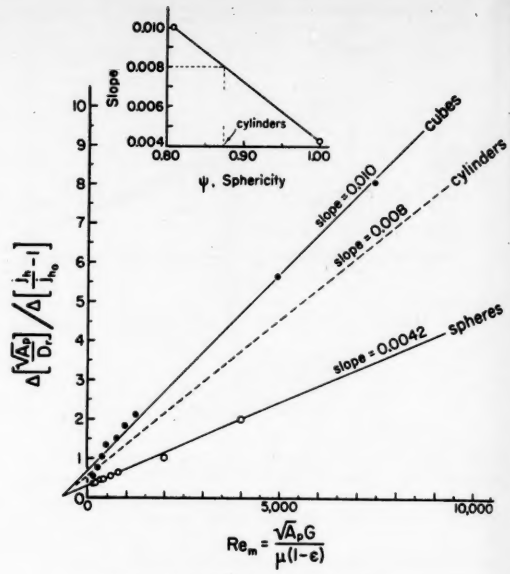

Fig. 7. Relationship of the quantity

$$\Delta\left[\frac{\sqrt{A_p}}{D_r}\right] \Big/ \Delta\left[\frac{j_h}{j_{h_o}} - 1\right]$$

with the modified Reynolds number, Re_m, for spheres and cubes.

taken as one, and for other particles this factor becomes less than unity.

A correlation of particle size and column diameter expressed as $\sqrt{A_p}/D_r$ was first established for spheres and involved plotting the values of j_h presented in Figure 4 against the ratio $\sqrt{A_p}/D_r$ for parameters of constant Reynolds number, as shown in Figure 6. Extrapolations of the resulting plots to $\sqrt{A_p}/D_r = 0$ produced heat transfer factors which have been designated as j_{h_o} and correspond to the case where the particle size is negligible in relation to column diameter. It is to be expected that for large values of $\sqrt{A_p}/D_r$ the curves of Figure 6 will approach a limiting j_h value. A relation between j_h/j_{h_o} and $\sqrt{A_p}/D_r$ in terms of the Reynolds number Re_h has been found to apply for spheres in the interval $100 < Re_h < 9{,}200$, which can be expressed empirically as

$$\frac{j_h}{j_{h_o}} = 1 + \frac{\sqrt{A_p}}{D_r} \log \frac{4984}{Re_h^{0.933}} \qquad (8)$$

where

$$j_{h_o} = \frac{0.535}{Re_h^{0.30} - 1.6} \qquad (9)$$

For $Re_h > 9{,}200$ the ratio j_h/j_{h_o} is unity and thus is consistent with the experimental results.

A similar procedure was applied to the data of the two sizes of cubes having edges of ¼ and ⅜ in. Before a shape factor for cubes was established, values of j_{h_o} were determined by extrapolating the curves resulting from plots of j_h vs. $\sqrt{A_p}/D_r$ for parameters of $\sqrt{A_p}G/[\mu(1-\epsilon)]$. The proper shape factor for cubes was determined through a trial-and-error procedure which consisted of applying assumed values of φ in Equation (7) until the resulting curve of j_{h_o} vs. Re_h for cubes became coincidental with the previously determined curve for spheres. For cubes the shape factor was found to be $\varphi = 0.81$. In addition, the relationship between j_h and j_{h_o} for cubes can be expressed conveniently as

$$\frac{j_h}{j_{h_o}} = 1 + \frac{\sqrt{A_p}}{D_r} \frac{23.1}{Re_h^{0.626}} \qquad (10)$$

where j_{h_o} is defined by Equation (9) and applies in the interval $100 < Re_h < 9{,}200$. It is noteworthy that, even though the variations of j_h with Re_h for cubes and spheres are different, the variation of j_{h_o} with Re_h is identical.

The extensive investigation of spheres and cubes was used as a basis to establish the variation of j_h with $\sqrt{A_p}/D_r$ for the only available heat transfer data for ¼-in. regular cylinders. Since these data were limited to one size of cylinders, values of j_{h_o} could not be obtained by

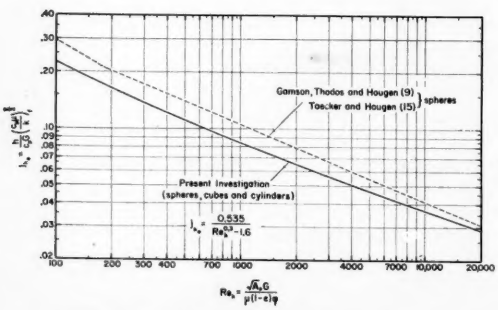

Fig. 8. Heat transfer factors for packed beds.

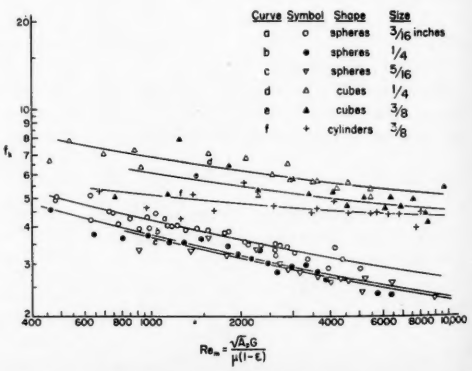

Fig. 9. Friction factors for packed beds of spheres, cubes and cylinders.

the method described for spheres and cubes, as at least two experimental values of $\sqrt{A_p}/D_r$ are required. To establish this relation for cylinders, values of $(j_h/j_{h_o}) - 1$ were plotted against $\sqrt{A_p}/D_r$ for spheres and cubes with parameters of the Reynolds number Re_m. This Reynolds number has been used here in order to establish j_{h_o} independently of φ. The resulting straight lines converged at the origin and produced reciprocal slopes, which were correlated against the Reynolds number Re_m, as shown in Figure 7. It was assumed that the slopes of the straight lines of Figure 7 for spheres and cubes were directly related to their respective sphericities (ψ) of 1.00 and 0.806 as shown in Figure 7. Sphericity represents the ratio of the surface area of a sphere having the same volume as a particle to the surface area of the particle. On the assumption that this relation also applies to cylinders of $\psi = 0.873$, a slope of 0.008 was obtained for regular cylinders to produce the dotted line of Figure 7. Direct readings for cylinders produced the quantity $\Delta[\sqrt{A_p}/D_r]/\Delta[(j_h/j_{h_o}) - 1]$, which was associated with the experimental values of j_h and $\sqrt{A_p}/D_r$ to define j_{h_o} for cylinders as follows:

$$\frac{j_h}{j_{h_o}} = 1 + \frac{\sqrt{A_p}}{D_r}\frac{10.78}{Re_h^{0.384}} \qquad (11)$$

In the same procedure as that used for cubes, a shape factor of $\varphi = 0.88$ was necessary to superimpose the data of cylinders on those of the spheres and cubes. The resulting plot of j_{h_o} vs. Re_h for this investigation, involving spheres, cubes, and cylinders, is presented in Figure 8 and is compared with the converted data of Gamson et al. (*9*) and Taecker and Hougen (*15*). These expressions produce for packed beds results that have been found to be consistent with actual practice involving the regeneration of catalysts used in hydroforming work.

In these heat transfer studies the shape factors φ for spheres, cubes, and cylinders were calculated independently. A comparison of these shape factors with particle sphericities presents a strong indication that the shape factors used in these studies and particle sphericities may be interchangeable for packed beds. A summary of the experimentally determined shape factors and calculated particle sphericities follows:

Particle shape	Shape factor φ	Sphericity ψ
Spheres	1.0	1.0
Cylinders	0.88	0.873
Cubes	0.81	0.806

Further work with irregularly shaped packings, such as partition rings, Raschig rings, and Berl saddles, is necessary before any definite conclusion can be reached regarding a relationship between the shape factor φ and ψ, the sphericity.

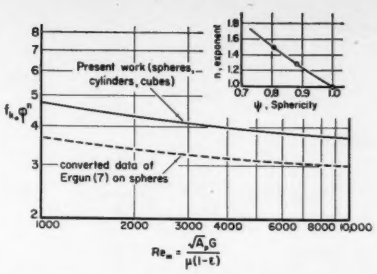

Fig. 10. Correlation of friction modulus and Reynolds number for packed beds.

INTERPRETATION OF PRESSURE-DROP DATA

Pressure-drop data are presented for 5/16-in. spheres in Table 2, and the complete data for all the spheres, cubes, and cylinders are presented elsewhere (*10*). The pressure drop due to the perforated electrodes has been subtracted from the total pressure loss to produce the pressure drops across the bed given in Table 2. Friction factors f_k have been calculated with a modification of Equation (1) in order to be consistent with the characterizing dimension of the packing $\sqrt{A_p}$. Thus Equation (1) becomes

$$\frac{g_c \Delta P}{L}\frac{\sqrt{A_p}}{Gu}\frac{\epsilon^3}{1-\epsilon} = f_k \qquad (12)$$

A summary of the calculated values of f_k appears in Table 2 for 5/16-in. spheres. All the values of f_k are presented as a function of the Reynolds number Re_m in Figure 9.

Figure 9 shows the existence of separate relationships for each particle shape and size. The friction factor f_k increases with decreasing particle size, which is opposite to the behavior of the heat transfer

TABLE 1. PROPERTIES OF PACKED BEDS

(Column diameter = 1⅞ in.; bed height = 2.0 in.)

No.	Particle shape	Type of metal	Particle size, in.	Total number of particles in bed	a, sq. ft./cu. ft.	ϵ, fractional void volume	$\frac{\sqrt{A_p}}{D_r}$
1*	Sphere	Monel	3/16	935	217	0.436	0.177
2	Sphere	Brass	¼	392	164.5	0.429	0.236
3	Sphere	Brass	5/16	190	126	0.453	0.296
4	Cube	Steel	⅜ (edge)	56	102	0.469	0.490
5	Cube	Steel	¼ (edge)	207	168.5	0.417	0.325
6†	Regular cylinder	Steel	¼	234	151	0.477	0.289
7‡	Regular cylinder	Steel	⅜	70	100	0.478	0.433

*Bed height of 2 3/16 in.
†Heat transfer studies only.
‡Momentum transfer studies only.

TABLE 2. HEAT AND MOMENTUM TRANSFER RESULTS FOR 5/16-in. SPHERES

Run	G, lb./(hr.)(sq. ft.)	ΔP, in. of water*	h, B.t.u./(hr.)(sq. ft.)(°F.)	$\frac{h}{C_pG}$	$\frac{\sqrt{A_p}G}{(1-\epsilon)}$	j_h	f_k
Air: $(c_p\mu/k)^{2/3} = 0.796$							
65	396	0.126	13.47	0.1415	741	0.113	5.77
66	816	0.338	21.30	0.1087	1562	0.0865	3.70
67	1,165	0.620	27.27	0.0974	2250	0.0775	3.39
68	1,511	0.930	28.38	0.0780	2900	0.0622	2.90
69	1,880	1.30	31.80	0.0704	3620	0.0562	2.73
70	2,240	1.81	36.32	0.0676	4320	0.0538	2.68
71	2,760	2.77	40.73	0.0615	5330	0.0490	2.72
Hydrogen: $(c_p\mu/k)^{2/3} = 0.800$							
72	122.8	—	82.48	0.1949	478	0.1561	
73	79.8	—	65.62	0.2395	309	0.1915	
74	49.1	—	51.54	0.3050	190	0.2440	
75	159.5	0.246	97.47	0.1765	616	0.1405	5.05
Carbon dioxide: $(c_p\mu/k)^{2/3} = 0.762$							
76	3,640	2.66	44.60	0.0613	8820	0.0467	2.33
77	2,660	1.82	33.43	0.0630	6450	0.0480	2.62
78	1,740	0.915	24.93	0.0717	4230	0.0547	3.40

*The pressure drop due to the perforated-plate electrodes has been subtracted from the total pressure drop to produce the values presented in this table.

factor j_h with particle size. The reason momentum and heat transfer are not directly related in packed beds is that momentum transfer involves surfaces, corners, and edges, whereas heat transfer is restricted to surface areas. The effect of reactor diameter is due to a difference in gas velocities at wall surfaces and through packing not in contact with the wall. The geometry of contact is different at the wall surface from that between particles in the bed, which are removed from the wall. Hence, the correlations for both momentum transfer and for heat transfer are altered in opposite directions, as shown by this investigation.

Since the friction-factor relationships of Figure 9 are nearly horizontal, the use of the shape factor φ in the Reynolds number Re_h did not prove adequate for correlating these data. In general, the pressure-drop data for each individual shape and size did not correlate as well as the corresponding heat transfer data. The lack of a good correlation for momentum transfer can be attributed to the thin beds employed, under which conditions the entrance and exit effects may be significant. Furthermore, for low flow rates the resulting pressure losses were very small and hence were difficult to measure. Consequently, the correlation of pressure drop was limited to the region $1{,}000 < Re_m < 10{,}000$.

The friction-factor data for spheres, cubes, and cylinders were analyzed in a manner similar to that used for the heat-transfer–factor correlation in order to establish the particle-size, column-diameter effect on f_k. Values of f_{k_o} representing friction factors at $(\sqrt{A_p}/D_r) \rightarrow 0$ were obtained for spheres, cubes, and cylinders to produce separate correlations for each shape when plotted against the Reynolds number Re_m. A single correlation for these shapes resulted when the shape factor φ was directly associated with the friction factor f_{k_o} in the dimensionless modulus $f_{k_o}\varphi^n$, where n is an exponent which can be related to sphericity. The value of n is unity for spheres, and for cylinders and cubes it was established by trial and error to be 1.29 and 1.50, respectively. A plot of the friction modulus $f_{k_o}\varphi^n$ vs. the Reynolds number Re_m for the range included between $Re_m = 1{,}000$ to 10,000 is presented in Figure 10 along with the relationship for n and the sphericity ψ. This correlation is compared with the converted results of Ergun (7) for spheres, which also appear in Figure 10. For the range $1{,}000 < Re_m < 10{,}000$, the friction modulus can be expressed empirically as

$$f_{k_o}\varphi^n = \frac{2.89}{Re_m^{0.05} - 0.81} \qquad (13)$$

The relationships of the friction factor f_k and the friction factor f_{k_o} for the limiting case when $(\sqrt{A_p}/D_r) \rightarrow 0$ can be expressed empirically for spheres, cubes, and cylinders as follows:

spheres

$$\frac{f_{k_o}}{f_k} = 1 + \frac{\sqrt{A_p}}{D_r} \log \frac{Re_m^{1.25}}{8.22} \qquad (14)$$

cubes

$$\frac{f_{k_o}}{f_k} = 1 + \frac{\sqrt{A_p}}{D_r} \frac{Re_m^{0.104}}{3.25} \qquad (15)$$

cylinders

$$\frac{f_{k_o}}{f_k} = 1 + \frac{\sqrt{A_p}}{D_r} \frac{Re_m^{0.193}}{4.91} \qquad (16)$$

COMPARISON OF HEAT AND MOMENTUM TRANSFER FACTORS

In order to investigate the possible existence of an analogy between the heat transfer factor, j_{h_o} and the momentum transfer factor f_{k_o} comparisons of these moduli were limited to the simple geometry existing for spheres which have values of $\varphi = 1.0$ and $n = 1.0$. The ratio of j_{h_o}/f_{k_o} was found to decrease steadily from 0.165 at $Re_m = 1{,}000$ to 0.100 at $Re_m = 10{,}000$. The existence of a direct relationship between these factors remains to be substantiated experimentally and is highly unlikely as long as the total momentum transfer cannot be resolved into the contributions due to skin friction and the impediments to flow created by edge and corner effects.

ACKNOWLEDGMENT

The authors wish to acknowledge the assistance of D. F. Mason and B. J. Sollami, who contributed to the experimental design of the equipment.

NOTATION

a = surface of particles per unit volume of bed, sq. ft./cu. ft.
A_p = surface area of individual particle, sq. ft.
c_p = heat capacity at constant pressure, B.t.u./(lb.)(°F.)
D_p = equivalent particle diameter, ft.
D_r = column diameter, ft.
f_k = friction factor for packed beds, $(g_c \Delta P/L)(\sqrt{A_p}/Gu)(\epsilon^3/1 - \epsilon)$
f_{k_o} = friction factor for $(\sqrt{A_p}/D_r) \rightarrow 0$
g_c = gravitational constant, 32.2 (lb.-mass)(ft.)/(lb.-force)(sec.)^2
G = superficial mass velocity, (lb.)/(hr.)(sq. ft.)
h = heat transfer coefficient, B.t.u./(hr.)(sq. ft.)(°F.)
h_g = gas-film heat transfer coefficient, B.t.u./(hr.)(sq. ft.)(°F.)
j_h = heat transfer factor, dimensionless
j_{h_o} = heat transfer factor for $(\sqrt{A_p}/D_r \rightarrow 0$
k = thermal conductivity, B.t.u./(hr.)(ft.)(°F.)
K = constant
L = bed height, ft.
n = exponent
P = pressure, lb.-force/sq. ft.
q = rate of heat transfer, B.t.u./hr.
Re' = modified Reynolds number, $D_pG/[\mu(1 - \epsilon)]$
Re_h = modified Reynolds number for heat transfer, $\sqrt{A_p}G/[\mu(1 - \epsilon)\varphi]$
Re_m = modified Reynolds number for momentum transfer, $\sqrt{A_p}G/[\mu(1 - \epsilon)]$
S = column cross-sectional area, sq. ft.
t = temperature of flowing gas, °F.
T = temperature of particle, °F.
u = average linear fluid velocity, ft./sec.
w = mass flow rate, lb./hr.

Greek Letters

ϵ = fractional void volume, dimensionless
μ = absolute viscosity, lb./(hr.)(ft.)
ρ = average fluid density, lb./cu. ft.
φ = particle shape factor, fraction of total participating surface of particle, dimensionless
ψ = particle sphericity, $\frac{\text{surface area of sphere having same volume as particle}}{\text{surface area of particle}}$, dimensionless

LITERATURE CITED

1. Amundson, N. R., *Ind. Eng. Chem.*, **48**, 26 (1956).
2. Anzelius, A., *Z. angew. Math. u. Mech.*, **6**, 291 (1926).
3. Arthur, J. R., and J. W. Linett, *J. Chem. Soc.*, Part 1, 416 (1947).
4. Blake, F. E., *Trans. Am. Inst. Chem. Engrs.*, **14**, 415 (1922).
5. Colburn, A. P., *Ind. Eng. Chem.*, **23**, 910 (1931).
6. ———, *Trans. Am. Inst. Chem. Engrs.*, **29**, 174 (1933).
7. Ergun, Sabri, *Chem. Eng. Progr.*, **48**, 89 (1952).
8. Furnas, C. C., *Ind. Eng. Chem.*, **22**, 721 (1930).
9. Gamson, B. W., George Thodos, and O. A. Hougen, *Trans. Am. Inst. Chem. Engrs.*, **39**, 1 (1943).
10. Glaser, M. B., Ph.D. thesis, Northwestern Univ., Evanston, Ill. (August, 1956).
11. Katz, S., and A. M. Reiser, *J. Math. Physics*, **33**, 256 (1954).
12. Löf, G. O. G., and R. W. Hawley, *Ind. Eng. Chem.*, **40**, 1061 (1948).
13. Satterfield, C. N., Hyman Resnick, and R. L. Wentworth, *Chem. Eng. Progr.*, **50**, 460 (1954).
14. Schumann, T. E. W., *J. Franklin Inst.*, **208**, 405 (1929).
15. Taecker, R. G., and O. A. Hougen, *Chem. Eng. Progr.*, **45**, 188 (1949).
16. Wilhelm, R. H., W. C. Johnson, and F. S. Acton, *Ind. Eng. Chem.*, **35**, 561 (1943).

Manuscript submitted October 3, 1956; revision received August 8, 1957; paper accepted September 4, 1957.

Fluid-particle Heat Transfer in Packed Beds

ERNEST B. BAUMEISTER and C. O. BENNETT

Purdue University, Lafayette, Indiana

Steady state heat transfer experiments were carried out in a 4-in. I.D. transite tube packed with 3/8-, 1/4-, and 5/32-in. steel spheres. Heat was generated in the pellets by means of a high-frequency induction coil surrounding the test section. Average heat transfer coefficients between the bed of spheres and a stream of air passing through the bed were calculated for Reynolds numbers of from 200 to 10,400. To ensure the reproducibility of the data, the bed was repacked six times for each pellet size.

A study of the effect of the tube-to-pellet–diameter ratio indicates that this effect is large for low values of the ratio, but much smaller for higher ratios. The results are presented both graphically and in terms of empirical equations. The analogies among heat, mass, and momentum transfer are discussed, and it was found that no simple relation between the heat transfer coefficient and the friction factor exists for packed beds with a gas as the fluid.

An attempt is made to predict the heat transfer rates for packed beds from heat transfer data for single spheres and from pressure-drop measurements for the packed bed; however, the rates predicted from the pressure-drop measurements are somewhat lower than the experimental results.

Packed beds have been used extensively in industry as catalytic reactors and also for heat transfer, absorption, and adsorption operations. Although many investigations have already been carried out to determine the heat transfer characteristics of packed beds, the direct application of the basic relationships developed to the design of packed beds has been held back by the inconsistancy of the data which have appeared in the literature.

Previous investigations have been carried out by both steady and unsteady state methods. In the steady state investigations the heat transfer coefficients are determined from a knowledge of the amount of heat transferred and the temperature difference between the pellets and the gas. In the unsteady state measurements the temperature history of the pellets and gas is measured and the coefficients are determined by a comparison of these data with the theoretical curves developed by Schumann (*17*). These curves were obtained from a solution of the differential equations describing the heat transfer in a bed of solids with no heat loss through the walls. Brinkley (*3*) extended the mathematical treatment to the case in which the solid generated heat. By using the concept of the effective thermal conductivity, Amundson (*1*) extended the treatment to include almost every conceivable case.

For the present investigation it was decided that an accurate investigation of the heat transfer relationships in packed beds could be obtained from a steady state system in which heat could be generated in the particles themselves at a sufficient rate to produce a large temperature difference between the particles and the gas passing through the bed. It was found that this could be accomplished by the use of a large high-frequency induction unit if metallic particles were used in a nonmetallic tube. Spheres were selected as particles so that the exact surface area would be known and also so that the data might be more readily interpreted for this regular packing.

It has been found that the ratio of tube to particle diameter has an effect on the heat transfer coefficient (*4*); therefore, three particle sizes were used, which allowed the ratio to vary from about 10 to 25. A bed diameter of 4 in. was selected so that pellets might be used which were large enough to permit the insertion of thermocouples without too great an effect. A bed height of 4 in. was used in order to decrease the end effects which might occur with a shorter bed.

As a bed is usually packed at random, the particles assume a different arrangement each time the bed is packed. In order to obtain data which would be

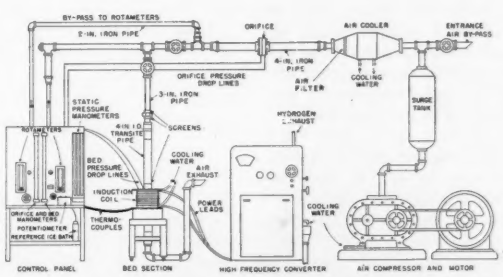

Fig. 1. Equipment layout.

Ernest B. Baumeister is with Atomics International, Canoga Park, California.

reproducible, the bed of spheres was emptied and repacked six times for each set of runs.

In order to interrelate heat and momentum transfer in the bed, pressure-drop measurements were also taken for each run.

EXPERIMENTAL APPARATUS AND PROCEDURE

Figure 1 shows a diagram of the experimental apparatus used in this investigation. Air, supplied by a blower, was passed through a cooler and a flow-metering instrument before entering the test section. The air entered the bed from the top and was discharged to the atmosphere after it passed through the bed. The cycloidal blower was designed to deliver 300 cu. ft. of air/min. when it was discharged at 15 lb./sq. in. gauge. The piping system was constructed of standard 2-, 3-, and 4-in. steel pipe. All valves used in the system were gate valves, to reduce the pressure drop through the system. The flow rates were measured by rotameters in the low flow range, and by an orifice for the higher flow rates.

The section containing the bed was constructed from a 4-in. I.D. Transite vent pipe ½ in. thick and 5 ft. long. This section was glued with an adhesive into sleeves welded to the steel-piping system. Figure 2 shows a detailed drawing of the packed section of the tube. The 4-in.–high test section was equipped with Bakelite flanges to facilitate removal and replacement of the packing. The packing support, which was constructed from a ½-in. wood fiber plate, consisted of a number of slits $\frac{3}{32}$ in. wide and spaced at distances of $\frac{3}{16}$ in. from center to center. Rubber gaskets were used with the flanges, and the bed was held in place by bolts machined from wood fiber. Pressure taps were drilled into the flanges at the entrance and exit of the bed on opposite sides of the flanges. An adhesive was used to connect the various parts of the bed, and glass wool insulated the bed and a section 3 in. above and below it.

Three different packings, 0.1555-, 0.2495-, and 0.3745-in.–diameter high-carbon-chrome–alloy steel ball bearings, were used in this investigation. Copper-constantan 30-gauge thermocouples were used throughout, and the thermocouples in the neighborhood of the induction coil were twisted in order to cancel the effect of the magnetic field on the generated electromotive force. No effect was observed on the thermocouple readings because of the electrical field. The thermocouples which measured pellet temperatures were placed in $\frac{1}{32}$-in. holes drilled into the center of the pellets, and the holes were filled with solder. At the bottom of the bed the pellets containing the thermocouples were spaced across the diameter of the bed so that the bottom layer of packing assumed a regular arrangement. The thermocouples measuring the air temperature at the exit of the bed were glued to the packing support directly below these pellets. At the top of the bed the pellets containing the thermocouples were evenly spaced across the diameter of the bed by means of a row of pellets glued together and to the tube wall. Thermocouples were also attached to the outside tube wall to obtain the heat loss through

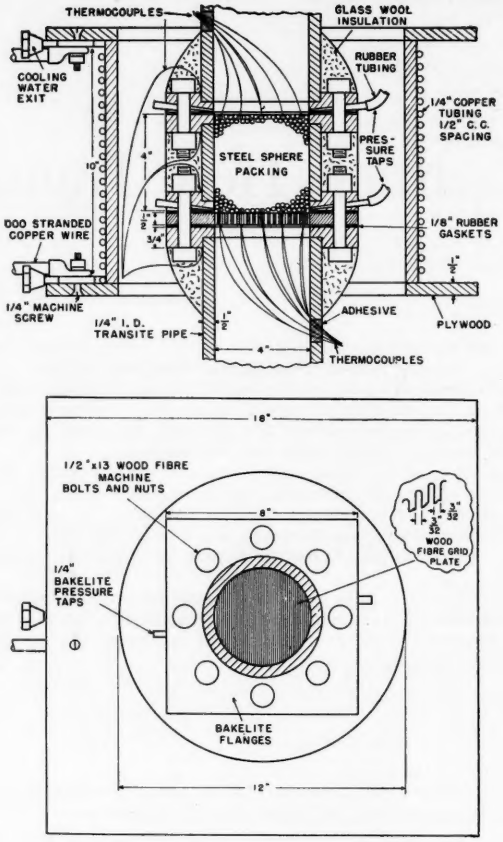

Fig. 2. Detail of bed and induction coil.

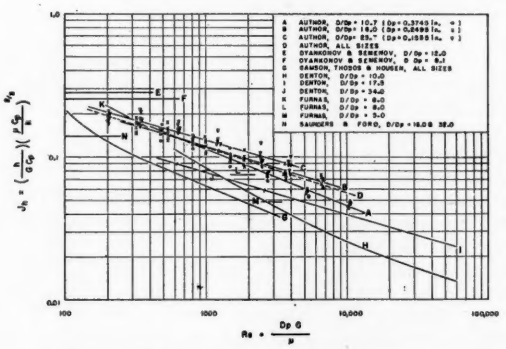

Fig. 3. Correlation of j_h with Reynolds number.

the wall. The air temperature was measured at five positions across the diameter at the exit of the bed, and since the air entered at a uniform temperature, only one temperature was required at the entrance of the bed. The pellet temperatures were measured at five positions across the diameter of the bed at both the entrance and exit of the bed. Suitable corrections, always very small, were made for the effects of radiation. The thermocouples used in the investigation were insulated up to the junctions. The maximum error due to conduction along the thermocouple leads was calculated to be less than 2%, which is well within the experimental error.

The induction coil used was 13 in. in diameter and 10 in. long and was constructed of ¼-in. copper tubing with ½-in. center-to-center spacing. The high-frequency current for the coil was supplied by a 20 kw. Ajax-Northrop converter. The spark gap of the converter operated in an atmosphere of hydrogen and produced current having a frequency of about 20,000 cycles.

The packing of the bed was carried out by placing the first two layers of pellets in the bed by hand, forming a regular packing. The rest of the bed was then filled by allowing the pellets to fall in place randomly from a stream of pellets at the center of the bed. The last layer of the bed was left out while the row of pellets containing the thermocouples was allowed to dry. Pellets were then filled in around this line of pellets to form a constant level at the top of the bed.

The air flow rate through the bed was controlled by an entrance bleed-off valve and by the flow-meter valves. Cooling water was used in the induction coil, the blower, and the high-frequency converter. The operating level of the converter was increased with increasing flow rate, and for each packing of the bed six different flow rates were used, the bed being repacked six times for each pellet size. For each run sufficient time was allowed for the temperatures in the bed to assume a steady state distribution. In addition to the temperature measurements, the static pressure at various points in the system and the pressure drop through the bed were also measured, and it was found that negligible pressure drop occurred across the empty bed.

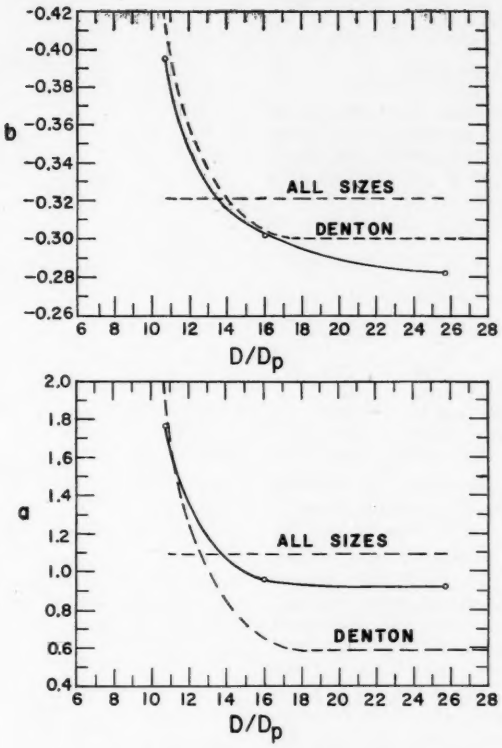

Fig. 4. Coefficients for j_h correlation.

EXPERIMENTAL RESULTS

The average heat transfer coefficients for the bed were calculated from the total heat generated in the pellets, the surface area of the pellets, and the mean temperature difference between the air stream and the pellets. The total heat generated by the pellets was determined as the sum of the sensible heat gain of the air passing through the bed and the heat loss through the wall. The latter was found to be quite small in comparison with the sensible heat. The heat transfer coefficient at the wall used to obtain the wall loss was obtained from the data of Leva (*13*). The mean driving force was calculated as the log mean temperature difference of the average driving force at the entrance and exit of the bed. The mean driving forces obtained in this investigation varied from about 4° to 30°F., depending on the flow rate and pellet size. The average driving forces at the entrance and exit of the bed were obtained from a graphical integration of the radial temperature differences versus the square of the radius. This produced an area mean driving force for the entire cross section. The data taken are too numerous to present here and may be found in reference *2*. A typical run is given in Table 1.

The inlet air temperature was measured above the top layer of pellets and the outlet air temperatures were measured below the bottom layer of pellets. The air temperatures corresponding to the pellet temperatures in each layer were obtained from the longitudinal air temperature gradient.

The average heat transfer coefficients obtained in this investigation are shown in Figure 3 in terms of j factors, along with the results of other investigators. The physical properties used in each case were taken at the arithmetic average temperature and pressure of the air between the entrance and exit of the bed. The air entered the bed at room temperature and attained temperatures up to 300°F. passing through the bed.

These data show a significant difference for each pellet size. Whereas the data for a given packing of the bed were found to be reproducible, the scattering of the

TABLE 1

EXPERIMENTAL DATA

Run 5B2
Pellet diameter = 0.2495 in.
Number of pellets = 3,996
Void fraction = 0.354
Total heat generation = 5,237 B.t.u./hr.
Mass velocity = 1,270 lb./(hr.)(sq. ft.)

	Outlet temp., °F.			Inlet temp., °F.	
r/r_0	Air	Pellet	r/r_0	Air	Pellet
0.843	280.9	293.9	0.750		117.9
0.469	277.0	290.0	0.375		105.8
0.000	258.6	271.6	0.000	89.1	106.3
0.463	275.3	288.3	0.375		104.4
0.843	283.1	296.1	0.750		119.2

data for a given pellet size is due to repacking the bed six times. Since a log-log plot of the data produced a straight line for the entire range studied, the data were correlated as

$$j_h = a\,Re^b \qquad (1)$$

A separate equation was obtained for each particle size as well as an equation which represented all particle sizes. These are listed in Table 2, and are somewhat

TABLE 2

CORRELATION OF j_h WITH REYNOLDS NUMBER

Pellet size, in.	a	b	95% Confidence limits, %
0.3745	1.58	−0.40	15.6
0.2495	0.96	−0.30	20.1
0.1555	0.92	−0.28	24.9
All sizes	1.09	−0.32	30.4

higher than those found by Gamson et al. (*10*), Denton (*4*), and Saunders et al. (*16*) and lower than those found by Dyankonov et al. (*5*). The experiments of Furnas (*9*) and of Saunders (curves *LMN*) were carried out under unsteady state conditions, and the Schumann curves were used to determine the heat transfer coefficients. In each case the heat was transferred from a hot gas to a bed of particles initially at a lower temperature. It is interesting to note that the values obtained by Furnas (*8*) (curve *K*), in which a pseudo steady state method of determining the coefficients was used, are in almost exact agreement with those of the authors. The data of Gamson (curve *G*) were obtained from experiments on the drying of wet catalyst carriers during the constant-rate drying period, and the coefficients were calculated on the assumption that adiabatic conditions prevailed in the bed. The bed was quite shallow in comparison with the particle size, and it was assumed that the entire surface of the pellets was wet. The curves of Denton (curves *HIJ*) are the results of experiments carried out by placing test spheres at various points in a packed bed. Heat was generated in the test spheres by means of a resistance heater inside each sphere. The experiments of Dyankonov (curves *EF*), which were published after the present work was under way, were carried out in approximately in the same way as those of this work, induction heating being used to generate heat in the pellets. The average temperature differences at the entrance and exit of the bed were taken as an arithmetic average of several values across the diameter of the bed. These values were not reported, but it was found in the present investigation that the temperature differences near the tube wall were much higher than those near the center of the bed, because of uneven heat generation in the bed. Therefore the actual mean difference would be somewhat higher than the arithmetic average difference. The flow rates and heat fluxes used for these experiments were much lower than those of the authors.

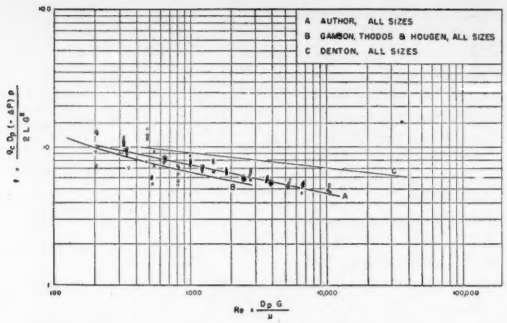

Fig. 5. Correlation of friction factor with Reynolds number.

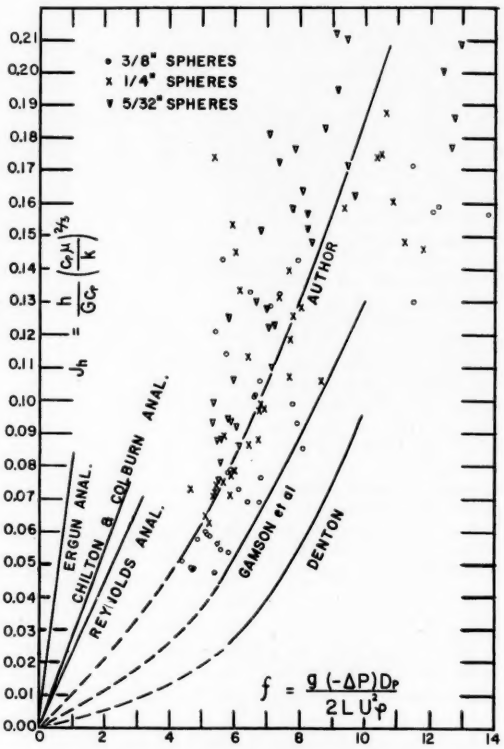

Fig. 6. Heat-transfer and pressure-drop analogies.

EFFECT OF TUBE- TO PARTICLE-DIAMETER RATIO

In correlating the heat transfer coefficients, it was found that the coefficient of the Reynolds number as well as the

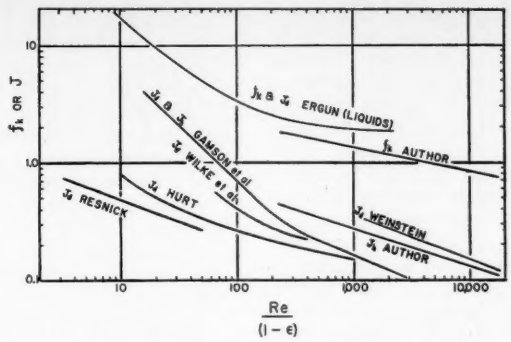

Fig. 7. Comparison of data for liquids and gases.

exponent varied with tube to particle diameter. Figure 4 shows the variation obtained from this experiment for the j_h correlation. The dotted line represents the data obtained by Denton. The following expressions were obtained:

$$a = 0.918[1 + 0.0148e^{0.565(18 - D/Dp)}] \quad (2)$$

$$b = -0.267 - \frac{0.257}{D/Dp - 8.70} \quad (3)$$

From these equations it can be seen that the effect of the ratio on the coefficient of the Reynolds number, a, becomes negligible above a value of about 18. The exponent, b, declines less rapidly as the ratio increases, but it can be seen that the effect of the ratio is still noticeable even at the highest ratios. These variations are due to the distortion in the packing at the tube wall. This wall effect is great for the smaller values of the ratio and diminishes as the ratio increases.

HEAT TRANSFER AND PRESSURE-DROP ANALOGIES

Figure 5 shows the pressure-drop data obtained in this investigation correlated in terms of Fanning friction factors. The data are represented by the equation

$$f = 30.7\, Re^{-0.20} \quad (4)$$

According to the analogies developed by Reynolds and by Chilton and Colburn for straight ducts, j_h could be expressed as a linear function of the friction factor. For packed beds these analogies can be expressed as

$$j_h = (Pr)^{2/3} \frac{\epsilon^3}{3(1-\epsilon)} f \quad (5)$$

for the Reynolds analogy and

$$j_h = \frac{\epsilon^3}{3(1-\epsilon)} f \quad (6)$$

for the Chilton and Colburn analogy. These equations are shown in graphical form in Figure 6 along with the data of this experiment. It can be seen that these analogies do not hold for this case and that the relationship between j_h and f is not linear as predicted. From the empirical equations developed for both, the relationship was found to be

$$j_h = 1.33\, Re^{-0.12} \frac{\epsilon^3}{3(1-\epsilon)} f \quad (7)$$

However, these analogies were developed for fluids flowing in straight ducts and would therefore not be expected to represent the data for a packed bed.

In correlating pressure-drop measurements from several investigations involving liquids, Ergun (6) described a friction factor which he defined as

$$f_k = \frac{(-\Delta P)}{L} \frac{g_c D_p}{\rho U^2} \frac{\epsilon^3}{(1-\epsilon)} \quad (8)$$

In another article (7) Ergun correlated mass transfer data obtained by a number of investigators and developed an analogy for packed beds which fit the data as follows:

$$J_d = f_k = 1.75 + 150 \frac{(1-\epsilon)}{Re} \quad (9)$$

where

$$J_d = \frac{6\epsilon k_g M_m}{G} \left(\frac{\mu}{D_f \rho}\right) \quad (10)$$

or for heat transfer this corresponds to

$$J_h = 6 \frac{\epsilon h}{G C_p} \left(\frac{C_p \mu}{k}\right) \quad (11)$$

This analogy is shown in Figure 7 along with the results of the authors as well as mass transfer data of other investigations.

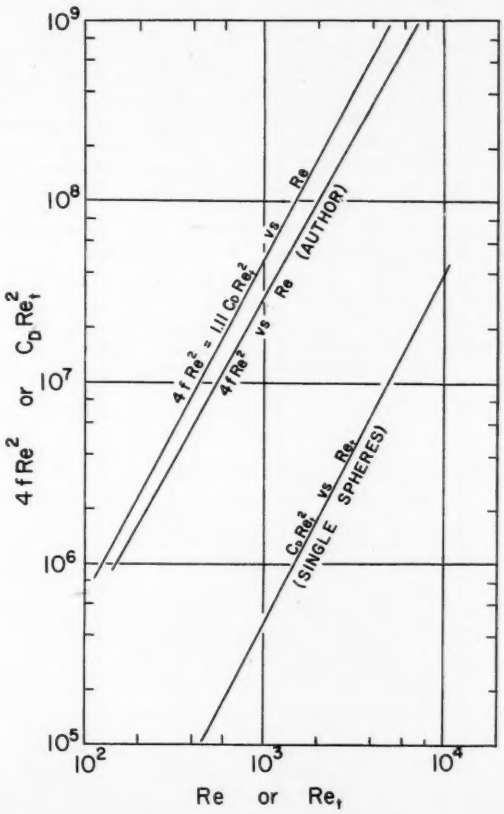

Fig. 8. Frictional resistance for single spheres and packed beds.

It can be seen that whereas this analogy works for liquids, the data for gases are quite different.

PREDICTION OF PACKED-BED TRANSFER RATES FROM RATES FOR SINGLE PARTICLES

It has been found that most of the pressure drop due to the flow around a single sphere takes place on the forward face of the sphere. Therefore, since the points of contact in a packed bed are at points of low pressure drop and the front faces of the spheres receive the full fluid stream, it is plausible that the pressure drop through a packed bed is an additive property of the pressure drop around single spheres. By assuming a model packing in a rhombohedral arrangement, Ranz (*14*) developed the following relation:

$$4f\,Re^2 = 1.111 C_D\,Re'^2$$

where Re′ is the Reynolds number based on the actual velocity at the front faces of the spheres in the bed. From the geometry of the packing it was calculated that

$$Re'/Re = 10.73$$

It has also been found that the heat and mass transfer rates around a sphere are at a maximum on the front face of the sphere, and therefore Ranz suggested that the transfer rates in packed beds would be the same as the transfer rates around a single sphere acted upon by a fluid stream with a velocity 10.73 times as great as the superficial velocity. Since this type of packing is idealized, it was suggested that for an actual bed the parameter to be used in predicting the transfer rates for the bed would be the ratio of Re'/Re as determined from pressure-drop data.

Figure 8 shows a plot of the pressure-drop data obtained in this investigation as well as the data for single spheres. It can be seen that the friction losses predicted by the model bed are slightly higher than those found by the authors, but they are in good agreement considering the crude model that was used for the mathematical development. From the data of this investigation, the parameter Re'/Re was found to be 9.4. Figure 9 shows the heat transfer rates for single spheres (*12*) and also the rates which would be predicted from this parameter in terms of Nusselt numbers. The predicted rates are somewhat lower than the data obtained in this investigation. The agreement is better near the low Reynolds number range, but it can be seen from the data that the rate of heat transfer from a single sphere is not affected so much by the Reynolds number as is that from the spheres in the packed bed.

SUMMARY

The average heat transfer coefficients for a packed bed vary with the ratio of tube to particle diameter for a given Reynolds number. The effect is quite significant for small values of this ratio and diminishes as the ratio is increased. Equations were developed which can be used to calculate the average heat transfer coefficient for a packed bed in terms of both the Reynolds number and the ratio of tube to particle diameter.

The analogies advanced for the simple interrelation of pressure drop, heat transfer, and mass transfer do not apply satisfactorily for packed beds when gas is used as the fluid.

By the method of Ranz, it was possible to predict the pressure drop for a packed bed fairly accurately. When the parameter suggested by this method was used, the predicted heat transfer coefficients were appreciably lower than the experimental values of this investigation.

ACKNOWLEDGMENT

The authors wish to acknowledge the financial support given by the American Cyanamid Company, The Eastman Kodak Company, and the Purdue University Engineering Experiment Station.

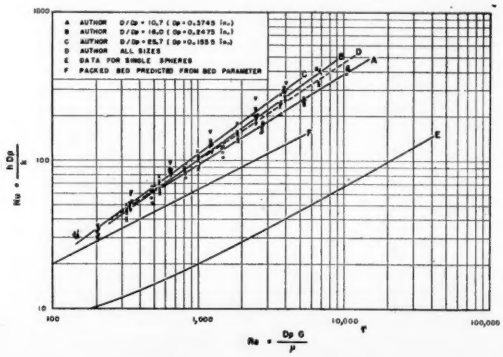

Fig. 9. Correlation of Nusselt number with Reynolds number.

NOTATION

- a = constant of proportionality
- b = exponent for j_h correlation
- C_p = fluid heat capacity
- D = tube diameter
- D_f = molecular diffusivity
- D_p = particle diameter
- f = Fanning friction factor
- f_k = Ergun friction factor
- G = mass velocity
- g_c = conversion factor
- h = average heat transfer coefficient
- j = Colburn analogy factor
- J = Ergun analogy factor
- k = fluid thermal conductivity
- k_g = mass transfer coefficient
- M_m = mean molecular weight
- P = Pressure
- Pr = Prandtl number
- Re = Reynolds number based on superficial velocity
- Re' = Re based on velocity through cross section open to flow
- U = superficial velocity

Greek Letters

- ϵ = void fraction
- μ = viscosity
- ρ = fluid density

LITERATURE CITED

1. Amundson, N. R., *Ind. Eng. Chem.*, **48**, 26 (1956).
2. Baumeister, E. B., Ph.D. thesis, Purdue Univ., Lafayette, Iud. (1957).
3. Brinkley, S. R., *J. Applied Phys.*, **18**, 582 (1947).
4. Denton, W. H., "Proceedings of the General Discussion on Heat Transfer," Inst. of Mech. Engrs. (London), p. 370 (1951).
5. Dyankonov, G. K., and G. A. Semenov, *Izvest. Akad. Nauk S.S.R. Otdel. Tekh. Nauk*, No. 7, 109 (1955).
6. Ergun, S. K., *Chem. Eng. Progr.*, **48**, 89 (1952).
7. *Ibid.*, p. 227.
8. Furnas, C. C., *Ind. Eng. Chem.*, **22**, 26 (1930).
9. ———, *Trans. A.I.Ch.E.* **24**, 142 (1930).
10. Gamson, B. W., George Thodos and O. A. Hougen, *Trans. A.I.Ch.E.*, **39**, 1 (1943).
11. Hurt, D. M., *Ind. Eng. Chem.*, **35**, 522 (1953).
12. Kramers, H., *Physica*, **12**, 61 (1946).
13. Leva, Max, *Ind. Eng. Chem.*, **39**, 857 (1947).
14. Ranz, W. E., *Chem. Eng. Progr.*, **48**, 247 (1952).
15. Resnick, W., and R. R. White, *Chem. Eng. Progr.*, **45**, 377 (1949).
16. Saunders, O. A., and H. J. Ford, *J. Iron and Steel Inst.*, **1**, (London), 290 (1940).
17. Schumann, T. E. W., *J. Franklin Inst.*, **208**, 405 (1929).
18. Weinstein, H., M.S. thesis, Purdue Univ., Lafayette, Ind. (1957).
19. Wilke, C. R., and O. A. Hougen, *Trans. A.I.Ch.E.* **41**, 455 (1945).

Manuscript received in editorial office on March 7, 1957; revision received on November 25, 1957; paper accepted November 26, 1957.

Local Boiling Coefficients on a Horizontal Tube

R. P. LANCE and J. E. MYERS

Purdue University, West Lafayette, Indiana

Local boiling heat transfer coefficients were experimentally determined for nucleate boiling around the outer circumference of horizontal copper tubing. The tubes used were of 16 B.W.G. hard-temper copper with outside diameters of 1 1/4 and 2 in.; the liquids boiled were methanol and *n*-hexane. The maximum peripheral variation occurred with the 1 1/4-in. tube in methanol where an over-all ΔT of 30.2°F. gave local outside coefficients varying between 249 and 548 B.t.u./(hr.)(sq. ft.)(°F.). The minimum variation was found to occur in the same system, in which an over-all ΔT of 72.3°F. gave coefficients varying between 856 and 910 B.t.u./(hr.)(sq. ft.)(F.°). The results, plotted in polar coordinates, showed a cardioid configuration for methanol with the maximum coefficients occurring at the bottom of the tube. The *n*-hexane results had the general shape of horizontal ellipses with maximum coefficients occurring at the sides of the tube.

A considerable amount of experimental work has been described in the technical literature in which nucleate, boiling heat transfer coefficients have been measured on the outer surfaces of horizontal tubes, cylinders, and wires. In almost all these studies the coefficients reported were considered to be average values representing the entire outer tube surface. As it was known that artificial agitation could cause significant increases in boiling coefficients, it appeared likely that the vapor rising from the lower portion of a horizontal tube should have an effect on the heat transfer characteristics of the upper portion of the same tube. The present investigation was made to determine some of the conditions under which this variation might be significant.

The only reference that could be found describing prior work of this nature is that of Katz et al. (*2*), who used a single apparatus for studying both boiling and condensing processes. Using a system in which steam condensed inside a horizontal tube and *n*-hexane boiled on the outside, they noted temperature variations around the periphery of the tube wall; however, these were attributed in part, to the collection of condensate along the bottom of the tube.

The effects of external agitation on a boiling system are described by McAdams (*4*) and Beecher (*1*), who report that at low temperature differences the heat flux was thereby increased. Robinson and Katz (*6*) observed that the average boiling coefficient measured on a horizontal tube was appreciably raised by the introduction of vapor beneath the tube. Myers and Katz (*5*) measured the average boiling coefficient for each tube of a vertical tier of four tubes and found that at all temperature differences studied the boiling coefficients obtained from the upper three tubes were significantly greater than for the bottom tube.

EXPERIMENTAL

The basic experimental apparatus consisted of a single copper tube passing horizontally through a vessel containing the liquid to be boiled. Hot water passing through the tube served as the heat source. The careful placing of thermocouples permitted measurement of the wall temperature, the bulk temperature of the fluid inside the tube, and the bulk temperature of the boiling fluid, all at the same longitudinal position. Carrying out a prior experimental program to determine a correlation between the inside film coefficient and the flow variables made it possible to predict the heat transfer coefficient for the inside surface at the point where the temperature measurements were made.

The following equation represents a heat balance at this point:

$$dq = h_i\, dA_i(T_i - T_w)$$
$$= h_o\, dA_o(T_w - T_o) \qquad (1)$$

This equation may be solved for the local boiling coefficient (h_o) to give

$$h_o = \frac{h_i D_i}{D_o} \frac{(T_i - T_w)}{(T_w - T_o)} \qquad (2)$$

Among the simplifying assumptions employed when the equations above were used was the use of a tube-wall temperature measured midway between the inner and outer tube surfaces to represent the temperature of each. Because Equation (2) involves a ratio of temperature differences, the errors thus produced in the numerator and denominator are not additive but subtractive. The maximum error in h_o resulting from this procedure was found to be 1.1% and the average 0.7%.

Further assumptions were that the inside film coefficient of heat transfer was independent of angular and longitudinal position and that the bulk temperature of the fluid inside the tube was equal to the temperature measured at the tube axis. A fourth assumption was that the contribution of peripheral heat conduction in the tube was negligible. In this latter case, if the existence of a vertical plane of symmetry is assumed, then it would follow that the temperature gradient would be zero at both the top and bottom of the tube. At all other points, however, the existence of

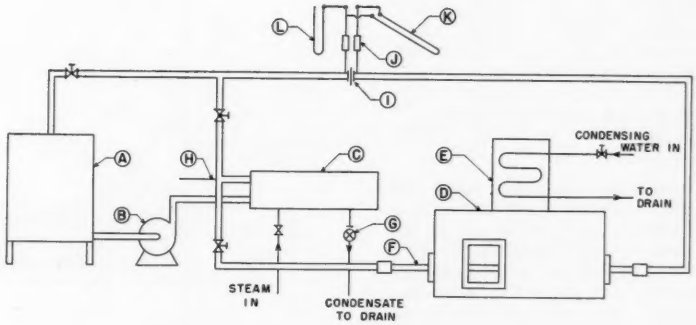

Fig. 1. Diagram of equipment.

R. P. Lance is at present with California Research Corporation, San Francisco, California.

unequal film coefficients would result in temperature gradients that would cause Equations (1) and (2) to be in error. To avoid this possibility, the section of the tube circumference being used for measurements was thermally insulated from the remainder of the circumference in a manner which will be described later.

APPARATUS

The apparatus, described above, is shown schematically in Figure 1. Distilled water was pumped from a 55-gal. drum into the tube side of a Ross (type BCF) heat exchanger, where it was heated by steam condensing on the shell side. The hot water leaving the exchanger flowed through the experimental boiler, then through an orifice, and back to the surge drum. Sufficient pressure was kept on the system so that vaporization was prevented at the orifice.

The boiler, shown in Figure 2, was an insulated rectangular tank 15 in. wide, 27 in. long, and 17 in. high, constructed from ⅛-in. sheet steel. It was fitted with a rectangular sight glass on each side and a multipass, finned-tube condenser. A drip pan placed beneath the condenser distributed the condensate to both sides of the boiler.

On each end of the boiler a packing gland was installed to permit easy rotation of the tube while a liquid seal was maintained. Copper tubes of two different diameters were employed as test sections. Circular cast-iron I-shaped flanges of identical outside diameter were constructed and soldered to each tube. The outer edges of these flanges rotated against the asbestos packing which provided the seal. The thermocouple leads were brought out through the flanges.

The test section of tubing was a 3-in. length shown in the detailed diagram, Figure 3. Two sizes were used, the dimensions of which are shown in Table 1.

TABLE 1—DIMENSIONS OF EXPERIMENTAL TUBES

	1¼-in. tube	2-in. tube
Wall thickness, in.	0.065	0.065
Inside diameter, in.	1.120	1.870
Outside area, sq. ft./ft.	0.327	0.523
Inside area, sq. ft./ft.	0.302	0.490
Inside cross-sectional area, sq. in	0.985	2.747
Total outside area for heat transfer, sq. ft.	0.681	1.091

The tube-wall thermocouple installation is illustrated in Figures 3 and 4. Two holes were drilled in opposite ends of the 3-in. test section and a single thermocouple wire, placed inside hypodermic tubing, was then soldered into each hole. The constantan thermocouple wire was connected to the upstream end of the test section and the copper wire to the downstream end. Because the small longitudinal gradient in the tube wall further diminished any minor error due to the voltage generated at the junction of the copper wire and tubing, the calibrated assembly thus gave the temperature of the wall at the point where the constantan wire made contact. After

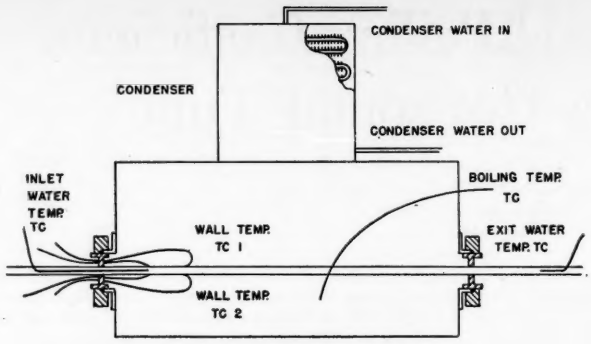

Fig. 2. Detail diagram of boiler.

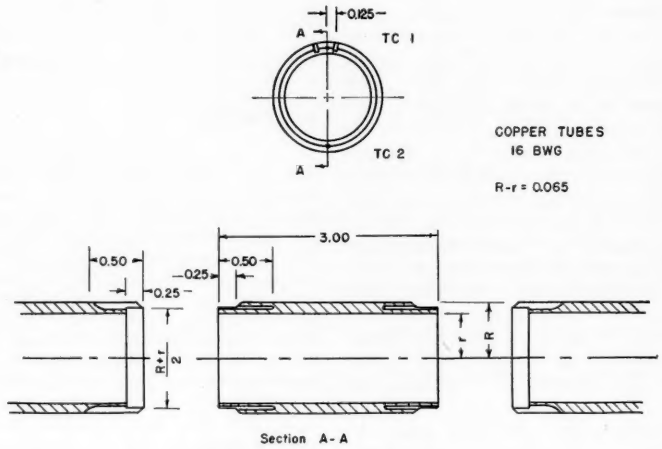

Fig. 3. Test-section details.

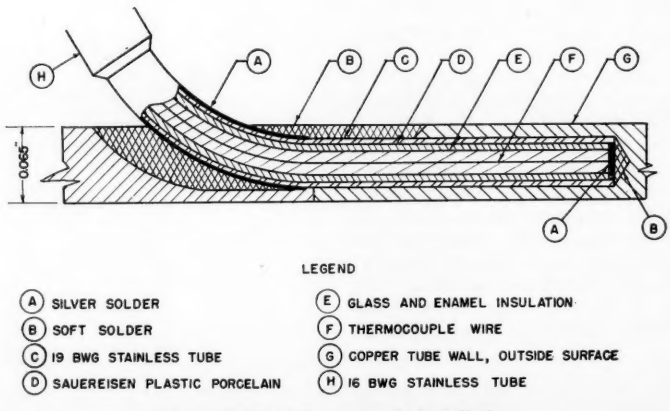

Fig. 4. Detail of thermocouple installation.

the thermocouple wires had been installed in the 3-in. test section, the assembly was soldered together and the surface of the copper tubing polished with size 0 emery paper. Temperature measurements indicated that the surface became stable after boiling for a period of 2 days.

To reduce the possibility of peripheral conduction the segment of the circumference containing the tube-wall thermocouple was thermally insulated by milling grooves on both sides of the thermocouple installation and filling those grooves with an insulating material. The grooves were 0.0312 in. wide and 0.005 in. deep. They were located a distance of 0.125 in. on either side of the thermocouple, thus insulating a 14-deg. segment of the 2-in. tube and a 23-deg segment of the 1¼-in. tube. The grooves were filled with sauereisen plastic porcelain 78, covered with a dilute solution of sodium silicate, and polished until smooth.

Copper-constantan thermocouples enclosed in stainless steel hypodermic tubing were used to measure water temperatures at the center of the copper tubing and the bulk temperature of the boiling fluid. The inlet water temperature was taken at a point 2 in. inside the boiling vessel at the same longitudinal position as the constantan wire of the tube-wall thermocouple. Thus the effective length of the tube was 25 in. The water and tube-wall thermocouples were calibrated by circulating hot water through the tube, which for this purpose was covered with heavy insulation.

Measurements were taken with two fluids used in the boiler: methanol of 99.85% purity, which was obtained from the Commercial Solvents Corporation, and *n*-hexane with a boiling range of 65° to 67°C., obtained from the United Fuel Gas Company.

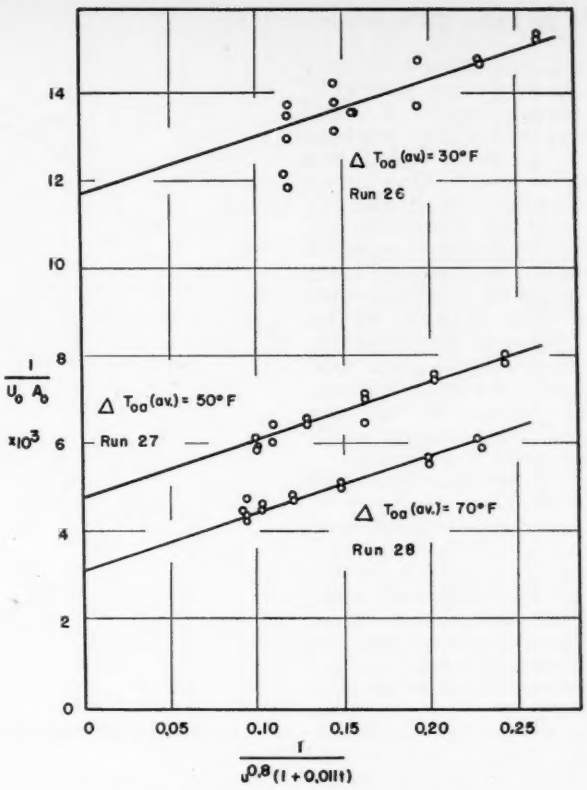

Fig. 5. Wilson plot for 1-1/4-in. tube.

DETERMINATION OF INSIDE FILM COEFFICIENTS

The film coefficients of heat transfer for the inside surface of the copper tubing were determined by the method of Wilson (7). The procedure involved keeping the boiling film resistance constant while varying the water film resistance. Since the boiling film coefficient of heat transfer has a unique value for each heat transfer rate in a given system, the criterion of constant heat flux was used as the method of obtaining constant-boiling film resistance.

As the purpose of the project was to determine the variation in local boiling coefficients, it may seem paradoxical that an "average" boiling coefficient should be assumed over the entire surface of the tube; however, as will be seen later the boiling coefficients were found to be nearly uniform at high boiling rates, and it was the information obtained from these runs which provided the key data for determining the inside film coefficients. The negligible effect of longitudinal variation is indicated by the fact that for nearly all runs the temperature decrease of the water passing through the tube was less than 5% of the over-all-temperature-difference driving force. Thus the concept of the average coefficient for

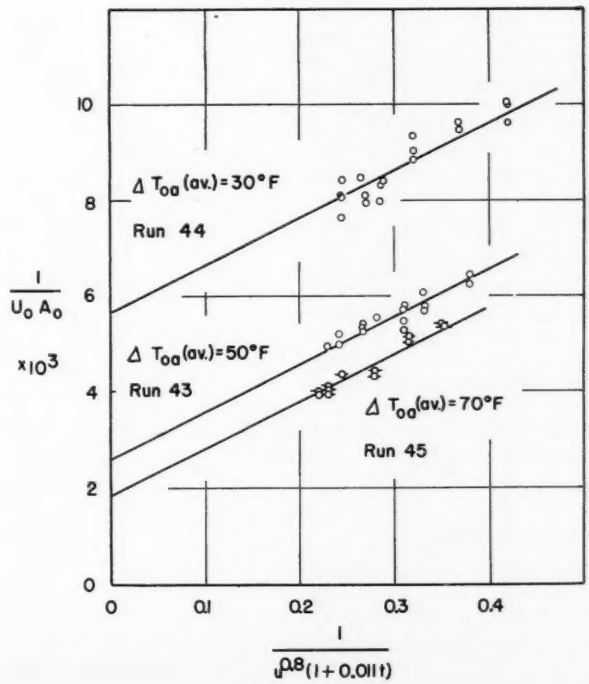

Fig. 6. Wilson plot for 2-in. tube.

purposes of the Wilson plot seems justified.

The Wilson plots, shown in Figures 5 and 6, represent the data taken solely for the determination of the inside coefficients of the two tubes. Methanol was used as the boiling fluid in both cases. Data are shown for three average over-all temperature differences, $\Delta T_{oa(avg)}$ = 30°, 50°, and 70°F. The average heat loads corresponding to these temperature differences were 2,300, 7,900, and 13,900 B.t.u./hr. for the 1¼-in. tube and 3,600, 9,700 and 16,100 B.t.u./hr. for the 2-in. tube. Obviously, the over-all-temperature-difference driving force could not be held constant during a set of runs, in addition to the heat flux, and so the values given as $\Delta T_{oa(avg)}$ represent merely a convenient method of designation.

Both sets of data show considerable scattering at the lowest heat-flow rates, owing to the low temperature differences observed (0.41 to 1.28°F.). If a possible error of ±0.1°F. is assumed for these readings and appropriate error values are taken for the other quantities entering the calculation, the possible errors in the ordinate values range between 11.1 and 29.8% for these two sets of data. The average possible errors are ±20.3% for run 26 (Figure 5) and ±16.1% for run 44 (Figure 6). However, the larger temperature differences observed for the other four runs result in much lower average possible errors of ±7.7% (run 27), ±5.4% (run 28), ±6.9% (run 43), and ±4.7% (run 45).

The best fitting straight lines on Figures 5 and 6 were established visually for the four runs at the high heat loads. Lines parallel to these were drawn for the two runs at low heat loads. This procedure is justified by the inclusion in the abscissa of the term representing the effect of water temperature on film coefficient.

The inside water film coefficients were obtained by the usual method of subtracting the ordinate intercepts from the ordinate values representing experimental runs. The values obtained for the 1¼-in. tube checked with the predicted coefficients by use of the Dittus-Boelter equation. Values obtained experimentally for the 2-in. tube were about 20% lower than the predicted values, possibly because of an entrance effect. The same external-flow system of 1-in. galvanized pipe was used for both tube sizes. The pipe-to-tubing connection was located 14 pipe diameters upstream from the boiler.

LOCAL BOILING COEFFICIENTS

Twelve sets of data were taken, from which local nucleate boiling coefficients were determined. The procedure involved all possible combinations of the two tubes, two boiling fluids, and three over-all temperature differences. The operating conditions are given in Table 2 and the

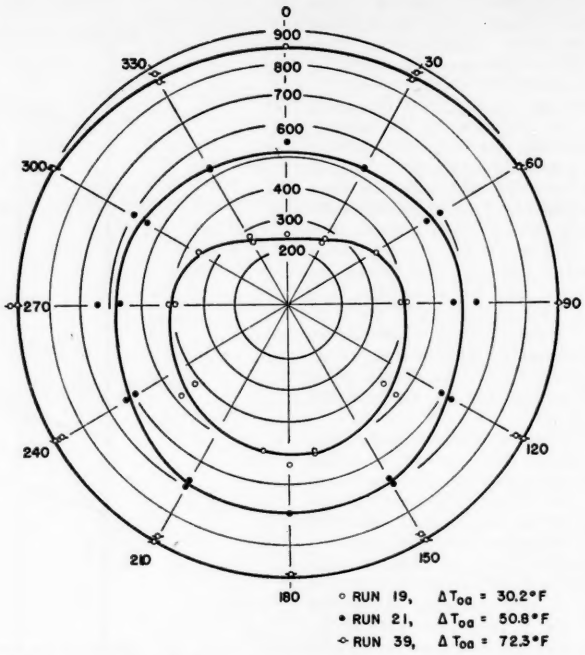

Fig. 7. Boiling coefficient profile—methanol; 1-1/4-in. copper tube.

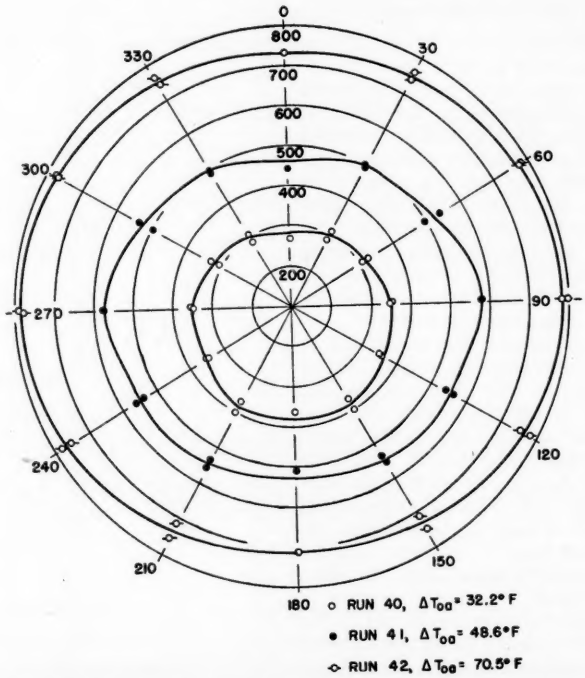

Fig. 8. Boiling coefficient profile—*n*-hexane; 1-1/4-in. copper tube.

experimental results in Figures 7 through 10.

The use of the Wilson plots described above was limited to obtaining inside film coefficients at only one water flow rate for each of the two tube sizes. This flow rate, chosen so as to be in the middle of the operating range—and at the same Reynolds number for each tube—was 58 lb./min. for the 1¼-in. tube and 97 lb./min. for the 2-in. tube.

The peripheral variation in heat transfer was determined by rotating the tube following each set of readings. The angular increment between reading positions was 30 deg., with the 0-deg. position taken as that in which the thermocouple was at the top of the tube. In each run two sets of readings were taken, with the tube being rotated 360 deg. in one direction and then 360 deg. in the opposite direction. The readings were averaged.

The experimental results are shown in Figures 7 through 10. Since there was little to distinguish one side of the tube from the other (the boiling vessel having a vertical plane of symmetry), the average coefficients referred to above were plotted on both sides of the graph and the best-fitting lines drawn through them. Each figure gives in polar coordinates the boiling coefficients plotted as a function of angular position at three values of the over-all-temperature-difference driving force.

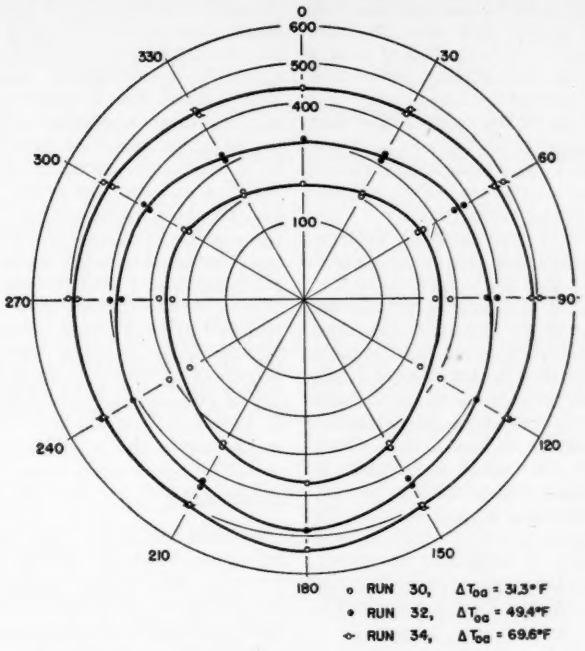

Fig. 9. Boiling coefficient profile—methanol; 2-in. copper tube.

EXPERIMENTAL RESULTS

The most obvious features of the results is the approach to radial symmetry as the temperature difference is increased. This probably indicates the dominant effect of local turbulence near the interface over the general agitation in the system when local heat transfer rates become high. Such a view would be substantiated by the results of Robinson (*6*), who found that the effect of artificial turbulence on heat transfer was negligible at high heat transfer rates.

The configurations measured by use of the two different fluids are quite unlike. For example, the ratio of maximum to minimum coefficients is greater for methanol than for *n*-hexane in all cases except one—that being the pair of runs (39 and 42) made on the 1.25-in. tube at the highest heat transfer rate. Even more obvious is the difference in the shape of the curves for the two fluids, the curves for methanol being of cardioid shape and the results from *n*-hexane of a generally elliptical shape, Table 2 contains a summary of the maximum and minimum coefficients measured for each run and the ratios of these extremes.

It had been anticipated that the maximum coefficients would occur at the 90- and 270-deg. positions as these would seem to be the points most affected by the vapor produced elsewhere on the tube. That this was the case for *n*-hexane

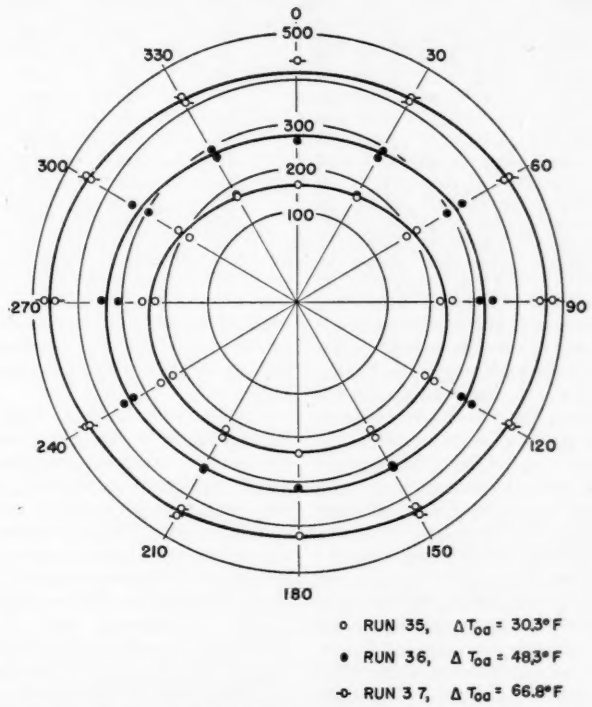

Fig. 10. Boiling coefficient profile—*n*-hexane; 2-in. copper tube.

and not for methanol may be due to the slightly lower coefficients found for *n*-hexane. This effect may also have been influenced by the fact that the volumetric latent heat for *n*-hexane of 26.9 B.t.u./cu. ft. was slightly lower than that for methanol, which was 33.0 B.t.u./cu. ft. Thus comparable heat transfer rates would produce a greater volume of *n*-hexane vapor than methanol vapor and accentuate the elliptical character of the results.

The boiling system was observed visually during the various runs and it was noticed that the bubbles formed on the bottom of the tube were somewhat larger than those formed on the sides. It might be expected from considerations of buoyancy that bubbles formed on the underside of the tube would be less easily dislodged than those on the remainder of the surface and would, as a result, grow larger. This would undoubtedly be another cause of lack of uniformity in the boiling coefficients around a tube. The experimental results at low heat loads all show a lack of horizontal symmetry, though why the coefficients are larger at the bottom than at the top is difficult to say.

No correlation expressing the variation in boiling coefficients around a tube is known to the authors, and because of the limited amount of such data available, no attempt was made to find one in this study. It is the authors' opinion that such a correlation, if found, might take the form of an expression for the boiling coefficient at high heat loads, modified by a coefficient expressing the angular variation at lower heat loads, where this variation becomes significant. The reference coefficient at high heat loads would be determined by the usual physical characteristics of the liquid-solid system, The second term would be an expression of the effects of the environment on local turbulence and would include such properties as would determine the volumetric rate of vapor evolution, velocity of bubble ascent, and the transport of momentum in the liquid-gas system.

CONCLUSIONS

1. Local nucleate boiling coefficients have been measured around horizontal tubes 1¼ and 2 in. in diameter and have been found to vary substantially with angular position on both tubes. The greatest variation on a tube in a single run was such that the maximum coefficient was 120% greater than the minimum.

2. The variation in local boiling coefficients decreases as the heat load is increased. At the maximum over-all temperature differences employed, the variation was about 10 to 20%.

3. The configurations obtained when the boiling coefficients were represented in polar coordinates were found to be quite dissimilar for the two liquids. The curves for methanol were of cardioid shape with maximum coefficients occurring at the bottom of the tube, and those for *n*-hexane resembled horizontal ellipses with maximum coefficients at the sides of the tube.

4. It appears that boiling coefficients reported in the literature as being measured on horizontal tubes are average coefficients, depending on the method of measurement. This may explain some of the discrepancies in the literature on boiling heat transfer.

TABLE 2

Run	Boiling fluid	Temp. of boiling fluid, °F.	Tube size, in.	ΔT_{0a}, °F.	Water rate, lb./min.	Inside coefficient, B.t.u./(hr.)(sq. ft.)(°F.)	Outside coefficient, B.t.u./(hr.)(sq. ft.)(°F.) Min.	Outside coefficient, B.t.u./(hr.)(sq. ft.)(°F.) Max.	Ratio of outside coefficients, $\frac{h_{max.}}{h_{min.}}$
19	Methanol	148.8	1.25	30.2	58.0	756	249	548	2.20
21	Methanol	148.0	1.25	50.8	58.0	788	515	708	1.37
39	Methanol	149.2	1.25	72.3	57.7	828	856	910	1.06
40	*n*-hexane	152.0	1.25	32.2	58.0	754	264	403	1.53
41	*n*-hexane	151.4	1.25	48.6	57.8	792	445	582	1.31
42	*n*-hexane	151.6	1.25	70.5	57.9	829	714	796	1.12
30	Methanol	149.3	2.00	31.3	97.1	331	205	368	1.79
32	Methanol	148.4	2.00	49.4	97.0	355	309	490	1.58
34	Methanol	148.4	2.00	69.6	96.5	394	438	542	1.24
35	*n*-hexane	152.0	2.00	30.3	97.0	333	164	258	1.57
36	*n*-hexane	151.6	2.00	48.3	97.0	357	260	356	1.37
37	*n*-hexane	151.6	2.00	66.8	96.8	394	414	478	1.15

A comparison of the results to determine the effect of tube diameter indicates that the ratio of maximum to minimum boiling coefficients is slightly greater for the 2-in. than for the 1¼-in. tube in five of the six possible cases when the over-all temperature difference is approximately the same. However, there is no good reason for using the equal temperature difference as a basis for comparison, and it would seem that no conclusions regarding tube diameter are relevant beyond the statement that there is a considerable variation in the boiling coefficient around both 1¼- and 2-in. tubes. Perhaps experimental data measured on smaller tubes would provide further useful information on this factor; however, the experimental difficulties would be considerably greater in such a program.

ACKNOWLEDGMENTS

The authors wish to acknowledge the generosity of the Wolverine Tube Company in supplying the tubing used in this investigation.

NOTATION

dq = heat transfer rate through differential segment of tube, B.t.u./hr.
dA_i = area of differential element inside the tube, sq. ft.
dA_o = area of differential element outside the tube, sq. ft.
D_i = inside diameter of tube, ft.
D_o = outside diameter of tube, ft.
h_i = local film coefficient of heat transfer on the surface dA_i, B.t.u./(hr.)(sq. ft.)(°F.)
h_o = local film coefficient of heat transfer on the surface dA_o, B.t.u./(hr.)(sq. ft.)(°F.)
t = average of tube inlet and outlet water temperatures, °F.
T_i = bulk temperature of the water inside the tube at point of measurement, °F.
T_w = wall temperature at point of measurement, °F.
T_o = bulk temperature of the boiling fluid at point of measurement, °F.
ΔT_{0a} = average value of over-all-temperature-difference driving force $(T_i - T_0)$, °F.
u = bulk water velocity in tube, ft./sec,
U_0 = average over-all heat transfer coefficient based on total outside tube area (A_0), B.t.u./(hr.)(sq. ft.)(°F.)

LITERATURE CITED

1. Beecher, Norman, S.M. thesis, Mass. Inst. Technol., Cambridge (1948).
2. Katz, D. L., G. H. Hanson, H. S. Kemp, and E. G. Opdyke, *Petroleum Refiner*, **25**, 419 (1946).
3. Lance, R. P., M.S. thesis, Purdue University, Lafayette, Ind. (1956).
4. McAdams, W. H., "Heat Transmission," 3 ed., p. 378, McGraw-Hill Book Company, Inc., New York (1954).
5. Myers, J. E., and D. L. Katz, *Chem. Eng. Progress Symposium Series* No. 5, p. 330 (1953).
6. Robinson, D. B., and D. L. Katz, *Chem. Eng. Progr.*, **47**, 317 (1951).
7. Wilson, E. E., *Trans. Am. Soc. Mech. Engrs.*, **37**, 47 (1915).

Manuscript submitted March 14, 1957; revision received August 19, 1957; paper accepted September 20, 1957.

Natural-convection Heat Transfer in Regions of Maximum Fluid Density

R. S. SCHECHTER, University of Texas, Austin, Texas

H. S. ISBIN, University of Minnesota, Minneapolis, Minnesota

One of the important factors affecting the rate of heat transfer by natural convection is the temperature-density relationship of the convecting fluid. The importance of this factor is amplified when the heat is being transferred to a medium which has a maximum density.

This investigation consisted of measuring the heat transfer rates, velocity gradients, and temperature profiles when heat is transferred from a flat vertical plate to water in the region of 4°C. In some experiments the flow in the boundary layer was observed to be downward while at other conditions of plate and fluid temperature a dual motion (both up and down) was noted, thus establishing a basic difference in the heat transfer mechanism and precluding a unified theory. Theoretical consideration is given to each mechanism and a criterion is derived to predict the flow regime which will prevail at fixed conditions of plate and bulk temperatures.

An analogue computer was used to establish theoretical velocity and temperature profiles. The theoretical values agree reasonably well with the measured values; however, the experimental temperature gradients near the wall were not sufficiently accurate to be extrapolated to determine a point heat transfer coefficient.

For the usual conditions governing natural convection, the following equations are used to describe the motion, heat conduction, and continuity conditions (*4*):

$$\rho\left(u\frac{\partial u}{\partial x}+v\frac{\partial u}{\partial y}\right) = g(\rho_\infty-\rho)+\mu\frac{\partial^2 u}{\partial y^2} \quad (1)$$

$$\frac{\partial u}{\partial x}+\frac{\partial v}{\partial y}=0 \quad (2)$$

$$u\frac{\partial T}{\partial x}+v\frac{\partial T}{\partial y}=\alpha\frac{\partial^2 T}{\partial y^2} \quad (3)$$

With boundary conditions

$$\begin{aligned} &t=t_p \quad u=0 \quad v=0 \quad \text{at} \quad y=0 \\ &t=t_\infty \quad u=0 \quad v=0 \quad \text{at} \quad y=\infty \end{aligned} \quad (4)$$

The coordinates for the vertical-plate geometry are given in Figure 1. The boundary-layer thickness is assumed to be small in comparison with the length of the plate and, therefore, the second derivatives with respect to x have been neglected. Further, Equations (1), (2), (3), and (4) are written with incompressibility of the fluid, steady state, two-dimensional flow, a constant surface temperature, and a constant density throughout the fluid assumed except in the evaluation of the quantity $(\rho_\infty - \rho)$.

This quantity, which appears in Equation (1), represents the driving force that produces the convection currents. This term is normally (i.e., for cases in which the density of the convecting fluid decreases uniformly with increasing values of the temperature) positive for a heating process and negative for a cooling process. A positive driving force indicates that the force is in the positive x direction.

The magnitudes and directions of the driving forces acting upon a convecting medium are a function of the temperature gradients within the boundary layer and the density-temperature relationship. In that the density of water is a maximum at 4°C., convective heat transfer to water in the region of 4°C. can produce a situation in which both positive and negative forces are acting on the fluid. An example is the forces which exist when a plate that is maintained at 12°C. is immersed in a water bath cooled to 1°C. The driving force is positive at those points within the boundary layer at which the water temperature is greater than 7.04°C., since the quantity $(\rho - \rho_\infty)$ is positive. The term $(\rho - \rho_\infty)$ becomes negative when the water temperature is less than 7.04°C. and is zero at 7.04°C. Owing to the existence of both positive and negative driving forces, fluid motion should occur in both the upward and downward directions simultaneously.

Dumore, Prins, and Merk (*1*) studied the heat transfer characteristics of ice spheres immersed in a water bath. They demonstrated experimentally that the heat transfer coefficient tended toward a minimum value at a bath temperature of 4.8°C. These experimenters suggested that the convective motion within the boundary layer becomes inverted at 4.8°C., the motion being upward when the bath temperature is less than 4.8°C. and downward when the bath temperature is greater. Upon this hypothesis, Merk (*6*) developed a theoretical expression relating the heat transfer coefficient for the physical properties of the fluid and the temperature difference which is in good agreement with the heat transfer coefficients measured by Dumore, Prins, and Merk. However, as has been pointed out, there is reason to suspect the formation of a dual motion rather than a simple inversion of the direction of motion.

QUALITATIVE OBSERVATIONS

An insight into the mechanism of natural convection in the region of maximum fluid density may be achieved by studying the fluid velocities within the boundary layers.

The velocities which are produced by density gradients in water, as measured by a visual technique, are about 1 cm./sec. Polystyrene particles (325–400 mesh) were introduced into the bath, and a beam of light was directed toward the plate. Light was reflected from the suspended particles and visually detectable by a lens system arranged as shown in Figure 2. A particle in motion could be observed and its speed determined by use of a stop watch and the increments of distance were furnished by an imposed grid system.

To test the accuracy of this technique of velocity measurement, three runs were performed in which the bulk temperature was fixed at such a level as to avoid maximum density within the boundary layer. The velocity distribution for this case has been computed numerically by Ostrach (*7*) using a digital computer and by Schechter (*10*) on an analogue computer. The experimental velocities are compared with the numerical solution obtained by Schechter and the results are shown in Figure 3. The experimental values of the velocity are consistently less than those predicted by the numerical solutions, the discrepancies probably being accounted for by the slightly greater particle density (1.05). The velocity measurements are within an accuracy of ±25%.

For those runs in which the bath temperature was maintained below 4°C. the velocity pattern behaved qualitatively as follows.

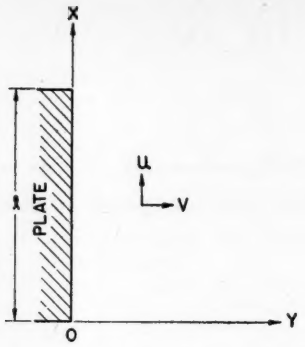

Fig. 1. Coordinate system for vertical plate.

1. As the plate is heated initially, the flow in the boundary layer is downward.
2. Increasing the plate temperature results in a decrease in the magnitude of the velocities.
3. If the plate temperature is increased sufficiently, a point of stagnation occurs near the plate surface; consequently, not only is the velocity at the surface of the plate zero, but the velocity gradient is also zero. It is under these conditions that the positive driving force near the surface offsets the negative force resulting from the viscous effects of the downward motion.
4. Any further increase in the plate temperature will result in a dual motion. The fluid near the plate will move upward and that in the outer portion of the boundary layer will move downward. A typical example of this dual motion is shown in Figure 4.

Those conditions which produce dual convection currents are termed *inverted convection regimes* and the cases in which only a falling or a rising film occur are called *normal*, or *unidirectional, convection regimes.*

A qualitative sketch of the velocity pattern existing at the upper edge of the plate is shown in Figure 5. In the inverted regime the portion of the fluid which is heated to a sufficiently high temperature will rise until it passes the upper edge of the plate. In the region above the heated plate the hot fluid will mix with the unheated fluid. When this interchange of heat has reduced the temperature level enough to yield a mixture having a density greater than that of the bulk fluid, the positive motion will be arrested and reversal of direction will occur. The result of this series of events is to produce a tendency for all the sensible heat being carried past the upper edge of the plate by the upward motion to return to the boundary layer in the form of sensible heat in the falling film. (This is true at least when a starting section is employed.) At the lower edge of the plate the situation is entirely different. Again the warm fluid mixes with the unheated fluid; however, the driving force remains negative and thus the heat continues to be carried downward.

THEORETICAL CONSIDERATIONS

The character of the heat transfer mechanism differs between the unidirectional and inverted convection regimes, and therefore each case will be considered separately.

Unidirectional Convection Regime

Approximate Solution: For many liquids the variation of the specific volume with temperature is reported in the literature in the form of a polynomial, such as

$$\frac{1}{\rho} = \frac{1}{\rho_0}(1 + A_1T + A_2T^2 + A_3T^3) \qquad (5)$$

Utilizing Equation (5), Merk (*6*) derived the buoyant force per unit mass as

$$g\left(\frac{\rho_\infty - \rho}{\rho}\right) = g\beta_\infty\theta_s(\phi + s_1\phi^2 + s_2\phi^3) \qquad (6)$$

Substituting Equation (6) for the driving-force term in Equation (1) yields

$$u\frac{\partial u}{\partial x} + v\frac{\partial u}{\partial y} = g\beta_\infty\theta_s(\phi + s_1\phi^2 + s_2\phi^3) + \nu\frac{\partial^2 u}{\partial y^2} \qquad (7)$$

If β_∞ is negative, the convection currents are always downward for a heating process, provided that dual convection currents do not exist. Consequently, it is convenient to translate the origin of the coordinate system to the upper edge of the plate.

Thus

$$w = 1 - x \quad \text{and} \quad p = -u \qquad (8)$$

Use of Equation (8) in Equations (7), (2), and (3) leads to the following set of equations for the downward convective current, which includes the density-temperature dependency:

$$p\frac{\partial p}{\partial w} + v\frac{\partial p}{\partial y} = \nu\frac{\partial^2 p}{\partial y^2} + g\gamma_\infty\theta_s(\phi + s_1\phi^2 + s_2\phi^3) \qquad (9)$$

$$\frac{\partial p}{\partial w} + \frac{\partial v}{\partial y} = 0 \qquad (10)$$

$$p\frac{\partial \phi}{\partial w} + v\frac{\partial \phi}{\partial y} = \alpha\frac{\partial^2 \phi}{\partial y^2} \qquad (11)$$

The boundary conditions are

$$p = 0 \quad \phi = 1 \quad \text{at} \quad y = 0$$
$$p = 0 \quad \phi = 0 \quad \text{at} \quad y = \infty \qquad (12)$$

The layers in which the velocity and the temperature differ significantly from the bulk conditions are thin. Each thickness has been termed the *boundary-layer* thickness and is denoted by the symbol δ. The thermal boundary layer is not, except in rare instances, equal to the hydrodynamic boundary layer; however for the purposes of this paper equal thicknesses have been assumed.

The velocity and temperature profiles are assumed to be expressible in the form of polynomials (*2*), which are

$$p = p_1\frac{y}{\delta}\left(1 - \frac{y}{\delta}\right)^2 \qquad (13)$$

and

$$\phi = \left(1 - \frac{y}{\delta}\right)^2 \qquad (14)$$

Integrating Equations (1) and (11) from 0 to δ with the aid of Equation (10) and substituting Equations (13) and (14) produces Equations (15) and (16):

$$\frac{d}{dw}\left(\frac{p_1^2\delta}{105}\right) = \delta\left[g\gamma_\infty\theta_s\left(\frac{1}{3} + \frac{s_1}{5} + \frac{s_2}{7}\right)\right] - \nu\frac{p_1}{\delta} \qquad (15)$$

and

$$\frac{d}{dw}\left(\frac{p_1\delta}{30}\right) = \frac{2\alpha}{\delta} \qquad (16)$$

Solving Equations (14) and (15) for δ and noting that $h_w = -2k/\delta$ yields the point Nusselt number:

$$Nu_w' = 0.669\,Pr^{1/2}(0.952 + Pr)^{-1/4}\cdot\left[Gr_w'\left(\frac{1}{3} + \frac{s_1}{5} + \frac{s_2}{7}\right)\right]^{1/4} \qquad (17)$$

The point heat transfer coefficient h_w is inversely proportional to the fourth root of w. By integration over the length of the plate, the average heat transfer coefficient is obtained:

$$\bar{h} = 4/3h_w \qquad (18)$$

The average Nusselt number is obtained by introducing Equation (18) into Equation (17) and eliminating h_w:

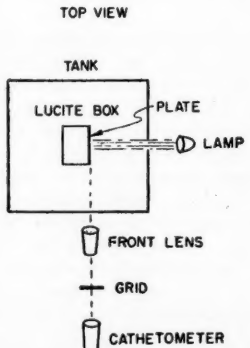

Fig. 2. Lighting system for velocity measurements.

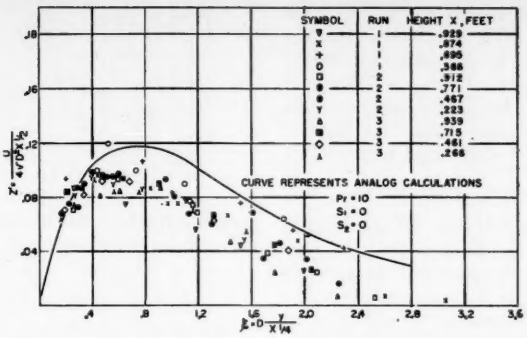

Fig. 3. Comparison of experimental and theoretical velocity distributions.

$$\overline{Nu} = 0.892\left[\overline{Gr}'\left(\frac{1}{3} + \frac{s_1}{5} + \frac{s_2}{7}\right)\right]^{1/4} \cdot Pr^{1/2}(0.952 + Pr)^{-1/4} \qquad (19)$$

Equations (17) *and* (19) *have no physical* significance if $[(1/3) + (s_1/5) + (s_2/7)]$ *is less than, equal to, or approaches zero.* A negative value of the quantity $[(1/3) + (s_1/5) + (s_2/7)]$ leads to a negative Nusselt number if either Equation (17) or (19) is employed. If $[(1/3) + (s_1/5) + (s_2/7)]$ equals zero, then Equations (17) and (19) indicate that the Nusselt number should be zero. This result, however, is not correct. The minimum value of the Nusselt number corresponds to that of a purely conductive process.

The results of analogue solutions (presented in the following sestion) indicate that a condition of stagnation prevails at the surface of the plate $[(\partial p/\partial y) = 0$ at $y = 0]$ when $[(1/3) + (s_1/5) + (s_2/7)]$ equals zero. Consequently, the sign of the quantity $[(1/3) + (s_1/5) + (s_2/7)]$ is a criterion for determining the type of convection currents which may be expected. A positive value indicates that the convection currents are normal; a negative sign points to an inverted flow regime.

Analogue Computer Solution: Equations (17) and (19) are derived from several assumptions. It is useful to verify these equations by a more exact method.

A stream function is defined as follows:

$$\frac{\partial \Psi}{\partial y} = p \quad \text{and} \quad \frac{\partial \Psi}{\partial w} = -v \qquad (20)$$

Substituting the stream function into Equations (10) and (11) yields

$$\frac{\partial \Psi}{\partial y}\frac{\partial^2 \Psi}{\partial w \partial y} - \frac{\partial \Psi}{\partial w}\frac{\partial^2 \Psi}{\partial y^2} = \nu \frac{\partial^3 \Psi}{\partial y^3} + g\gamma_\infty \theta_s(\phi + s_1\phi^2 + s_2\phi^3) \qquad (21)$$

$$\frac{\partial \Psi}{\partial y}\frac{\partial \phi}{\partial w} - \frac{\partial \Psi}{\partial w}\frac{\partial \Psi}{\partial y} = \alpha \frac{\partial^2 \phi}{\partial y^2} \qquad (22)$$

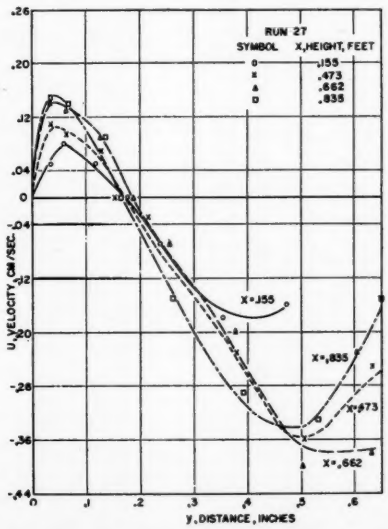

Fig. 4. Typical velocity distributions in inverted regime.

The boundary conditions are

$$\frac{\partial \Psi}{\partial y} = 0\ \frac{\partial \Psi}{\partial w} = 0\ \phi = 1 \text{ at } y = 0$$
$$\frac{\partial \Psi}{\partial y} = 0\ \frac{\partial \Psi}{\partial w} = 0\ \phi = 0 \text{ at } y = \infty \qquad (23)$$

In order to reduce this system of partial differential equations to a system of ordinary differential equations, Pohlhausen's (*8*) substitutions are used. They are

$$\xi = \frac{cy}{w^{1/4}} \qquad (24)$$

where

$$c = \sqrt[4]{\frac{g\gamma_\infty \theta_s}{4\nu^2}} \qquad (25)$$

and

$$\eta(\xi) = \phi(w, y) \qquad (26)$$

$$z(\xi) = \frac{\Psi(w, y)}{4\nu c w^{1/4}} \qquad (27)$$

Substituting Equations (24), (26), and (27) into Equations (21) and (22) yields the following system of ordinary differential equations:

$$z''' + 3zz'' - 2(z')^2 + \eta + s_1\eta^2 + s_2\eta^3 = 0 \qquad (28)$$

$$\eta'' + 3P_r\eta' = 0 \qquad (29)$$

with boundary conditions

$$z = 0\ z' = 0\ \eta = 1 \text{ at } \xi = 0$$
$$z' = 0\ z'' = 0\ \eta = 0 \text{ at } \xi = \infty \qquad (30)$$

Numerical solutions for this system of equations would be extremely difficult to obtain without the aid of a computing machine. A Reeves Electronic Analogue Computer was used to solve the set of Equations (28), (29), and (30). A schematic diagram of the wiring circuit is shown in Figure 6. The symbols used are those suggested by Korn and Korn (*5*).

The technique of trial and error is involved in obtaining the analogue solutions, because all the initial conditions (initial conditions refer to the values of the functions and their derivatives at $\xi = 0$) must be known in order to start the solution on the computer; hence, values of z'' and η' at $\xi = 0$ were assumed and if the boundary conditions at $\xi = \infty$ were fulfilled, the assumed initial values are correct.

A series of analogue solutions was obtained for a value of the Prandtl number equal to 10 (approximately that of water). Each solution is termed a *result.* The values of the two parameters, s_1 and s_2, were chosen so that result I corresponds to the situation in which the bulk temperature is 0°C. and the plate temperature is 1°C. By the same token, result II corresponds to a plate temperature at 2°C. and a bulk temperature of

0°C. Solutions were obtained for 1°C. increments of plate temperature up to and including a plate temperature of 14°C. the bulk temperature being held constant at 0°C.

The value of z'' at $\xi = 0$ is zero when the plate temperature is 14°C. (result XIV). This is the transition point. Any further increase in the plate temperature would result in inverted convection currents. *In the inverted-convection regime, Pohlhausen's substitutions are no longer valid because they require that the velocities and temperatures at* $y = \infty$ *equal the velocities and temperatures at* $w = 0$ ($\xi = \infty$ at both $y = \infty$ and at $w = 0$). This limits the application of Equations (28), (29), and (30) to normal convective regimes.

It is of interest to note that for a bulk temperature of 0°C. the value of $[(1/3) + (s_1/5) + (s_2/7)]$ is zero at a plate temperature of 13.60°C., a value which is in excellent agreement with the value of 14°C. obtained as the transition point from the more exact analogue solutions.

Figures 7 and 8 show the velocity and temperature patterns as the plate temperature is increased. As the plate temperature is increased (increasing result numbers), the initial slope of the velocity and temperature curves decreases. The initial temperature gradient varies from -1.185 at $s_1 = s_2 = 0$ to -0.882 at the transition point, a change of 34%. This illustrates the necessity of considering parameters s_1 and s_2 when natural-convection heat transfer coefficients are computed in a region of maximum density. A summary of all analogue solutions is presented in Table 1.

A comparison of the approximate analytical solution, Equation (19), and the analogue solutions is shown in Table 2. The average Nusselt number can be computed from the analogue data by applying the following relationship:

$$\overline{Nu} = -0.943(\overline{Gr}')^{1/4}\left(\frac{d\eta}{d\xi}\right)_{\xi=0} \qquad (31)$$

The approximate solution yields results which are low near the transition point. The average Nusselt number calculated from Equation (19) is 14% less than the value indicated by the analogue solution when $[(1/3) + (s_1/5) + (s_2/7)]$ equals $+0.064$. The disagreement becomes more pronounced as the value of $[(1/3) + (s_1/5) + (s_2/7)]$ approaches zero.

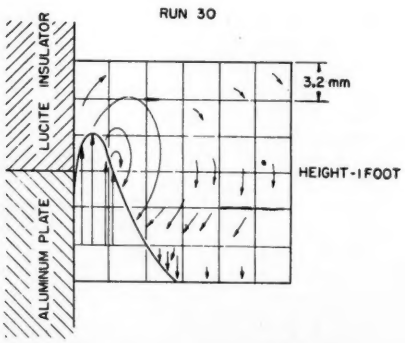

Fig. 5. Flow patterns at top of plate for inverted regime.

Inverted Convection Regime

Conditions for Model: All the sensible heat in the rising fluid which passes the upper edge of the plate will be assumed to return to the boundary layer in the form of sensible heat in the falling layer. This can be expressed as follows:

$$\left(\int_0^\delta u\phi\, dy\right)_{x=l} = 0 \qquad (32)$$

As a corollary, all heat transferred from the plate must pass the lower edge of the plate in the form of sensible heat of the falling film. This can be expressed as follows:

$$\left(\int_0^\delta u\phi\, dy\right)_{x=0} = -\frac{\bar{h}l}{C_p\rho} \qquad (33)$$

The velocity profile which was assumed in deriving the approximate solution for the case of normal convection [Equation (13)] must be altered to conform to the pattern of dual motion. Since there is both a positive and a negative flow, the velocity, u, will be equal to zero at some point within the boundary layer. This may be called point of zero velocity, δ_i. A polynomial of fourth order is assumed which satisfies both the boundary conditions plus a smooth-fit condition $[(du/dy) = 0$ at $y = \delta]$ and a zero at $\delta_i (u = 0$ at $y = \delta_i)$. This polynomial is

$$u = \frac{E(x)}{2}\left\{\left[\left(\frac{y}{\delta}\right) - 3\left(\frac{y}{\delta}\right)^3 + 2\left(\frac{y}{\delta}\right)^4\right] - G\left[\left(\frac{y}{\delta}\right) - 2\left(\frac{y}{\delta}\right)^2 + \left(\frac{y}{\delta}\right)^3\right]\right\} \qquad (34)$$

The introduction of the new variable δ_i yields a system of two equations and three unknowns. In order to render this system solvable, a net vertical downward flow will be postulated such that

$$\int_0^\delta u\, dy = C_0 \qquad (35)$$

Equation (35) implies that none of the fluid medium enters or leaves the boundary layer except at the top or the bottom of the plate.

Equation (14) will be taken to be valid in the inverted regime as well as for normal convection.

Approximate Solution: If Equation (6) is substituted into Equation (1) and the resulting expression integrated from 0 to δ (it being assumed that the hydrodynamic-boundary-layer thickness equals the thickness of the thermal boundary layer), one obtains with the aid of Equation (2)

$$\frac{d}{dx}\int_0^\delta u^2\, dy = \int_0^\delta g\beta_\infty\theta_s(\phi + s_1\phi^2 + s_2\phi^3)\, dy - \nu\left(\frac{\partial u}{dy}\right)_{y=0} \qquad (36)$$

Similarly if Equation (3) is integrated between the same limits with the aid of Equation (2), one gets

$$\frac{d}{dx}\int_0^\delta u\phi\, dy = -\alpha\left(\frac{d\phi}{dy}\right)_{y=0} \qquad (37)$$

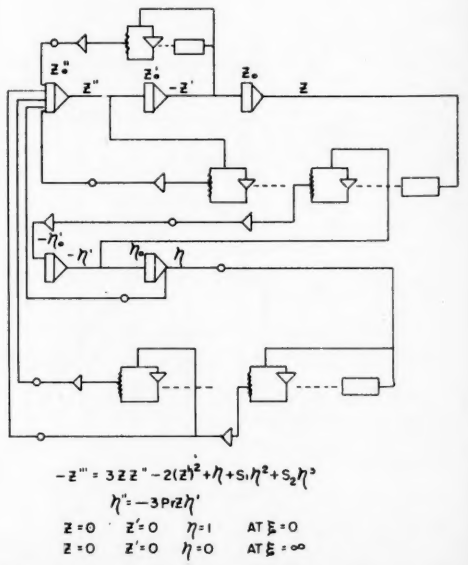

Fig. 6. Analogue-computer circuit and equations used in numerical solutions.

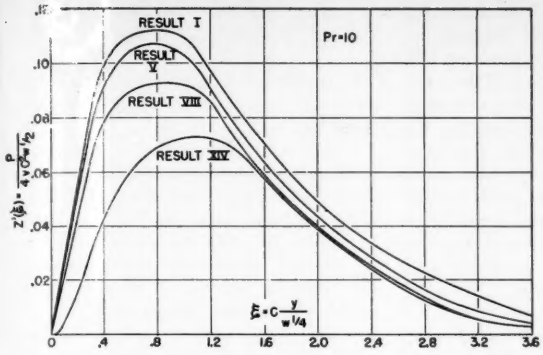

Fig. 7. Theoretical solutions obtained from analogue computer.

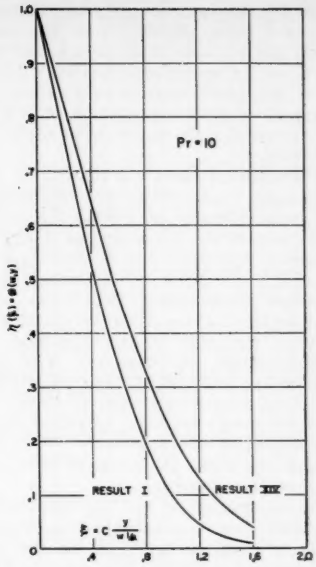

Fig. 8. Theoretical solutions obtained from analogue computer.

If the inertia term is neglected [left-hand side of Equation (36)], the system of Equations (14), (32), (33), (34), (36), and (37) can be handled in much the same manner as in the Squire-Eckert approach. The final equations for the point and average Nusselt numbers are the following:

$$Nu_x = 0.489\left[Gr_x Pr\left(\frac{1}{3}+\frac{s_1}{5}+\frac{s_2}{7}\right)\right]^{1/4} \quad (38)$$

$$\overline{Nu} = 0.652\left[\overline{Gr}Pr\left(\frac{1}{3}+\frac{s_1}{5}+\frac{s_2}{7}\right)\right]^{1/4} \quad (39)$$

[Other forms of Equations (38) and (39) have been obtained (*10*) by use of a model in which the condition given by Equation (33) has been replaced.]

The experimental observations indicate a finite boundary layer at $x = 0$; however, Equation (38) predicts an infinite point heat transfer coefficient, or zero boundary-layer thickness. The sensible-heat flow is accounted for in the following manner. The substitution of the polynomials relating ϕ and u to δ [Equations (14) and (34)] into Equation (33) and the integration lead to

$$(E\delta)_{z=0} = 105\,\frac{\bar{h}l}{\rho C_p} \quad (40)$$

Equation (40) indicates that, even though the boundary-layer thickness is extremely small, the velocity is so large at this point that the requisite quantity of heat leaves the boundary layer.

EXPERIMENTAL

A 1-ft.-square vertical heated plate was mounted within a large insulated tank containing water. The inside dimensions of the tank are 26 in. in length by 36 in. in width, by 36 in. in depth. To retain conditions of interest, it was necessary to maintain the bulk temperature of the water below 4°C.; consequently, the entire apparatus was installed in a constant-temperature room which enabled the experiments to be conducted in an ambient temperature approximately equal to that of bulk-water temperature.

Vertical temperature gradients within the tank were minimized through the use of a copper-coil cooling system positioned vertically along the walls of the tank. The coolant, a solution of ethylene glycol and water, was pumped through the coils from a refrigerated constant-temperature bath.

The heated test section was made from a 12- by 12- by $\frac{3}{4}$-in. aluminum plate. Grooves were milled into the back of the plate and into these grooves were fitted porcelain insulators containing No. 20 B. & S. gauge nichrome IV wire. The insulators were fixed into place with sauereisen electrical cement. Four parallel heater circuits were used, each independently controlled. The wires were spaced so that each carried an equal heat load when the convection currents were normal. A detailed analysis of the required spacing was done by Weingarden (*12*). Figure 9 shows the spacing and also the wiring of the four heater sections. These sections are designated I, II, III, and IV as shown in the sketch. The numbered circles represent the positions of the ten 20-gauge copper-constantan thermocouples which were mounted into the back of the plate to within $\frac{1}{16}$ in. of the heat transfer surface.

As shown in Figure 10, the plate was mounted onto a Lucite box, which was filled with vermiculite to minimize heat losses. The box was positioned in the tank by vertical bar mounts.

The power supply consisted of four 6-volt storage batteries and a rectifier, placed in parallel. The voltage of the rectifier was adjusted so that only a slight current was

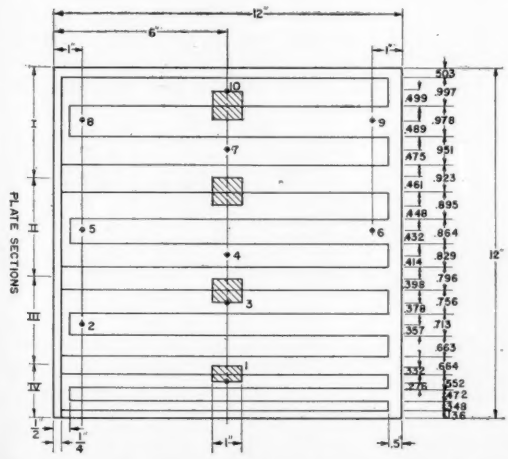

Fig. 9. Location of heater coils and thermocouples in test section.

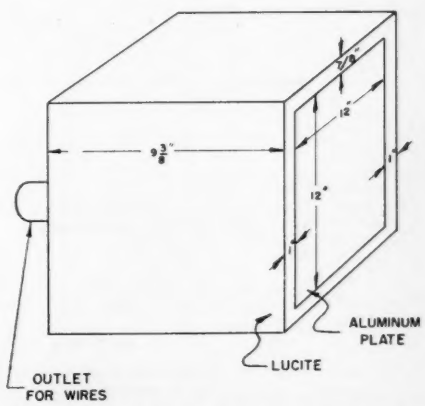

Fig. 10. Mounting of test plate in Lucite box.

drawn from the batteries. This gave voltages with less than 1% drift over an 8-hr. period and reduced instantaneous fluctuations. During operation the voltage drops across the heater circuits and calibrated manganin resisters were measured. From this information the power input could be calculated.

A temperature probe was constructed for the purpose of obtaining point coefficients. The probe consisted of a brass tube with a fork attachment at one end as shown in Figure 11. Across the tips of the fork was soldered a thermistor, which served as a resistance thermometer. This device was mounted into a slider. A vernier caliper was fixed on the slider so that changes of position might be measured with an accuracy of ±0.003 in. The thermistor used is a glass-coated bead 0.015 in. in diameter with 0.001-in. platinum lead wires extending from each end.

Figure 12 shows the complete electrical wiring of the apparatus.

The thermocouples and the thermistor were calibrated in the assembled apparatus. Beckman thermometers, set at the ice point, served as secondary standards. The estimated accuracy of the calibration was 0.01°C.

TEST RUNS

A total of twenty runs was made in which the flow in the boundary layer was unidirectional. The fluid film was rising during runs 1, 2, and 3 (the bulk temperature of the water being greater than 4°C.), and during runs 4 through 20 the film was falling. Runs 21 through 30 deal with the inverted-flow regime. In order to reduce the temperature gradients within the bath, ice was introduced into the bath before runs 4 to 10, 13 to 18, and 21 to 25 were made. (Ice was not introduced during the other runs in order to obtain data with higher bulk temperatures.) in all runs the water level was maintained at least 10 in. above the upper edge of the plate. Despite all precautions a temperature gradient still persisted during all the runs. The maximum vertical gradient was approximately 0.30°C./ft. with ice present within the tank. Without ice in the tank, the maximum temperature gradient was about 1.6°C./ft., and the mean gradient was 0.65°C./ft. Heat losses were neglected in the evaluation of heat transfer coefficients. For nearly all runs the maximum estimated heat loss ranged from 2 to 4.3% of the total heat input.

The viscosity was evaluated at the wall temperature as suggested by Schmidt and Beckmann (*11*). All other fluid properties were evaluated at the arithmetic mean of the wall and bulk temperatures.

DISCUSSION OF RESULTS

Standard Runs

The data for the initial three runs are given in Table 3. These runs were conducted with the bulk-water temperature maintained at a level to avoid the region of maximum density (i.e., $T_\infty > 4$°C.). The results of the experimental Nusselt numbers are shown together with the theoretical value [computed from Equation (19) with $s_1 = s_2 = 0$]. The maximum deviation of the experimental Nusselt number from the theoretical value is 7%. The experimental values are lower than the theoretical values, which may in part be attributed to the starting sections used along the upper and lower edges of the plate. These sections would tend to yield a thicker boundary layer and hence a smaller heat transfer coefficient. In the computation of the Grashof number for these three runs, the coefficient of expansion was calculated by the method suggested by Saunders (*9*),

$$\beta_f = \frac{\rho_\infty - \rho_f}{\rho_f(T_f - T_\infty)}$$

The coefficient of expansion for all other runs was calculated by employing either β_∞ or γ_∞.

Unidirectional convection: A comparison of the experimental average Nusselt numbers for falling films with the values obtained from Equation (19) is presented in Figure 13, with the exception of one experiment, the percentage deviation of the experimental values of the Nusselt number from the theoretical values is less than 13%, with a mean deviation of 4.7%. The largest deviations occur when the value of $[(1/3) + (s_1/5) + (s_2/7)]$ becomes small (i.e., less than 0.1). These deviations are to be expected, for as noted under Theoretical Considerations, the Nusselt number approaches a minimum value rather than zero.

Inverted Convection: The comparison of the predicted Nusselt number for the inverted regime with the experimental is shown in Figure 14. Except for runs 24 and 25, which are 15.6 and 42% in error, respestively, the maximum deviation for all runs in the inverted regime was less than 10% and the mean deviation was 3.3%. The theoretical value of the Nusselt number is expected to be smaller than the experimental value as the absolute value of the quantity $[(1/3) + (s_1/5) + (s_2/7)]$ approaches zero. Run 25 represents conditions in which the absolute value of $[(1/3) + (s_1/5) + (s_2/7)]$ is exceedingly small (0.00577), and hence the 42% deviation is not surprising. As noted previously, the model used for the theoretical equation does not provide for the conduction of heat through the stagnant film.

Velocity and Temperature Distributions: Figures 3, 14, 15, and 16 compare the results of the velocity and temperature measurements with those obtained from the solutions on the analogue computer. The agreement appears to be quite good for the case of the temperature profiles. Although the velocity data deviate somewhat from the predicted values, the authors believe that these deviations are due to the experimental difficulties en-

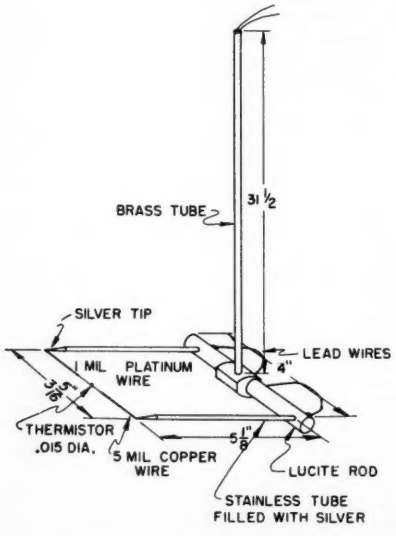

Fig. 11. Temperature probe.

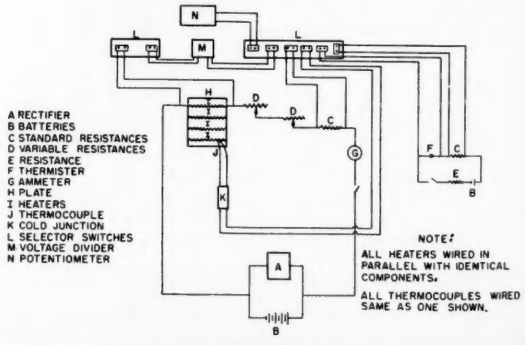

Fig. 12. Electrical circuit.

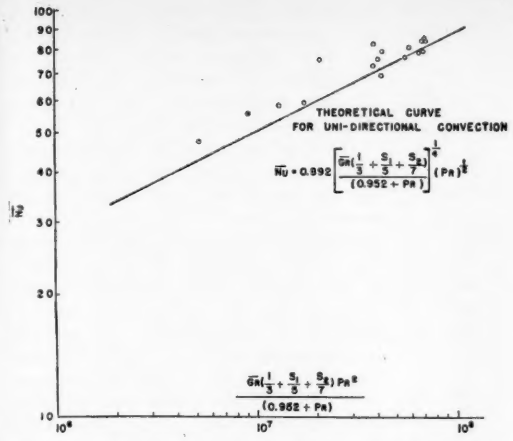

Fig. 13. Comparison of theoretical and experimental results for unidirectional convection.

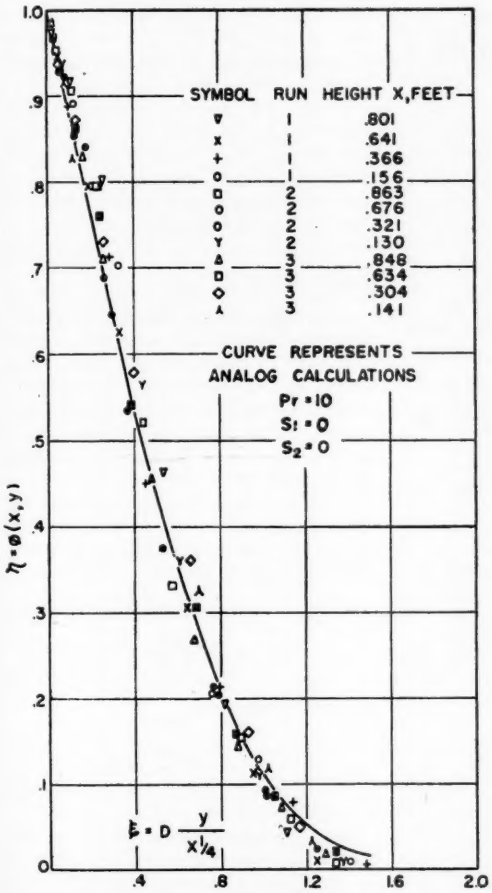

Fig. 15. Comparison of experimental and numerical temperature distributions.

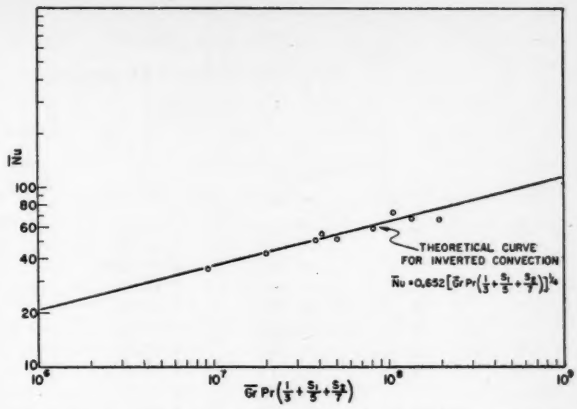

Fig. 14. Comparison of experimental and theoretical results, inverted regime.

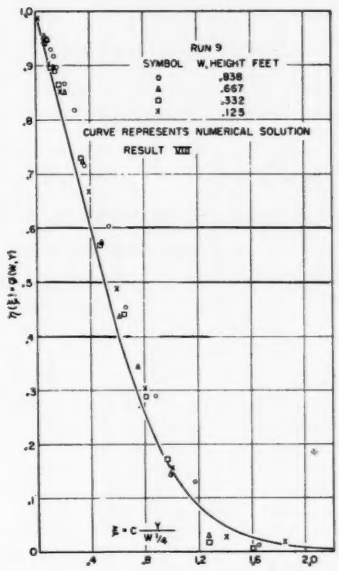

Fig. 16. Comparison of experimental and theoretical temperature distributions.

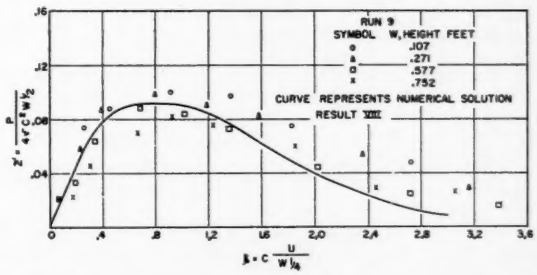

Fig. 17. Comparison of experimental and theoretical temperature distributions.

countered in attempting accurately to measure velocities of the magnitude encountered in natural convection.

The results presented in Figures 3 and 15 are those obtained from the standard runs. The data shown in Figures 16 and 17 are representative of all data taken in the unidirectional regime.

Two techniques of ascertaining the validity of the constant-net-flow assumption were tried; however, the experimental difficulties masked the comparisons. The velocity profiles at several positions along the plate were integrated and a deviation of $\pm 25\%$ from the constant-flow assumption was found. The point of zero velocity, δ_i, was measured for several runs and compared with the value for δ_i, solved from Equations (32), (34), (35), (36), and (37). The theoretical values for δ_i ranged from one-third to almost twice the experimental values. (Out of fourteen comparisons, only two theoretical values exceeded the experimental values.) One

TABLE 1

ANALOGUE RESULTS

Unidirectional Convection Regime

	Parameters			Analogue computer results	
Result*	P_r	S_1	S_2	$\left(\frac{d\eta}{d\xi}\right)_{\xi=0}$	$\left(\frac{d^2z}{d\xi^2}\right)_{\xi=0}$
0	10	0	0	−1.185	0.440
I	10	−0.132	0.00106	−1.173	0.415
II	10	−0.264	0.00420	−1.157	0.390
III	10	−0.396	0.00945	−1.146	0.380
IV	10	−0.528	0.0168	−1.134	0.360
V	10	−0.660	0.0263	−1.118	0.340
VI	10	−0.792	0.0378	−1.091	0.310
VII	10	−0.924	0.0515	−1.073	0.290
VIII	10	−1.056	0.0672	−1.041	0.260
X	10	−1.320	0.105	−1.025	0.240
XI	10	−1.452	0.127	−0.972	0.165
XII	10	−1.584	0.151	−0.959	0.140
XIII	10	−1.716	0.178	−0.921	0.110
XIV	10	−1.848	0.206	−0.882	0
For Result 0, the following values have been reported (7):				−1.169	0.4192

*Bulk water temperature, 0°C.; plate temperature corresponds to result number in °C.

TABLE 2

COMPARISON OF ANALOGUE AND APPROXIMATE SOLUTIONS

Unidirectional Convection Regime

			Approximate [Equation (19)]	Analogue Results	
Pr	s_1	s_2	$\frac{\overline{Nu}}{(\overline{Gr}')^{1/4}}$	$\frac{\overline{Nu}}{(\overline{Gr}')^{1/4}}$	$\frac{1}{3}+\frac{s_1}{5}+\frac{s_2}{7}$
10	0	0	1.176	1.117	0.333
10	−0.132	0.00105	1.154	1.106	0.307
10	−0.266	0.00420	1.129	1.091	0.281
10	−0.396	0.00945	1.103	1.081	0.255
10	−0.528	0.0168	1.074	1.069	0.230
10	−0.660	0.0263	1.044	1.054	0.205
10	−0.792	0.0378	1.010	1.029	0.180
10	−0.924	0.0515	0.974	1.012	0.155
10	−1.056	0.0672	0.934	0.982	0.131
10	−1.320	0.105	0.836	0.967	0.084
10	−1.452	0.127	0.771	0.917	0.061
10	−1.584	0.151	0.685	0.904	0.036
10	−1.716	0.178	0.546	0.868	0.015
10	−1.848	0.206	0	0.832	−0.007

TABLE 3

STANDARD RUNS*

Comparisons of Experimental and Theoretical Results

Run	T_p, °C.	T_∞, °C.	$\frac{1}{3}+\frac{s_1}{5}+\frac{s_2}{7}$	$\overline{Gr} \times 10^{-7}$	Pr	$\overline{Nu}$ theoretical†	$\overline{Nu}$ experimental
1	13.36	9.24	0.333	6.992	8.59	103.4	96.9
2	11.71	8.84	0.333	4.189	8.98	92.1	86.1
3	9.83	7.78	0.333	2.124	9.52	78.9	75.5

*The unidirectional heat transfer tests for runs 1, 2, and 3 represent critical evaluations of the experimental procedures and therefore are termed *standard* runs.

†Equation (19): $\overline{Nu} = 0.892\left[\overline{Gr}'\left(\frac{1}{3}+\frac{s_1}{5}+\frac{s_2}{7}\right)\right]^{1/4} Pr^{1/2}(0.952+Pr)^{-1/4}$.

For $\left(\frac{1}{3}+\frac{s_1}{5}+\frac{s_2}{7}\right) = 0.333$, Equation (19) reduces to Eckert's theoretical equation.

$Nu = 0.68\left(\frac{Pr}{0.952+Pr}\right)^{1/4}(Pr\,\overline{Gr}')^{1/4}$ (fluid properties evaluated at film temperature)

inaccuracy of the theoretical treatment is the assumption that the thermal boundary layer thickness equals that of the hydrodynamic boundary layer. Howrath (3) has demonstrated that this ratio should be of the order $(Pr)^{1/2}$.

The profiles presented in Figure 19 serve to support the assumption concerning the return of sensible heat to the boundary layer. If the product $u\phi$ is measured at several points and the resulting curve graphically integrated, 108% of the sensible heat contained in the rising portion of the boundary layer is found in the falling stream. The velocity measurements shown in Figure 19 were taken at $x = 0.833$ ft., and the temperature profile is for a height of 0.828 ft. from the lower edge of the plate. Thus if all the sensible heat passing the upper edge of the plate reenters the boundary layer, the falling film would be expected to contain an amount of heat equal to that of the rising film plus the quantity of heat convected to the falling stream in the upper 0.172 ft. of the plate.

Point heat transfer coefficients were calculated by extrapolating the temperature profile to $y = 0$ and determining the temperature gradient at the wall. As this method did not yield consistent results, it is not reported here.

CONCLUSIONS

Convective heat transfer is greatly influenced by the presence of a density maximum in the convecting fluid, which leads to two convective mechanisms, each of which must be considered separately. These two convective regimes have been termed *normal*, or *unidirectional*, convection and *inverted* convection. A test was devised to predict the type of regime that will prevail for given conditions of plate and bulk temperature. This test may be stated as follows:

If

$$\frac{1}{3}+\frac{s_1}{5}+\frac{s_2}{7} < 0$$

inverted convection

$$\frac{1}{3}+\frac{s_1}{5}+\frac{s_2}{7} \geq 0$$

normal convection

Heat transfer coefficients can be predicted for both regions with a deviation in the Nusselt number of ±10%, provided that $[\frac{1}{3}+(s_1/5)+(s_2/7)] > 0.05$, by use of Equation (19) or (39), depending on the convective regime.

ACKNOWLEDGMENT

The research was supported by a grant from the National Science Foundation to the Department of Chemical Engineering. A fellowship from the Allied Chemical and Dye Corporation is also gratefully acknowledged.

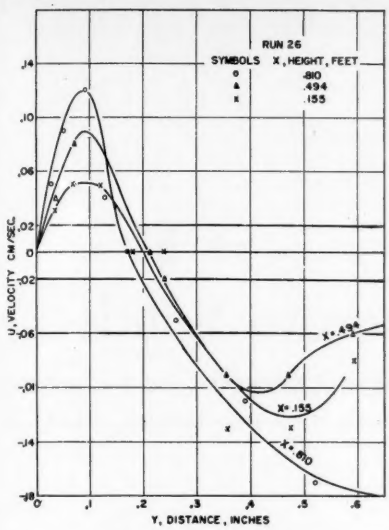

Fig. 18, Comparison of experimental and theoretical velocity distributions.

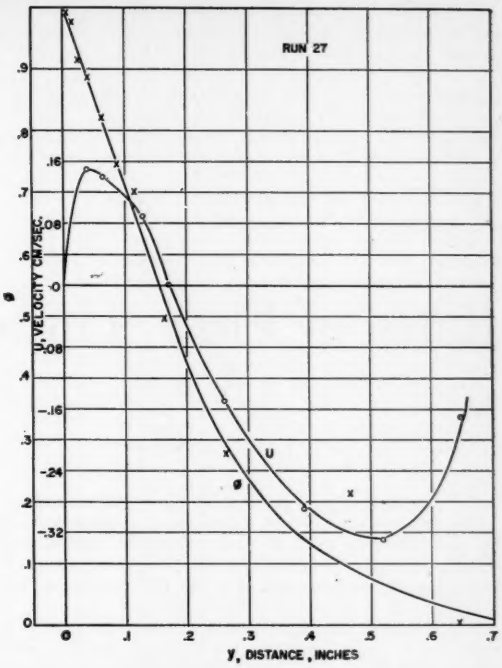

Fig. 19. Typical velocity distributions in inverted regime.

NOTATION

A_1, A_2, A_3 = constants in equation of state

C_p = heat capacity of fluid

$C = \sqrt[4]{\dfrac{g\gamma_\infty \theta_s}{4\nu^2}}$

$D = \sqrt[4]{\dfrac{g\beta_f \theta_s}{4\nu^2}}$

E = function of x

$G = 1 + 2\dfrac{\delta_i}{\delta}$

$Gr_w' = \dfrac{g\gamma_\infty \theta_s w^3}{\nu^2}$

$\overline{Gr_w}' = \dfrac{g\gamma_\infty \theta_s l^3}{\nu^2}$

$Gr_x = \dfrac{g\beta_\infty \theta_s x^3}{\nu^2}$

$\overline{Gr} = \dfrac{g\beta_\infty \theta_s l^3}{\nu^2}$

g = acceleration due to gravity

h_x, h_w = point heat transfer coefficients

$\bar{h}$ = over-all heat transfer coefficient

k = thermal conductivity of fluid

l = height of plate

$Nu_w = \dfrac{h_w w}{k}$

$Nu_x = \dfrac{h_x x}{k}$

$\overline{Nu} = \dfrac{\bar{h} l}{k}$

$N = 1 + A_1 T_\infty + A_2 T_\infty^2 + A_3 T_\infty^3$

p = velocity, positive for downward motion

p_1 = function of w only

$Pr = \dfrac{C_p \mu}{k}$

$s_1 = \dfrac{(A_1 + 3A_2 T_\infty)\theta_s}{N\beta_\infty}$

$s_2 = \dfrac{A_3 \theta_s^2}{N\beta_\infty}$

T = temperature of fluid at a point

T_∞ = bulk temperature at fluid

T_p = surface temperature of plate

$T_f = \dfrac{T_p + T_\infty}{2}$

u = velocity in x direction, positive for upward motion

v = velocity in y direction

$w = 1 - x$

x = distance in vertical direction

y = distance in horizontal direction

Greek Letters

$\alpha = \dfrac{k}{C_p \rho}$

$\beta_\infty = \dfrac{A_1 + 2A_2 T_\infty + 3A_3 T_\infty^2}{N}$

$-\gamma_\infty = \beta_\infty$

δ = boundary layer thickness

δ_i = distance measured from plate to point of velocity inversion

$\theta_s = T_p - T_\infty$

μ = dynamic viscosity

ν = kinematic viscosity

ρ = density of fluid

ρ_∞ = density of fluid evaluated at T_∞

ρ_f = density of fluid evaluated at T_f

$\phi = \dfrac{T - T_\infty}{T_p - T_\infty}$

Ψ = stream function

LITERATURE CITED

1. Dumore, J. M., H. J. Prins, J. A. Merk, *Nature*, **172**, 460 (1953).
2. Eckert, E. R. G., "Introduction to the Transfer of Heat and Mass" McGraw-Hill Book Company, Inc., New York (1950).
3. Howrath, Leslie, "Modern Developments in Fuid Dynamics," vol. 1, Oxford University Press, New York (1953).
4. Jakob, Max, "Heat Transfer," vol. 1, Wiley and Sons, Inc., New York (1950).
5. Korn, G. A., and T. M. Korn, "Electronic Analog Computers," McGraw-Hill Book Company, Inc., New York (1952).
6. Merk, H. J., *Appl. Sci. Research.* **4**, Sec. A, 435 (1953).
7. Ostrach, S., *Natl. Advisory Comm. Aeronaut. Tech. Note* 2635 (1952).
8. Pohlhausen, E., in Jakob, *op. cit.*
9. Saunders, O. A., *Proc. Roy. Soc.* (*London*), **A172**, 55 (1939).
10. Schechter, R. S., Ph.D. thesis, Univ. Minn., Minneapolis (1956).
11. Schmidt, E., and W. Beckmann, in Jakob, *op. cit.*
12. Weingarden, Morris J., M.S. thesis, Univ. Minn., Minneapolis (1955).

Manuscript received in editorial office Feb. 27, 1957; revision received Oct. 4, 1957; paper accepted Oct. 28, 1957.

Rates of Flow Through Microporous Solids

E. R. GILLILAND, R. F. BADDOUR, and J. L. RUSSELL

Massachusetts Institute of Technology, Cambridge, Massachusetts

Rates of flow of pure gases, both those with no adsorption and those with appreciable adsorption, were studied as a function of pressure level, pressure drop, and temperature for flow through 1/2-in.-diameter cylindrical plugs of activated carbon and of unsintered Vycor glass. Adsorption isotherms for the pure gases on Vycor glass were measured over the range of variables covered in the flow studies. A few measurements were made for bulk liquid flowing through a Vycor plug.

Permeabilities, which are proportional to the rate of flow per unit of pressure drop, were satisfactorily correlated for hydrogen, helium, argon, and nitrogen by employing existing gas-phase flow theory. Permeabilities considerably larger than the values predicted from the nonadsorbed gas correlation, sometimes more than seventeen times as large, were observed for ethylene, propylene, and isobutane flowing through a Vycor plug. For the hydrocarbon-Vycor systems, permeabilities for vapor flow are as much as sixty times larger than for bulk liquid flow.

The unusual flow phenomena for the hydrocarbon-Vycor systems are attributed to a rapid transport in the adsorbed layer. The total transport is treated as being the sum of gas-phase and adsorbed-layer flow. An equation describing adsorbed-layer movement is derived by utilizing a force balance together with thermodynamic principles. The resulting equation has just one empirical constant, and its use requires adsorption-isotherm data. It correlates very well the surface flow rates for the major range of the variables covered in this investigation. Rate measurements were made for adsorbed-layer concentrations ranging from about one tenth of a monolayer up through the capillary condensation region. Deviations in the one constant form of the equation are observed below one tenth of a monolayer. The available literature data on flow in adsorbed layers are reasonably well correlated by the same equation.

A number of processes used in industry today involve the transport of gas within the structure of microporous solids. Catalytic reactors, adsorption units, and gaseous separation barriers are typical units in which these solids are utilized. Satisfactory techniques exist in the literature for predicting nonadsorbed-gas flow rates through these solids; however, for many processes the gas adsorbs on the solid and it is possible for a net migration to occur both in the gas phase and in the adsorbed layer. Very few definitive data are available on rates of movement within the adsorbed layer, and even less is known about the mechanism of this movement.

It was the major purpose of this investigation to study the main variables affecting transport in adsorbed layers and to develop a better quantitative and qualitative understanding of the nature of this flow. Sounder fundamental knowledge of the phenomenon should result in better correlations of rates of adsorbed-gas flow and subsequently in better design procedures for commercial units.

J. L. Russell is at present with Dow Chemical Company, Midland, Michigan.

DEVELOPMENT OF SURFACE-FLOW EQUATION

A mathematical picture is developed below for transport in adsorbed layers by use of fundamental dynamic and thermodynamic principles. The derivation presented below employs a two-dimensional force balance on an adsorbed film; an alternative approach employs a mechanical-energy balance on the adsorbed layers (*20*).

Fowler and Guggenheim (*13*) and others, in statistical treatments of adsorption, have assumed that adsorbed films have a two-dimensional property analogous to the pressure of a three-dimensional gas phase. This property ϕ is called the *spreading pressure*. It represents the force per unit width necessary to compress the adsorbed film, or conversely that needed to keep it from spreading over clean surface.

Using the concept of a spreading pressure and assuming that the shear stress between the adsorbed layer and the solid is proportional to the average rate of movement of adsorbed molecules past the surface, one may make a force balance on the film

$$-uC_R\,dl = d\phi \qquad (1)$$

This balance neglects any shear stress between the adsorbed layer and the gas phase.

Babbitt (*1*) proposed a relation of the

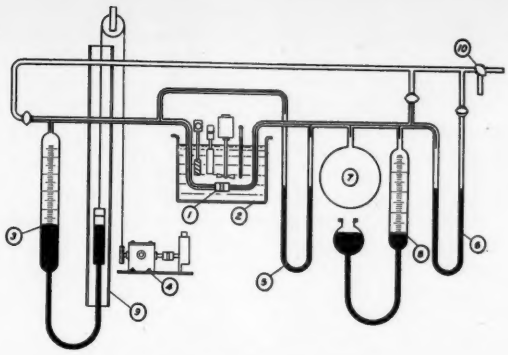

Fig. 1. Pure-gas–flow-rate apparatus.

same form as Equation (1) for describing flow of gases through so-called "nonporous" solids, e.g., metals. Using a relation between ϕ and the amount adsorbed that was derived statistically, he analyzed a limited number of data for hydrogen flow through iron and copper as a function of pressure level. His relation satisfactorily explained the shape of the curves of flow rate vs. pressure level.

In order to develop a general relation between ϕ and the concentration in the adsorbed layer, a solid-gas system at isothermal equilibrium is considered. For such a system it can readily be shown that

$$d\bar{F}_G = d\bar{F}_s \tag{2}$$

It can be deduced from the properties of ϕ that

$$\frac{(\partial \bar{F}_s)}{(\partial \phi)} T = A_m \tag{3}$$

With the assumption that the perfect gas law is applicable, Equations (2) and (3) may be transformed to

$$RT \frac{dp}{p} = A_m \, d\phi = \frac{1{,}000 s_s \, d\phi}{x} \tag{4}$$

If it is assumed that equilibrium exists between the gas phase and the adsorbed layer during flow, Equations (1) and (4) may be combined to give the desired form of a general equation for flow of an adsorbed layer.

$$u = -\frac{RT}{1{,}000 C_R s_s} \frac{x}{p} \frac{dp}{dl} \tag{5}$$

It is noted that Equation (5) contains a free-energy gradient as the potential for flow. Either $\bar{F}_G$, $\bar{F}_s$, or $\bar{F}_{ads}$ may be used as the gradient, where $\bar{F}_{ads}$ is the total free energy of the adsorbed nolecules per mole of adsorbate.

In applying Equation (5) to flow through a microporous solid plug, one assumes that the adsorbed layer travels in a tortuous path along the actual pore lengths. This effect can be accounted for by

$$dl = k \, dl_p \tag{6}$$

Also

$$u_p = \frac{u}{k} \tag{7}$$

The adsorbed-layer transport through a cylindrical plug, for flow normal to its faces, is related to the average net velocity of the adsorbed film u_p by

$$\frac{N_s}{A_p} = x \rho_{app} u_p \tag{8}$$

Combining Equations (5) through (8) and integrating for the case where both N_s and the product $C_R s_s$ are constant results in the following relation:

$$\frac{N_s}{A_p} = \frac{RT \rho_{app}}{1{,}000 k^2 C_R s_s L_p} \int_{p_2}^{p_1} \frac{x^2}{p} \, dp \tag{9}$$

In the derivation of Equation (9) it is also assumed that resistances to flow at the two interfaces, such as adsorption-desorption resistances, are negligible compared with the resistance inside the plug.

For special isotherm cases it is possible to integrate Equation (9) directly. Several such integrations have been made (*20*). The utility of Equation (9) can best be evaluated in the light of experimental results on adsorbed-layer flow.

EXPERIMENTAL

Experimentally, rates of flow of pure gases, both nonadsorbed and appreciably adsorbed, were studied as a function of pressure level, pressure drop, and temperature for flow through ½-in.-diameter cylindrical plugs of activated carbon and of unsintered Vycor glass. A sketch of the apparatus employed in these measurements is shown in Figure 1.

In essence, the experimental technique consisted of flowing a pure gas through a porous plug that was held in neoprene tubing (1) immersed in a constant-temperature bath (2). After a pure gas was introduced through the stopcock (10), constant-volume sections on both sides of the plug were closed, and mercury was fed into an upstream burette (3), thus forcing gas through the plug. Owing to a large volume downstream (7), the downstream pressure (6) was relatively insensitive to the flow and was maintained constant during a run by leveling bulb (8). Runs were continued until the pressure drop (5) attained the steady state value corresponding to the permeability of the plug for the operating conditions. At steady state the volumetric rate of gas flow through the plug, at the upstream pressure and temperature, equaled the constant rate of mercury flow into the upstream burette, as controlled by a constant-speed motor (4), which lifted a cylinder of mercury at a constant rate up a guide rack (9). The very low volumetric flow rates, 0.4 to 350 cc./hr., necessitated the use of a volumetric displacement technique for measuring rates.

Tests with steel plugs illustrated that any combined flow through the tubing, and between the steel plugs and the tubing, was negligible relative to rates through the porous plugs. Flow between the porous plugs and the tubing was also shown to be insignificant by evaluation of the nonadsorbed-gas flow mechanisms and by illustrating reproducibility in different tubing environments.

Flow rates of hydrogen, helium, argon, and nitrogen through the two types of plugs were studied over a mean pressure-level range of a few mm. Hg to about 1,130 mm. Hg, a pressure-drop range of a few mm. Hg to about 385 mm. Hg, and a temperature range of 25° to 85°C. These gases were considered to be negligibly adsorbed. Measurements for isobutane flowing through a carbon plug at 25°C, were made over an approximate mean pressure range of 8 to 630 mm. Hg. Rate studies were made with ethylene, propylene, and isobutane flowing through a Vycor plug at 0°, 25°, and 40°C. For these measurements the mean pressure varied from about 10 to 1,100 mm. Hg and pressure drops varied from about 3 to 725 mm. Hg. A measurement of the bulk liquid rate for isobutane flow through the Vycor plug was made at 0°C. Also, the bulk liquid rate of isooctane flow through the Vycor plug was determined by forcing the liquid through the plug at room temperature and under nitrogen pressure.

Adsorption isotherms for the pure hydrocarbon gases on Vycor glass were measured over the range of variables covered in the adsorbed-gas rate studies. Effects of particle size on the isotherms were studied over a range of 10 to 200 mesh. In addition, the plug used for the rate studies was later ground up for a further check on the isotherms. The equipment employed for the equilibrium studies was a standard constant-volume apparatus. Nitrogen-surface areas and porosities of the two solids were independently determined by standard techniques. All the original data are on file (*20*).

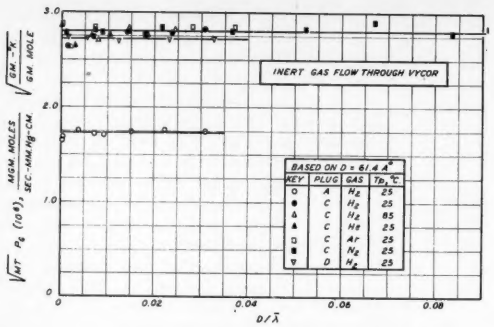

Fig. 2. Inert-gas flow through Vycor.

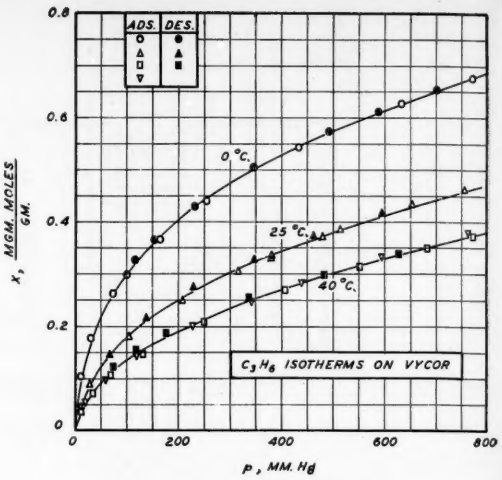

Fig. 3. C_3H_6 isotherms on Vycor.

RESULTS AND DISCUSSION

1. Nonadsorbed Gas Rates

Carbon. The mechanism of nonadsorbed-gas flow through activated-carbon plugs has the characteristics of slip flow. The results are satisfactorily correlated (*20*) by a form of the slip-flow equation suggested by Carman and Arnell (*4*). A slight increase in rates above the slip-flow correlation was observed at low pressures and is similar to that observed by Carman (*4*) for nonadsorbed-gas flow through compressed-powder beds.

Vycor. Measurements for the flow of nonadsorbed gases through several Vycor plugs are presented in Figure 2. The Vycor plug discussed hereafter, plug C, had a cross-sectional area of 1.412 sq. cm. and a thickness of 0.372 cm. The data are plotted and correlated in a manner suggested by the molecular-flow equation, derived by Knudsen (*19*) for a gas flowing down a capillary of radius r and length L, as

$$\frac{N_G}{1{,}000} = \frac{8}{3}\,\frac{\pi r^3}{\sqrt{2\pi RTM}}\,\frac{(2-f)}{(f)}\,\frac{\Delta p'}{L} \qquad (10)$$

The main criterion for molecular flow is that the capillary diameter be small compared with the mean free path of the gas at the mean pressure level. In the abscissa in Figure 2 D is the average pore diameter of the porous glass, which is believed to be reasonably uniform. The value of $D = 61.4$ Å. for Vycor was determined from nitrogen adsorption and mercury-helium density measurements. The mean free path was calculated from Equation (11), which is a transformation of a relationship given by Jeans (*18*):

$$\bar{\lambda} = \frac{3\mu}{\bar{p}'\sqrt{M}}\sqrt{\frac{\pi RT}{8}} \qquad (11)$$

The maximum deviation of the data from the constant value for $\sqrt{MT}P_G$ is about $\pm 5\%$ and the mean deviation is approximately $\pm 2\%$. P_G is the gas phase permeability $(N_G L_p)/\Delta P A_p$. Since the ordinate does not depend on $\bar{\lambda}$, the gas-phase flow rates do not depend on pressure level or the gas viscosity. In addition the mole flow rates per unit pressure drop vary inversely as $\sqrt{MT}$. These characteristics lead to the conclusion that molecular flow is the main mechanism of gas-phase transport through Vycor for the range of variables covered.

The correlation in Figure 2 and Equation (10) has been combined with a pore model for Vycor similar to that employed by Barrer (*2*), to evaluate pore-structure characteristics. This model is comprised of parallel capillaries of equal radii which travel in tortuous paths and have a tortuosity factor k equal to 2.56 (*3*). With a value for the porosity of 0.31 and for the real solid density of 2.05, the internal surface area of the Vycor plug C may be calculated to be 118 (10^4) sq. cm./g. This compares favorably with a value of 143 (10^4) sq. cm./g. as determined by nitrogen adsorption.

2. Equilibria

Some adsorption isotherms for the hydrocarbons on Vycor are given in Figures 3 and 4. Adsorption points are those taken with an increasing pressure level between runs and desorption points are those taken with a decreasing pressure level. The mean deviation of the points from the curves is $\pm 2\%$. Isotherm values are not affected appreciably by particle size. Data on the plug employed in the rate studies are within a few per cent of those shown in Figures 3 and 4.

For the isobutane isotherm at 0°C., shown in Figure 4, a hysteresis loop is observed which is similar to other capillary condensate regions reported for Vycor (*10*). The closing of the hysteresis loops and the flattening of the isotherm above about 950 mm. Hg indicates a saturation condition within the pores. At an amount adsorbed of 2.03 mg. moles/g., with the density of the adsorbed phase being assumed equal to the bulk-liquid density, the volume of adsorbed phase per unit of total volume is equal to 0.286. Since this is close to the porosity value of 0.31, it is concluded that the voids are full of isobutane in a state similar to its bulk-liquid form.

Heats of adsorption increase in the order of ethylene, isobutane, and propylene. This illustrates that the unsaturation or polarity effect plays a major part in adsorption on Vycor.

3. Absorbed Gas Rates

Carbon. Permeability measurements, taken for isobutane flowing through the carbon plug, are satisfactorily predicted by the nonadsorbed-gas correlation because of a large gas-phase flow through macropores, which masks any surface-flow contribution to the total rates. If the gas-phase component were reduced, as in a bulk diffusion system, it might be possible for the surface flow to be appreciable.

The plugs were made of bonded carbon particles and the extra voids encountered between particles would markedly increase the gas-phase rate. Flood and Tomlinson (*11, 12, 22*) have observed appreciable surface rates for pure adsorbed-gas flow through solid-carbon rods.

Vycor. Data for the total flow rates of hydrocarbons through Vycor are presented in Figures 5 and 6 for C_3H_6 at 0°, 25°, and 40°C., and for i-C_4H_{10} at 0°C. Some sample data are presented in Table 1. The remaining data are on file (*20*). The predicted ordinate, based on the nonadsorbed-gas correlation, is shown and the dashed lines represent extrapolations of the correlation. It is obvious that the data are not adequately predicted by this correlation.

Hydrocarbon permeabilities are considerably larger than the values predicted

from a nonadsorbed-gas correlation, sometimes being more than seventeen times as large. The permeabilities vary considerably with pressure level and increase rapidly as the temperature is lowered. In addition, the effects of pressure at low mean pressures are unusual. For the hydrocarbon-Vycor systems, permeabilities at pressures below the vapor pressure are greater than bulk-liquid permeabilities, sometimes being more than forty to sixty times as large. It is clear that the flow does not have the characteristics of normal diffusion.

In Figure 6 the solid curves are the best ones through the adsorption and desorption points, respectively. The observed hysteresis occurs over a pressure range comparable to the one found in the equilibrium curve, shown in Figure 4. The permeability of isobutane at 0°C., just below the vapor pressure, where the voids of Vycor are approximately full of a liquidlike phase, is about forty times that observed for bulk-liquid flow just above the vapor pressure. If a pore model is employed for Vycor, the bulk-liquid permeabilities of isobutane and isooctane may be predicted by Poisseuille's Law (*20*).

In an analysis of the possible causes of the deviations observed with the hydrocarbon-Vycor systems (*20*), the flow phenomena are attributed to a rapid transport in the adsorbed layer itself. The ratios of surface to gas-phase flow are high enough to allow a reliable quantitative analysis to be made for surface flow with the following assumptions. Any net flux between the gas phase and the adsorbed layer is neglected and surface rates are evaluated as the difference between the total rates and the values predicted by the nonadsorbed-gas correlation; a correction factor is applied to the gas-phase prediction which estimates the effect of the adsorbed layer in blocking off cross-sectional area available for gas-phase flow. The simplest case for this blocking is assumed, namely, that the adsorbed layer is distributed uniformly over the surface of the Vycor and that the density of the adsorbed phase equals the bulk-liquid density.

GENERAL DATA TREATMENT

Equation (9) predicts that a plot of $N_s L_p/A_p$ vs $\int_{p_1}^{p_2} (x^2/p)\, dp$ should give a straight line through the origin. Typical plots of this nature are given in Figures 7 and 8. These figures were constructed by utilizing the surface-flow rates calculated from Figures 5 and 6 and the isotherm curves given in Figures 3 and 4. In general, the order of points along the abscissas are the same as in Figures 5 and 6.

The solid lines in Figure 7 are the best straight lines through the origin fitting the results above $\bar{x} = 0.06$, corresponding to about one-tenth of a monolayer. A point was obtained at $N_s L_p/A_p = 7.07\ (10^{-6})$ and $\int_{p_1}^{p_2} (x^2/p)\, dp = 15.02\ (10^{-2})$ which is about 8% below an extension of the line for 0°C. points. Above the $\bar{x} = 0.06$ the maximum deviations from such straight lines for ethylene and propylene are about ±30% for two points. For approximately fifty other points the maximum deviation runs about ±10 to 15%, and the mean deviation is approximately ±6 to 7%. For the limited amount of data below $\bar{x} = 0.06$ for ethylene and propylene, ranging down to about one-fortieth of a monolayer, the points are consistently above the correlating line drawn for higher amounts adsorbed. The points below $\bar{x} = 0.06$ correspond to the lowest pressure runs in Figure 5. Such data points are as much as 2.5 times the straight-line value.

For the isobutane results plotted in Figure 8, the solid line is the best line through the origin fitting the points above $\bar{x} = 0.09$, corresponding to above about one-fifth of a monolayer. The mean deviation from such lines above $\bar{x} = 0.09$ for all the isobutane measurements, including about thirty points, is about ±12%. As observed with ethylene and propylene, the points at very low amounts adsorbed are considerably higher than the straight lines used in correlating the data at higher amounts adsorbed. Below $\bar{x} = 0.09$, down to one-thirtieth to one-fortieth of a monolayer, points at 25° and 40°C. for isobutane are as much as five to six times the values given by the straight lines drawn.

Of particular interest is the fact that the one constant form of the hydrodynamic equation, Equation (9), satisfactorily correlates the results presented in Figure 8 from less than about one-fifth of a monolayer up through the hysteresis region to a condition where the voids are full of a liquidlike phase.

The derivation of Equation (9) did not employ any assumptions as to the degree to which the capillaries were filled with adsorbed phase. It was assumed that if a gas phase is present, any shear due to gas flow is negligible. The velocity of adsorbed-phase transport in Equation (5) is simply taken to be proportional to the spreading pressure gradient or to a free-energy gradient. Apparently, the proportionality constant, which is thought to be a measure of the resistance to flow at the solid-boundary layer, is the same with the isobutane-Vycor syxtem for all levels of adsorption above one-fifth of a monolayer, including the condition of full capillaries.

At first sight, the high permeabilities just below the vapor pressure seem anomolous relative to the low bulk-liquid permeabilities just above the vapor pressure. It is possible to understand this phenomenon by considering the work input in the two cases. The molal-free-energy change per unit pressure drop is much larger in taking a mole from one face of the plug to the other when vapor is present at the faces than when bulk liquid is present. In other words, the spreading pressure gradient across the plug is considerably greater in the former case. This leads to the conclusion that the high rates just below the vapor pressure are obtained at the expense of a greater work input. Thus, as might be expected, it is possible that the energy dissipation per unit of flow through the plug is approximately the same just above and below the vapor pressure.

It is concluded that Equation (9) correlates very well the surface-flow rates for the major range of variables covered in this investigation.

LOW $\bar{x}$ DEVIATION

The deviations from the correlation at very low amounts adsorbed imply that the resistance to movement in very dilute surface concentrations is less than that at higher amounts adsorbed. A possible surface-flow mechanism which is consistent with the observed low resistance to flow is that the force fields of neighboring high-energy sites overlap, and at low amounts adsorbed, where the neighboring high-energy sites are empty, migration occurs along a low-resistance path from high-energy site to high-energy site. When the high-energy sites begin to fill as adsorption is increased, the movement will tend to be from high to low in view of the fact that neighboring high-energy sites are occupied and not immediately available to a molecule. The experimental results indicate that the resistance of the path from high to high is less than the average resistance afforded by the actual paths to and from both high- and low-energy sites when higher amounts are adsorbed. Further experimental work is necessary to correlate adequately the transport at very low amounts adsorbed.

EFFECT OF Δp

In general, Equation (9) predicts that the surface-flow rate per unit of gas-phase pressure drop will depend upon the pressure drop. The observed surface permeabilities for hydrocarbons did not show a detectible change with pressure gradient over the range employed, which was relatively small. For the conditions of these tests and the isotherms involved, $\int_{p_1}^{p_2} (x^2/p)\, dp \cong (\bar{x}^2/\bar{p})\, \Delta p$, which masks any pressure-drop effect. Consequently, the data do not provide an adequate test of the effect of pressure drop.

EFFECT OF TEMPERATURE AND GAS PROPERTIES

On the assumption that s_s is constant and equal to the specific surface, as measured by nitrogen adsorption, C_E's

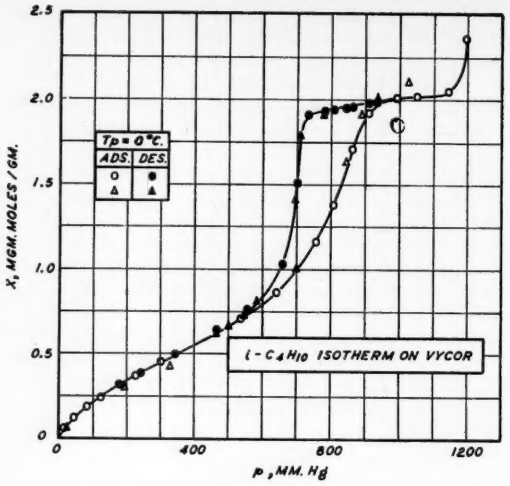

Fig. 4. $i - C_4H_{10}$ isotherm on Vycor.

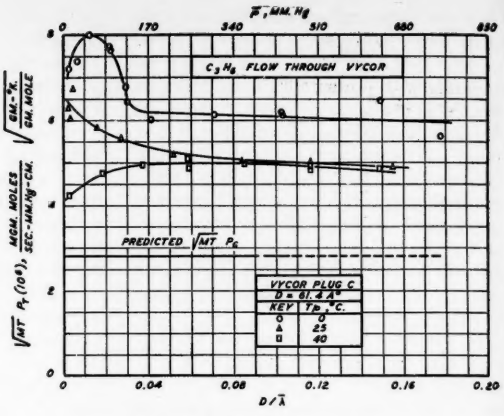

Fig. 5. C_3H_6 flow through Vycor.

may be evaluated from the slopes of the lines in plots like Figures 7 and 8 with Equation (9). The coefficient of resistance is believed to be characteristic of only the nature of the solid surface and the adsorbed molecule. The coefficients of resistance decrease rapidly as temperature increases, and the effect is well correlated by an Arrhenius type of equation. Figure 9 shows a plot of ln C_R vs. $1/T$ for ethylene, propylene, and isobutane on Vycor. For all the hydrocarbons, activation energies are approximately 3,000 cal./g. mole, and the ratio of the activation energy to the heat of adsorption varies from about 0.4 to 0.5.

The resistance coefficient at $1/T = 0$, C_{R_0}, increases in the order of ethylene, isobutane, and propylene. Heats of adsorption increase in the same order, showing that the magnitude of the attractive forces between the solid and the absorbed layer plays a major role in determining flow rates in adsorbed layers.

LITERATURE DATA

Numerous investigators have observed phenomena attributed to movement of an adsorbed layer through microporous solids (*3, 5, 6, 7, 11, 12, 14, 15, 16, 17, 22, 23, 24, 25*). Perhaps the most reliable quantitative values for surface flow that are available are the results of Carman and coworkers (*5, 6, 7*) and some of the measurements of Flood and Tomlinson (*11, 12*). These data have been analyzed (*20*) and the surface-flow rates are reasonably well correlated by Equation (9) for a fairly wide range of conditions. Presented in Table 2 are coefficient-of-resistance values for some of these literature data that are well correlated by Equation (9). Values extrapolated from Figure 9 are also given for comparison with the present results at comparable temperatures.

In view of Carman's data for pure adsorbed gas flow through compressed-powder beds, C_R's for surface flow of difluorodichloromethane through a silica-powder bed fall between values for isobutane and propylene on a Vycor (silica) plug at comparable temperatures. Reported values (*7*) for the heats of adsorption of difluorodichloromethane on the silica powder also fall between those obtained for isobutane and propylene on Vycor, for comparable fractions of surface covered. A coefficient of resistance for difluorodichloromethane flowing through a compressed–carbon-black–powder bed is larger than the C_R's obtained in this investigation at a comparable temperature, as is the measured heat of adsorption. As in the present studies, data below about one-fifth of a monolayer on the compressed beds, including surface-transport measurements for carbon dioxide, are consistently higher than predicted by Equation (9). The ratio of surface rates to the value predicted by Equation (9) increases as the amount adsorbed decreases. Surface rates in a capillary condensate region for difluorodichloromethane and sulfur dioxide moving through a silica-powder bed are not satisfactorily correlated by the one constant form of the hydrodynamic equation at higher amounts adsorbed. As the amounts adsorbed increase in the capillary condensate region, the surface rates become increasingly larger than the values extrapolated from data at lower

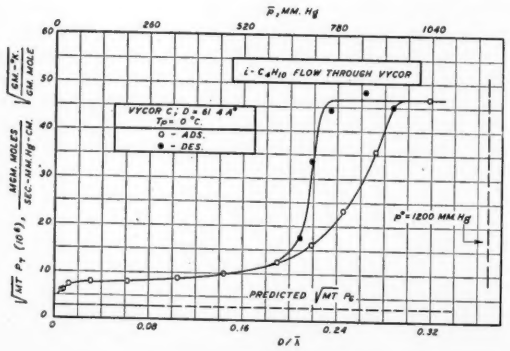

Fig. 6. $i - C_4H_{10}$ flow through Vycor.

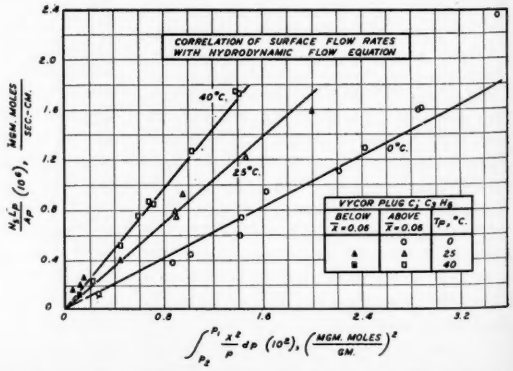

Fig. 7. Correlation of surface flow rates with hydrodynamic flow equation.

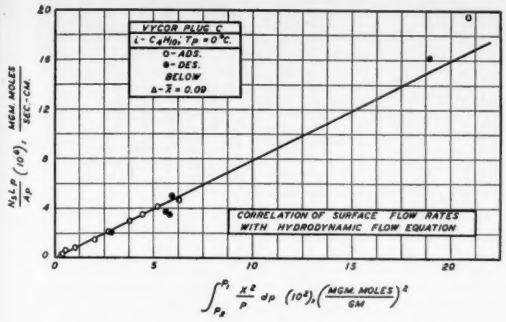

Fig. 8. Correlation of surface flow rates with hydrodynamic flow equation.

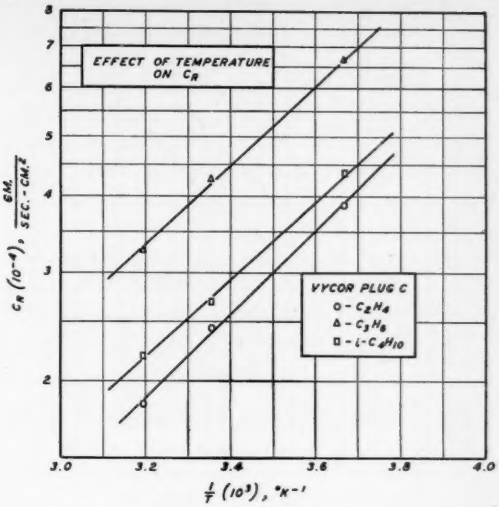

Fig. 9. Effect of temperature on C_R.

amounts adsorbed by means of Equation (9). In general, it might be expected that the resistance to surface transport would tend to decrease as the thickness of the adsorbed layer increased, or as a greater portion of the molecules were moving outside the influence of the surface-force fields.

Adsorbed-layer rates in a capillary condensate region for flow of water through an activated-carbon rod (*11, 12*) are satisfactorily correlated by Equation (9).

It is concluded that Equation (9) correlates literature data for a range of conditions wide enough to illustrate its utility very well. More data are needed to define the variation in the resistance coefficient at very low amounts adsorbed and for some of the capillary-flow data. The reasonable and consistent variation in the C_R's given in Table 2 indicates that Equation (9) correctly characterizes the physical factors involved for conditions where it is applicable.

TABLE 1

SAMPLE DATA, $i - C_4H_{10}$ AT 0°C.

$\bar{p}$, mm.Hg	Δp, mm.Hg	$\bar{x}$, mg. moles / g.	$\frac{N_T}{\Delta p}(10^7)$, mg. moles / (sec.)(mm.Hg)
		Adsorption Points	
20.5	10.2	0.072	1.74
22.6	10.8	0.077	1.81
41.2	16.7	0.116	2.09
103	9.3	0.216	2.29
203	17.9	0.35	2.36
342	27.1	0.51	2.61
469	32.6	0.63	2.96
618	34.1	0.83	3.71
712	30.0	1.03	4.82
799	23.1	1.34	6.98
887	16.5	1.84	10.8
1,033	52.8	2.03	14.1
		Desorption Points	
937	14.0	1.99	13.6
859	42.2	1.97	14.6
766	11.6	1.93	13.4
712	14.2	1.69	10.2
679	26.0	1.24	5.32

FICK'S LAW

Another possible method of correlating the absorbed-layer flow values is with Fick's Law, which has been almost invariably taken to apply by previous workers (*3, 6, 7, 8, 9, 14, 21, 23*). Recently (*12, 23*) the case for flow in a capillary which is full of condensed phase has been treated as a modified type of Poiseuille's Law transport.

For surface transport through a porous plug with tortuous transport paths, an integrated form of Fick's Law is

$$\frac{N_s}{A_p} = D_s \frac{\rho_{app}}{k^2} \frac{\Delta x}{L_p} \qquad (12)$$

Typical surface diffusivities are given in Figures 10 and 11 for the propylene runs and for isobutane at 0°C. All points are shown except those corresponding to the four highest rate measurements given in Figure 6 for isobutane, when the plug voids were approximately full of adsorbed phase. It was inconvenient to place these points on the figure as they are far off scale. If Equation (12) is applied to these four points, diffusion coefficients of approximately 5 (10^{-3}) sq. cm./sec. at $\bar{x} = 2$ are obtained. The solid lines represent the best curves through the plotted points.

The surface diffusivities for all the hydrocarbons vary greatly with the amount adsorbed. Generally the diffusivities rise rapidly when the amount adsorbed corresponds to less than a monolayer, as in Figure 10 and up to about $\bar{x} = 0.45$ in Figure 11. For these regions the diffusivities often increase as much as tenfold over the range of concentrations covered. Above a monolayer, as seen in Figure 11, the diffusivity goes through a maximum and minimum and is appreciably different for adsorption and desorption runs at a given $\bar{x}$. When diffusion coefficients vary in such a manner with concentration, the utility of the concept of a diffusivity, as it is normally defined, has been lost for correlating purposes. Surface diffusivities calculated from the correlation with Equation (9) are represented by the dashed curves in Figure 11.

It is concluded that Equation (9), which is based on a force-balance derivation, is a more satisfactory means of correlating surface-rate data than are previous approaches which employ diffusion coefficients.

CONCLUSIONS AND RECOMMENDATIONS

1. Permeabilities of pure adsorbed gases through microporous solids are often considerably higher than values predicted from correlations based on nonadsorbed-gas–flow data. The deviations are due to a transport in the adsorbed

TABLE 2

COEFFICIENTS OF RESISTANCE

Investigator	System	T_p, °C.	$C_R(10^{-5})$, g. / (sec.)(cm.²)
(*7*)	CF_2Cl_2-carbon-black–powder bed	−21.5	1.32
		20	1.02
(*7*)	CF_2Cl_2-silica-powder bed	−33.1	1.22
		−21.5	0.85
(*11*),(*12*)	H_2O-activated-carbon rod	35	11.8
(*20*)	*Vycor (silica) ethylene	−33.1	0.88
		−21.5	0.65
(*20*)	*Vycor (silica) propylene	−33.1	1.43
		−21.5	1.07
(*20*)	*Vycor (silica) isobutane	−33.1	0.91
		−21.5	0.69

*Extrapolated values.

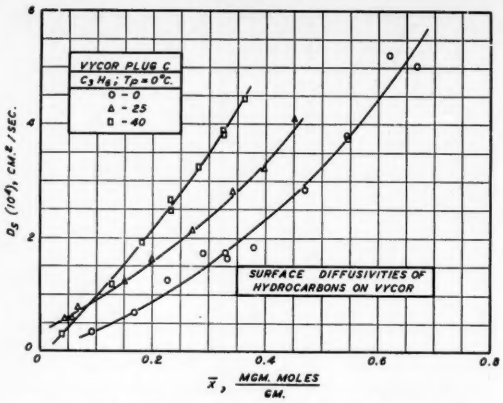

Fig. 10. Surface diffusivities of hydrocarbons on Vycor.

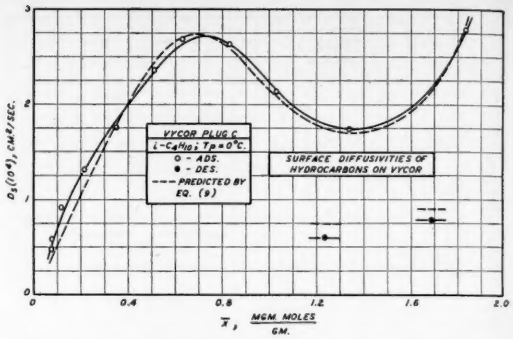

Fig. 11. Surface diffusivities of hydrocarbons on Vycor.

layer, which can often be a major portion of the total transport and can even be the controlling mechanism of flow.

2. An equation for surface flow has been developed which is related to general isotherm values and one empirical constant, by considering the movement in the adsorbed layer to be a hydrodynamic phenomenon. This equation satisfactorily correlates available surface-flow data for a wide range of conditions, and upon being combined with existing gas-phase–transport theories, total adsorbed-gas rates are satisfactorily correlated.

3. Further experimental data are required to study quantitatively deviations from the one constant form of the hydrodynamic equation. It is recommended that the force-balance approach to adsorbed-phase flow be applied to the flow of gases through so-called "nonporous" solids, such as plastic membranes and metals.

ACKNOWLEDGMENT

This work was accomplished with the aid of fellowships from the E. I. duPont de Nemours and the Eastman Kodak companies.

NOTATION

A_m = total area over which adsorbed molecules are mobile, per mole of adsorbate, sq. cm./g. mole
A_p = plug cross-sectional area, sq. cm.
C_R = coefficient of resistance, g./(sec. (sq. cm.)
C_{R_0} = coefficient of resistance at $1/T = 0$, g./(sec.)(sq. cm.)
D = diameter of capillary or pore, cm.
D_S = surface diffusivity, sq. cm./sec.
f = fraction of molecules emitted diffusely after collision
$\bar{F}_{ads}$ = free energy of the molecules in the adsorbed layer, per mole of absorbate, ergs/g. mole
$\bar{F}_G$ = molal free energy in gas phase, ergs/g. mole
$\bar{F}_S$ = total free energy of the solid and the adsorbed molecules, per mole of adsorbate, ergs/g. mole
k = tortuosity factor
l = distance along surface in direction of flow, cm.
l_p = distance in direction of net flux, or along axial length of plug, cm.
L = capillary length, cm.
L_p = plug length, cm.
M = molecular weight, g./g. mole
N_G = gas-phase–flow rate, mg. moles/sec.
N_S = adsorbed-layer flow rate, mg. moles/sec.
N_T = total flow rate, mg. moles/sec.
p, p' = gas-phase pressure, mm. Hg, dynes/sq. cm.
$\Delta p, \Delta p'$ = gas-phase pressure drop, mm. Hg, dynes/sq. cm.
P_G = gas-phase permeability, $N_G L_p/\Delta p A_p$, mg. moles/(sec.)(mm. Hg)(cm.)
P_T = total permeability, $N_T L_p/\Delta p A_p$, mg. moles/(sec.)(mm. Hg)(cm.)
r = radius of capillary, cm.
R = gas constant
s_s = specific surface of solid over which adsorbed molecules are mobile, sq. cm./g.
T = temperature, °K.
u = average rate of movement of adsorbed molecules past the solid surface,(moles/sec.)/(moles/cm.), cm./sec.
u_p = component of film "velocity" u in direction of net flux or along plug length, cm./sec.
x = amount adsorbed, mg. moles/g.

Greek Letters

Δx = difference in amounts adsorbed on two faces of plug, mg. moles/g.
λ = mean free path at mean gas pressure level in system, cm.
μ = gas viscosity, poise
ρ_{app} = apparent density of solid, g./cc.
ϕ = spreading pressure, dyne/cm.

LITERATURE CITED

1. Babbitt, J. D., *Can. J. Res.*, **28A**, 449 (1950).
2. Barrer, R. M., *J. Phys. Chem.*, **57**, 35 (1953).
3. ———, and J. A. Barrie, *Proc. Roy. Soc.* (London), **A213**, 250 (1952).
4. Carman, P. C., *ibid.*, **203**, 55 (1950).
5. *Ibid.*, **A211**, 526 (1952).
6. ———, and P. leR. Malherbe, *ibid.*, **A203**, 165 (1950).
7. Carman, P. C., and F. A. Raal, *ibid.*, **A209**, 38 (1951).
8. Clausing, P., *Ann. physik.*, **7**, 489 (1930).
9. Damkohler, G., *Z. Phys. Chem.*, **A174**, 222 (1935).
10. Emmett, P. H., and T. W. DeWitt, *J. Am. Chem. Soc.*, **65**, 1253 (1943).
11. Flood, E. A., R. H. Tomlinson, and A. E. Leger, *Can. J. Chem.*, **30**, 389 (1952).
12. *Ibid.*
13. Fowler, R., and E. A. Guggenheim, "Statistical Thermodynamics," Chap. 10, University Press, Cambridge (1952)
14. Haul, R., *Z. angew. Chem.*, **62**, 10 (1950).
15. Hodgins, J. W., E. A. Flood, and J. R. Dacey, *Can. J. Res.*, **24B**, 167 (1946).
16. Hoogschagen, J., *Ind. Eng. Chem.*, **47**, No. 5, 906 (1955).
17. Huckins, H. E., and Karl Kammermeyer, *Chem. Eng. Progr.*, **49**, 180 (1953).
18. Jeans, J. H., "An Introduction to the Kinetic Theory of Gases," University Press, Cambridge (1946).
19. Knudsen, M., *Ann. physik.*, **28**, 75 (1909).
20. Russell, J. L., Sc.D. thesis, Mass. Inst. Technol., Cambridge (1955).
21. Sears, G. W., *J. Chem. Phys.*, **22**, No. 7, 1253 (1954).
22. Tomlinson, R. H., and E. A. Flood, *Can. J. Res.*, **26B**, 38 (1948).
23. Wicke, E., and R. Kallenback, *Kolloid Z.*, **97**, 135 (1941).
24. Wicke, E., and U. Voight, *Z. angew. Chem.*, **B19**, 94 (1947).
25. Wheeler, A., "Advances in Catalysis," vol. 3, p. 249, Academic Press, New York (1951).

Manuscript submitted November, 1956; revision received September 6, 1957; paper accepted September 16, 1957.

Film-penetration Model for Mass and Heat Transfer

H. L. TOOR and J. M. MARCHELLO

Carnegie Institute of Technology, Pittsburgh, Pennsylvania

The two major models of the mechanism of mass and heat transfer between two phases are the film theory (*12*) and the penetration theory (*2, 3*). The film theory assumes that there is a region in which steady state molecular transfer is controlling; the penetration theory assumes that the interface is continuously replaced by eddies and that unsteady state molecular transfer into the eddies controls the transfer in this region.

There are three classes of problems to which these theories have been applied: (1) transfer between a solid and a fluid in turbulent flow; (2) transfer between two fluids, at least one of which is in turbulent flow; and, (3) transfer between two fluids in an apparatus of discontinuous geometry such as packed column. In flow in a packed column the concept of surface renewal by eddies is replaced by that of a laminar liquid which mixes at discontinuities in the packing (*2*). If the flow is laminar except at the points of mixing, neither the film theory nor the analysis developed below will apply to the liquid phase.

In the absence of any other resistances the film theory predicts a first-power dependence of the transfer rate on the diffusivity or thermal conductivity, and the penetration theory predicts a square root dependence. Danckwerts (*3*) has shown that neither the film nor penetration theory is completely valid for a packed column, and Hanratty (*5*) points out that at high Schmidt numbers the penetration theory gives better results than the film theory.

The purpose of this paper is to show that the film and penetration theories are not separate, unrelated concepts but rather are limiting cases of a more general model and that the two theories, rather than being mutually exclusive, are actually complementary.

THEORETICAL DEVELOPMENT

The boundary layer extending from the front end of a flat plate or from the inlet to a conduit will be considered. A laminar zone is assumed to exist which is bounded by a turbulent region, and heat or mass is being transferred between the surface and the fluid. For a short distance along the plate the transfer must be by an unsteady state mechanism, for the penetration of the diffusing substance will take a finite contact time (corresponding to a finite distance along the surface) to reach the edge of the film. Some distance along the surface the transfer will reach its steady value and there will be no more accumulation in the film. The short distance corresponds to the penetration theory, the long distance to the film theory, and for intermediate distances the transfer process has the characteristics of both mechanisms.

The transfer between a gas and stirred liquid, which as postulated by Danckwerts has its surface randomly replaced by eddies of fresh fluid from the bulk of the liquid, will be considered. If the eddies remain in the surface a short period of time, each element may be assumed to absorb matter or heat at the interface by unsteady state conduction. As the life of an element increases, the penetration into the element increases and again, after a long enough time, a steady gradient will be set up in the element, no more accumulation will take place, and material will be transferred through the element. Thus the old elements obey the film theory, the young ones the penetration theory, and the middle aged ones have characteristics of both mechanisms. In this intermediate case the penetration has reached the inner side of the element but the steady gradient has not yet been attained. If elements of all ages are present, all three types of transfer take place simultaneously and the model which includes all the cases might be called the *film-penetration* model.

To put this discussion on a quantitative basis it is necessary to modify the Danckwerts-Higbie theory as follows:

The transfer equation is

$$\frac{\partial C}{\partial \theta} = D \frac{\partial^2 C}{\partial y^2} \qquad (1)$$

This neglects all velocity gradients.

The boundary conditions are

$$\theta = 0, \quad C = C_L \qquad (2)$$

$$y = 0, \quad C = C_i \qquad (3)$$

$$y = L, \quad C = C_L \qquad (4)$$

C_i and C_L are assumed independent of θ. The difference between this model and the penetration model is due to Equation (4). It is assumed here that at some distance L below the surface the concentration remains constant at C_L and that a freshly formed surface has this concentration. This condition allows the transfer into an old element to approach the steady state value although the penetration model, which makes L infinite, excludes this limit.

The assumptions have a number of interpretations. At the free surface of a well-stirred liquid in contact with a gas the authors assume, with Danckwerts, that eddies penetrate the surface from the bulk of the liquid and in so doing displace older surface elements, which return to the liquid bulk. The bulk concentration is held constant in time by using, say, a continuous-flow stirred tank.

Below the surface the liquid is well mixed and if the average thickness of the surface elements can be considered to be L, then the concentration at $y = L$ is held constant in time at C_L, the bulk concentration, by the high rate of turbulent transfer from this point to the bulk. That is, the eddies enter the surface with the concentration C_L, since they come from the turbulent region, and when the penetration into any element reaches L, the diffusing material is immediately carried into the bulk by turbulent transfer. In a similar manner the concentration at $y = 0$ is held constant by the high rate of transfer from the gas to the interface. If we admit that the turbulent transfer coefficient is not infinite, so that there is a concentration gradient below L, then eddies may be visualized as entering the surface with the average concentration over the region bounded by the planes $y = L$ and $y = 2L$, and this concentration approaches C_L as the turbulent coefficient increases. It is also necessary that the amplitude of the concentration oscillations at L during the life of a surface element be much less than $C_i - C_L$.

This analysis implies that surface elements differ from other fluid elements in that they may be bombarded on their lower face by a number of eddies before they are displaced from the surface and that because of surface tension an element in the surface is in a stable position and may be removed only by an extra large "kick" from below. The same analysis may also be applied with little change to the fluid-solid interface in a continuous-flow stirred tank, but if the fluid bulk has a mean velocity some modifications are necessary.

At the interface between a solid and a moving turbulent fluid, as in steady flow in a conduit, it is well known that the fluid is in a state different from that of the outer turbulent regions, for the eddying motion is damped by the presence of the wall. Consequently, it is convenient to visualize the fluid adjacent to the wall as a laminar film of average thickness L which is mixed at various intervals by disturbances from the surrounding fluid. The mixing is presumed to occur over a short axial distance and to be violent enough, not only to eliminate the concentration gradient which has built up in the film but to remove the fluid bodily and replace it by fresh fluid from the region $y > L$. If the fluid is highly turbulent in this outer region, then the concentration in the film after mixing is C_L, which now is the bulk concentration, and the concentration at L will always be held at C_L by the turbulent transfer from the plane L to the bulk. In order for C_L to be independent of the age of an element, the mixing must be frequent enough so that the bulk concentration does not change appreciably in the distance between two successive mixings. (This qualification also applies to the penetration model and will be examined later.)

Since the transfer coefficient from $y = L$ to the liquid bulk is not infinite, the assumption that the concentrations at $\theta = 0$ and $y = L$ are the same [Equations (2) and (4)] necessitates, as in the previous case, that the concentration gradient from $y = 0$ to $y = L$ be much steeper than the gradient from $y = L$ to $y = 2L$. In addition, it is now necessary that the concentration in the region $y = L$ to $y = 2L$ does not change appreciably over the distance between two successive mixings and that between mixings the amplitude of the concentration fluctuations at L is small.

The first of these examples has been approached from the penetration viewpoint, the second from the film viewpoint, but the assumptions which have been made make the two cases identical. There is a strong implication in the previous discussion that there is a velocity gradient in the film in the case of conduit flow, but for the sake of simplicity this gradient is neglected.

The solutions of Equations (1) to (4) are available (*1*) and from the solutions the instantaneous transfer rates are found to be, in the nomenclature of mass transfer,

short times

$$N = \Delta C \sqrt{\frac{D}{\pi\theta}} \cdot \left[1 + 2 \sum_{n=1}^{\infty} \exp\left\{-\frac{n^2 L^2}{D\theta}\right\}\right] \qquad (5a)$$

long times

$$N = \Delta C \frac{D}{L} \cdot \left[1 + 2 \sum_{n=1}^{\infty} \exp\left\{-n^2\pi^2 \frac{D\theta}{L^2}\right\}\right] \qquad (5b)$$

These equations are equivalent, but the first converges rapidly for short times and the second for long times. The equations show clearly that for short times the penetration theory is approached,

$$N = \Delta C \sqrt{\frac{D}{\pi\theta}} \qquad (6)$$

and for long times the film theory is approached,

$$N = \Delta C \frac{D}{L} \qquad (7)$$

It can now be seen that what is meant by short times is that the group $(\theta D)/(L^2)$ is small.

The penetration theory holds for the region $\theta \ll (L^2/D)$ and the film theory is valid for the region $\theta \gg L^2/D$. The comparison can be seen in Figure 1, which shows clearly that the film and penetration theories are asymptotes of the film-penetration model.

In general, the point rates given above are of less interest than the average rates, and for transfer across a surface consisting of a multiplicity of surface ages the mean rate is

$$\bar{N} = \frac{1}{A'} \int_0^{A'} N \, dA \qquad (8)$$

or in terms of a surface-age distribution function,

$$\bar{N} = \int_0^{\infty} N\psi(\theta) \, d\theta \qquad (9)$$

If the lives of all elements are the same, the Higbie distribution function applies (*3*),

$$\psi(\theta) = \frac{1}{\theta'} \quad \theta < \theta' \qquad \psi(\theta) = 0 \quad \theta > \theta' \qquad (10)$$

and Equation (5) with (9) and (10) gives short time

$$\bar{N} = \Delta C 2\sqrt{\frac{D}{\pi\theta'}} \left[1 + 2\sqrt{\pi} \cdot \sum_{n=1}^{\infty} ierfc \frac{nL}{\sqrt{D\theta'}}\right] \qquad (11a)$$

long time

$$\bar{N} = \Delta C \frac{D}{L} \left[1 + \frac{2}{\pi^2} \frac{L^2}{D\theta'} \left(\frac{\pi^2}{6} - \sum_{n=1}^{\infty} \exp\left\{-n^2\pi^2 \frac{D\theta'}{L^2}\right\}\right)\right] \qquad (11b)$$

ierfc is the integral of the complementary error function and is tabulated (*1*).

The Danckwerts distribution function assumes that the elements of surface are replaced in a random fashion, so that (*2*)

$$\psi(\theta) = Se^{-S\theta} \qquad (12)$$

If this is used in place of Equation (10) the averaging process yields

short average life (rapid replacement)

$$\bar{N} = \Delta C \sqrt{DS} \left[1 + 2 \cdot \sum_{n=1}^{\infty} \exp\left\{-2nL\sqrt{\frac{S}{D}}\right\}\right] \qquad (13a)$$

long average life (slow replacement)

$$\bar{N} = \Delta C \frac{D}{L} \left[1 + 2 \cdot \sum_{n=1}^{\infty} \frac{1}{1 + n^2\pi^2 \frac{D}{SL^2}}\right] \qquad (13b)$$

Equation (11) reduces to the penetration theory with the Higbie distribution for short times ($\theta' D/L^2$ small),

$$\bar{N} = 2\Delta C \sqrt{\frac{D}{\pi\theta'}} \qquad (14)$$

and to the film theory for long times. In the latter limit the point rate and average rate are the same, and so this asymptote is given by Equation (7). At the former limit all the elements of surface are too young for the penetration to reach L, and at the latter limit most of the surface is old enough to have been completely penetrated.

Equation (13) contains instead of the contact time the variable S, which is the fraction of the surface replaced by fresh fluid per unit time. When the surface is replaced at a rapid rate (SL^2/D large), most of the surface is too young to have been penetrated and Equation (13) reduces to Danckwerts's equation

$$\bar{N} = \Delta C \sqrt{DS} \qquad (15)$$

When $(SL^2)/D$ is small, the major part of the surface has been completely penetrated and Equation (13) reduces to Equation (7), the surface having the characteristics of a film.

Equations (11) and (13) converge rapidly and only a small error is made by dropping higher order terms in Equations (11*a*), (11*b*), and (13*a*) and neglecting the constant in the denomenator of the series in Equation (13*b*). The equations then reduce to

Higbie Distribution

young, $Z' < 1.0$

$$\bar{N} = 2\Delta C \sqrt{\frac{D}{\pi\theta'}} \cdot \left[1 + 2\sqrt{\pi} ierfc \frac{L}{\sqrt{D\theta'}}\right] \qquad (16a)$$

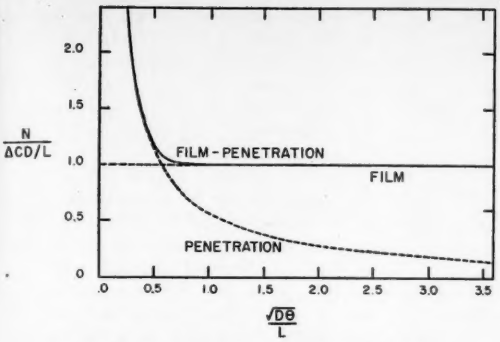

Fig. 1. Point transfer rates as a function of time.

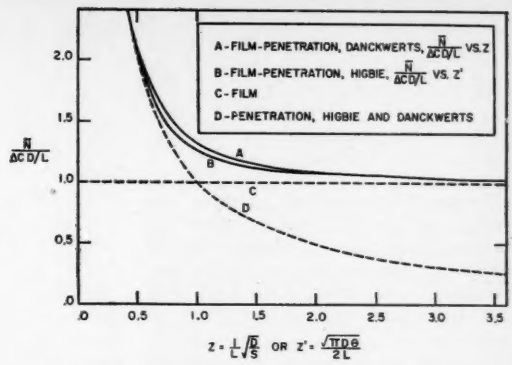

Fig. 2. Mean transfer rates as a function of time.

old, $Z' > 1.0$

$$\bar{N} = \Delta C \frac{D}{L}\left[1 + \frac{1}{3}\frac{L^2}{D\theta'}\right] \qquad (16b)$$

Danckwerts Distribution

young, $Z < 1.0$

$$\bar{N} = \Delta C\sqrt{DS} \cdot\left[1 + 2\exp\left\{-2L\sqrt{\frac{S}{D}}\right\}\right] \qquad (17a)$$

old, $Z > 1.0$

$$\bar{N} = \Delta C \frac{D}{L}\left[1 + \frac{1}{3}\frac{SL^2}{D}\right] \qquad (17b)$$

where

$$Z' = \frac{\sqrt{\pi}}{2}\frac{\sqrt{D\theta'}}{L} \qquad (18)$$

$$Z = \frac{1}{L}\sqrt{\frac{D}{S}} \qquad (19)$$

Since the variables Z' and Z are ratios of film coefficients to penetration coefficients, the equations can be written in terms of D/L and Z' or Z. Figure 2 shows the equations plotted with Z' as the abscissa for Equation (16) and Z as the abscissa for Equation (17). It is clear that the two functions are very closely related, and in fact it would be difficult to distinguish between them experimentally. When Z and Z' are 1.0, the film- and penetration-theory rates are the same and it can be seen that for Z and $Z' < 1$ the film-penetration theory rapidly approaches the penetration theory but for Z and $Z' > 1$ it converges rapidly to the film theory.

It is interesting to note that a five- or tenfold variation in Z or Z' is enough to change a surface from what is essentially a film to one which has the characteristics of a renewed surface. Consequently, a surface defined in the hydrodynamic sense (L and θ' or S fixed) may change from a film mechanism at low Schmidt numbers to a penetration mechanism at high Schmidt numbers.

Similar conclusions may be drawn regarding other types of distribution functions. In general, for surfaces in which old elements predominate, the film theory is valid and the transfer rate varies with the first power of D but, if young elements predominate, the penetration theory applies and the rate varies with the one-half power of D.

The previous discussion applies equally to heat transfer as well as mass transfer and all the foregoing equations have their heat transfer analogues.

The analogue of Equation (13) is

$$\bar{q} = 2\Delta t\sqrt{k\rho c_p S} \cdot\left[1 + 2\sum_{n=1}^{\infty}\exp\left\{-2nL\sqrt{\frac{S}{\alpha}}\right\}\right] \qquad (20a)$$

$$\bar{q} = \Delta t\frac{k}{L}\left[1 + 2 \cdot\sum_{n=1}^{\infty}\frac{1}{1 + n^2\pi^2\dfrac{\alpha}{SL^2}}\right] \qquad (20b)$$

and the other equations can be written in a similar fashion.

TRANSFER FROM A SOLID TO A LIQUID

An example of the application of these equations is the transfer from a solid to a fluid in turbulent flow. Mass transfer terminology will be employed in this discussion. The common assumption of a laminar film at the solid surface leads to the conclusion that at low values of the diffusivity (high Schmidt numbers) the over-all transfer rate is proportional to the first power of the diffusivity, since the molecular transfer is controlling. Other authors have pointed out that this is inconsistent with experiment, and Lin, Moulton, and Putnam (*9*) as well as Diessler (*4*) have introduced an eddy diffusivity into the film region to make analogy calculations fit the data at high Schmidt numbers. Hanratty (*5*) has also shown that concentration profiles in this region are fitted better by the penetration theory than by the film theory.

The procedure to be followed here is to apply the film-penetration model near the wall in place of the other models in order to determine whether the characteristic shift from a film model to a penetration model is consistent with available data.

It is assumed that the distance L in the model corresponds to a fixed value of y^+, and L is given by

$$L = \frac{L^+ d}{\sqrt{f/2}N_{Re}} \qquad (21)$$

Since θ' and S must be fixed entirely by the hydrodynamics, for smooth tubes with fully developed flow and constant physical properties they must be given by

$$S = \frac{V}{d}f_1(N_{Re}) \qquad (22)$$

$$\theta' = \frac{d}{V}f_2(N_{Re}) \qquad (23)$$

Figure (2) shows that use of either of these variables will give similar results, and so one considers only the Danckwerts distribution function and assumes a power relationship for $f_1(N_{Re})$,

$$S = a\frac{V}{d}(N_{Re})^m \qquad (24)$$

Equations (17) and (19) with (21) and (24) yield for the transfer coefficient from the interface to point L,

$Z < 1.0$

$$\frac{k_f}{V} = \sqrt{\frac{a}{N_{Sc}}(N_{Re})^{m-1}} \cdot\left[1+2\exp\left\{-2L^+\sqrt{\frac{aN_{Sc}(N_{Re})^{m-1}}{f/2}}\right\}\right] \qquad (25a)$$

$Z > 1.0$

$$\frac{k_f}{V} = \frac{\sqrt{f/2}}{L^+N_{Sc}} \cdot\left[1 + \frac{aL^{+2}N_{Sc}(N_{Re})^{m-1}}{3f/2}\right] \qquad (25b)$$

where

$$k_f = \frac{\bar{N}}{C_i - C_L} \tag{26}$$

$$Z = \frac{1}{L^+}\sqrt{\frac{f/2}{aN_{Sc}(N_{Re})^{m-1}}} \tag{27}$$

Except at high Schmidt numbers $1/k_f$ is only part of the total resistance to transfer, and the measured transfer coefficients contain the effects of the resistance in all regions of the fluid. It is possible from the work of Lin, Moulton, and Putnam (*9*) to obtain an equation for k_f which, in combination with analogy calculations in the buffer and turbulent regions, is consistent with experimental data over wide ranges of the Schmidt and Reynolds numbers. This equation is of the form

$$\frac{k_f}{V\sqrt{f/2}} = f_3(N_{Sc}) \tag{28}$$

and is shown in Figure (3) for k_f defined over the region $y^+ = 0$ to $y^+ = 5$.

When Equation (25) is in the form above and the equation for the friction factor,

$$\frac{f}{2} = 0.023(N_{Re})^{-0.2} \tag{29}$$

is used,

$Z < 1.0$

$$\frac{k_f}{V\sqrt{f/2}} = \sqrt{\frac{a}{0.023}\frac{1}{N_{Sc}}}\,(N_{Re})^{m-0.8/2} \cdot\left[1 + 2\exp\left\{-2L^+\sqrt{\frac{a}{0.023}N_{Sc}} \cdot(N_{Re})^{m-0.8/2}\right\}\right] \tag{30a}$$

$Z > 1.0$

$$\frac{k_f}{V\sqrt{f/2}} = \frac{1}{L^+N_{Sc}} \cdot\left[1 + \frac{aL^{+2}}{0.069}N_{Sc}(N_{Re})^{m-0.8}\right] \tag{30b}$$

If there is to be no Reynolds-number–Schmidt-number interaction in these equations, the constant m must be set equal to 0.8. Equation (30) is then of the same form as Equation (28),

$Z < 1.0$, high N_{Sc}

$$\frac{k_f}{V\sqrt{f/2}} = \sqrt{\frac{a}{0.023}}\frac{1}{\sqrt{N_{Sc}}}\left[1 + 2 \cdot\exp\left\{-2L^+\sqrt{\frac{a}{0.023}}\sqrt{N_{Sc}}\right\}\right] \tag{31a}$$

$Z > 1.0$, low N_{Sc}

$$\frac{k_f}{V\sqrt{f/2}} = \frac{1}{L^+N_{Sc}} \cdot\left[1 + \frac{aL^{+2}}{0.069}N_{Sc}\right] \tag{31b}$$

and

$$Z = \frac{1}{L^+}\sqrt{\frac{0.023}{a}}\frac{1}{\sqrt{N_{Sc}}} \tag{32}$$

Setting L^+ equal to 5 and adjusting the parameter a gives the results shown in Figure 3, where the curves for three values of a are presented.

The curve of Lin, Moulton, and Putnam (*9*), which has a slope of -1 at low Schmidt numbers, changes to a slope of $-\frac{2}{3}$ at high Schmidt numbers. The present model changes from a slope of -1 at low Schmidt numbers to a slope of $-\frac{1}{2}$ at high Schmidt numbers. This change in slope is a characteristic of the model, and variation of the constants in Equation (25) merely causes a shift in the transition points. As a increases in Figure 3, for example, the transition region shifts to higher Schmidt numbers but it follows from Figure 2 that the transition is essentially completed over the same hundredfold variation in Schmidt number in all cases.

The data of Linton and Sherwood (*10*) and Lin, et al. (*8*) over a range of N_{Sc} from 300 to 3,000 can be compared directly with these curves, but to avoid confusion these data are not shown. Although the data scatter somewhat they are more in agreement with the line of slope $-\frac{2}{3}$ than $-\frac{1}{2}$.

The data of Johnson and Huang (*7*), however, obtained in a stirred tank over a range of Schmidt number from 200 to 15,000, indicate a $-\frac{1}{2}$ power on Schmidt number which is consistent with the present model, since all these data are at high Schmidt numbers. This disagrees with the slope of $-\frac{2}{3}$ in conduits at high Schmidt numbers and it may be that transfer in agitated vessels differs basically from transfer in conduits. In terms of the present model the difference could be due to the presence of a velocity gradient in the fluid near the wall of a conduit, which may not be present in the stirred tank. Since the model neglects this gradient it would check the stirred-tank data, but not the conduit data. Clearly, more mass transfer data are needed before any positive conclusions can be drawn, especially at high Schmidt numbers in conduits and low Schmidt numbers in stirred tanks.

If the penetration model does hold at high Schmidt numbers, it cannot be true at low Schmidt numbers. This is shown in Figure 3, where the line of slope $-\frac{1}{2}$ is extended to low values of N_{Sc} and is off at least a factor of 10. In the same manner the line of slope -1 corresponding to the film theory is off a factor of 10 at high Schmidt numbers so that neither model alone can fit the data over the entire range.

However, the film-penetration model, which contains the foregoing models as limits, is fairly consistent with available rate data in conduits over the full range, and since it reduces to the penetration theory at high Schmidt numbers, it is also consistent with concentration profiles (*5*) as well as with Johnson and Huang's (*7*) data.

Both the eddy diffusivity and film-penetration models are crude representa-

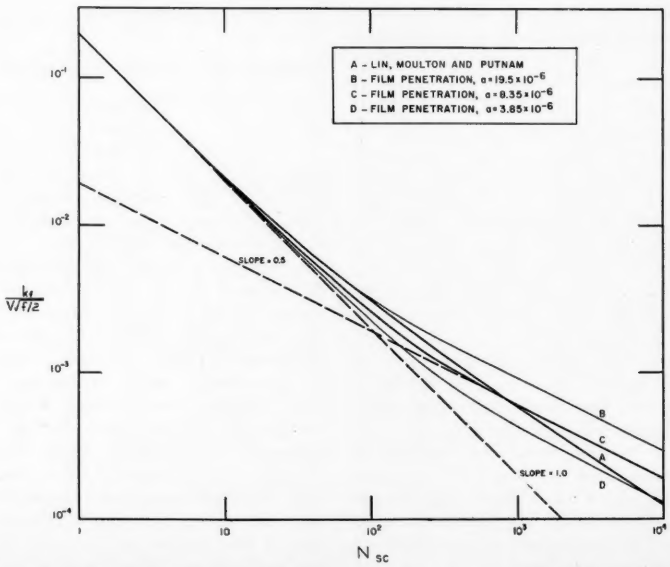

Fig. 3. Transfer coefficients from wall to $y^+ = 5$ as a function of Schmidt number.

tions of a very complicated process; however, the latter model gives a clearer (and possibly more misleading) picture of the exchange mechanism between the wall and the fluid. In this case one pictures masses of fluid moving from the buffer layer to the wall and displacing the fluid previously near the wall. This renewal takes place at a rate described by

$$S = a\frac{V}{d}(N_{Re})^{0.8} \qquad (33)$$

if it is assumed that there is no $N_{Re} - N_{Sc}$ interaction in k_f. Thus this assumption makes the fractional rate of surface renewal vary with velocity in the same manner as the shear stress. Rough calculations indicate that the momentum transferred by this interchange is a small fraction of the total momentum transfer.

For water at 70°F. in a 1-in. tube S varies with N_{Re} as shown in Table 1. Since Figure 2 shows that the transfer equations are essentially the same whether the renewal is assumed to be random or to occur at a fixed age of the surface elements, it can be considered that θ' is the average life of the elements at the surface, and from Equations (18), (19), and (33) one can write

$$\theta' = \frac{4}{\pi}\frac{1}{S} = \frac{4}{\pi}\frac{d}{aV}(N_{Re})^{-0.8} \qquad (34)$$

Some values of θ' are given in Table 1.

It is interesting to examine the assumption made earlier that C_L is constant over the life of a surface element. Since the form of the distribution function has been shown to be immaterial, it is simplest to show that C_L does not vary significantly over the average life of a surface element, θ'. This variation can take place only if the elements are moving along the wall (if oscillations are neglected at a point).

A material balance along a differential length of tube yields

$$\frac{\pi d^2}{4} V\, d\bar{C} = k_L(C_i - \bar{C})\pi\, d\, dx \qquad (35)$$

and integrating over the distance between two successive mixings, x', with C_i constant yields

$$\frac{\bar{C}_2 - \bar{C}_1}{C_i - \bar{C}_2} = \left(\exp\left\{\frac{4k_L x'}{dV}\right\} - 1\right) \qquad (36)$$

The change in concentration at $y = L$ is approximately related to the bulk-concentration change by

$$C_{L_2} - C_{L_1} = \frac{k_L}{k_f}(\bar{C}_2 - \bar{C}_1) \qquad (37)$$

and combining Equations (36) and (37) gives

$$\frac{C_{L_2} - C_{L_1}}{C_i - \bar{C}_2} = \frac{k_L}{k_f}\left(\exp\left\{\frac{4k_L x'}{dV}\right\} - 1\right) \qquad (38)$$

A sufficient condition for C_L to be treated as constant is that the group on the left approach zero. If the average velocity of the fluid in the region from $y^+ = 0$ to $y^+ = 5$ is taken as the velocity at $y^+ = 2.5$ and since $x' = \bar{u}_f\theta'$,

$$x' = 2.5V\sqrt{f/2}\,\theta' \qquad (39)$$

and using the Colburn equation for k_L and Equation (34) for θ' results in the exponent in Equation (38) being

$$\frac{4k_L x'}{dV} = \frac{40a}{\pi}\left(\frac{f}{2}\right)^{3/2}(N_{Sc})^{-2/3}(N_{Re})^{-0.8} \qquad (40)$$

In the worst case this exponent is less than 10^{-7} and since k_L/k_f is less than 1, Equation (38) shows that any variation of C_L due to the displacement of a surface element along the wall is indeed negligible.

TABLE 1

RATE OF SURFACE RENEWAL AND AVERAGE LIFE OF SURFACE ELEMENTS
Water, 70°F., 1-in. tube, $a = 8.35 \times 10^{-6}$

N_{Re}	S, sec.$^{-1}$	θ', sec.
1×10^4	0.21	6.2
5×10^4	3.6	0.36
1×10^5	13.0	0.10

CONCLUSIONS

The transfer to young elements of a surface follows the penetration theory, since the penetration has not reached the outer edge of the elements, and the transfer into the old elements follows the film theory, for the steady state has been attained in these elements.

At low Schmidt numbers the steady gradient is set up very rapidly in any new surface element so that unless the rate of renewal is high enough to remove a large fraction of the surface elements before they are penetrated, most of the surface is, in the foregoing sense, old. Steady state transfer then takes place through what is essentially a film and the effect of surface renewal is negligible.

As the Schmidt number increases, the time necessary to set up the steady gradient increases rapidly, and even low rates of surface renewal are sufficient to keep most of the elements from being penetrated. The transfer then follows the penetration theory and the transfer rate is a function of the rate of surface renewal.

When conditions are such that a surface contains appreciable quantities of young and old elements, as well as middle-aged ones, the transfer characteristics are intermediate between the film and penetration types.

NOTATION

a = constant
A = area
A' = total area
c_p = heat capacity
C = concentration
$\bar{C}$ = bulk concentration
C_L = concentration at $y = L$
C_i = interfacial concentration
ΔC = $C_i - C_L$
d = diameter
D = diffusivity
f = Fanning friction factor
f_1, f_2, f_3 = functional symbols
k = thermal conductivity
k_f = film mass transfer coefficient
k_L = mass transfer coefficient
L = thickness of region in which molecular transfer is controlling
L^+ = value of y^+ at $y = L$
m = constant
N = point mass transfer rate
$\overline{N}$ = mean mass transfer rate
N_{Re} = Reynolds number, $dV\rho/\mu$
N_{Sc} = Schmidt number, $\mu/\rho D$
$\bar{q}$ = mean heat transfer rate per unit area
S = fractional rate of surface renewal
Δt = interfacial temperature minus temperature at $y = L$
V = mean velocity
x = axial distance
x' = distance between two successive mixings
y = distance from interface
y^+ = $(L/d)\sqrt{f/2}N_{Re}$
Z = $(1/L)\sqrt{D/S}$
Z' = $(1/2L)\sqrt{\pi D\theta'}$

Greek Letters

α = thermal diffusivity
θ = time
θ' = contact time
μ = viscosity
ρ = density
$\psi(\theta)$ = surface-age distribution function

LITERATURE CITED

1. Carslaw, H. S., and J. C. Jaeger, "Conduction of Heat in Solids," pp. 252, 255, Oxford University Press, London (1947).
2. Danckwerts, P. V., *Ind. Eng. Chem.*, **43**, 1460 (1951).
3. ———, *A.I.Ch.E. Journal*, **1**, 456 (1955).
4. Diessler, R. G., *Natl. Advisory Comm. Aeronaut. Tech. Note* 3145 (1954).
5. Hanratty, T. J., *A.I.Ch.E. Journal*, **2**, 359 (1956).
6. Higbie, R., *Trans. Am. Inst. Chem. Engrs.*, **31**, 365 (1935).
7. Johnson, A. I., and Chen Huang, *A.I.Ch.E. Journal*, **2**, 412 (1956).
8. Lin, C. S., E. B. Denton, H. S. Gaskill, and G. L. Putnam, *Ind. Eng. Chem.*, **43**, 2136 (1951).
9. Lin, C. S., R. W. Moulton, and G. L. Putnam, *ibid.*, **45**, 636 (1953).
10. Linton, W. H., Jr., and T. K. Sherwood, *Chem. Eng. Progr.*, **46**, 258 (1950).
11. McAdams, W. H., "Heat Transmission," 3 ed., McGraw-Hill Book Company, Inc., New York (1954).
12. Whitman, W. G., *Chem. & Met. Eng.*, **29**, 147 (1923).

Manuscript received in editorial office on May 8, 1957; revision received on November 6, 1957; paper accepted November 7, 1957.

Effect of Superatmospheric Pressures on Nucleate Boiling of Organic Liquids

RUSSELL B. MESLER and J. T. BANCHERO

The University of Michigan, Ann Arbor, Michigan

Superatmospheric pressures greatly reduce the temperature differences in nucleate boiling of organic liquids. Since nucleate boiling is characterized by bubble formation at the heating surface, it seems logical to investigate the pressure difference that causes bubble formation. It has been found that for organic liquids the difference in vapor pressure corresponding to the temperature difference behaves in a regular manner with pressure but does not vary greatly. This regular behavior permits prediction of temperature differences at higher pressures with a knowledge of only vapor-pressure and boiling data at one pressure. New boiling data have been obtained in the investigation.

Of all the variables known to influence nucleate boiling, the one single variable which exerts the most marked effect is pressure. This fact was perhaps first pointed out by Cichelli and Bonilla in 1945 (7). As an example of the pronounced effect, these investigators showed that raising the pressure on benzene from atmospheric up to 645 lb./sq. in. abs. decreased the temperature difference from 63° to 3°F. at a heat flux of 50,000 B.t.u./(hr.)(sq. ft.). Despite this large effect, pressure has not been recognized as a significant independent variable in itself. Instead the effect of pressure has been thought of in terms of its effect on other liquid or vapor properties which were changed by an increase in pressure.

The most prominent characteristic of nucleate boiling is that once a certain temperature is exceeded, a large increase in the number of bubbles is brought about by only a slight increase in the surface temperature. This behavior at once suggests that a certain temperature is necessary to allow bubble growth; however, the logical criterion for bubble growth is the difference in pressure between the vapor pressure of the liquid at the temperature of the surface and the pressure of the system.

One might well expect that at different system pressures roughly the same pressure difference would be necessary for the bubbles to form rapidly. However, the temperature difference corresponding to a particular difference in vapor pressure is a very sensitive function of the pressure and the vapor pressure-temperature equilibrium. Thus, just as the pressure determines the boiling temperature it also determines the temperature difference necessary to give a particular difference in vapor pressure.

Assuming that for bubble growth at different pressures it is necessary to exceed the same pressure difference between the vapor pressure of the liquid at the heating surface and the pressure of the system, then, by picturing the increasing slope of the vapor-pressure curve, one can see how the temperature difference for bubble growth decreases rapidly with increasing pressure.

Perhaps the reason that pressure has not been considered a primary variable in boiling is that the first studies and correlations were made either close to or entirely at atmospheric pressure (*2, 5, 9, 10, 13, 14, 15, 19*). Jakob's 1935 correlation based on data at atmospheric pressure failed to show the improved heat transfer at higher pressures; therefore in 1938 he modified it. Later, when dimensionless correlations were proposed to include the effect of pressure, this effect was included either superficially or only insofar as it affected the physical properties which had been used to correlate boiling data.

It has been universal practice to use dimensional analysis to arrive at nucleate-boiling correlations; however, dimensional analysis, as it has been used, usually requires that the data at constant pressure fit an equation of the type $q/A =$ constant (ΔT^n). To evaluate n, one plots the data on a log q/A vs. log ΔT plot. Plotting the data in this way does not show clearly the sudden way the heat flux rises as the temperature difference becomes large enough to support nucleate boiling.

Two other related experimental facts bear out this idea that a certain pressure difference is necessary to support nucleate boiling. One is that in subcooled boiling it is the temperature of saturated vapor and not the bulk temperature of the liquid which correlates the data. The other is a special case of the first. With mercury, where the density is high, there is an appreciable effect of small liquid heads above the heating surface when the pressure is near atmospheric (*4*). Measurements show that the temperature of the mercury above the heating surface is uniform and close to the equilibrium temperature corresponding to the pressure over the mercury.

An examination of the published data lends support to the idea that the pressure difference remained relatively the same for the same liquid at different pressures. It is apparent that more data are required. One important fact that is apparent is that water is an exception. The decrease in the temperature difference with pressure is not so great for water as it is for organic liquids. That water should not behave as an organic liquid in this respect is to be expected in view of its other unique behavior. Its maximum heat flux is three to five times as great as for organic liquids; its temperature differences in nucleate boiling at atmospheric pressure are about half the normal temperature differences of organic liquids; its physical properties, such as thermal conductivity, surface tension, specific heat, and critical pressure, are outside the ranges of those of organic liquids.

DESCRIPTION OF EQUIPMENT

The apparatus consisted principally of a stainless steel pressure vessel containing the boiling surface. A general view of the apparatus is shown in Figure 1; details appear in Figures 2, 3, and 4.

The boiling surface was the outside surface of a type-304 stainless steel tube. The outside diameter of the tube was 0.0643 in. and the wall thickness 0.0082 in. The tube was suspended in the pressure vessel by two electrodes, which also supplied the electrical current with which the tube was heated. A thermocouple was located inside the tube midway between the supporting electrodes.

A three-phase full-wave rectifier supplied direct current to heat the tube. The rectifier was supplied from a variable-voltage transformer, which furnished the means of varying the heat generated in the tube. The vessel was insulated with Fiberglas, which was placed between the vessel and its angle-iron support structure. Additional insulation was placed on top of the vessel.

The pressure was controlled by two external heaters, which supplied heat to the vessel, one being a high-power heater and the other a low-power.

The thermocouples used were 30 gauge copper-constantan made from one lot of

R. B. Mesler is at present at the University of Kansas, Lawrence, Kansas.

wire. Sauereisen cement was used to insulate the junctions electrically from the tube wall. Lengths of the 0.065-in. O.D. tubing were used to contain all thermocouple junctions. One end was silver-soldered shut and the thermocouple was threaded into the tube from the other end. A diagram of the thermocouple circuit is shown in Figure 5.

The outside diameter of the boiling tube, which was measured to 0.0001 in., was found to be uniform to within 0.0002 in. The length of the boiling section was measured to 0.0005 in. with a caliper and a 2- to 3-in. micrometer. The wall thickness was calculated as 0.0082 in. by weighing measured lengths of tubing. A number of samples were mounted in plastic and polished so that the cross section might be examined. Examination of the cross section with a projection microscope at approximately 100 diameters magnification revealed variations in the tube wall of only 2%.

EXPERIMENTAL METHODS AND PROCEDURES

The liquids used were acetone, benzene, ethanol, and Freon 113 (1, 1, 2-trichlorotrifluoroethane). Each liquid represented a different family of compounds.

In preparation for a run the vessel was disassembled, cleaned with the liquid to be boiled, and dried. The boiling tube was polished in as reproducible a manner as possible, crocus cloth being brought back and forth along the length of tube.

The vessel was purged of air by allowing vapor to escape during the heating period preceding the actual test. In the heating process the high-powered heater caused violent boiling in the vessel, which was allowed to subside before the tube current was turned on. The tube current was gradually increased. Before a heat flux of 25,000 B.t.u./(hr.)(sq. ft.) was exceeded, it was ascertained that boiling had begun, so that there was no possibility of film boiling occurring. If the boiling initiated during the heating period was allowed to die away completely, as much as thirty minutes was sometimes required before the tube began to boil. Although the boiling began at some one point, it quickly spread along the tube.

Initial Atmospheric Runs

The heat flux was raised to 50,000 to 60,000 B.t.u./(hr.)(sq. ft.) except in the case of Freon 113, where it was limited to 30,000. These heat fluxes were chosen to give high values of the heat flux but still avoid the complication of film boiling. Preliminary readings were taken, and after half an hour or longer, a complete set of data at atmospheric pressure and various heat fluxes was taken.

A set of data at constant pressure consisted of readings at ten or more values of the heat flux. Half of these were taken as the heat flux was decreased and half as it was increased. At each heat flux readings were taken of the tube current, the tube thermocouple voltage, the vapor and liquid thermocouple voltages, and the pressure. The boiling was observed visually. Then the Powerstat was turned to give a new value of the heat flux. About 2 min. was required to take the readings at each heat flux. Either before or after the run the voltage across the tube, the shunt voltage, and the tube current were measured.

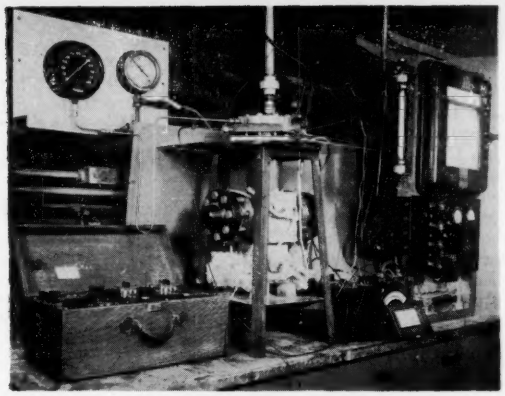

Fig. 1. General view of the apparatus.

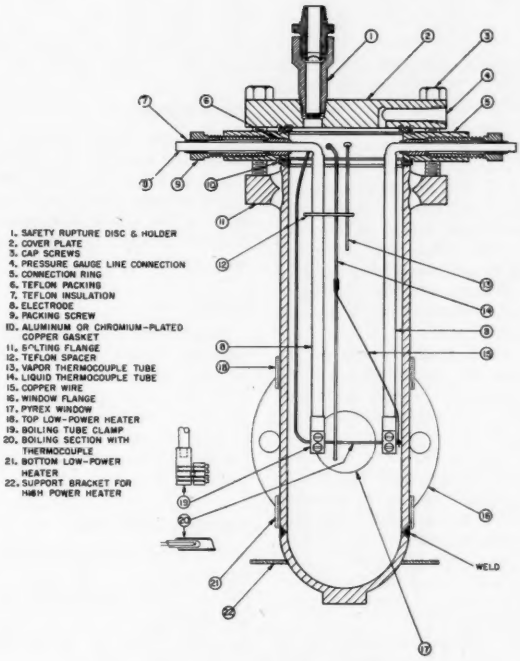

Fig. 2. Sectional view of the pressure vessel.

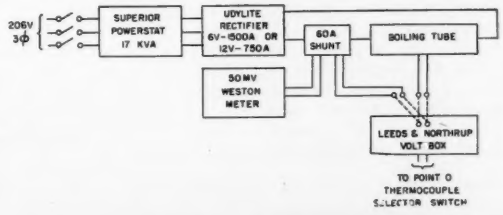

Fig. 3. Boiling-tube power supply.

If the liquid thermocouple voltage indicated a change, the current through the low-power heater was altered accordingly. When an adjustment was made, the new value of either the voltage or current was recorded, and thus the liquid temperature was maintained constant to within 2°F. and usually within 1°F.

Removing the insulation from around the vessel made it possible to dissipate all the heat generated in the boiling tube even when boiling Freon 113 at 117°F. At 450°F. with all the insulation in place it was necessary to add about 400 watts to maintain the temperature.

The lowest value of the heat flux at which readings were taken was usually 8,000 to 12,000 B.t.u./(hr.)(sq. ft.). At this heat flux the tube was still boiling, and at the lower pressures it was possible to count the number of bubble columns. In no case was the heat flux lowered to such a value that boiling ceased during a set of measurements at constant pressure.

Normally the tube was allowed to boil overnight and the atmospheric run repeated before measurements were taken at higher pressures.

Pressure Runs

The pressures to be run were selected on the basis of giving approximately equal reductions in the value of the difference between the surface and the liquid-saturation temperatures. From preliminary measurements the pressures were chosen as 15, 25, 40, 65, 115, 265, and 515 lb./sq. in. abs. For benzene and Freon 113 the two highest pressures were chosen as 215 and 365 lb./sq. in. abs. This was done for Freon 113 so as to not exceed the 495 lb./sq. in. critical pressure and for benzene so as to not exceed the 482°F. limitation of the Teflon packing used.

A complete set of pressures was run at one time to give as consistent data as possible. Consecutively higher pressures were used because it was easier to heat than to cool the vessel.

The high-power heater was used to increase the pressure. Between 15 and 30 min. was required to increase the pressure one step. The tube current was turned off during the heating because of the violent boiling caused by the high-power heater. After the heater was turned off, the boiling was allowed to subside before the tube current was turned on.

When the tube current was turned on, it was increased in steps to approximately the same maximum value as at atmospheric pressure. Preliminary readings were taken while the low-power heaters were being adjusted to give the desired liquid temperature. The tube was allowed to boil 15 to 20 min. while this was being done, before a run was made.

The liquid level was not maintained constant for various pressures but was allowed to increase as the density decreased. The level at the highest pressure was calculated to be 3 to 4 in. higher than at atmospheric pressure for the various liquids. Preliminary data indicated that changes in level at atmospheric pressure showed no significant effect on the boiling.

Final Atmospheric Run

When the run at the highest pressure was completed, all heat to the vessel was turned off and the vessel was allowed to cool. A day or so later the vessel was heated and another run was made at atmospheric pressure. In most instances air had leaked back into the vessel, probably because of differential contraction on cooling. It was necessary to purge the vessel again. During the pressure runs some vapor generally escaped through unnoticeable leaks, but never was the amount greater than 400 ml. This always left the tube submerged at least 1 in. in liquid.

After the atmospheric run the vessel was allowed to cool. The cover plate and the connector ring were removed, the liquid level was measured, and the appearance of the tube was noted.

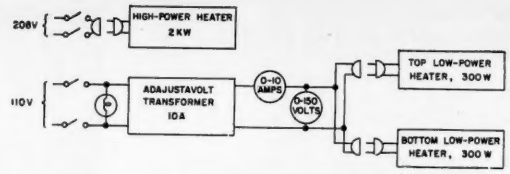

Fig. 4. Heater power supplies.

Ripple Voltages

The root mean square ripple voltage across the boiling tube was measured and found to be 5.5% of the dc voltage. The ripple voltage, therefore, accounted for only 0.3% of the power dissipated by the direct current. It was neglected in computing the heat flux.

Boiling Tubes

One boiling tube was used to obtain the data on ethanol, benzene, and acetone and another to obtain the data on Freon 113. Two tubes were ruined in attempts to boil Freon 113 at too high heat fluxes. In film boiling the tube acquired a dark adherent coating which could not be removed by polishing with crocus cloth.

Treatment of the Data

The heat flux was computed from the measurements of the outside diameter of the tube, the length of the boiling section, the resistance of the boiling section, the calibration of the shunt millivolt meter with its leads, and the reading of the shunt millivolt meter.

The temperature drop across the tube wall was calculated with the following assumptions:

1. Heat generation is uniform in the wall of the tube.
2. The cross section of the tube is uniform.
3. The temperature of the outside surface of the tube is constant.
4. There is no heat flow to the interior of the tube.

The resulting relationship is

$$T_i - T_o = \frac{q/A_o}{2k} r_o \left[1 - \frac{\ln (r_o/r_i)^2}{(r_o/r_i)^2 - 1} \right] \quad (1)$$

where T = temperature, r = radius, q/A_o = heat flux, and k = thermal conductivity. The subscripts i and o refer to the inside and outside of the tube wall. The thermal conductivity of stainless steel varies only 5%/100°F. according to Kreith and Summerfield (*16*). The thermal conductivity was taken at 212°F., and the temperature drop across the tube wall became

$$T_i - T_o = 3.78 \times 10^{-5} q/A_o \quad (2)$$

Experimental Accuracy

The temperatures are probably accurate to 0.2°F. and the heat flux is accurate to about 2.6% at 50,000 B.t.u./(hr.)(sq. ft.) and 5% at 10,000. The accuracy of the calculated temperature drop across the tube wall is probably better than 15%.

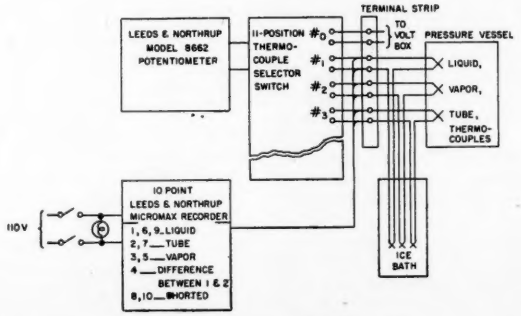

Fig. 5. Thermocouple circuit.

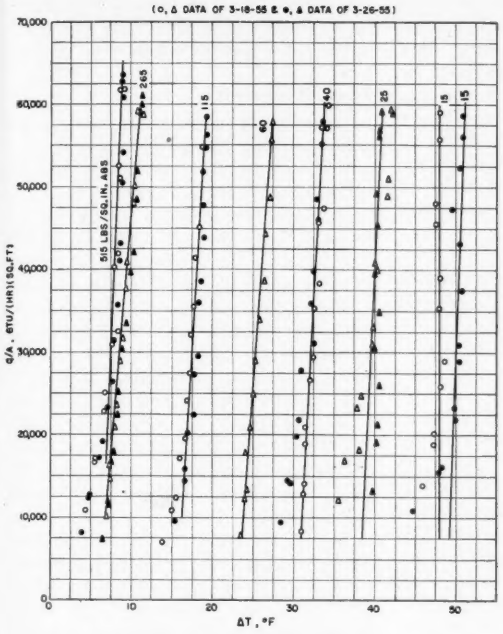

Fig. 6. Superatmospheric boiling data for acetone.

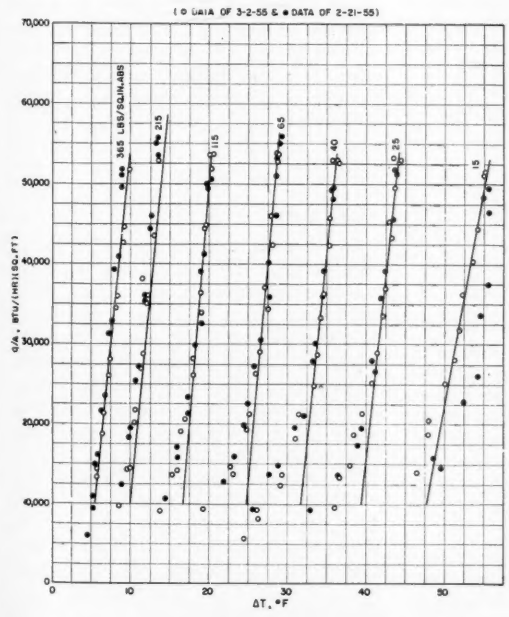

Fig. 7. Superatmospheric boiling data for benzene.

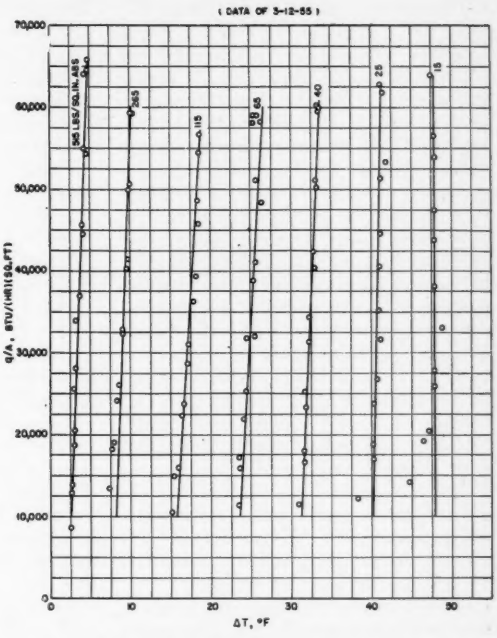

Fig. 8. Superatmospheric boiling data for ethanol.

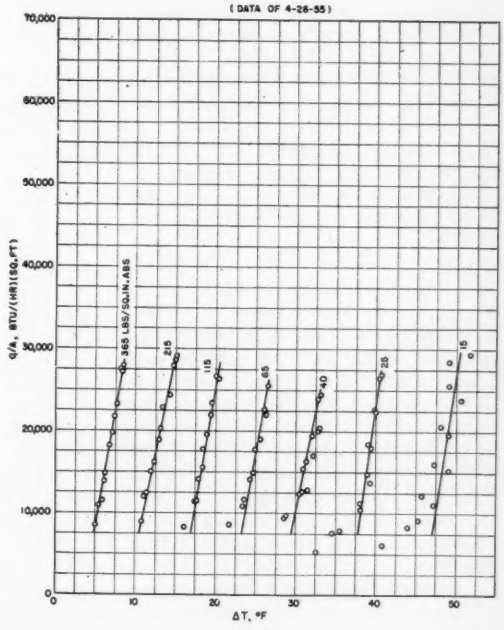

Fig. 9. Superatmospheric boiling data for Freon 113.

RESULTS

Plots of Data

Plots of heat flux vs. temperature difference at various pressures for acetone, benzene, ethanol, and Freon 113 are given in Figures 6, 7, 8, and 9. The results are given in Table 1.* Plots for atmospheric pressure are given separately in Figures 10 and 16 to show the shifts in the curves before, during, and after a sequence of superatmospheric pressure runs. In all the plots the temperature difference is the difference between the vapor-thermocouple temperature and the boiling-tube thermocouple temperature, with the difference corrected for temperature drop across the tube. The vapor temperature was used because it is believed to be a better measure of the liquid-saturation temperature. In no instance did the liquid- and vapor-thermocouple temperatures differ by more than 2°F. and usually by less.

The data were taken with both increasing and decreasing heat fluxes. Since the readings were not different except in a very few cases, the two sets of readings are not distinguished on the plots.

Two independent series of pressure runs were made with acetone. The agreement is good although a 7°F. difference exists between two of the atmospheric runs. Both series were preceded by boiling overnight. The temperature difference increased in one case and decreased in the other after the pressure runs.

Two series of pressure runs were also made with benzene. The liquid was the same but the surface was polished between runs. The atmospheric temperature difference decreased about 7° before the pressure run in the second set. Both series showed a 5°F. difference in the temperature difference between just before and after the pressure runs.

For ethanol at atmospheric pressure the temperature difference increased 3° overnight before the pressure run and then decreased the same amount after the run.

Freon 113 gave experimental difficulties. It film-boiled twice, once at 42,000 B.t.u./(hr.)(sq. ft.) and once at 60,000. Subsequently the heat flux was limited to about 30,000 but the bubbles were smaller than usual, the temperature differences low, and the surface was quickly fouled. This may have been due to small particles dispersed in the liquid. The first three samples taken from the shipping cylinder were cloudy. Finally, the vessel was given an especially good cleaning, all copper was replated with chromium, and clear liquid was charged in. The clear liquid was then boiled, and although it still gave a low temperature difference, it gave a normal boiling appearance. A pressure run was made and on reboiling at atmospheric pressure the temperature difference had increased 13°. Then another pressure run was made and a subsequent atmospheric test showed the temperature difference to be unchanged. Tube-temperature fluctuations at atmospheric pressures were larger for Freon 113 than for other liquids.

Figures 11, 12, 13, and 14 compare the data of this investigation with those of Cichelli and Bonilla (*7*) for benzene and ethanol. Figure 14 also shows the data of Perry (*21*) for ethanol. For the data of Cichelli and Bonilla the steeper slopes do not occur until somewhat higher heat fluxes. Although the exact values of the two sets of data differ slightly, as would be expected, both sets of data show the same effect of pressure.

Figure 15 compares the data of Perry for acetone at atmospheric pressure with those of this investigation. Figure 16 compares the atmospheric results of Corty (*8*) for Freon 113 with those of this investigation. Corty boiled Freon 113 on both a highly polished copper surface and a highly polished nickel-plated surface but offered no explanation of the shift to lower temperature differences on subsequent days for the data from the nickel surface.

Surface-temperature Fluctuations

With nucleate boiling at atmospheric pressure the tube thermocouple did not show a constant temperature, as it did at higher pressures. The fluctuations were rapid and changed in less than a second at times. A plot of the thermocouple voltage against time made with a recorder showed random behavior, the fluctuations being more prominent at lower heat fluxes in the nucleate boiling region. Similar fluctuations have been reported in the literature (*6*).

With the tube in purely convective heat transfer the temperature varied over much larger values but more slowly. This was interpreted to mean that the tube temperature was a function of the circulation in the vessel and that the tube was acting like a hot-wire anemometer.

Tests were made to determine whether the temperature difference in nucleate boiling was also a function of circulation. Varying the heat input into the vessel, which would give more violent agitation, did not affect the nucleate-boiling temperature difference. This is in agreement with an observation by Addoms (*1*) and by Robinson and Katz (*22*).

When the tube-thermocouple voltage was measured, an average value was taken and the violence of the fluctuations noted. The actual temperature fluctuation of the surface would be greater than that indicated by the thermocouple for other than the slowest fluctuations.

At pressures above atmospheric no fluctuations were noted. Because of the fluctuations at low pressures, no data were taken at pressures below atmospheric. Because of the more violent fluctuations at low heat fluxes, data were not taken in the convection or transitional regions.

Visual Observations

The effect of pressure was to make the bubbles rising from the tube smaller until at the highest pressures the bubbles appeared like a fog rising above the tube. At pressures up to 50 to 100 lb./sq. in. gauge a heat flux of 5,000 to 10,000 B.t.u./(hr.)(sq. ft.) gave 10 to 30 bubble columns along the 2-in. length of tube. At higher pressures the bubbles were too small to count in individual columns. The number of columns at the same heat flux increased with pressure.

At low heat fluxes and low pressures bubbles originated almost entirely at the top of the tube. With higher heat fluxes bubbles appeared at the bottom of the tube, and at the highest heat fluxes bubbles almost completely covered the surface of the tube. At the highest heat fluxes bubbles coalesced above the tube to form large volumes of vapor. When film boiling was encountered, the vapor surrounded the tube, and large volumes of vapor would break off and rise to the surface.

When Freon 113 first boiled, the number of vapor columns rising from the tube was far greater and the bubbles were smaller than for the other liquids. As mentioned previously, later runs showed the normal behavior.

The appearance of the surface after a series of pressure runs varied. In every case the surface still had a shine but was colored brown or tan of various intensities. The discoloration was not even and showed numerous pockmarks or small dark rings.

DISCUSSION OF RESULTS

Boiling Curves

In the plots of heat flux vs. the difference between the surface and the saturated-liquid temperatures, the most striking feature is the steepness of the curve in the nucleate-boiling region. Furthermore, the curve appears to be quite linear in this region. The effect of higher pressures is to displace the steep portion of the curve in a parallel manner toward lower temperature differences.

To examine this effect further, the available data were plotted and lines were drawn through the data at the higher heat fluxes so as to represent the data as well as possible. The reciprocal slopes of these lines were computed and are tabulated in Table 2.*

The reciprocal slopes were examined rather than the slopes because it is less

*Tabular material has been deposited as document 5497 with the American Documentation Institute, Photoduplication Service, Library of Congress, Washington 25, D. C., and may be obtained for $3.75 for photoprints or $2.00 for 35-mm. microfilm.

*See footnote in column 1.

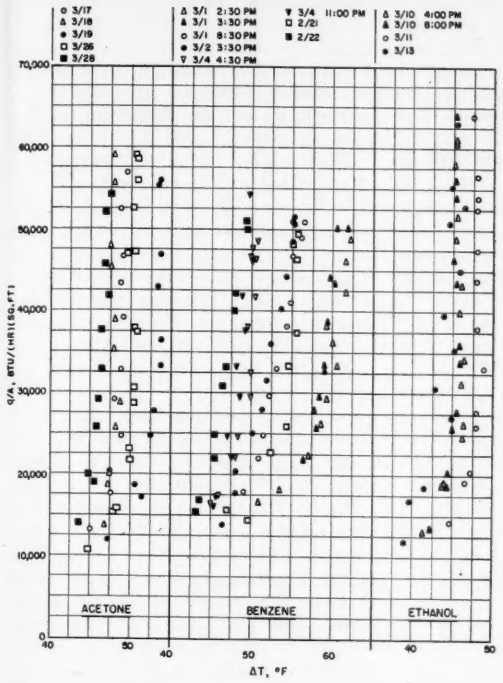

Fig. 10. Atmospheric boiling data for acetone, benzene, and ethanol.

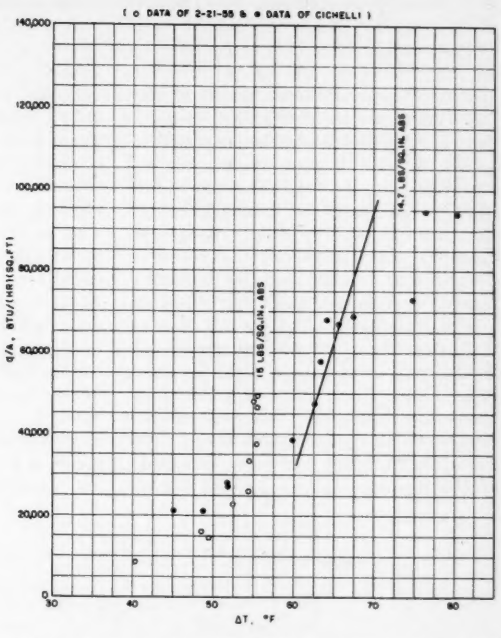

Fig. 12. Atmospheric boiling data for benzene compared with data of Cichelli and Bonilla (7).

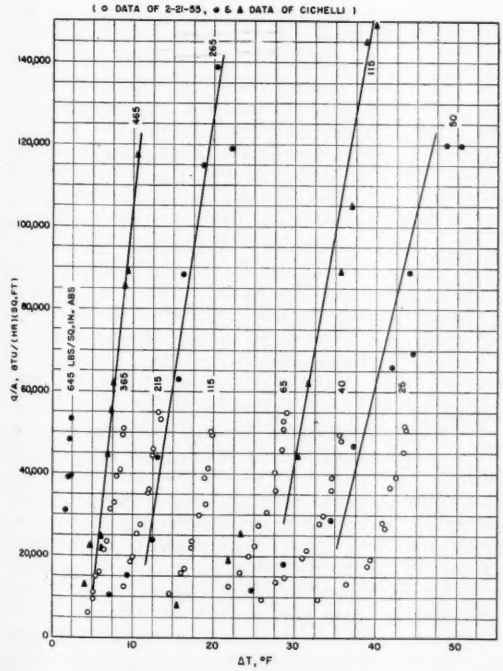

Fig. 11. Superatmospheric boiling data for benzene compared with data of Cichelli and Bonilla (7).

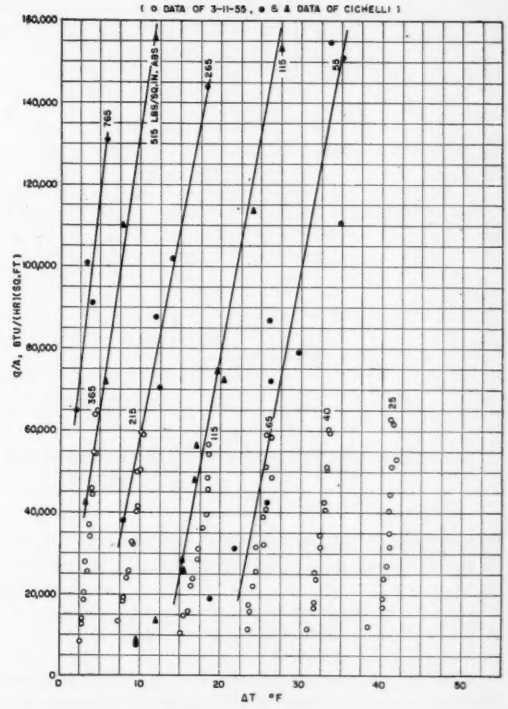

Fig. 13. Superatmospheric boiling data for ethanol compared with data of Cichelli and Bonilla (7).

misleading to consider the heat flux as the independent variable, the nucleate boiling region covering only a small range of temperature differences while the range of heat fluxes is not so limited. The reciprocal slopes are conveniently treated in terms of the increase in the temperature per 100,000 B.t.u./(hr.)(sq. ft.).

The reciprocal slopes were gathered from the data of Corty (*8*), Cichelli and Bonilla (*7*), Perry (*21*), Kaulakis and Sherman (*15, 2*), and this investigation. However, only the reciprocal slopes from Cichelli and Bonilla and this investigation apply to superatmospheric pressures.

The reciprocal slopes do not show a consistent decrease with pressure. Although some sets show a slight decrease, in no case is the decrease so great as the temperature difference; other sets remain relatively constant, and still others show a random variation. The large variability of the reciprocal slopes for the atmospheric data of this investigation is due to the fluctuations of the tube temperature.

The data of Kaulakis and Sherman and of Perry show exceptionally high values, as high as 40°F./100,000 B.t.u./(hr.)(sq. ft.), for the reciprocal slopes. However, Perry's own data show more values of 10 to 18 for the same liquids. If these extremely high values, as well as the zero values from this investigation, are excluded as not representative, the range of values is from 5 to 20. An average value is about 10.

It should be kept in mind that the slopes in Table 2 calculated from the data of Cichelli and Bonilla are based on very few points and are thus subject to error. Table 2 gives the range of heat fluxes over which the data fall near the straight lines drawn through the data. If this range was limited by the range of the data, that fact is noted by an asterisk. The linearity of the steep portion of the curve extends above the range investigated here and appears from the data of Kaulakis and Sherman (*15, 2*), Perry (*21*), and Cichelli and Bonilla (*7*) to extend to almost the maximum heat flux.

The shifts with pressure of the heat-flux vs. temperature-difference curves will again be considered. Since a principal characteristic of the nucleate-boiling region is the necessity of slightly exceeding a certain temperature, it is not difficult to reason that this temperature is required to permit the bubble growth and evolution associated with nucleate boiling. The most appropriate driving force for bubble growth is a pressure difference. More particularly, the pressure difference would be the difference in pressure between the vapor pressure of liquid at the temperature of the surface and the pressure of the system. For the data obtained in this investigation this difference was calculated corresponding to the temperature differences at a constant heat flux of 50,000 B.t.u./(hr.)(sq. ft.), or 25,000 in the case of Freon 113. The results are tabulated in Table 3. This pressure difference for each set of data varies by no more than a factor of 2, and the temperature difference varies by a factor of 8 to 10.

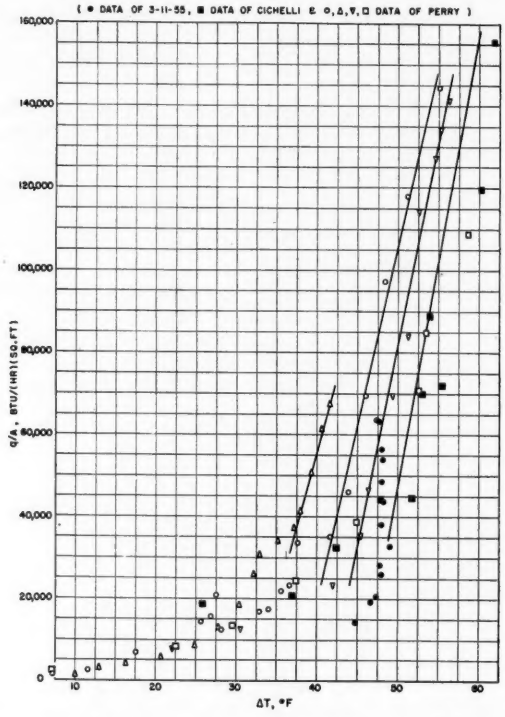

Fig. 14. Atmospheric boiling data for ethanol compared with data of Cichelli and Bonilla (*7*) and of Perry (*21*).

There appear to be two independent effects. One is the constant slope of the lines and the other their displacement. To separate the two effects it seems logical to extrapolate the lines to zero heat flux and to use the intercept as a measure of the displacement of the lines. The vapor-pressure difference calculated from this extrapolated temperature difference should be a better measure of the pressure difference to permit bubble growth than that evaluated at q/A = 50,000. Extrapolating to zero heat flux is the more feasible of several possible methods of attempting to separate variables (heat flux and pressure). One disadvantage is the departure of the data from a linear behavior at low heat fluxes. The extrapolation *does not imply* that the data should fall on the extrapolated line since at low heat fluxes convective heat transfer becomes predominant. Another more logical possibility might be to stop the extrapolation (or interpolation) just above the transition from nucleate boiling to convection. However, this transition is gradual and a transition region exists. No clear-cut definition exists which separates the nucleate-boiling region from the transition region. It is not logical to define nucleate boiling simply as the appearance of bubbles, since with very few bubbles heat transfer is still largely by convection. The pressure differences calculated from these temperature differences are shown in Table 3 and are plotted in Figure 17 against log pressure. In addition, the pressure difference divided by its average value in the relatively constant region for the respective liquid is plotted against log pressure in Figure 18. The pressure difference was normalized by dividing by an average value to take advantage of the decreased variance of an average, compared with a single, value.

This last plot brings all the data to a common curve except for one point at the highest pressure for acetone. An examination of the highest pressure ΔT vs. q/A curve for acetone reveals abnormal behavior, but the reason for this behavior is not known. The behavior of the pressure difference is to increase about 20% with an increase in pressure from atmospheric to about 100 lb./sq. in. Above this pressure the pressure difference decreases apparently toward zero at the critical pressure. Detailed analysis of the behavior of the pressure differences at pressures of 365 lb./sq. in. and above is complicated by the decrease in accuracy of the data and of the extrapolation to

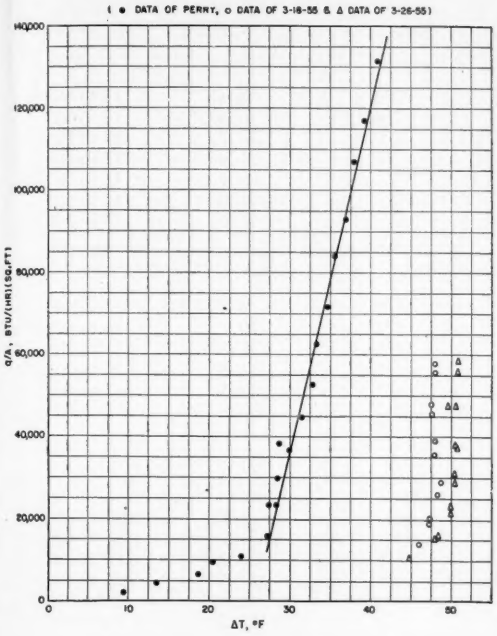

Fig. 15. Atmospheric boiling data for acetone compared with data of Perry (*21*).

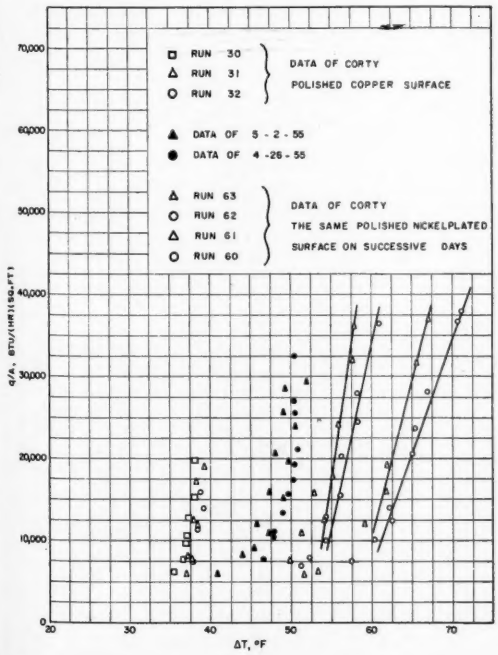

Fig. 16. Atmospheric boiling data for Freon 113 compared with data of Corty (*8*).

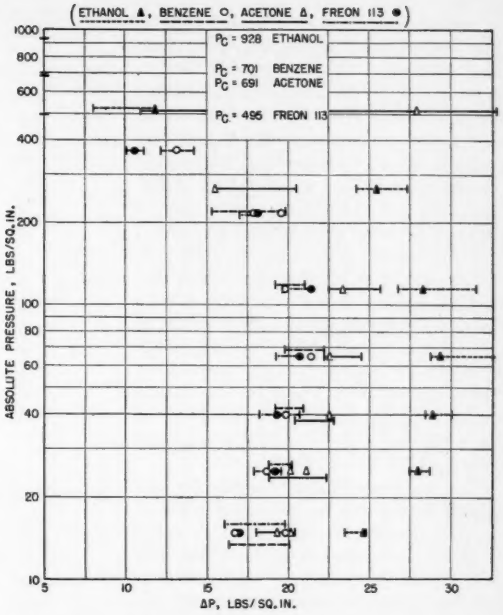

Fig. 17. The difference between the pressure and the vapor pressure of the liquid evaluated at extremely extrapolated values of the surface temperature at zero heat flux, the difference being plotted vs. pressure.

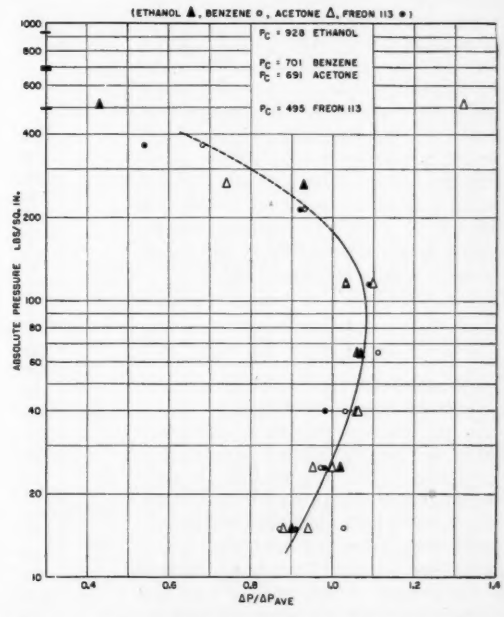

Fig. 18. Values at various pressures of the normalized difference between the pressure and the vapor pressure of the liquid at the surface temperature extrapolated to zero heat flux.

zero heat flux. At these pressures the temperature differences are less than 7.5°F.

Because the common curve of $\Delta P/\Delta P_{avg}$ vs. log pressure represents data from four distinctly different organic liquids, it should apply for a wide range of other organic liquids. With the use of the curve, the vapor pressure of the liquid, the average slope of the boiling curve, and one nucleate-boiling temperature difference, the nucleate-boiling curve at any pressure between atmospheric and about two thirds of the critical can be predicted. As an example of this prediction the nucleate boiling data for *n*-pentane were predicted and compared with the data of Cichelli and Bonilla (*7*). The comparison is shown in Figure 19. The prediction, which agrees with the data to within about 2°F., was made on the basis of $\Delta T = 50°$ at $q/A = 50{,}000$ for nucleate boiling at 22 lb./sq. in. abs.

The nucleate-boiling curves for an organic liquid can be estimated without any boiling data for the liquid. A value of 50°F. estimates to within 50% the value of the temperature difference at a heat flux of 50,000 B.t.u./(hr.)(sq. ft.) for atmospheric boiling of various organic liquids. This is seen by examining Table 4, which lists data from the literature. With this value of 50°F. the superatmospheric behavior can be predicted.

Theory

A theory has been proposed by Corty (*8*) and others (*11*) to account for the phenomenon encountered in nucleate boiling. It is reasoned that as a bubble leaves a surface it leaves behind a much smaller bubble with a radius of the order of magnitude of 10 μin. The size of the bubble left behind is the all-important factor. It is its size that determines what specific temperature the surface temperature must exceed to maintain nucleate boiling. Perhaps several small bubbles are left behind by the departing bubble. According to capillary theory the excess pressure inside a spherical bubble is

$$\Delta P = \frac{2\sigma}{r} \qquad (3)$$

This pressure difference must be exceeded to cause growth of the bubble.

An important fact which supports this theory is that the surface temperature can exceed the temperature usually giving nucleate boiling for a time without the occurrence of boiling. This commonly occurs with increasing heat flux before boiling has started. Then some portion of the surface starts to boil and the boiling quickly spreads across the surface. Such behavior was observed in this investigation and by others (*3*, *8*).

Still further support for the theory is the way in which bubbles rise from particular points on the surface. The behavior is as if a departing bubble left

Table 2. Values of Reciprocal Slopes and Temperature Differences

Temperature, °F.	Pressure, lb./sq. in. abs.	$\frac{d(\Delta T)}{d(q/A)} 10^5$	ΔT, °F. $q/A = 50{,}000$	Range of heat flux $(q/A)(10^{-3})$
Acetone (3/19/55)				
418	515	3.8	8.4	15 to 60*
345	265	7.0	10.4	15 to 60*
270	115	6.0	18.7	15 to 60*
236	65	7.7	27.0	15 to 60*
191	40	5.4	33.9	15 to 60*
162	25	0	41.6	15 to 60*
134	15	0	47.6	15 to 60*
	15	2.2†		
Acetone (3/26/55)				
418	515	3.2	8.8	15 to 60*
345	265	7.2	10.7	15 to 60*
270	115	3.4	19.0	15 to 60*
191	40	6.1	32.8	15 to 60*
162	25	4.7	40.5	15 to 60*
134	15	1.7	50.2	15 to 60*
	15	3.8†		
Benzene (2/21/55 and 3/2/55)				
460	365	10	9.2	25 to 50*
397	215	10	13.2	25 to 50*
331	115	8.4	20.0	25 to 50*
280	65	9.0	28.5	25 to 50*
242	40	10.4	35.8	25 to 50*
209	25	10.4	43.7	25 to 50*
177	15	15.6 9.2†	55.3	25 to 50*
	15	19.8 5.4		
	15	18.8 7.6		
	15	14.6 0		
Benzene: Cichelli and Bonilla (*7*)				
538	645	—	2.2	30* to 50*
491	465	5.2	7.1	20 to 120*
418	265	7.5	14.0	20 to 140*
331	115	9.0	30.5	40 to 150*
256	50	12.0	38.5	40 to 120*
177	14.7	15.8	63.0	40 to 70*
Ethanol				
409	515	4.0	4.3	10 to 60*
350	265	4.0	9.9	20 to 60*
286	115	6.4	18.6	10 to 60*
250	65	6.0	25.8	10 to 60*
223	40	5.0	33.2	15 to 60*
199	25	2.5	41.6	20 to 60*
175	15	0	46.5	20 to 60*
		7.5†		
Ethanol: Cichelli and Bonilla (*7*)				
449	765	5.7	—	70* to 130*
409	515	7.5	3.9	45* to 150*
350	265	9.9	9.0	40* to 140*
286	115	9.3	17.2	25 to 200*
239	55	9.6	25.2	30 to 150*
173	14.7	9.3	50.2	45 to 150*
Freon 113			$q/A = 25{,}000$	
376	365	17.0	8.0	10 to 30*
318	215	20.8	14.2	10 to 30*
259	115	17.0	19.9	10 to 30*
213	65	17.8	25.4	10 to 25*
179	40	20.0	33.0	10 to 25*
148	25	14.0	40.3	10 to 25*
119	15	15.4	50.0	10 to 30*
		0†		

*Upper or lower limit of the data (see text).
†Repeat runs where results were not reproducible.

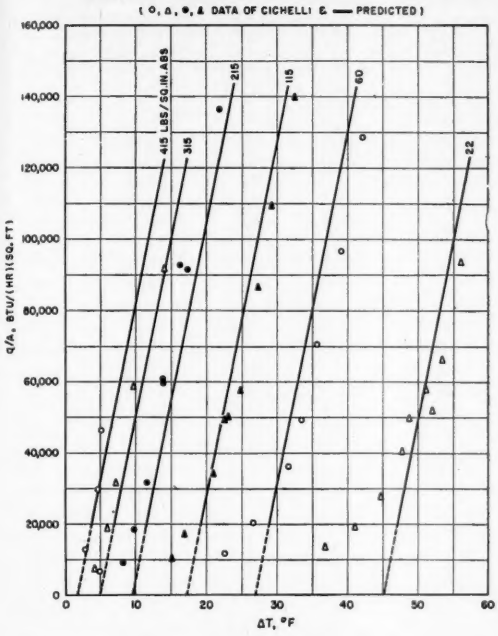

Fig. 19. Comparison of the predicted superatmospheric boiling data for *n*-pentane with data of Cichelli and Bonilla (*7*).

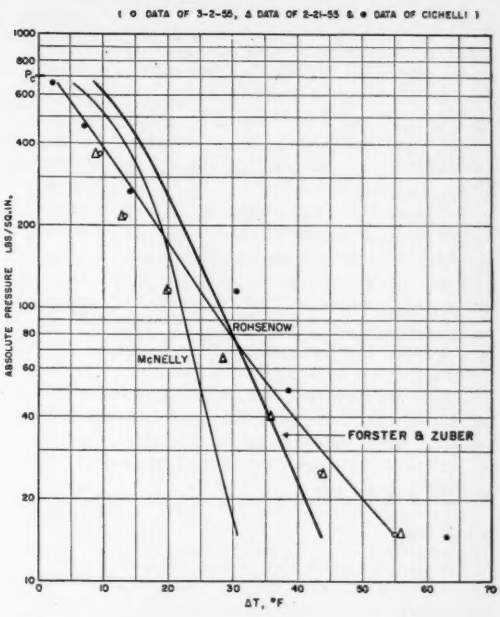

Fig. 21. Superatmospheric temperature differences at q/A = 50,000 B.t.u./(hr.)(sq. ft.) for benzene compared with Rohsenow's (*23*), Forster and Zuber's (*12*), and McNelly's (*17*) predictions.

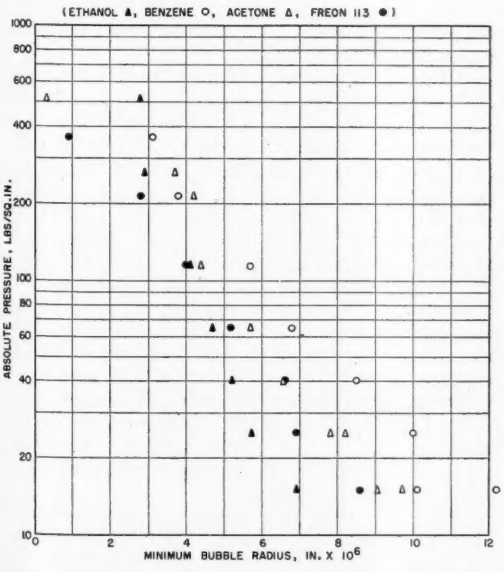

Fig. 20. Minimum radii of bubbles that are able to grow under the pressure differences shown in Figure 17.

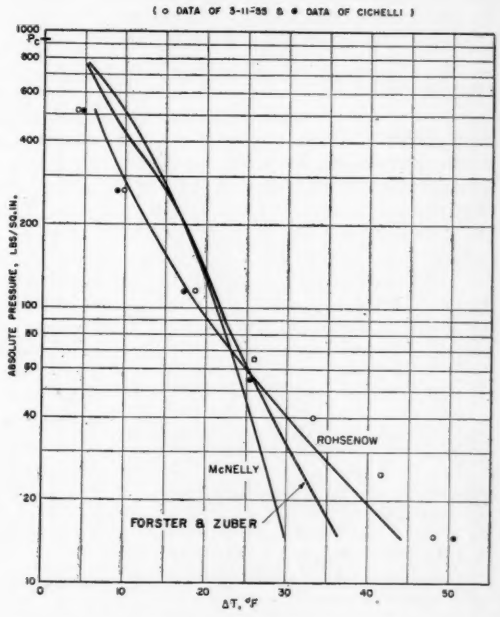

Fig. 22. Superatmospheric temperature differences at q/A = 50,000 B.t.u./(hr.)(sq. ft.) for ethanol compared with Rohsenow's (*23*), Forster and Zuber's (*12*), and McNelly's (*17*) predictions.

behind a smaller bubble from which the next departing bubble could grow.

A spherical bubble being assumed, the equilibrium radii corresponding to the pressure differences shown in Figure 17 were calculated. These are shown in Figure 20. At atmospheric pressure the radii range from 7 to 12 μin. This is the same variation that Corty obtained (*n*-pentane, 13.5 μin.; diethyl ether, 7.5; Freon 113, 6.9 and 5.0).

A decrease in radius with pressure is shown for all four liquids. At the highest pressure the radii for acetone and Freon 113 are much smaller than those for benzene and ethanol. This may not be significant because accuracy of the data is poor at high pressures. The radii always decrease with increasing pressure. The pressure difference from which these radii were calculated first increased with pressure from atmospheric to 100 lb./sq. in. and then decreased with further increase in pressure.

Bubble Size

The bubbles from the boiling surface were much smaller at higher pressures, particularly at pressures over 200 lb./sq. in.

Recent work of Van Wijk, Vos, and Van Stralen (*25*) showed that for binary mixtures certain compositions gave much smaller bubble sizes than others. They also found that the compositions which gave the smallest bubbles also gave the highest burn-out heat fluxes. Data of Cichelli show that the burn-out heat flux increases with pressure up to close to the critical temperature but then decreases. These observations seem to give a clue to the better understanding of burn-out heat flux.

Recent Correlations

Two correlations have been proposed recently which claim to predict the effect of pressure on nucleate boiling. Rohsenow (*23*) published the following correlation in 1952:

$$\frac{h}{k_L}\sqrt{\frac{g_c\sigma}{g(\rho_L-\rho_V)}} = \frac{1}{C_{sf}} \cdot\left[\frac{q/A}{\mu_L\lambda}\sqrt{\frac{g_c\sigma}{g(\rho_L-\rho_V)}}\right]^{0.667}\left[\frac{C_L\mu_L}{k_L}\right]^{-0.7} \quad (4)$$

McNelly (*17*) published an equation in 1953:

$$\frac{hD}{k_L} = 0.225\left[\frac{Dq/A}{\lambda\mu_L}\right]^{0.69}\left[\frac{PD}{\sigma}\right]^{0.31} \cdot\left[\frac{\rho_L}{\rho_V}-1\right]^{0.33}\left[\frac{C_L\mu_L}{k_L}\right]^{0.69} \quad (5)$$

In these two equations h is the heat transfer coefficient, k the thermal conductivity, D a length which is arbitrary since it cancels out, g_c the conversion factor in Newton's law of motion, g the acceleration of gravity, σ the surface tension, ρ the density, q/A the heat flux, μ the viscosity, λ the latent heat of vaporization, C the heat capacity, and P the absolute pressure. C_{sf} is a constant depending upon both the liquid and the surface. The subscripts L and V refer to the liquid and vapor, respectively.

Forster and Zuber (*12, 24*) published an equation which they derived to correlate nucleate boiling data and which they tested only at maximum heat flux. Perkins and Westwater (*20*) compared boiling data predicted from the Forster and Zuber equation with experimental data that they obtained for nucleate boiling of methanol at atmospheric pressure. The Forster and Zuber equation is

$$\left[\frac{C_L\rho_L\sqrt{\pi\alpha_L}q/A}{k_L\lambda\rho_V}\right]\left[\frac{2\sigma}{\Delta P}\right]^{1/2}\left[\frac{\rho L}{g_c\Delta P}\right]^{1/4} = 0.0015\left[\frac{P_L}{\mu_L}\left(\frac{C_L\rho_L\Delta T\pi\alpha_L}{\lambda\rho_V}\right)^2\right]^{0.62} \cdot\left[\frac{C_L\mu_L}{k_L}\right]^{0.33} \quad (6)$$

Here ΔT is the temperature difference between the surface and the liquid saturation temperature, α is the thermal diffusivity, and ΔP is the pressure difference between the equilibrium vapor pressures corresponding to the temperatures in ΔT.

Table 3. Values of the Pressure and Temperature Differences

Pressure, lb./sq. in. abs.	q/A = 50,000 ΔT, °F.	ΔP, lb./sq. in.	ΔT, °F.	ΔP, lb./sq. in.	Extrapolated to q/A = 0 ΔT, °F.	ΔP, lb./sq. in.	$\frac{\Delta P}{\Delta P_{avg}}$
Acetone	3/18/55		3/26/55				
515	8.4	37.5	8.8	39.5	6.3	28	1.32
265	10.4	28.6	10.7	29.4	5.8	15.5	.74
115	18.7	28.5	19.0	29.0	15.5	23.3	1.10
65	27.0	27.0			23	22.5	1.06
40	33.9	25.5	32.8	24.5	30.5	22.5	1.06
25	41.6	23.1	40.5	22.4	39	20.2	.95
					37.5	21.2	1.0
15	47.6	18.6	50.2	20.1	47.5	18.6	.88
					50	19.9	.94
Benzene	2/21/55		3/2/55				
365	8.8	25.6	9.6	27.9	4.5	13.1	.68
215	13.0	26.0	13.3	26.6	9.2	17.8	.93
					10	19.6	
115	19.9	25.5	20.1	25.8	15.7	19.8	1.03
65	28.5	25.1	28.5	25.1	24.3	21.4	1.11
40	35.8	23.4	35.8	23.4	30.7	19.8	1.03
25	43.8	21.2	43.6	21.1	38.5	18.7	.97
15	55.6	20.7	55.0	20.4	46.6	16.7	.87
					53.0	19.8	1.03
Ethanol							
515	4.3	23.3			2.2	11.8	.43
265	9.9	33.2			7.7	25.4	.93
115	18.6	35.3			15.2	28.3	1.03
65	25.8	33.4			23.0	29.3	1.07
40	33.2	31.5			31.0	28.9	1.06
25	41.6	29.6			40.0	28.0	1.02
15	46.2	24.6			48.0	24.6	.90
Freon 113	q/A = 25,000						
365	8.0	23.5			3.6	10.6	.54
215	14.2	29.8			8.8	18.1	.92
115	19.9	27.7			15.6	21.4	1.09
65	25.4	24.3			22.0	20.7	1.06
40	33.0	23.4			28.0	19.3	.98
25	40.3	21.6			36.7	19.2	.98
15	49	19.6			45.9	17.9	.91
	50.6	20.6					

For comparison of these correlations with data obtained here, a plot of the temperature differences at a heat flux of 50,000 B.t.u./(hr.)(sq. ft.) vs. log pressure was prepared. Figure 21 shows the plot for benzene and Figure 22 for ethanol. Also plotted are interpolated values from the data of Cichelli and Bonilla. The physical properties to evaluate the equations were taken from Mesler (*18*).

Rohsenow's equation shows the best agreement. To use Rohsenow's equation the value of C_{sf} must be evaluated experimentally. Values of C_{sf} proposed by Rohsenow to fit the data of Cichelli and Bonilla were used for Figures 21 and 22. These values have a 5.5-fold variation, which he attributes to undeterminable surface factors.

Both Rohsenow's and McNelly's correlations at constant pressure are of the form

$$\Delta T = \text{constant}\ (q/A)^n \quad (7)$$

where n is 0.333 for Rohsenow's and 0.31 for McNelly's correlation. Accordingly,

the quantity $[d(\Delta T)]/[d(q/A)]$ at constant heat flux varies as ΔT whereas for the data of this investigation the quantity was shown to be almost independent of ΔT.

The predicted value of the reciprocal slope at a heat flux of 50,000 B.t.u./(hr.)(sq. ft.) decreases from 33.3°F./100,000 B.t.u./(hr.)(sq. ft.) at ΔT = 50°F. to 6.7 at ΔT = 10°F.

CONCLUSIONS

The results of this investigation substantiate the fact that higher pressures always reduce the difference between the surface and the liquid-saturation temperatures at a constant heat flux in nucleate boiling.

In this study it was determined that the nucleate-boiling data for organic liquids are well represented by straight lines on a *linear* plot of heat flux vs. the temperature difference. This observation is verified by data in the literature as well as by data of this investigation. In the transitional region between the convection and nucleate-boiling regions the temperature differences increase more rapidly with increasing heat fluxes than in the nucleate-boiling region. Also, close to the maximum heat flux the increase is more rapid.

The reciprocal slopes of the lines representing nucleate-boiling data are in the range of from 5° to 20°F./100,000 B.t.u./(hr.)(sq. ft.). An average value is about 10. They are, at least to a first approximation, independent of pressure.

The effect of pressure is to shift the lines representing nucleate boiling to lower temperature differences. Extrapolating the nucleate-boiling lines to zero heat flux makes it possible to consider separately the effect of pressure and the effect of heat flux on the temperature difference.

The pressure difference between the pressure of the system and the vapor pressure of the liquid at the surface temperature, extrapolated to zero heat flux, behaves in a regular manner. This pressure difference increases about 20% between atmospheric pressure and about 100 lb./sq. in. and then apparently tends to zero at the critical pressure. The behavior, which is not shown by water, is illustrated in Figure 18.

Corty (*8*), on the basis of a theory which he formulated, suggested that a pressure difference such as is defined here would behave somewhat as it does. His theory supposes that departing vapor bubbles leave behind much smaller bubbles attached to the surface. The temperature of the surface must be high enough so that the vapor pressure is great enough to permit the small attached bubbles to grow.

By taking the reciprocal slopes of the lines representing the nucleate boiling data as 10°F./100,000 B.t.u./(hr.)(sq. ft.) and by using the aforementioned behavior of the pressure difference, one can predict the temperature differences in nucleate boiling at pressures from atmospheric to about two-thirds the critical pressure. The prediction requires either a knowledge or an assumption of a nucleate-boiling temperature difference at some pressure and heat flux. A value of 50°F. estimates to within 50% the atmospheric nucleate-boiling temperature difference at a heat flux of 50,000 B.t.u./(hr.)(sq. ft.) for organic liquids. This prediction does not require a knowledge of any of the physical properties except vapor pressure.

Rohsenow's (*23*) equation adequately predicts the effect of pressure on the nucleate boiling of the organic liquids studied in this investigation, for which physical-property data are available at superatmospheric pressures. McNelly's (*17*) and Forster and Zuber's (*12*) equations give poorer predictions particularly in underestimating temperature differences at lower pressures and overestimating temperature differences at higher pressures.

The effect of superatmospheric pressure on the appearance of nucleate boiling is to make bubbles smaller. At 350 to 500 lb./sq. in. the bubbles are almost too small to be seen individually.

Experimental results obtained showed the importance of repeating boiling runs and of being able to take the data over a time period which is short compared with the time over which random variations are obtained.

Table 4. Values of Nucleate-Boiling Temperature Differences at Atmospheric Pressure

	q/A = 25,000 B.t.u./(hr.)(sq. ft.) ΔT, °F.	q/A = 50,000 B.t.u./(hr.)(sq. ft.) ΔT, °F.
This investigation		
Acetone		46 to 54
Benzene		49 to 62
Ethanol		44 to 48
Freon 113	48 to 51	
Cichelli and Bonilla (*7*)		
Benzene		61 to 67
n-Pentane (22 lbs./sq. in.)		49 to 51
n-Heptane		38 to 48
Ethanol		50 to 53
Kaulakis and Sherman (*15*)		
Water		17 to 19
iso-Butanol		50
iso-Propanol		45
n-Butanol		38
Banchero, Barker and Boll (*3*)		
Oxygen		23 to 29
Corty (*8*)		
Freon 113	38 to 66	
n-Pentane	23 to 39	
Ether	36 to 50	
Perry (*21*)		
Acetone		32
Butanol		46
Ethanol		39 to 49
Water		21 to 25

LITERATURE CITED

1. Addoms, J. N., Sc.D. thesis, Mass. Inst. Technol., Cambridge (1948).
2. Akin, G. A., and W. H. McAdams, *Trans. Am. Inst. Chem. Engrs.*, **35**, 137–155 (1939); also *Ind. Eng. Chem.*, **31**, 487–491 (1939).
3. Banchero, J. T., G. E. Barker, and R. H. Boll, "Heat-Transfer Characteristics of Boiling Oxygen," Engr. Res. Inst., Univ. Mich., Ann Arbor (1951).
4. Bonilla, C. F., et al., *U.S.A.E.C. N.Y.O.-7638* (1956).
5. Bonilla, C. F., and C. W. Perry, *Trans. Am. Inst. Chem. Engrs.*, **37**, 685–705 (1941).
6. Buchberg, H., U.S.A.E.C., C.O.O. 24, (1951).
7. Cichelli, M. T., and C. F. Bonilla, *Trans. Am. Inst. Chem. Engrs.*, **41**, 755–787 (1945); also "Heat Transfer Lectures," N.E.P.A.-979-I.E.R.-13, 150-186, U.S.A.E.C. (1949).
8. Corty, Clyde, Ph.D. thesis, Univ. Mich., Ann Arbor (1951).
9. Cryder, D. S., and A. C. Finalborgo, *Trans. Am. Inst. Chem. Engrs.*, **33**, 346–361 (1937).
10. Cryder, D. S., and E. R. Gilliland, *Ind. Eng. Chem.*, **24**, 1382–7 (1932); also *Refrig. Eng.*, **25**, 78–82 (1933).
11. Ellion, M.E., Ph.D. thesis, Calif. Inst. Technol., Pasadena (1953).
12. Forster, H. K., and Nathan Zuber, *A.I.Ch.E. Journal*, **1**, 531–5 (1955).
13. Insinger, T. H., Jr., and Harding Bliss, *Trans. Am. Inst. Chem. Engrs.*, **36**, 491–516 (1940).
14. Jakob, Max, "Heat Transfer," vol. 1, John Wiley and Sons, Inc., New York (1949).
15. Kaulakis, A. F., and L. M. Sherman, S.B. thesis, Mass. Inst. Technol., Cambridge (1938).
16. Kreith, F., and M. Summerfield, *Progress Report* 4–68, Jet Propulsion Lab., Calif. Inst. of Technol., Berkeley (1948).
17. McNelly, M. J., *J. Imp. Coll. Chem. Eng. Soc.*, **7**, 18–34 (1953).
18. Mesler, R. B., Ph.D. thesis, Univ. Mich., Ann Arbor (1955).
19. Myers, J. E., and D. L. Katz, *Refrig. Eng.*, **60**, 56–59 (1952); also *Chem. Eng. Progr. Symposium Ser.*, **5**, 107–114 (1953).
20. Perkins, A. S., and J. W. Westwater, *A.I.Ch.E. Journal*, **2**, 471–6 (1956).
21. Perry, C. W., Ph.D. thesis, John Hopkins Univ., Baltimore, Md. (1940).
22. Robinson, D. B., and D. L. Katz, *Chem. Eng. Progr.*, **47**, 317–324 (1951).
23. Rohsenow, W. M., *Trans. Am. Soc. Mech. Engrs.*, **74**, 969–975 (1952).
24. Westwater, J. W., in "Advances in Chemical Engineering," (ed. by Drew and Hoopes) Academic Press, Inc., New York (1956).
25. Van Wijk, W. R., A. S. Vos, and S. J. D. Van Stralen, *Chem. Eng. Sci.*, **5** (1956).

Manuscript submitted April 15, 1957; revision received September 16, 1957; paper accepted October 17, 1957.

Mass Transfer from a Soluble Solid Sphere

F. H. GARNER and R. D. SUCKLING

The University of Birmingham, Birmingham, England

Mass transfer from 3/8- and 1/2-in.–diameter spheres of adipic acid and from 3/8-, 1/2-, 5/8- and 3/4-in.–diameter spheres of benzoic acid into a controlled stream of water passing in laminar flow through a 3-in.–diameter pipe is found to be correlated by the single equation $N_{Sh} = 2 + 0.95\ N_{Re}^{0.5}\ N_{Sc}^{0.33}$ for sphere Reynolds numbers between 100 and 700. The limitations on the application of this equation, due to mass transfer by natural convection, are discussed. Correlations are also obtained for transfer from separate regions of the sphere surface.

Skin-friction-drag coefficients for single fixed spheres have been calculated from reported pressure distributions for Reynolds numbers between 100 and 1,000.

Good agreement is obtained between the mass transfer j factor and other reported values for heat transfer, but comparison with the calculated frictional forces indicates that the equality proposed by Colburn (*3*) does not hold, because the distributions of the mass transfer and the skin friction over the surface differ.

Mass transfer from single spheres to a liquid has received little attention and the analogy between mass and momentum transfer has not been investigated, chiefly because of the lack of data for the values of the skin friction of a sphere.

This work forms part of the more general study of mass transfer processes being undertaken at present in the Chemical Engineering Department of Birmingham University and it was considered that this work would provide data of use for predicting not only mass transfer from solid surface but also for predicting outside film coefficients in liquid-liquid extraction and gas absorption.

The relation between momentum and mass transfer from single spheres with liquid is unknown largely because of lack of knowledge of the skin friction around a sphere and there have been few investigations of the rate of solution at various points around a sphere corresponding to a sphere freely falling or rising in a liquid.

Such knowledge is highly desirable in that a solid sphere is the prototype of an undistorted liquid drop or gas bubble, and it has been shown that the flow conditions around a drop or bubble are precisely analogous to those around a solid sphere (*10*), contrary to some of the supporters of the penetration theory who postulate slip at fluid interfaces.

MOMENTUM TRANSFER

When a real fluid flows over a solid body there is normally no slip between the fluid and the solid surface and there is a velocity gradient outward from the surface, resulting in a net force on the body acting in the direction of the fluid stream, called the *skin friction drag*.

For flow over cylinders or spheres the flow pattern is not symmetrical forward and aft of the body, owing to the dissipation of energy by the internal viscous forces. The pressure difference across the body results in another force, known as *form drag*, acting on the body in the direction of the fluid stream. Summation of these two drag forces gives the total drag force experienced by the body, and these forces are usually expressed in terms of a dimensionless drag coefficient which for a sphere may be written as

$$C_D = \frac{\text{drag force}}{\frac{1}{2}\rho V_0^{\,2}\pi r^2} \qquad (1)$$

For spheres the total drag is usually determined by measurement of the terminal velocity of freely falling spheres, but this gives no indication of the relative importance of skin friction and form drag. The contribution of the frictional drag can be found directly only from an analysis of the hydrodynamic conditions over the sphere surface, usually based upon the variation of the normal pressure over the surface. Values obtained in this way by McNown and Newlin (*20*) indicate that skin friction represents less than 7% of the total drag over the range of Reynolds numbers between 6×10^3 and 2×10^5. For lower Reynolds numbers, Tang, Duncan and Schweyer (*30*) have derived an expression for the estimation of the skin friction, but as it is based upon pressure data determined at a Reynolds number of 16.5×10^4, it is not suitable for Reynolds numbers of 10^3 and below, since the conditions over the surface are very different.

The values obtained for the skin friction in the present work are calculated from pressure distributions determined by Grafton (*12*). These were obtained from a ½-in.–diameter phosphor-bronze sphere mounted in the center of a stream of water flowing through a 3-in.–diameter pipe. The velocity, under streamline flow conditions, was varied from 10^2 and 10^3 Reynolds numbers. The method of analysis used involves the calculation of the hydrodynamic boundary-layer thickness δ, which can be used to determine the intensity of the skin friction over the surface. Graphical integration is then used to obtain the skin-friction drag coefficient.

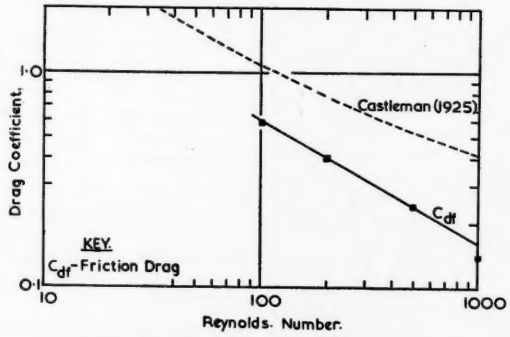

Fig. 1. Amended values for drag coefficients.

Numerous methods of mathematical analysis are available for the surface up to the position of separation of the forward flow. Of these the method of Tomotika (*31*) was used, based on his solution of the momentum integral equation of Milikan (*22*) for a three-

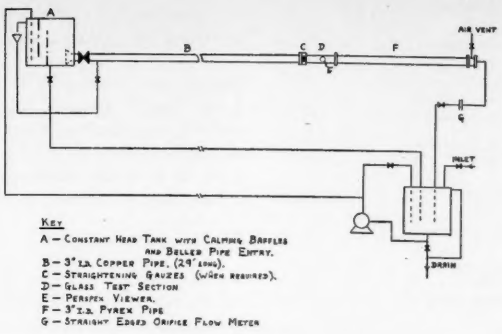

Fig. 2. Diagrammatic arrangement of apparatus.

dimensional boundary layer, the Pohlhausen quartic velocity distribution being assumed within the layer.

The area beyond separation, i.e., the wake region, is less susceptible to mathematical analysis; Grafton (*12*) derived a solution of Milikan's equation by the assumption of a quartic velocity distribution with two further assumptions. Since the pressure measurements in the wake region show little variation, pressure was assumed to be constant over the surface within the wake and, in addition, no discontinuity in the boundary-layer thickness is assumed at separation. With these assumptions Grafton obtained the expression

$$\delta^2 = 34.054\left(\frac{\nu}{U}\right)\phi(\theta_1) \qquad (2)$$

where $\phi(\theta_1)$ is a trigonometric function of θ_1, the angle measured from the rear stagnation point, and U is the velocity at the outer edge of the boundary layer. Since the value of U in the wake is not known, it is expressed in terms of the circulation velocity in the wake as indicated by red-ink traces of the flow patterns. This circulation velocity is also assumed constant and its value at the actual values of the boundary-layer thickness are found by making the value of δ continuous at the separation point.

The chief disadvantage of this method of solution is the need for a red-ink trace of the flow pattern within the vortex region. The assumptions are also open to the following criticisms: The assumption of constant pressure over the surface implies a constant velocity at the outer edge of the boundary layer but the results show that the velocity alters quite rapidly close to the rear stagnation point and the separation point, although over most of the region it is almost constant; and also observation of the circulation by means of aluminum particles indicates that the velocity is not constant around the vortex, the fluid being accelerated along the outer edge of the wake and retarded near the sphere surface. Despite these limitations, and in the absence of any other method, it is felt that this method gives a useful indication of the conditions within the wake.

The skin–friction-drag coefficients obtained from these calculations are given in Table 1 together with the calculated circulation velocities and the free stream velocity. It will be noted that at Reynolds number 1,000 the circulation velocity is predicted to be twice the main-stream velocity. This is not possible, as the main stream provides the driving force for the vortex by means of viscous forces. At the lower end of the range at $N_{Re} = 82$, Grafton (*12*) observed a circulation velocity equal to one half the main stream velocity and this agrees with the values predicted at Reynolds numbers of 200 and 500. In these two cases the wake skin friction is 8.2 and 7.3%, respectively, of the value for the forward flow area. In the absence of any alternative method of calculation, the skin friction in the wake is assumed to be 7½% of that for the forward flow area for all cases in the region under consideration. The values of the skin–friction-drag coefficients recalculated on this basis are given in Table 2.

The negative values given for the wake are explained by the flow along the surface being in the reverse direction to that of the main stream and so producing a drag in the reverse direction. These amended values and the curve presented by Castleman (*2*) for the total drag coefficient are illustrated in Figure 1.

MASS TRANSFER PROCESSES

At the interface between a soluble solid and a liquid a saturated solution is formed as shown by Ward and Brooks (*32*). Transfer of the solute into the main body of the fluid occurs in three ways, dependent upon the conditions. For an infinitely small sphere in an infinite stagnant fluid, transfer will be by molecular diffusion alone but, as the sphere size increases, natural convection currents are set up owing to the difference in density between the pure solvent and the solution. This induced flow helps to carry solute away from the interface. The third mode of transfer, forced convection, closely resembles natural convection except that the flow pattern is imposed upon the fluid by an external force. In practice, all three modes of transfer are usually present.

The reported values of mass transfer by molecular diffusion alone are usually obtained by extrapolation from results obtained for small spheres under natural convection conditions. Fuchs (*8*) showed theoretically that the limiting value of the dimensionless mass transfer Sherwood number (KD/D_v) is 2.0 when the sphere becomes infinitely small. This limiting value was confirmed by Langmuir (*16*) from a consideration of the experimental results of Morse (*23*) on diffusion from small spheres of iodine in natural convection and by Whytlaw-Gray and Patterson (*33*) for the sublimation of benzophenone spheres in still air.

Under convective conditions, either natural or forced, a relationship for mass transfer similar to the relationships obtained for heat transfer may be expected, of the form

$$N_{Sh} = f(N_{Re}N_{Sc}N_{Gr'}) \qquad (3)$$

where N_{Sh}, N_{Re}, N_{Sc} and $N_{Gr'}$ are respectively the Sherwood, Reynolds, Schmidt, and Grashof numbers for the mass transfer. Such a relationship has been obtained theoretically by Eckert (*6*) from a consideration of the boundary conditions.

For transfer under natural-convection conditions, where the Reynolds number is unimportant, this expression reduces to

$$N_{Sh} = f(N_{Sc}N_{Gr'}) \qquad (4)$$

The data obtained by Ranz and Marshall (*26*) for the evaporation of water drops in still air are correlated by an expression of this form, namely,

$$N_{Sh} = 2.0 + 0.60N_{Gr'}{}^{0.25}N_{Sc}{}^{0.33} \qquad (5)$$

Most other work, both theoretical and practical, produces results of the form

$$N_{Sh} = \text{constant} \times (N_{Gr'}N_{Sc})^{0.25} \qquad (6)$$

The most reliable form of this seems to be that derived by Merk and Prins (*21*), which for heat transfer from a sphere is written as

$$N_{Nu} = 0.558(N_{Gr'}N_{Pr})^{0.25} \qquad (7)$$

However, this takes no account of the effect of the "plume" of hot air rising above the sphere.

Under forced convection conditions where the Grashof number is unimportant the general expression becomes

$$N_{Sh} = f(N_{Re}N_{Sc}) \qquad (8)$$

which boundary layer theory suggests should take the form

$$N_{Sh} \propto N_{Re}{}^{0.5}N_{Sc}{}^{0.33} \qquad (9)$$

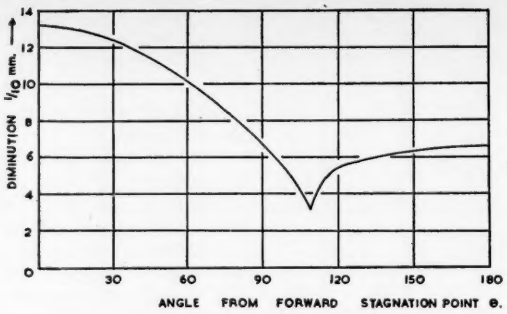

Fig. 3. Distribution of mass transfer.

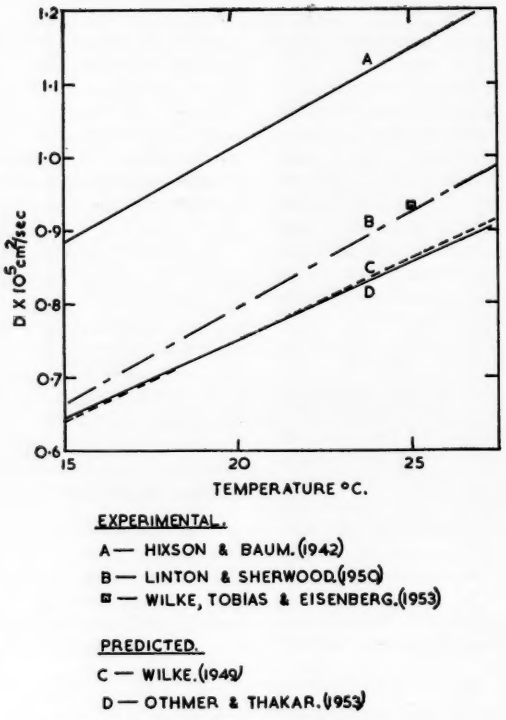

Fig. 4. Diffusivity data for benzoic acid in water.

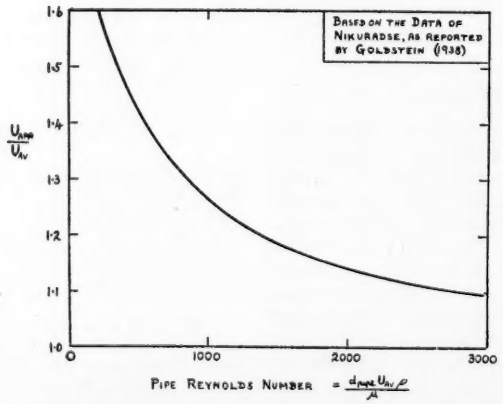

Fig. 5. Velocity at sphere position in distributed flow.

Correlations of this form have been obtained by experiment over quite a wide range of Reynolds numbers; Frössling (*7*) from a study of the mass transfer from liquid spheres of nitrobenzene, aniline, and water and from solid spheres of naphthalene to air for diameters of 0.02 to 0.18 cm. derives a relationship which may be written in the form

$$N_{Sh} = 2.0 + 0.55 N_{Re}^{0.5} N_{Sc}^{0.33} \quad (10)$$

for Reynolds numbers between 2 and 1,000. Similarly at slightly higher Reynolds numbers, 600 to 2,600, Axel'rud (*1*) obtains the expression

$$N_{Sh} = 0.82 N_{Re}^{0.5} N_{Sc}^{0.33} \quad (11)$$

for the dissolution of potassium chloride and potassium nitrate spheres in water by use of dissolution periods of 3 to 4 min.

In the field of heat transfer Kramers (*14*), from a study of heat losses from induction-heated spheres, proposes the slightly different expression

$$N_{Nu} = 2.0 + 1.3 N_{Pr}^{0.15} + 0.66 N_{Re}^{0.5} N_{Pr}^{0.31} \quad (12)$$

for the range $0.5 > N_{Re} > 2{,}000$.

In intermediate regions where neither the Reynolds nor the Grashof number can be neglected no satisfactory relationships have been reported. Dryden, Strang, and Withrow (*5*) note that the mass transfer from a packed bed depends upon the direction of flow, i.e., upward or downward, at low Reynolds numbers, which indicates that the natural- and forced-convection flows are interacting. The results of Kramers and Frössling quoted above suggest that the Grashof number is unimportant above $N_{Re} = 1$, but these results were obtained in air and for small-diameter spheres, which give very small Grashof numbers. The only suggested correlations in this intermediate region are the one due to Ranz and Marshall (*26*), who propose a vectorial addition of the velocities, using a natural-convection velocity based upon a modified Grashof number, and the suggestion of Garner and Grafton (*9*) that the transfers due to the two processes are simply additive.

Variation of the transfer rate around the sphere has not been widely studied. Distributions are reported by Frössling (*7*) and by Garner and Grafton (*9*), but the importance of the wake area in mass transfer is not widely known.

EXPERIMENTAL PROCEDURE

The apparatus, shown diagrammatically in Fig. 2, consists essentially of a 3-in. I.D. horizontal water tunnel fitted with reservoir tanks and a recirculation system. A 30-gal. reservoir fitted with calming baffles discharges through a belled entry into a 29-ft. length of 3-in. I.D. straight copper pipe. This is followed by a 1-ft. working section of 3-in. I.D. glass pipe and a further 5-ft.

TABLE 1

CALCULATED CIRCULATION VELOCITIES AND DRAG COEFFICIENTS

Reynolds Number	100	200	500	1,000
Free stream velocity, cm./sec.	0.811	1.62	4.05	8.11
Wake velocity, cm./sec.	0.063	0.90	2.05	16.0
Ratio, wake: stream	0.077	0.55	0.51	1.97
Skin–friction-drag coefficients				
Front	0.640	0.438	0.260	0.155
Wake	−0.001	−0.036	−0.019	−0.145
Total	0.64	0.40	0.24	0.01

TABLE 2

AMENDED VALUES OF SKIN–FRICTION-DRAG COEFFICIENT

Reynolds number	100	200	500	1,000
Skin–friction-drag coefficient				
Front	0.640	0.438	0.260	0.155
Wake	−0.048	−0.033	−0.020	−0.012
Total	0.59	0.40	0.24	0.14

section of glass pipe. The water then flows through a square-edged orifice meter into a tank, from which it is pumped back to the reservoir. Three interchangeable orifice plates are used in the flow meter, which operates a carbon tetrachloride U-tube manometer. With this system the average velocity in the 3-in. pipe can be measured over the range of 0.006 to 0.15 ft./sec.

The belled entry and long length of pipe (approximately 120 diameters) ensure a typical parabolic flow distribution with a minimum of disturbance in the working section. A pack of six 30/30 mesh 33 S.W.G. phosphor-bronze-gauze flow distributors can be placed when required at the end of the copper section to give a flatter velocity front. The actual velocity profile at the sphere position, two pipe diameters downstream from the gauzes, then depends upon the water flow rate, varying from near parabolic at very low flows to nearly flat at high flows.

The spheres of benzoic and adipic acids used in this work were prepared by compressing the acid into pellets in a hand press. This gave pellets having a smooth surface, with no definite crystalline arrangement such as casting would produce. Uniformly high pellet densities of 1.29 to 1.30 g./cc. for benzoic acid and 1.33 to 1.34 g./cc. for adipic acid were obtained by this method. The sphere sizes were ⅜, ½, ⅝, and ¾-in.–diameter in benzoic acid and ⅜ and ½ in. in adipic acid.

All the spheres were supported from downstream on a 5-in.–long $\frac{1}{16}$-in.–diameter brass rod, mounted on a ⅛ by $\frac{1}{32}$-in. brass strip forming a diameter of the 3-in. I.D. test line. The end of the rod was thinned to fit into a 0.046-in.-diam. hole drilled along a radius of the pellet. The supporting rod was fixed so as to be coaxial with the test line.

Dissolution of the spheres was followed photographically with a Bolex 16-mm. ciné camera and back lighting. Single exposures were made at the beginning and end of the dissolution period. The film was projected by means of a Kodascope projector, and drawings of the silhouettes were made approximately twelve times the actual sphere size. In order to reduce the optical distortion caused by the cylindrical pipe wall, a perspex block was cut with one face curved to fit against the pipe wall and the opposite face plane. Cross wires attached to this block served to locate the final photograph with respect to the initial one. The refractive index of the perspex was slightly greater than that of the water in the pipe line, and so a correction factor for the slight optical distortion was calculated in each specific case by comparing the apparent dimensions of equal actual lengths in the natural and distorted planes. The diminution was then measured at 10-deg. intervals around the circumference of the corrected silhouettes.

RESULTS

A typical distribution of the transfer around the surface is shown in Figure 3. The transfer rates for the total surface, the forward flow area (i.e., the area upstream of separation), and the wake area are found from these distributions by graphical integration over the surface, the rates for the forward and rear stagnation points from the terminal values of these curves, and the rates expressed in terms of the Sherwood number.

In order to express the results in terms of the Schmidt and Sherwood numbers, it is necessary to find values for the diffusivity of the materials used. A survey of the literature revealed no experimental data for adipic acid and, since it is difficult to determine the diffusivity experimentally with any degree of accuracy, it was evaluated by the prediction method of Othmer and Thakar (*24*). In order to make the results for adipic and benzoic acids comparable the diffusivity of the latter material was determined in the same way. The agreement between the predicted and experimental values for benzoic acid is good, as shown in Figure 4, where the values predicted by the methods of Othmer and Thakar (*24*) and Wilke (*34*) are compared with the experimental data reported by Linton and Sherwood (*17*) and Hixson and Baum (*13*), and an isolated value quoted by Wilke, Tobias, and Eisenberg (*35*). The values reported by Hixson and Baum were used by Garner and Grafton (*9*) in calculating the results for the dissolution of ½-in.–diameter benzoic acid spheres; as there is a wide discrepancy between these values of the diffusivity and the predicted values, the results of Garner and Grafton have been recalculated by means of predicted values before being combined with the results obtained in the present work.

Since a range of velocity profiles has been used in this work the choice of the velocity used in the Reynolds number is important. The first choice was the velocity at the sphere position, i.e., the approach velocity. This was taken as the average velocity over the cross-sectional area of the sphere and for parabolic flow varied between 1.94 and 1.97 times the average stream velocity, depending upon the size of the sphere. When the gauzes were in position the approach velocity was determined from the correlations of Nikuradse for the development of a parabolic front from uniform distributed flow. The variation of the mean velocity at the sphere position with pipe Reynolds number based upon the average fluid velocity is shown graphically in Figure 5.

By means of the approach velocity the results for the forward stagnation point are shown in Figure 6. Two distinct lines were obtained, one for the parabolic velocity front and the other for the distributed flow. It was then decided to use the average fluid velocity as the basis of the Reynolds number, and this produces quite satisfactory agreement between the two sets of data as shown in Figure 10. The average fluid velocity was therefore used for all the mass transfer correlations.

The experimental results and the calculated values of the film coefficient and the Sherwood number for ⅝-in.–diameter benzoic acid spheres are given in Tables 3 and 4, being typical of the results obtained.* Figures 7 to 11 show the results obtained for the over-all transfer and the transfer from the forward flow region, the wake region, the forward stagnation point, and the rear stagnation point respectively. The following expressions are proposed to correlate these results.

Over-all transfer

$$N_{Sh} = 2 + 0.95 N_{Re}^{0.5} N_{Sc}^{0.33} \quad (13)$$

Forward flow area transfer

$$N_{Sh} = 2 + 1.08 N_{Re}^{0.5} N_{Sc}^{0.33} \quad (14)$$

Wake area transfer

$$N_{Sh} = 2 + 0.67 N_{Re}^{0.5} N_{Sc}^{0.33} \quad (15)$$

Forward stagnation point

$$N_{Sh} = 2 + 1.68 N_{Re}^{0.5} N_{Sc}^{0.33} \quad (16)$$

Rear stagnation point

$$N_{Sh} = 2 + 0.87 N_{Re}^{0.5} N_{Sc}^{0.33} \quad (17)$$

All for the range $100 < N_{Re}^{0.5} N_{Sc}^{0.33} > 300$

Considerable scatter is apparent in the results shown, even for the over-all transfer. This is thought to be introduced in the measurement of the diminution from the projected silhouettes. Even though the

*Tabular material has been deposited as document 5494 with the American Documentation Institute, Photoduplication Service, Library of Congress, Washington 25, D. C., and may be obtained for $1.25 for photoprints or 35-mm. microfilm.

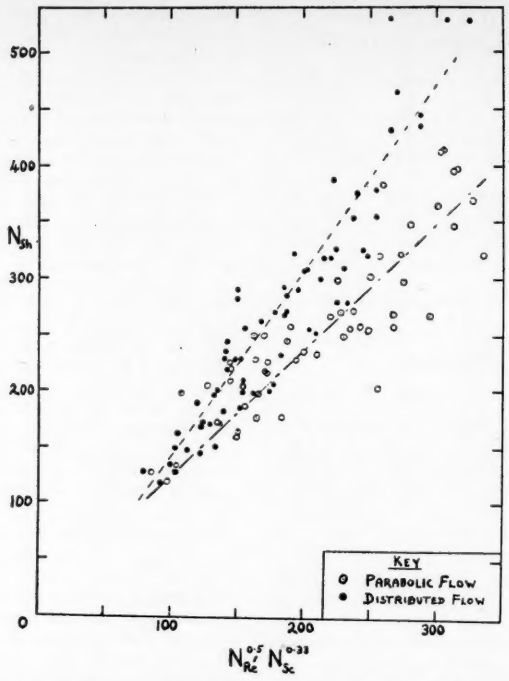

Fig. 6. Mass transfer from forward stagnation point (based on approach velocity).

projected images were approximately twelve times life size the average diminution to be measured was about 6 mm.; thus small errors in measuring either the initial or final silhouette are greatly magnified when the difference is taken. Greater dissolution is not permissible, as it would result in an appreciable change in the Reynolds number and so alter the conditions around the sphere; this change in conditions may account for some of the scatter observed at present. Ideally, the dissolution should be kept as small as possible and the magnification made much greater than that used herein.

The values reported for the separate regions of the sphere also scatter for the same reason and from an additional cause. Accurate measurement is dependent upon the final silhouette being located accurately with respect to the initial one. This was done as carefully as possible by means of the cross wires in the optical system, but again small errors here become large percentages of the actual diminution. Despite this scatter the lines are quite well defined and there is no apparent distinction between different sphere diameters, materials, or velocity profiles.

DISCUSSION OF RESULTS

The general variation of mass transfer rate over the surface of a solid sphere in a controlled stream of water is well defined and is clearly indicated by the results obtained from these dissolutions as illustrated in Figure 3. The exact form of the variation depends upon the Reynolds number of the flow, but over the range studied the example shown is typical. At lower Reynolds numbers the results of Frössling (*7*) indicate that the distribution becomes more uniform.

In general terms this distribution may be explained by means of the boundary-layer concept on the assumption that the mass transfer and hydrodynamic boundary-layer thicknesses are in a constant ratio under a given set of conditions. Progressing from the forward stagnation point around the sphere, the boundary-layer thickness increases and, as the concentration difference across the layer is constant, the concentration gradient will become less steep, thus reducing the point value of the mass transfer rate. A similar process will occur over the surface in the wake commencing at the rear stagnation point. Since the fluid within the wake is continually circulating and is not discharged into the main body of the fluid until the flow attains very high Reynolds numbers, the solute must diffuse from the outer boundary of the vortex region into the bulk of the fluid, and a relatively dilute solution is returned to the rear stagnation point. If this were not the case, the concentration in the wake would build up and the rate of mass transfer from this region would become much lower than that observed. The importance of the wake is therefore due to the large extra surface made available for transfer and to the vortex motion supplying a stream of relatively solute-free solvent to the rear stagnation point.

It will be seen from Figure 3 that there is a pronounced minimum in the mass transfer distribution over the surface. The effect of Reynolds number upon the position of this minimum is shown in Figure 12 together with the curve reported by Garner and Grafton (*9*) for the movement of the hydrodynamic separation point. The values of the Reynolds number are based upon the approach velocity, as defined earlier.

The sphere is a three-dimensional axisymmetrical body and this region of minimum transfer appears as a ring around the surface in the rear half of the sphere, but since all the mass transfer observations have been made from silhouettes the minimum transfer region is seen as two points, one near the top and the other near the bottom of the circle. Throughout this discussion therefore it is referred to as the *point of minimum transfer*. Similarly in the hydrodynamic case a ring of separation is formed at the back of the sphere, but for the purposes of this discussion this also is referred to as a point.

From simple theory it would appear that the separation point and the point of minimum mass transfer should coincide since the hydrodynamic boundary layer attains its maximum thickness at the separation point. This coincidence is observed over the central portion of the curves (Figure 12), but there is distinct separation at either end. At Reynolds numbers above 400 the minimum mass transfer occurs a few degrees behind the separation point. This appears to be due to the presence of a small region of near-stagnant fluid, immediately behind the separation point, in which transfer occurs only very slowly. As the separation point moves further back over the surface with decrease in Reynolds number the angle between the surface and the separating stream line becomes greater and there is less tendency for this stagnant pocket to be formed. The minimum transfer point is also seen to be after the observed position of separation at low Reynolds numbers. In this region, however, natural-convection currents are becoming important and these may induce conditions over the surface which correspond to a different Reynolds number from that of the main fluid stream. Observations by Keey (*15*) on mass transfer from spheres by natural convection indicate the presence of a ring of minimum mass transfer, similar to that obtained in this work, in the region of 150 deg. from the top of the sphere. This corresponds to the state of zero flow in the hydrodynamic case and the "separation point" should be at 180 deg.

For the mass transfer work in general the Schmidt number varies from about 1,100 to 2,200, and, with the Reynolds number based on the average velocity, the range covered lies between 60 and 660; the two materials used show a

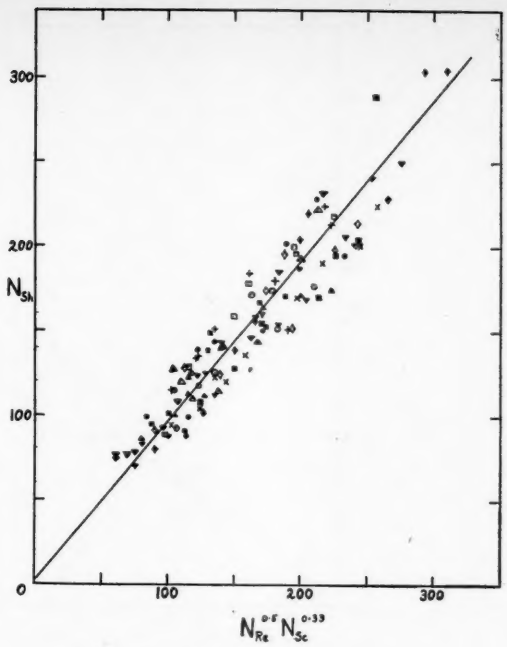

Fig. 7. Over-all mass transfer.

Sphere	Parabolic Flow	Distributed Flow
Benzoic Acid		
3/8" diam	△	▲
1/2" diam	□	■
5/8" diam	▽	▼
3/4" diam	◇	◆
Adipic Acid		
3/8" diam	⊙	●
1/2" diam	×	+

Key to Figures 7 to 15.

distinct difference in solubility, adipic acid being about five times as soluble as benzoic acid, and so it seems that the expression obtained for the over-all transfer:

$$N_{Sh} = 2 + 0.95 N_{Re}^{0.5} N_{Sc}^{0.33}$$

is of general application for values of the group $N_{Re}^{0.5} N_{Sc}^{0.33}$ between 100 and 300 and for sphere diameters not greater than 3/4 in. The inclusion of the constant term satisfies the condition derived by Fuchs (*8*) for transfer by purely molecular diffusion, but no term is included to allow for the natural-convection effects since these appear to be negligible over this range.

This independence of sphere diameter is confirmed by the work of Kramers (*14*) and Tang, Duncan, and Schweyer (*30*) on heat transfer and of Powell (*25*) and Frössling (*7*) on mass transfer. The value of the forced-convection term is in good agreement with that predicted by Grafton (*12*) from the hydrodynamic measurements used earlier in the evaluation of the drag coefficient. This agreement holds not only for the over-all transfer but also for the transfer from the individual parts of the sphere.

At values of the group $N_{Re}^{0.5} N_{Sc}^{0.33}$ less than 100 it is thought that natural-convection effects are becoming important. This is illustrated by the direction of the axis of apparent flow, which is defined as normal to the plane of minimum mass transfer and would, if there were no disturbing forces, lie along the axis of the fluid stream, i.e., along the pipe axis. In practice its position varies with Reynolds number as shown in Figure 13 for 5/8-in.-diameter benzoic acid spheres. At zero Reynolds number mass would be transferred by natural convection only and the axis of apparent flow would be vertical, i.e., at 90 deg. to the pipe axis; as the Reynolds number is increased from zero the two flows interact to produce a net flow directed somewhere between the two individual components. The actual values given in Figure 13 are only approximate since the experimental method was not designed for measurements of this nature, but the effect of increasing Reynolds number can be clearly seen. Above $Re > 100$ the effect of the natural-convection currents is relatively small and the direction of the apparent flow axis becomes constant, presumably along the pipe axis. This result is in line with the deviation noted in the lower Reynolds-number range of the separation-point curve. As a result of this rotation of the flow axis, the forward stagnation point, which in the mass transfer work is taken as the point of maximum transfer, does not coincide with the one defined from hydrodynamic considerations except for Reynolds numbers greater than 200.

Relatively little mass transfer data are available at Reynolds numbers below 60 and no precise relationship can be derived, but an indication of the behavior can be obtained as follows. If it be assumed that the expression derived by Merk and Prins (*21*) for heat transfer from spheres by natural convection, viz.,

$$N_{Nu} = 0.558(N_{Gr} N_{Pr})^{0.25} \qquad (7)$$

has a parallel in mass transfer, then the expression

$$N_{Sh} = 0.60(N_{Gr'} N_{Sc})^{0.25} \qquad (18)$$

may be obtained by making a small addition for the effect of the "tail," which is neglected by Merk and Prins. Assuming a temperature of 20°C. and taking

$$N_{Gr'} = \frac{gD^3}{\nu^2} \frac{\Delta\rho}{\rho}$$

and

$$N_{Sc} = \frac{\nu}{D_v},$$

one obtains the values listed in Table 5.

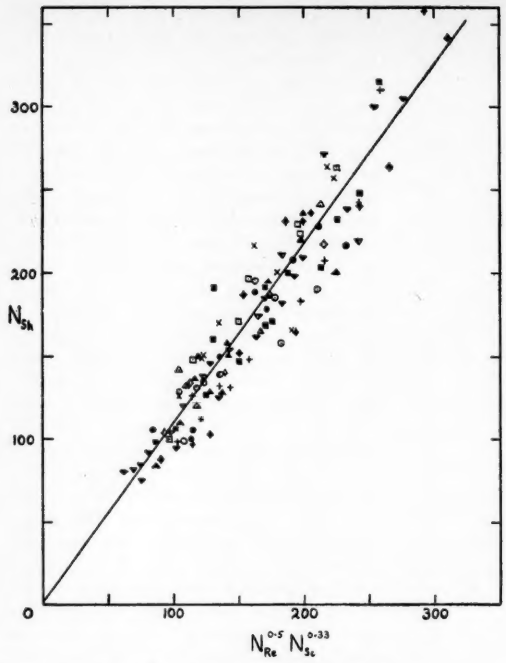

Fig. 8. Mass transfer from forward flow area. See key on Figure 7.

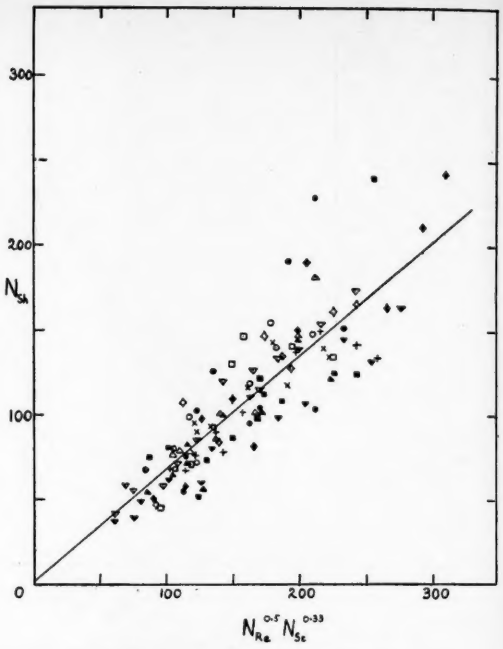

Fig. 9. Mass transfer from wake area. See key on Figure 7.

The Grashof numbers are based upon solution densities determined in this department by Keey (*15*). The transfer at zero Reynolds number can then be described by the expression

$$N_{Sh} = 2.0 + 0.60(N_{Gr'} N_{Sc})^{0.25} \quad (19)$$

which includes the term for the transfer by molecular diffusion. This shows that under these conditions the mass transfer depends upon the sphere size, but in the present study of forced convection the results for all sphere sizes fall on a common line for Reynolds numbers greater than 100 (corresponding to values greater than 110 for the group $N_{Re}^{0.5}$, $N_{Sc}^{0.33}$). So it is suggested that a series of curves exists below this value, where each curve represents the interaction between forced- and natural-convection forces for a given-sized sphere when the forces act perpendicularly, as in this work. If larger diameter spheres were used, the Grashof numbers for the natural-convection transfer would be larger and so presumably the effect would extend to higher Reynolds numbers; thus the correlation obtained in this work is limited to values of $N_{Gr'} N_{Sc} = 1.3 \times 10^8$.

This series of curves could then satisfy the theoretical requirement of Fuchs (*8*) that

$$\left(\frac{dN_{Sh}}{dN_{Re}}\right)_{N_{Re}=0} = 0$$

which is not satisfied by the general correlation proposed for high Reynolds numbers or by many of the previously reported correlations.

The apparatus used in the present work is not suitable to verify the existence of these curves, partly because of the difficulty of flow control and partly because any greater rotation of the flow axis than that experienced at present would require a complex correction for the optical distortion. To facilitate further study in this region a low-speed, vertical water tunnel is under construction; the vertical flow direction will eliminate the rotation of the flow axis due to natural-convection effects and so simplify observations.

The relative importance of the wake in mass transfer is clearly shown in Figure 14. At the lower end of the range, at $N_{Re} = 70$, the wake contributes about 8% of the total transfer; whereas above $N_{Re} \simeq 500$ the curve flattens out, with the wake contributing about 25% of the total. In the range studied there is no indication that the two halves of the sphere will become equally important as observed for cylinders at Reynolds number, 40,000 by Lohrisch (*18*).

The ratio of the mass transferred from the two areas may be written as

$$\text{ratio} = \frac{\text{mass transferred from forward flow area/sec.}}{\text{mass transferred from wake area/sec.}}$$

$$= \frac{2 + 1.08 N_{Re}^{0.5} N_{Sc}^{0.33}}{2 + 0.67 N_{Re}^{0.5} N_{Sc}^{0.33}} \frac{A_F}{A_W} \quad (20)$$

where A_F and A_W represent the surface areas covered by the forward flow and the wake respectively. Over the range to which these mass transfer relationships apply the values of the second terms are much greater than the constant term, which may therefore be neglected and the expression for the ratio reduced to

$$\text{ratio} = 1.6 \frac{A_F}{A_W} \quad (21)$$

This simple expression suggests that the wake transfer is independent of the size of the vortex region since the outer surface of this grows in extent with Reynolds number faster than the sphere surface included within the wake increases; thus the controlling factor in the total transfer from the wake region

TABLE 5

VALUES OF GRASHOF AND SCHMIDT NUMBERS FOR VARIOUS SPHERES

Spheres, diameter, in.	$N_{Gr'}$	N_{Sc}	$0.60 (N_{Gr'} N_{Sc})^{0.25}$
Benzoic acid			
3/8	3,360	1,340	27.7
1/2	7,970	1,340	34.3
5/8	15,550	1,340	40.6
3/4	26,880	1,340	46.5
Adipic acid			
3/8	34,250	1,525	51.0
1/2	81,200	1,525	63.3

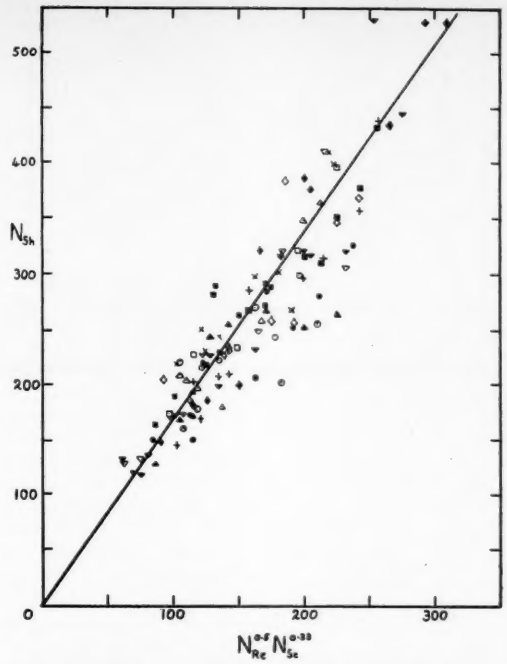

Fig. 10. Mass transfer from forward stagnation point. See key on Figure 7.

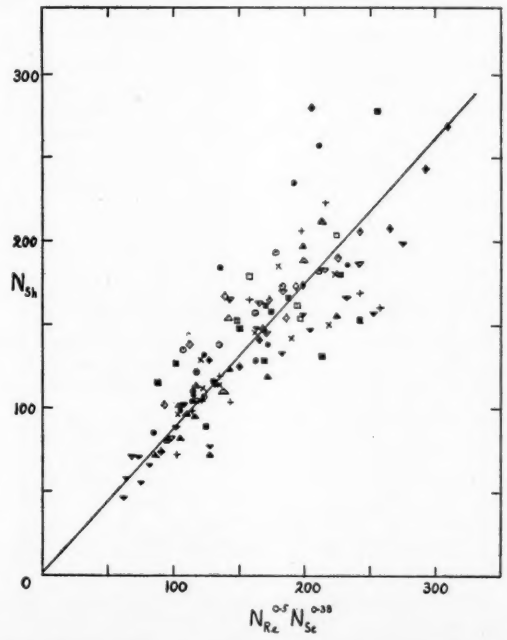

Fig. 11. Mass transfer from rear stagnation point. See key on Figure 7.

appears to be the area of solid surface included within the wake region rather than the extent of the interface available for transfer of solute from the circulating fluid within the wake to the main bulk of fluid.

Thus, over the region to which the mass transfer correlations apply, the mass transfer ratio is determined by the ratio of the areas, which in turn is determined by the position of the separation point. The curve obtained in Figure 14 is, therefore, similar to that obtained for the movement of the separation point, and the results are best correlated by the use of the approach velocity.

It appears then that the position of the separation point and the relative importance of the wake are dependent upon the conditions over the surface as defined by the approach velocity of the fluid, whereas the actual rate of solute transfer is determined by the total mass of fluid flowing. This suggests that there may be a difference between the two processes of mass and momentum transfer for the case of a sphere.

Over most of the region considered above the wakes are of the stable, circulating variety but at Reynolds numbers above 500, periodic oscillations occur at the back of the wake, according to observations reported (*9*) and these might be expected to increase the transfer from the wake. No such effect is noted in this work, but since the highest Reynolds number attained is 660 and the scatter of the data obtained for the wake is quite wide such an effect is not excluded.

ANALOGY BETWEEN MASS AND MOMENTUM TRANSFER

The idea of an analogy between heat, mass, and momentum was first proposed by Reynolds, in the form

$$\frac{K}{G_M} = \frac{h}{C_P G} = \frac{f}{2} \qquad (22)$$

where G is the mass velocity of the fluid

G_M is the molal mass velocity

and $f/2$ is the friction factor

This simple analogy applies under only very limited conditions, mainly for transfer in gases in turbulent flow. The j-factor theory proposed by Colburn (*3*) is a modified form of the original and attempts to allow for the effect of the laminar-flow region over the surface of the body. This is done by introducing the Prandtl and Schmidt numbers to produce the following empirical relationships:

$$\frac{K}{G_M}(N_{Sc})^{2/3} = j_D$$

$$= \frac{h}{C_P G}(N_{Pr})^{2/3} = j_H = \frac{f}{2} \qquad (23)$$

In this form the analogy appears to be of rather wider application although still intended primarily for turbulent-flow conditions.

The term $f/2$ is a measure of the resistance to the fluid motion and for flow in pipes is the Fanning factor. For spheres, however, only that portion of the drag due to skin friction is used since form drag is produced by the pressure difference across the sphere, which has no analogue in the other transfer processes. Moreover, it has recently been suggested by Tang, Duncan, and Schweyer (*30*) that the quantity used should be the total frictional force on the sphere surface and not the skin-friction-drag coefficient. This seems very probable since the drag coefficient contains only the component of the frictional force in the direction of flow and thus requires that the drag in the wake be subtracted from that for the forward flow area; whereas for heat and mass transfer the total transfer from the whole surface is taken, regardless of direction.

The mass transfer data obtained for the over-all transfer in the present work have been expressed in terms of the j factor and are plotted against Reynolds number based on the average velocity in Figure 15. For Reynolds numbers greater than 100 a straight line of slope -0.5 is obtained. This is in agreement with the dependence of the Sherwood number on the square root of the Reynolds number shown in Figure 7, since the j factor can be rewritten for dilute solutions as follows:

$$j_D = \frac{K}{U}(N_{Sc})^{2/3} = N_{Sh}N_{Re}^{-1}N_{Sc}^{-1/3} \tag{24}$$

Then from Figure 15

$$j_D \propto N_{Re}^{-1/2} \tag{25}$$

$$\therefore N_{Sh} \propto N_{Re}^{1/2}N_{Sc}^{1/3} \tag{26}$$

Since the j-factor theory is derived primarily for turbulent conditions no allowance is made for the effect of transfer by natural convection and so at low flow rates the transfer predicted by the relation

$$j_D = \text{constant} \times N_{Re}^{-0.5}$$

is lower than that which actually occurs. This is shown clearly in Figure 15, where the line curves upward at Reynolds numbers below 100. This also agrees with the earlier finding that natural convection becomes important in this region (Figure 13). Even in Figure 15, however, the data are too few and scattered to permit the dependence upon sphere size in this region to be determined properly.

Comparison among the three transfer processes is made in the following table and shown graphically in Figure 16.

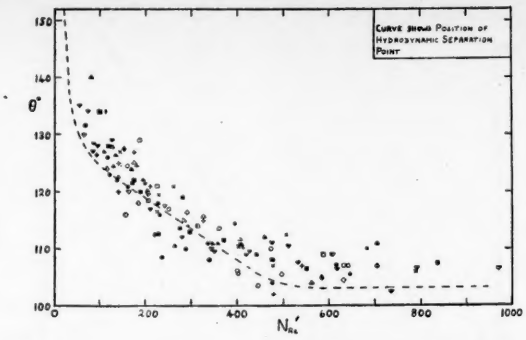

Fig. 12. Variation of position of minimum mass transfer. See key on Figure 7.

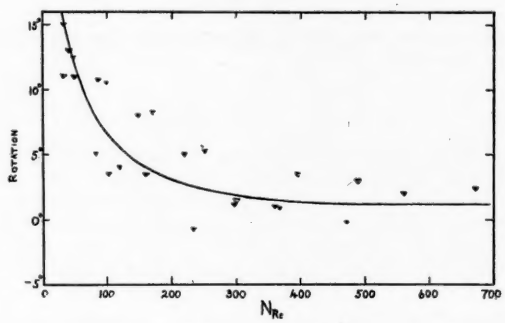

Fig. 13. Augular rotation of apparent flow axis. See key on Figure 7.

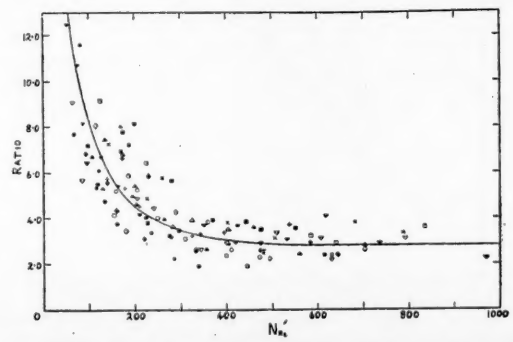

Fig. 14. Ratio of mass transfer (front: wake). See key on Figure 7.

TABLE 6

COMPARISON OF HEAT, MASS, AND MOMENTUM TRANSFER FOR SPHERES

Reynolds No.	100	200	500	1,000
j_D	0.095	0.067	0.042	0.029
j_H	0.102	0.074	0.049	0.035
$C_f/2$	0.104	0.072	0.044	0.025

The mass transfer line is that obtained in this work; that for heat transfer is as quoted by Sherwood and Pigford (*28*) and is a rearranged form of the line recommended for single spheres by McAdams (*19*); and the momentum transfer values are calculated from the skin-friction data presented earlier by means of the total frictional force and the total surface area instead of the component in the direction of flow and the sphere cross-sectional area, as in the drag-coefficient evaluation. The wake now contributes 12% of the forward flow area value compared with 7½% for the drag coefficient and a contribution ranging from 8 to 30% for the mass transfer.

Within experimental error the agreement among the three terms appears quite good and this suggests that the analogy among the transfer processes is applicable to spheres in this Reynolds-number region, when the total frictional force is used as the analogous momentum transfer quantity.

This difficulty in the selection of the analogous drag force does not arise for flow along flat plates or through pipes since form drag is absent and the frictional forces always act in the direction of flow, so that it is not necessary to consider separate components. In these cases the problem is simplified further by the absence of a wake. Thus there seems no reason why the analogy should not apply in these cases, and most experimental evidence suggests that it does. However, as a result of a study of wetted-wall columns, Stirba and Hurt (*29*) suggest that the analogy may apply only under very strictly controlled conditions. They propose that since mass is transferred by the movement of specific molecules rather than by collisions and is the slowest of the three transfer processes, it is the most susceptible to slight degrees of turbulence. This explanation is advanced to account for extremely high mass transfer rates observed in wetted-wall columns under conditions which by all hydrodynamic criteria were laminar, and it is suggested that similar slight unnoticed turbulence may exist in other mass transfer processes. By this theory the mass transfer should be greater than the term used to represent the frictional forces, and the increased transfer may be a phenomenon confined to wetted-wall columns and where there is a pseudostreamline flow at liquid interfaces.

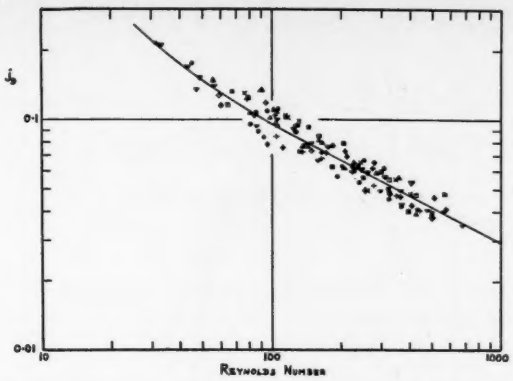

Fig. 15. Mass transfer j factor values. See key on Figure 7.

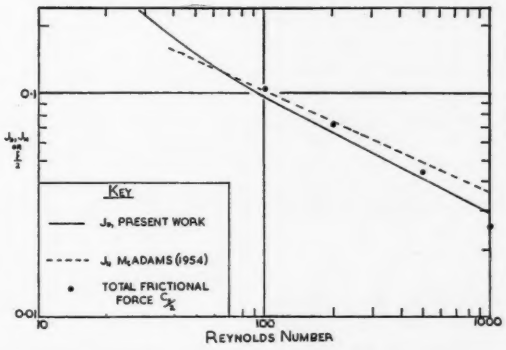

Fig. 16. Comparison of heat, mass, and momentum transfer for spheres.

Considering flow past solid bodies Sherwood (*27*) reports close agreement between the j factors for heat and mass transfer and the skin-friction-drag coefficients given by Goldstein (*11*) for cylinders at Reynolds numbers between 400 and 10,000. If, however, it is accepted that the frictional quantity most nearly analogous to the heat and mass transfer is the total frictional force as used above and not the drag coefficient, the agreement is found to be not nearly so good. From the values given earlier it will be seen that for spheres the total frictional force is about 50% greater than the corresponding value of the drag coefficient and that there must be a corresponding distinction in the case of cylinders, although possibly not so great. Thus if the drag-coefficient values and the j factors are in close agreement, the total frictional force values and the j factors cannot be and the accuracy of the analogy becomes open to question.

It also appears that the good agreement obtained for spheres in the present work may be fortuitous, for in momentum transfer a constant addition of 12% of the forward flow value has been made to allow for the effect of the wake whereas the mass transfer results indicate that the transfer from the wake varies from 8 to 30% of the forward flow value (Figure 14). If the analogy is strictly correct, the contributions of the two portions of the surface should be in the same ratio for both transfer processes, and the distributions of skin friction and mass transfer over the surface should be the same. A typical skin-friction distribution is shown in Figure 17. Comparison of this with the mass transfer distribution (Figure 3) indicates considerable dissimilarity over the forward region of the surface. This again indicates that the analogy does not apply.

CONCLUSIONS

These remarks may be summarized as follows: at low Reynolds numbers some material is transferred by the process of natural convection which has no counterpart in the transfer of momentum and so the complete analogy cannot apply; at higher Reynolds numbers, still in

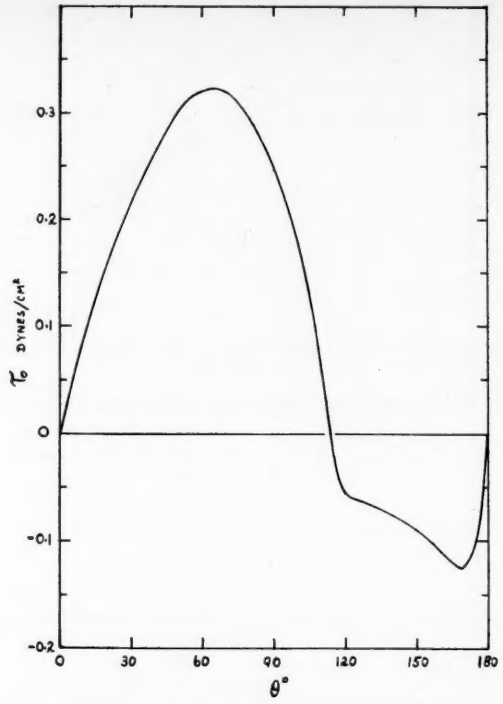

Fig. 17. Intensity of skin friction round sphere $N_{Re} = 200$.

streamline flow conditions, the distributions of mass transfer and skin friction over the surface differ so that the analogy again does not apply. Since conditions around a cylinder are similar to those around a sphere, except that the flow may be treated as two-dimensional instead of three, the same objections to the application of the complete analogy will apply.

Thus for flow around bluff bodies it seems that while the analogy between heat and mass transfer may be applicable, the extension to include momentum transfer is not.

NOTATION

C_D = drag coefficient, dimensionless
C_f = coefficient of total frictional force, dimensionless
D = diameter of sphere
D_v = diffusivity
C_P = specific heat of the fluid
g = gravitational acceleration
h = heat transfer coefficient
k = thermal conductivity
K = mass transfer film coefficient
r = radius of sphere
U_o = undisturbed velocity of flow
U = velocity at the outer edge of the boundary layer
U_{app} = fluid velocity, at sphere position
U_{avg} = average fluid velocity
β = coefficient of cubical expansion
δ = hydrodynamic boundary-layer thickness
θ = angle point of the surface subtended with the forward stagnation point
θ_1 = angle point on surface subtended with the rear stagnation point
μ = absolute viscosity
ν = kinematic viscosity
ρ = density
$\phi(\theta_1) = 1/\sin^2\theta(\frac{1}{2}\theta - \frac{1}{4}\sin 2\theta)$

$N_{Gr} = \dfrac{dD^3\beta\,\Delta T}{\nu^2}$ = Grashof number for heat transfer

$N_{Gr'} = \dfrac{gD^3}{\nu^2}\dfrac{\Delta\rho}{\rho}$ = Grahof number for mass transfer

$N_{Nu} = \dfrac{hD}{k}$ = Nusselt number

$N_{Pr} = \dfrac{C_P\mu}{k}$ = Prandtl number

$N_{Re} = \dfrac{DU_{avg}}{\nu}$ = Reynolds number based on the average velocity

$N_{Re'} = \dfrac{DU_{app}}{\nu}$ = Reynolds number based on the approach velocity

$N_{Sc} = \dfrac{\nu}{D_v}$ = Schmidt number

$N_{Sh} = \dfrac{KD}{D_v}$ = Sherwood number

LITERATURE CITED

1. Axel'rud, G. A., *J. Phys. Chem. (U.S.S.R.)*, **27**, (10), 1446 (1953).
2. Castleman, R. A., *Natl. Advisory Comm. Aeronaut. Tech. Note*, 231 (1925).
3. Colburn, A. P., *Trans. Am. Inst. Chem. Engrs.*, **29**, 174 (1933).
4. Davies, Mansel, and D. M. L. Griffiths, *Trans. Faraday Soc.*, **49**, (12), 1405 (1953).
5. Dryden, C. E., D. A. Strang, and A. E. Withrow, *Chem. Eng. Progr.*, **49**, 191 (1953).
6. Eckert, E. R. G., "Introduction to Heat and Mass Transfer," McGraw-Hill Book Company, Inc., New York (1950).
7. Frossling, N., *Gerl. Beit. zur. Geophysik.*, **52**, 170 (1938).
8. Fuchs, N., *J. Phys. (U.S.S.R.)*, **6**, 224 (1934).
9. Garner, F. H., and R. W. Grafton, *Proc. Roy. Soc. (London)*, (1954), **A224**, 64.
10. Garner, F. H. *Chem. Ind.*, p. 141 (1956).
11. Goldstein, S., "Modern Developments in Fluid Dynamics," Oxford University Press (1938).
12. Grafton, R. W., Ph.D. thesis, Univ. Birmingham, (1953).
13. Hixson, A. W., and S. J. Baum, *Ind. Eng. Chem.*, **34**, 120, (1942).
14. Kramers, H. A., *Physica*, **12**, 61 (1946).
15. Keey, R. B., Unpublished work, University of Birmingham (1955).
16. Langmuir, I., *Phys. Rev.* **12**, 368 (1918).
17. Linton, W. H., and T. K. Sherwood, *Chem. Eng. Progr.* **46**, 258 (1950).
18. Lohrisch, W., *Forsch. Arb.*, **322**, 1 (1929).
19. McAdams, W. H., "Heat Transmission," 3 ed., McGraw-Hill Book Company, Inc., New York (1951).
20. McNown, J. S., and J. T. Newlin, "Proc. First U. S. National Congress of Appl. Mech." (1951).
21. Merk, H. J., and J. A. Prins, *App. Sci. Res.*, **A4**, 11 (1953).
22. Milikan, C. B., *A.S.M.E. Trans.*, **54**, 2 (1932), *A. P. M.*, 29.
23. Morse, H. W., *Proc. Amer. Acad. Arts. Sci.*, **45**, 363 (1910).
24. Othmer, D. F., and M. S. Thakar, *Ind. Eng. Chem.* **45**, 589 (1953).
25. Powell, R. W., *Trans. Inst. Chem. Engrs.*, **18**, 36 (1940).
26. Ranz, W. E., and W. R. Marshall, *Chem. Eng. Progr.*, **48**, 141 (1952).
27. Sherwood, T. K., *Ind. Eng. Chem.*, **42**, 2077 (1950).
28. ———, and R. L. Pigford, "Absorption and Extraction," 2 ed., McGraw-Hill Book Company, Inc., New York (1952).
29. Stirba, Clifford and D. M. Hurt, *A.I.Ch.E. Journal*, **1** (2), 178 (1955).
30. Tang, Y. S., J. Duncan, and H. E. Schweyer, *Natl. Advisory Comm., Aeronaut. Note* 2867 (1953).
31. Tomotika, S., A.R.C.R. and M. No. 1678 (1936).
32. Ward, A. F. H., and L. H. Brooks, *Trans. Faraday Soc.*, **48**, 1124 (1952).
33. Whitelaw-Gray, R., and H. S. Patterson, "Smoke," Edward Arnold Company, London (1932).
34. Wilke, C. R., *Chem. Eng. Progr.*, **45**, 218 (1949).
35. ———, C. W. Tobias, and Myron Eisenberg, *Chem. Eng. Progr.*, **49**, 663 (1953).

Manuscript submitted February 4, 1957; paper accepted September 12, 1957.

Axial Dispersion and Void-cell Mixing Efficiency in Fluid Flow in Fixed Beds

JAMES J. CARBERRY, Yale University, New Haven, Connecticut

A most vital interest has recently been manifested in the subject of axial dispersion of fluids flowing through fixed beds. The contribution of Aris and Amundson in a recent issue of this Journal (*1*) demonstrates for an impulse input of tracer what Kramers and Alberda (*6*) showed for a sinusoidal input, namely that such a bed may be profitably viewed as a series of perfect mixers. Aris and Amundson further showed by a comparison of mixing and turbulent diffusion distribution functions that the limiting value of the Peclet number $D_v v/E$ should be about 2 in the range of fully developed turbulence in a packed bed. McHenry and Wilhelm (*7*) have demonstrated this point theoretically and, for gas systems, experimentally.

It is the purpose of this communication to supplement the aforementioned derivations by a consideration of axial dispersion in terms of a void-cell mixing-efficiency model (*2*).

THEORY

Axial dispersion of a fluid flowing through a vessel, pipe, or packed bed is conveniently defined for the moment as that phenomenon which results in a distribution of residence times for a differential element of fluid entering the apparatus. Thus, for a vessel of volume V, carrying a fluid entering at a volumetric flow rate F, the nominal holding or residence time is $V/F = \theta$. All species entering the vessel have a residence time equal to θ only if there exists a complete absence of forward and/or backward dispersion, termed *axial mixing.*

Unpacked Vessels

Consider the turbulent flow of a fluid in a pipe. If all entering masses of fluid are in residence for a time $\theta = V/F$, there is then no axial dispersion and this condition is achieved only at very high values of the Reynolds number. On the other hand consider the situation encountered in a well-stirred vessel where "perfect mixing" prevails. Clearly a wide distribution of residence times results in this case.

Defining an axial dispersion coefficient E by the differential equation

$$E \frac{\partial^2 C}{\partial X^2} - v \frac{\partial C}{\partial X} = \frac{\partial C}{\partial t}$$

one encounters the two extremes:

Piston flow	$E = 0$
Perfect mixing	$E \to \infty$

Consider a vessel of nominal holding time θ. If under conditions of steady state flow, a pulse of tracer material is instantaneously injected into the vessel, then the effluent concentration C as a function of time is

$$C = \frac{Q}{V} e^{-t/\theta} \qquad (1)$$

Figure 1 shows the concentration-time profile for the cases of (*a*) perfect mixing and (*b*) piston flow for an impulse input.

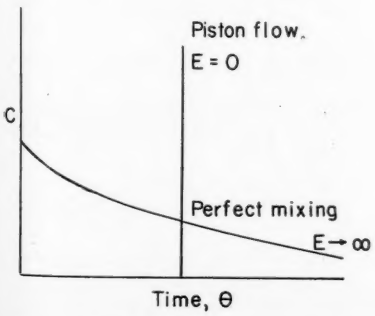

Fig. 1. Pulse dispersion for piston and perfect-mixer flow.

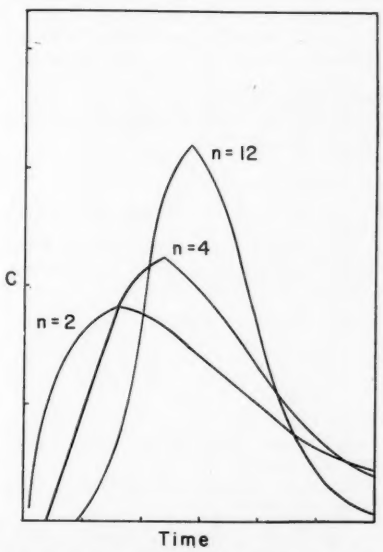

Fig. 2. Pulse dispersion in n perfect mixers. Equal total holding time.

Packed Beds

What has been said above concerning the limits of axial dispersion in unpacked conduits can, with some qualifications, be said of packed columns. Clearly the case approaching perfect mixing ($E \to \infty$) is encountered in fluidized beds, as has been demonstrated by tracer studies (*5*).

Ergun (*4*) provided substantial evidence for the existence of near-perfect mixing in fixed-bed studies. Certainly, shallow fixed beds of large diameter exhibited perfect mixer characteristics.

The other extreme, that of piston flow in any packed bed ($E = 0$), is virtually nonexistent. This may be shown simply; as any packed bed must consist of a series of randomly arrayed void cells, it is fruitful to consider the behavior of a pulse input imposed upon a series of these bed cells, each of holding time θ_n. In this case the concentration-time behavior for the effluent of the nth perfect-mixing cell is given by

$$C = \frac{G}{\theta_n^n} \frac{t^{n-1} e^{-t/\theta}}{(n-1)} \qquad (2)$$

For several beds of the same total retention time T, the cell holding time is obviously $\theta_n = T/n$. Equation (2) has been solved for three equal total-volume beds composed of two, four, and twelve perfect mixers. The resulting dispersions are plotted in Figure 2. It is apparent that the minimum dispersion occurs when n is a maximum. The limit is the case of n approaching infinity. Since any real bed consists of a finite number of cells, it is clear that even in the limiting case of perfect mixing in each void cell there exists, nevertheless, a finite axial dispersion. Hence, for a bed of many

(*Continued on page 17M*)

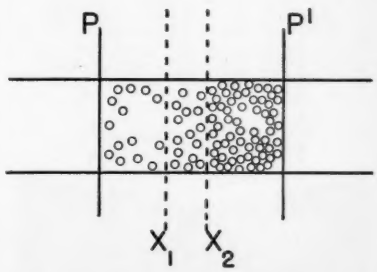

Fig. 3. Einstein's kinetic-diffusion model.

J. J. Carberry is with E. I. du Pont de Nemours & Company, Inc., Wilmington, Delaware.

Longitudinal Dispersion in a Packed Bed

J. M. PRAUSNITZ, University of California, Berkeley, California

McHenry and Wilhelm (*2*) recently reported measurements of axial diffusivity in packed beds and found good agreement between their results and those predicted on the basis of a stirred-tank model. The purpose of this note is to suggest an alternate model which gives a somewhat more detailed picture of the mechanism of longitudinal mixing. The proposed model was suggested by the work of G. I. Taylor and is, in fact, a generalization of Taylor's result (*4*) for an unpacked pipe as applied to the more complex geometry of a packed bed.

Taylor's analysis shows that the phenomenon of longitudinal dispersion is a consequence of radial mixing in a shear flow. In a packed bed radial mixing is a result of side-stepping, which occurs whenever a fluid element encounters a particle of packing and, in order to pass it, is forced to make a radial detour. In making a radial side-step the fluid element, in general, also goes to a region having a different axial velocity. Since the two necessary conditions for longitudinal dispersion, viz., radial diffusion and radial velocity gradients (within a void space), both exist in packed beds, longitudinal dispersion in such systems is to be expected.

A simple, generalized, mixing-length model for longitudinal dispersion can be developed by considering the observations made by an observer traveling with the mean flow velocity V_0. These observations are shown schematically in Figure 1. At a certain instant two events are observed:

1. Fluid element A, having coordinates $(r_0 z_{-1})$ and traveling at the mean velocity V_0, encounters a solid particle and, in order to by-pass it, side-steps to position r_1, where its velocity is changed to V_1.

2. Fluid element B, having coordinates $(r_0 z_1)$ and traveling at the mean velocity V_0, encounters a solid particle and, in order to by-pass it, side-steps to position r_{-1}, where its velocity is changed to V_{-1}.

If the flowing fluid is a solution, with the solute concentration at z_1 given by c_1 and that at z_{-1} by c_{-1}, as a result of the events described above there is a net flux of solute across the plane which is moving with the average velocity V_0:

$$(V_1 - V_0)c_{-1} + (V_{-1} - V_0)c_1 = \text{net flux} \qquad (1)$$

The velocity increments in excess of the mean can be related to the velocity gradient within a pore by the relation

$$(V_1 - V_0) = -(V_{-1} - V_0) = l_r \frac{\partial V}{\partial r} \qquad (2)$$

where l_r is a radial scale of turbulence. This radial scale represents an average side-stepping distance.

Similarly, the concentrations at z_{-1} and z_1 are related by

$$c_1 - c_{-1} = l_z \frac{\partial c}{\partial z} \qquad (3)$$

where l_z is an axial scale of turbulence. This axial scale represents an average "by-passing" distance. Substitution of (2) and (3) into (1) gives

$$\text{net flux} = -l_z l_r \frac{\partial V}{\partial r}\frac{\partial c}{\partial z} = -E_z \frac{dc}{\partial z} \qquad (4)$$

The axial eddy diffusivity E_z is therefore given by

$$E_z = l_z l_r \left[\frac{\partial V}{\partial r}\right] \qquad (5)$$

where $[\partial V/\partial r]$ is a velocity gradient which is characteristic of flow through the void spaces of a packed bed.

An approximate numerical value of the eddy diffusivity in a packed bed can be obtained by substituting into Equation (5) the results of recent concentration fluctuation studies (*3*) and by assuming a reasonable value for the characteristic velocity gradient. Concentration fluctuation data in packed beds showed that $l_r = \frac{1}{4} d_p$ and, through an approximate calculation, that $l_z = 7 l_r$. Assignment of a numerical value for the characteristic velocity gradient is necessarily somewhat arbitrary. However, from dimensional considerations a reasonable estimate is

$$\frac{\partial V}{\partial r} \approx \frac{V}{d_p} \qquad (6)$$

Substitution in Equation (5) gives an approximate numerical value for the axial Peclet group. Rounded to the nearest integer the result is

$$Pe_z \approx \frac{V d_p}{E_z} \approx 2 \qquad (7)$$

The purpose in presenting this mixing-length model is not to compute a theoretical axial Peclet group but rather to provide some insight into the fundamental difference between axial and radial mixing. The numerical value of the Peclet group calculated above is of very limited significance

(*Continued on page 22M*)

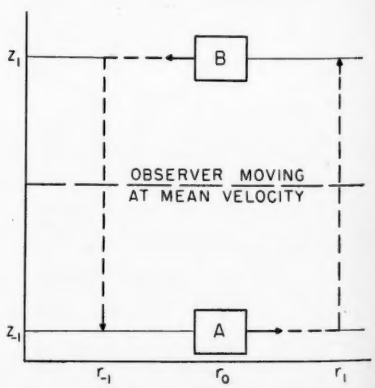

Fig. 1. Mechanism for longitudinal dispersion.

(*Continued from page 13M*)

perfect-mixing cells the axial dispersion of matter corresponds to a finite value of E.

Now consider the effects of imperfect mixing in the bed cells. Mixing efficiency is a function of turbulence and retention time for a given fluid. It follows that fluid velocity and cell size control mixing efficiency. Cell size is a function of particle diameter D_p. Thus, it may be assumed that

$$E = kD_pv \qquad (3)$$

The ratio $D_pv/E = 1/k$ is defined as the Peclet number Pe.

For a given velocity a mixing time θ_p is required for perfect mixing; the time is provided by the cell dimension (a function of D_p) and the number of such cells. Imperfect mixing may therefore be characterized as the situation where the cell retention time θ_n is less than the required perfect-mixing time θ_p. Thus more than one cell is required to achieve the perfect mixing time. For a bed of n_p void cells, the effect of imperfect mixing is to endow the bed with the dispersion characteristics of a bed of n mixers. Since $n < n_p$, a greater dispersion and therefore larger E result.

Imperfect mixing may be also viewed profitably as the result of by-passing or short circuiting and dead-space retention. This simply states that of x particles entering a void cell, a fraction passes through the cell in a time much shorter than the holding time θ_n, while another fraction is retained for a period much greater than this holding time. Obviously a distribution of retention times results which is characterized by a dispersion coefficient E. The similarity of this process to molecular diffusion offers an opportunity for a more quantitative treatment.

Fick's first law of diffusion states that the rate of species transport via diffusion is proportional to the concentration gradient; that is

$$\text{rate} = -D_m \frac{dC}{dX} \qquad (4)$$

where D_m is the proportionality constant, or diffusion coefficient. Consider a field of particles and a zone $(X_2 - X_1)$ bound by lines P and P' as shown in Figure 3. The transport of U molecules from left to right may be expressed, per unit area, as

$$U_a = \tfrac{1}{2}C_a(X_2 - X_1) \qquad (5)$$

since it is argued that probability dictates an equal chance of molecules going in either direction.

The transport from right to left is by similar reasoning

$$U_b = \tfrac{1}{2}C_b(X_2 - X_1) \qquad (6)$$

The net diffusion is then

$$U_b - U_a = \tfrac{1}{2}(X_2 - X_1)(C_b - C_a) \qquad (7)$$

Now if $X_2 - X_1$ is small, Fick's first law may be written as

$$\text{rate} = D_m \frac{(C_b - C_a)}{(X_2 - X_1)} \qquad (8)$$

The rate of net transport in a time interval θ_D is

$$(\text{rate})\,\theta_D = D_m \frac{(C_b - C_a)}{(X_2 - X_1)} (\theta_D) \qquad (9)$$

Since rate $\theta_D = U_b - U_a$, then

$$D_m \frac{(C_b - C_a)}{(X_2 - X_1)} \theta_D = \tfrac{1}{2}(X_2 - X_1)(C_b - C_a) \qquad (10)$$

which results in

$$D_m = \frac{(X_2 - X_1)^2}{2\theta_D} \qquad (11)$$

The diffusion time constant is thus

$$\theta_D = \frac{(X_2 - X_1)^2}{2D_m}, \qquad (12)$$

the well-known Einstein relationship.

Relations for a Real Bed

If a packed bed of length L, containing n mixing units, is visualized, then the height of one mixer is L/n. Since the mixing coefficient E is a measure of up- and downstream dispersion or diffusion, the time constant for axial mixing may be written

$$\theta_a = \frac{(L/n)^2}{2E} \qquad (13)$$

Fluid retention or holding time per mixing length for a bed velocity v is

$$\theta_n = \frac{L/n}{v} \qquad (14)$$

As a perfect mixer is one in which retention and mixing times are equal, then

$$\frac{L/n}{v} = \frac{(L/n)^2}{2E} \qquad (15)$$

and the number of mixers in terms of L, v, and E is

$$n = \frac{Lv}{2E} \qquad (16)$$

As $E \to \infty$ for $n = 1$, then for a small number of mixers (*6*), Equation (16) is best written

$$n - 1 = \frac{Lv}{2E} \qquad (16a)$$

From Equation (16) it follows that the height of a mixing unit is given by

$$\text{H.M.U.} = 2E/v \qquad (17)$$

Ideal Bed Model

Consider now a bed in which each cell is a perfect mixer formed by particles of diameter D_p. The length of each perfect

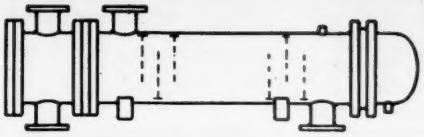

Type SG straight tube, outside packed lantern gland design. Eliminates undetected fluid inter-leakage.

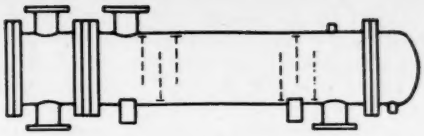

Type S pull-through floating head design. For condensing, heating services . . . easy maintenance.

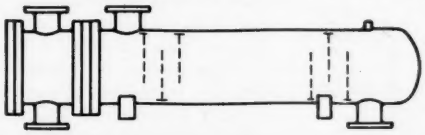

Type R U-tube design. Low cost construction, for non-fouling service.

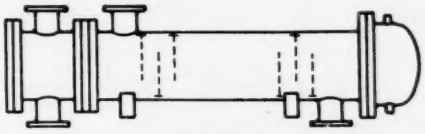

Type ST conventional straight tube, split ring, floating assembly construction.

Standardized Heat Exchangers cut your costs!

Straight tube, fixed tube sheet design. Types V and V-1—for easy mechanical cleaning.

Again and again through the years we have been called upon by customers to design and manufacture Heat Exchangers of almost identical size and construction. Now, we have standardized the building of some units most commonly ordered and can produce these quickly and economically from stock material. There are of course many other advantages to selecting Heat Exchangers of standard design, including substantial savings in their purchase price. Standard designs permit us to supply accurate prints quickly for your piping and other layouts. Also, duplicate parts can be supplied promptly if you need emergency repairs, greatly reducing downtime.

Our engineers will gladly assist you in selecting a standard Whitlock Heat Exchanger suited to your requirements. Write us and compare our prices with those of comparable equipment by any other manufacturer. Send for Bulletin 250.

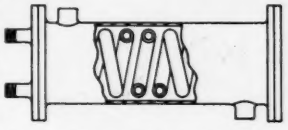

Type C coil type heat exchangers. For high tube side pressures.

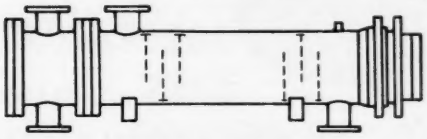

Floating head heat exchangers. Type SO with outside packed head—no concealed, bolted and gasketed joints.

THE WHITLOCK MANUFACTURING CO.
183 South Street, West Hartford 10, Conn.
In Canada: Darling Bros., Ltd., Montreal

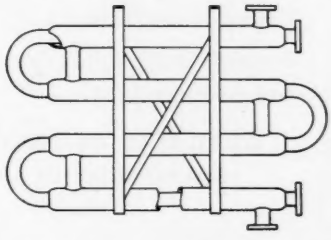

Double pipe heat exchangers. For counter-temperature flow conditions and low flow rates.

Whitlock

Designers and builders of bends, coils, condensers, coolers, heat exchangers, heaters, piping, pressure vessels, receivers, reboilers.

mixing cell will be some fraction γ of particle diameter D_p (*1*). This fraction γ will be about unity or less, depending on the packing arrangements; therefore, the number of perfect mixers is

$$n_p = L/(\gamma\ D_p) \qquad (18)$$

For any bed, one may define a mixing efficiency as the ratio of actual mixers n to the limiting number in the perfect-mixing–cell case n_p:

Mixing efficiency $e = n/n_p$ or

$$e = (Lv/2E)/(L/\gamma D_p) = D_p v/2E \qquad (19)$$

Since $D_p v/E = Pe$, then

$$e = (\gamma/2)Pe \qquad (20)$$

As γ is a constant for a fixed bed, then Equation (20) expresses the quantitative relationship between the Peclet number for axial dispersion and void-cell mixing efficiency. Further, the limiting value of the Peclet number is easily predicted from the foregoing argument, for as the void cells approach the perfect-mixer ideal, $e \rightarrow 1$ and

$$Pe = 2/\gamma \qquad (21)$$

Since γ is approximately 1, then the limiting value of the Peclet number is about 2. Equation (21) can be rewritten

$$Pe = 2/(\gamma/e) \qquad (22)$$

if

$$\gamma/e = l \qquad (23)$$

Then l is simply a measure of mixing length for any bed.

$$l = 2/Pe = 2E/D_p v \qquad (24)$$

i.e., l is the number of particle diameters equivalent to one mixing unit.

Since by Equation (17) H.M.U. $= 2E/v$ then

$$l = \text{H.M.U.}/D_p \qquad (25)$$

Thus by utilization of Einstein's simple diffusion model in terms of mixing inefficiency in a void cell, it is shown how the Peclet number is directly related to void-cell mixing efficiency in a packed bed; further, the limiting value of the Peclet number is derived in a manner which is both simple and logical.

In addition, insofar as the friction factor for packed beds reflects to some degree cell turbulence in terms of expansion and contraction losses, one may predict a marked decrease in the height of a mixing unit as the character of fluid flow approaches the regime of incipient and developed turbulence in a packed bed. It follows that significantly high values of H.M.U. will be encountered in the low flow regions usually employed in many fixed-bed processes such as ion exchange. Results of axial dispersion studies (*2*) soon to be published (*3*) confirm these comments.

NOTATION

C	=	concentration of tracer
D_p	=	particle diameter, length
D_m	=	molecular diffusivity, length²/time
e	=	cell mixing efficiency
E	=	axial dispersion coefficient, length²/time
F	=	volumetric flow rate, volume/time
G	=	constant
H.M.U.	=	height of a mixing unit, length
k	=	proportionality constant, Equation (3)
l	=	number of particle diameters per mixing length
L	=	bed length
n	=	number of mixers, $L_s/2E$
n_p	=	number of perfect mixers, $L/\gamma D_p$
Pe	=	Peclet number, $D_p v/E$
Q	=	quantity of injected tracer
t	=	time
T	=	total residence time
U	=	number of particles transported in a diffusion field
v	=	average fluid velocity in packed bed, length/time
V	=	vessel volume
X	=	distance parameter in Einstein model
γ	=	fraction of a particle diameter equal to a perfect-mixer length
θ	=	holding time
θ_n	=	cell holding time
θ_p	=	perfect mixing time

LITERATURE CITED

1. Aris, Robert, and N. R. Amundson, *A.I.Ch.E. Journal*, **3**, 280 (1957).

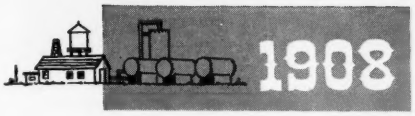

1958

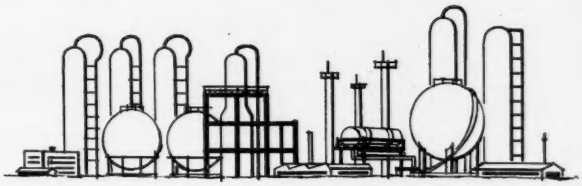

this GOLDEN ANNIVERSARY is your GOLDEN OPPORTUNITY!

May 1958 CHEMICAL ENGINEERING PROGRESS will be a spectacular issue commemorating the "Chemical Engineers' Golden Jubilee"

The American Institute of Chemical Engineers' 50th Anniversary marks a major milestone in the progress of the Chemical Process Industries, from the celluloid era to today's rocket fuels. From vital discoveries in basic research, through the entire scope of chemical engineering, A.I.Ch.E. will celebrate fifty fabulous years of achievement.

A salute to the past is only part of the celebration. The main theme of the Jubilee program next June at Philadelphia will be "A Look to the Future." Here is the real significance of May CHEMICAL ENGINEERING PROGRESS for all advertisers—chemical engineers dedicated to the growth and development of all chemical industries.

This is truly a *golden opportunity* for manufacturers to instill both their corporate and their product messages in the minds of responsible chemical engineers—men whose decisions are essential to the purchase and specification of practically all chemicals, equipment, materials and engineering services in the chemical process industries.

Highlights of May C.E.P. include a History of Chemical Engineering and A.I.Ch.E., and a survey of Chemical Engineering Around the World, plus other fascinating features and timely engineering articles. This matchless editorial selection insures intensive readership.

Take full advantage of this unusual opportunity to invest in your company's future in the growing C.P.I. Join the many advertisers who are planning special product progress stories to relate their company growth to the Golden Jubilee of A.I.Ch.E.

The May 1958 issue of C.E.P. will be a big issue—your big opportunity to get big results. Be sure to reserve *adequate* space.

CEP CHEMICAL ENGINEERING PROGRESS

Published for chemical engineers by the
American Institute of Chemical Engineers
25 West 45th Street, New York 36, N. Y.

50 FABULOUS YEARS OF ENGINEERING ACHIEVEMENT

2. Carberry, J. J., D. Eng. dissertation, Yale Univ., New Haven (1957).
3. ———, and R. H. Bretton, to be published.
4. Ergun, S. K., *Chem. Eng. Progr.*, **48**, No. 5, 227 (1952).
5. Gilliland, E. R., and E. A. Mason, *Ind. Eng. Chem.*, **47**, 1191 (1949).
6. Kramers, H., and G. Alberda, *Chem. Eng. Sci.*, **2**, 173 (1953).
7. McHenry, K. W., and R. H. Wilhelm, *A.I.Ch.E. Journal*, **3**, No. 1, 83 (1957).

(*Continued from page 14M*)

because of the uncertainties in the approximations involved; the very good agreement with experimental results is probably fortuitous. However, even if somewhat different approximations had been used, the order of magnitude would still have been correct.

An interesting consequence of the mixing-length model is that it provides a qualitative prediction of the effect of void fraction on the axial Peclet group. As the void fraction rises, the bed becomes more loosely packed. The mixing-length model suggests that this loosening is accompanied by a small decrease in the velocity gradient and a slight increase in radial scale l_r. To a first approximation these effects will tend to cancel one another. However, the axial scale l_z, which is a measure of the by-passing length, would be expected to increase considerably. As a result the model predicts that an increase in void fraction produces a larger axial eddy diffusivity or a smaller Peclet group. Current experimental work (*1*) at Berkeley confirms this result.

ACKNOWLEDGMENT

The author is grateful to Theodore Vermeulen for helpful discussions.

LITERATURE CITED

1. Jacques, G., and Theodore Vermeulen, paper to be published.
2. McHenry, K. W., and R. H. Wilhelm, *A.I.Ch.E. Journal*, **3**, 83 (1957).
3. Prausnitz, J. M., and R. H. Wilhelm, *Ind. Eng. Chem.*, **49**, 978 (1957).
4. Taylor, G. I., *Proc. Roy. Soc.* (*London*), **A223**, 446 (1954).

INDEX OF ADVERTISERS